

# POLITECNICO DI TORINO

Corso di Laurea Magistrale

in Ingegneria Biomedica

Tesi di Laurea Magistrale

Design and test of bioinspired specimens by using  
tensile testing machine and Digital Image Correlation



Relatori

Prof. Cecilia Surace

Prof. Oliver Ruiz Grimaldo

Candidato:

Elena Ingrassia

Anno Accademico 2020/2021

## Abstract

The aim of this work is to identify, among several materials, the most suitable to simulate the mechanical behavior of an anatomic tendon/ligament, with the ultimate goal of inserting it in a 3D multi-material model for surgical training applications. For this purpose, dog-bone-type specimens with bioinspired patterns were designed and obtained using the Stratasys 3D J750™ Digital Anatomy™ Printer (DAP), combining the same polymeric material (Agilus30) with different hardness values. A biomimetic approach was followed taking into account some natural hierarchical structures, such as tendon and bamboo, which improve mechanical properties on a macroscopic level. To better characterize the mechanical behavior of these specimens, two different techniques were employed, uniaxial tensile test and Digital Image Correlation (DIC). The latter, particularly, also aimed to verify the reliability of the standard used to compute the mechanical parameters. The obtained data showed an inconsistency between the strain obtained from the mechanical tests following the ASTM D638 Standard and the strain obtained in optical way by using the DIC. The conclusion was that the latter was a more accurate method than the other, since the whole field of deformation is analyzed, not only that of the constant section of the specimen. A comparison between the mechanical features of the specimens allowed to evaluate the most performing combinations of hardness value and pattern. Basing on such considerations and keeping the same fiber/matrix ratio, other two patterns were designed, inspired by highly performant materials, jute and nylon. Then, these specimens underwent a FEM analysis to evaluate how, by modifying only the pattern, the specimens' mechanical response could vary.



# Summary

<b>1. Introduction</b>	<b>1</b>
1.1 <i>Hierarchical structures in natural and man-made materials</i>	1
1.1.1 Tendon/ligament	1
1.1.2 Wool	2
1.1.3 Silk	3
1.1.4 Bamboo	4
1.1.5 Jute	5
1.1.6 Flax (Linen)	6
1.1.7 Hemp	7
1.1.8 Nylon	7
1.2 <i>Three-dimensional (3D) printing</i>	8
1.2.1 Additive manufacturing different methods	8
1.2.2 General and medical applications	11
1.2.3 Stratasys 3D J750™ Digital Anatomy™ Printer (DAP) and available materials	12
<b>2. Mechanical theoretical background</b>	<b>15</b>
2.1 <i>Standards for the mechanical characterization of the proposed pattern</i>	15
2.1.1 ASTM D638 – 14	15
2.1.2 ASTM D412 – 16	15
2.2 <i>Mechanical tests theory</i>	15
2.2.1 Tensile test	16
2.2.2 UTS tensile testing machine	16
2.2.3 Stress-strain curve	19
2.3 <i>Tendon/ligament mechanical behavior</i>	20
2.3.1 Pathological conditions	22
<b>3. Digital Image Correlation</b>	<b>23</b>
3.1 <i>Introduction</i>	23
3.1.1 Basic principles of the Digital Image Correlation	23
3.1.2 History	23
3.1.3 DIC vs traditional techniques	23
3.2 <i>DIC working principles</i>	24
3.2.1 Speckle pattern preparation	24

3.2.2	Image acquisition .....	26
3.2.3	Image analysis .....	30
3.3	<i>VIC-3D System (VIC-EDU)</i> .....	34
3.3.1	Equipment.....	34
3.3.2	VIC-3D software .....	35
3.3.3	Testing guide .....	35
<b>4.</b>	<b>Design and preparation of the specimens .....</b>	<b>43</b>
4.1	<i>Polymeric materials to mimic tendon/ligament behavior</i> .....	43
4.2	<i>Pattern layouts</i> .....	44
4.2.1	Tendon-like (TL) pattern .....	45
4.2.2	Tendon-mimic (TM) pattern .....	46
4.2.3	Bamboo-like (BL) pattern .....	47
4.2.4	Helix bamboo-like (HB) pattern .....	48
4.3	<i>Shore A values combinations</i> .....	49
4.3.1	TL pattern hardness values .....	50
4.3.2	TM pattern hardness values .....	50
4.3.3	BL pattern hardness values .....	51
4.3.4	HB pattern hardness values .....	51
4.3.5	Base materials .....	52
4.4	<i>3D Printing of the specimens</i> .....	52
<b>5.</b>	<b>Mechanical tests and results.....</b>	<b>54</b>
5.1	<i>Experimental setup</i> .....	54
5.1.1	Setup of the UTS (UltimateTensile Stress) testing machine and output .....	55
5.1.2	DIC setup and calibration .....	55
5.2	<i>Post processing</i> .....	59
5.2.1	Processing of the mechanical data .....	59
5.2.2	Processing of the DIC data .....	67
5.2.3	Direct measurements vs DIC system .....	73
5.3	<i>Discussion and conclusion</i> .....	108
<b>6.</b>	<b>Design and testing simulation of the new patterns .....</b>	<b>115</b>
6.1	<i>YS and JF: new bioinspired pattern</i> .....	115
6.2	<i>Finite element (FEM) mechanical simulation</i> .....	116

6.2.1	Model setup .....	116
6.2.2	Analysis settings.....	121
6.2.3	Results.....	122
6.3	<i>YS and JF patterns vs specimen V</i> .....	127
6.3.1	Testing machine stress vs equivalent stress .....	127
6.3.2	Deformation along Y-axis vs extensometer E2 .....	129
6.4	<i>Final considerations about the two new patterns</i> .....	130
<b>7.</b>	<b>Conclusions and future developments .....</b>	<b>132</b>
	<b>Figures summary .....</b>	<b>133</b>
	<b>Tables summary .....</b>	<b>137</b>
	<b>References .....</b>	<b>138</b>



# 1. Introduction

## 1.1 Hierarchical structures in natural and man-made materials

During the decades Nature has developed materials with several optimized properties simultaneously, as strength, stiffness or compliance [1]. The exceptional properties of these materials are attributable to their hierarchical structure, particularly to its functional adaptation at all levels of hierarchy [2]. Hierarchical structures are assemblages of molecular aggregates, with the addition of other phases [1]. The composite is organized in discrete levels of scales [3], whose number defines the hierarchical order [1]. The material shows different features and properties between the molecular, nanoscopic, microscopic, and macroscopic scales [3], [4]. The mechanical properties are modulated and optimized by specific interactions between the hierarchies. In every material, it is possible to identify a RVE, that is the smallest volume which have the same mechanical or physical properties of the whole [1]. Despite being really complex structures, an adequate adhesion between components gives the whole system structural integrity [3]. Hierarchical structures can be found in both natural and man-made materials [1], even if the strategies of Nature are different than those of Engineering: the sets of elements, the way they are made, and the adaptation capability to changing environmental conditions are not comparable [2].

Almost all biological load-bearing materials are composed of fibers, which optimize the mechanical behavior of the systems. The nature of the fibers gives the whole structure several features:

- Anisotropy, because the direction of the fibers influences the properties of the material.
- Hierarchies, because of the assembly of microfibrils in fibers.
- Heterogeneity.
- Non-linear stress-strain curve [1].
- In general, strength in tension, but weakness in compression [2].

Therefore, fibers are ideal tension elements [1]. They can be based on different chemical substances: polypeptides, polysaccharides, and chitin [1], [2].

### 1.1.1 *Tendon/ligament*

Examples of protein-based (polypeptides) fibrous materials are the tendon and the ligament, which have the same type of collagen fibrils as bone, but they are not mineralized [2]. Both are composed of dense connective tissue, but with different morphology and function. Ligaments originate and insert on bones, binding them together, to maintain correct bone and joint geometry. Tendon, instead, connects the muscle to the bone, by transmitting to it forces and displacements to stabilize them or produce motion [3]–[6]. They have similar compositions: water, collagen, elastin, and proteoglycans. In ligament, collagen (70-80%) is primarily of type I with some type III, while in

tendon collagen type I is 95% and collagen type V is also present; these types vary their amount during tissue development. The elastin is about 10-15% in ligament, but less than 3% in tendon composition [4], [6]. Their structure is hierarchically organized in the same way, except that, in tendon, collagen fibers are arranged into bundles (or fascicles), groups of parallel fibers, that are difficult to separate because they are strictly interconnected [5]. Fascicles are supported by the endotenon, a perfused and innervated connective tissue [6]. The collagen structure has six discrete scales of architecture (Fig. 1), which can be seen through scanning electron microscope (SEM), optical microscope (OM), electron microscope (EM), and X-ray diffraction (x ray). It progressively becomes more complex from nano- to macroscales [3]. At the molecular level, three alpha-helix chains coil together to form the tropocollagen molecule, with a triple helix structure. Five tropocollagen molecules aggregate to form a microfibril, with a diameter of about 40 Å; it is held together with hydrophobic interactions. Microfibrils associate to form a subfibril (20 nm in diameter) and then fibrils (50-500 nm in diameter). At the top of the scale there are collagen fibers (100-300 μm). In the tendon only, these building blocks are further grouped in parallel arrangements to form fascicles or fiber bundles [3], [6], [7]. Tendon fascicle is a composite of collagen fibrils in a proteoglycan-rich matrix, which binds the fibrils together [2], [7]. Finally, at the largest scale, groups of fascicles are bound together to form the tendon organ [4]. At all the hierarchies, the orientation of the components is along the axis of the tendon; therefore, the structure, which is subjected almost exclusively to uniaxial tension, perfectly withstands deformations in this direction [3]. However, in many ligaments the collagen fibers are not strictly parallel; indeed, the ligament adapts to provide optimal strength at each angle of the joint [6].

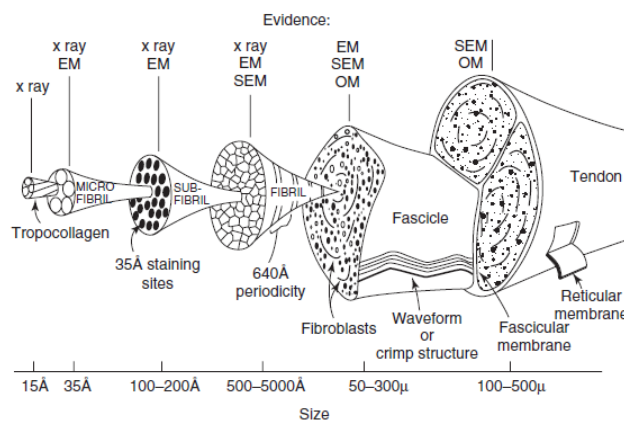


**Figure 1.** Hierarchical structure of collagen fibers in tendon [4].

### 1.1.2 Wool

Wool is a multicomponent fiber (Fig. 3), classified as a composite structure, which allows its warmth-retaining and many other properties [8]. It is a protein-based material, chemically composed of  $\alpha$ -keratin, a fibrous protein, mainly characterized by carbon, hydrogen, nitrogen, and sulfur. The large amount of lipids and carbohydrates strongly affects the fibers' function and properties. The three main components of the wool fiber are cuticle, cell membrane complex (or medulla) and cortex (Fig. 2) [9], [10]. Cuticle surrounds the fiber, forming its surface structure, and consists of three major components: epicuticle, exocuticle, and endocuticle. The epicuticle is the exterior resistant and

hydrophobic layer [10]. The exocuticle contains a great amount of cystine cross-links, giving an extreme insolubility to the material. The endocuticle is the inner part of this structure and is the most vulnerable part. The cuticle cells are responsible for several surface unique properties of wool fibers, such as felting and shrinking, due to their overlapping cuticular scales (Fig. 2) [9], [10].

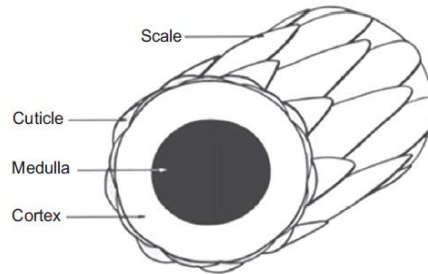


**Figure 2.** Three main components of wool fiber [10].

Cortex, with a 20  $\mu\text{m}$  diameter, includes para-cortex and ortho-cortex cells, which play a determinative role in physical, chemical and mechanical properties of wool. These two cells have a helical bilateral arrangement along the fiber axis, which gives a crimp structure to the wool fibers [10]. The elementary unit of the wool fiber is called protofibril and has a 2 nm diameter. In a protofibril there are three  $\alpha$ -helix molecules, which occupy 64.6% of the total CSA. Eleven protofibrils form a rod-like microfibril of 7-8 nm diameter and take up 68.8% of the CSA of this latter structure. The cortical cells, which have a 4  $\mu\text{m}$  diameter, are made of macrofibrils (diameter of 0.4  $\mu\text{m}$ ), arrangements of microfibrils, which are helically wound in a compact assemblage only in ortho-cortex cells. As a result of the analysis carried out by *Fan et al.*, the microfibrils occupy 70% of the total CSA of the cortex [8].

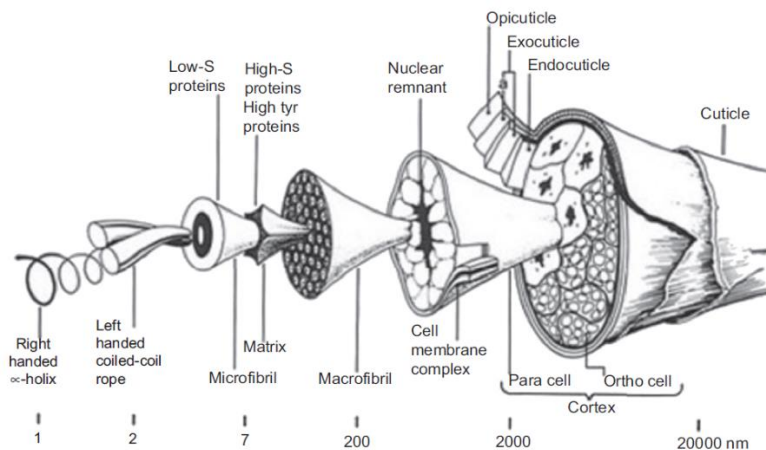


**Figure 3.** Hierarchical structure of a wool fiber [10].

### 1.1.3 Silk

Silk fibers are protein-based materials. In nature, silks are produced by several different organisms, such as silkworms, honeybees, spiders, beetles, ants, mussels, and certain crustaceans [11]. The mechanical performances of silk fibers, as for the other hierarchical structures, are largely controlled by the fibers' unique structures and the specific cooperativity of the different layers, whose size has a range between the nano- and mesoscale level [11], [12]. One single silk fiber is a bundle of thinner

fibrils aligned along its long axis. The fibers have a width which ranges from nanometers to sub-micrometers [13] and have a five levels hierarchical architecture (Fig. 4). Their primary structure is a sequence of amino acids and is what determines the variation of the mechanical properties from an organism to another. There are two basic structural proteins in this sequence, fibroin and sericin proteins. The latter acts as the glue that links the formers, forming H-chains, which are responsible for the unique mechanical behavior, as they can self-assemble through hydrogen bonds into discrete  $\beta$ -sheet nanocrystals ( $\beta$ -crystallites) or  $\alpha$ -helices, the secondary structure of the silk fibers.  $\beta$ -crystallites give silk materials stronger mechanical properties, while  $\alpha$ -helices can lead to better extensibility. The tertiary structure, of the order of 10-20 nm, is a highly compact and organized 3D protein structure, being composed of  $\beta$ -sheets from different molecules bound by weak interactions. At the fourth level there are the mesoscopic structural units of silk's hierarchical structure, that are the nanofibrils (100 nm), each of which is a  $\beta$ -crystallite network, made of amorphous chains that link the crystallites together. The next level (five) is a network of highly well-oriented, twisted nanofibrils, bound by strong physical contact when forming the silk fibers, which have a size of 1-2  $\mu\text{m}$ . Finally, at the macroscale, the silk fibers compose, for instance, a spider web [11], [12].

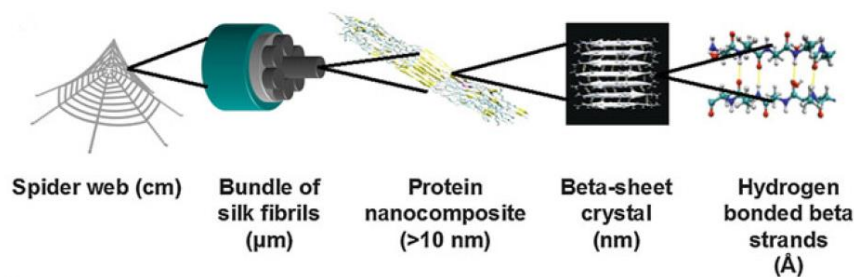


**Figure 4.** The five levels of the hierarchical structure of spider silk [11].

### 1.1.4 Bamboo

Bamboo fibers belong to the polysaccharides-based materials [1], since they are composed of cellulose. They are stalk fibers, being collected from the stalks of the plant [14]. They have been long used for several industrial applications, such as textiles, paper, and construction, due to some advantages that characterize them, like mechanical properties, low price, sustainability, durability, biodegradability, and rapid growth rate [15]. Their structural details were examined by means of swelling experiments and the results were analyzed through light microscope and X-ray diffraction studies [16]. On the macroscale the bamboo fiber is a hollow tube with micron-scale fiber bundles organized into a polylamellate structure with alternating broad and narrow lamellae [15], [16]. The conducting elements, like vessels, sieve tubes, and companion cells, are located within the fiber. It has a hierarchical structure, because between micro- and nanoscale every fiber is organized in fiber bundles dispersed in a lignin matrix, which holds the cellulose microfibrils together (Fig. 5) [15]. In the polylamellate construction the cellulose microfibrils of the two alternated layers have a crisscross arrangement. Indeed, the microfibrils of the narrow lamellae have a perpendicular orientation to the longitudinal axis of the fiber, while in the broad lamellae they are oriented almost parallel to this axis, even if a slight gradual increase in the angle from the middle lamella to the

lumen can be seen [16]. This hierarchical structure gives to the bamboo fiber really good mechanical properties, such as extremely high tensile strength, flexural strength, and global rigidity. The modulus of elasticity is positively maximized by the axial orientation of the bamboo microfibrils in the fiber and their lignification increases the transverse rigidity [15]. The degree of lignification differs among the lamellae: in the narrow layers there is a higher lignin content than in the broad ones [15], [16]. By measuring the mechanical behavior of various bamboo structural entities, it has been demonstrated that a single bamboo fiber has better mechanical properties than a fiber bundle. This is because its strength is higher than that of the bond between bamboo fiber and the matrix [15].

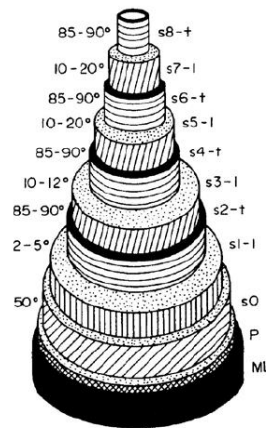


*Figure 5. Hierarchical arrangement of a bamboo fiber with its polylamellate structure [16].*

### **1.1.5 Jute**

Like the bamboo fiber, the jute belongs to the plant fibers, being composed of cellulose. It falls into the bast fiber or skin category, since it is collected from the skin or bast surrounding the stem. It is one of the most common used plant fibers [14]. It comes in two varieties: white jute and Tossa jute, which is soft, smooth and stronger than the other [17]. The fibers are off-white to brown and have a length of 1-4 meters [18]. Jute fiber is composed of 64.4% cellulose, 12% hemicellulose, 11.8% lignin, and contains other elements, such as pectin, water soluble, wax and water [14], [17]. It is a multicellular fiber, formed as a cylindrical sheath made with single fibers joined together by a 3D network from top to bottom of the stem. Each fiber is a group of about 5-15 cells, composed of cellulose-based helical crystalline microfibrils (helical angles: 20-30 degrees), connected to a complete layer by amorphous lignin and hemicellulose. These cells have a polygonal cross-section with rounded corners, divided by this natural cement, called middle lamella. Each cell has thick cell wall and lumen, the central canal with about oval cross-section (Fig. 6). The composite cell wall is made by sticking together multiple layers in one outer thin primary and three inner thick secondary cell walls. The cell walls differ in composition and in the spiral angle of the cellulose microfibrils: in the primary wall the fibrils are arranged in crisscross manner, whereas in the secondary wall fibrils are almost spiral wound and parallel, as shown in fig. 6 [14], [17], [19]. The tensile properties of the jute fiber are influenced by its diameter, which can vary between 40 and 80  $\mu\text{m}$ , producing a tensile strength ranging from 1000 to 480 MPa [14], [17]. It has high specific properties, such as a high

tensile strength and stiffness and low density and extensibility. Moreover, it has a good dimensional stability [17], [18].

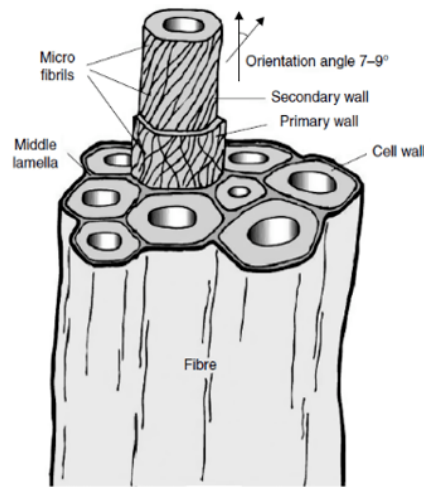


Figure 6. Jute fiber hierarchical structure [19].

### 1.1.6 Flax (Linen)

Flax fibers belong to the group of bast (stem) fibers too. At the macroscopic level, a flax stem is composed of bark, phloem, xylem, and a central void. The cross-sectional area of a single bundle contains between 10 and 40 fibers, linked mainly by pectin. The microscopic architecture of a flax fiber has a hierarchical organization, being made of concentric cell walls with a small open channel in the middle, that is the lumen (Fig. 7). There is an outer layer with a flexible primary wall (0.1 – 0.5  $\mu\text{m}$  thick), coated with a polymer matrix. This wall is composed of unaligned fibrils providing a superficial protective layer. 80% of the fibre cross-section is composed of a secondary wall, made of 3 sub-layers (S1, S2 and S3) and several microns thick. Each of the sub-layers is characterized by a particular angle that the aligned fibrils make with the fiber axis. S2 contains numerous crystalline cellulose micro-fibrils and amorphous hemicellulose which form an angle of  $10^\circ$  with the fiber axis and give fiber its high tensile strength. These microfibrils are constituted of cellulose chains in an amorphous matrix and are grouped in longitudinal bundles distributed circularly around a central wooden cylinder, to form mesofibrils. [14], [20], [21].

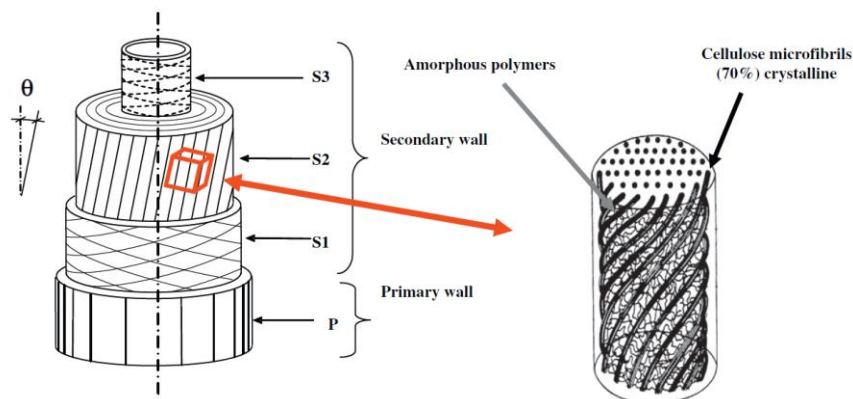


Figure 7. Hierarchical structure of flax fiber, showing the different arrangement of the microfibrils in the sub-layers ( $\theta=10^\circ$ ), with a zoom on the composition of a bundle of microfibrils (mesofibril).

### 1.1.7 Hemp

Hemp fiber is one of the strongest and stiffest natural fibers. Its cross-section has an irregular shape along its length, having a diameter which ranges from 0.6 to 4.5 cm. It consists of different hierarchical microstructures, as shown in fig. 8. The primary bast fibers are in the phloem and consist of a bundle of fibers crossing the whole plant stem in length. They are composed of about 70% cellulose, 18% hemicellulose, 5% lignin, 0.8% pectin, and 6.2% wax. Each constituent contributes to give the overall properties to the fiber. The bast fiber has a multi-celled structure, containing numerous lumens fixed together with a pectin-lignin matrix, each of which represents the next level of microstructure, the technical fiber, which has a diameter ranging from 50 to 100  $\mu\text{m}$ . This fiber contains elementary fibers bonded together with lignin and pectin. A typical elementary fiber, which has a diameter of approximately 22-25  $\mu\text{m}$  and a length of 15-25 mm, has a multi-layered cell wall with a primary and a secondary wall, made of three layers, as the flax. The different cell wall layers are made up of macrofibrils (diameter of 10-50 nm), a group of microfibrils embedded in a matrix of hemicellulose. The smallest building element (basic unit) of the cellulose skeleton is the microfibril, which has a diameter of about 5-10 nm and a length ranging from 100 nm to several micrometers. It is made up of amorphous and crystalline parts [22]–[24].

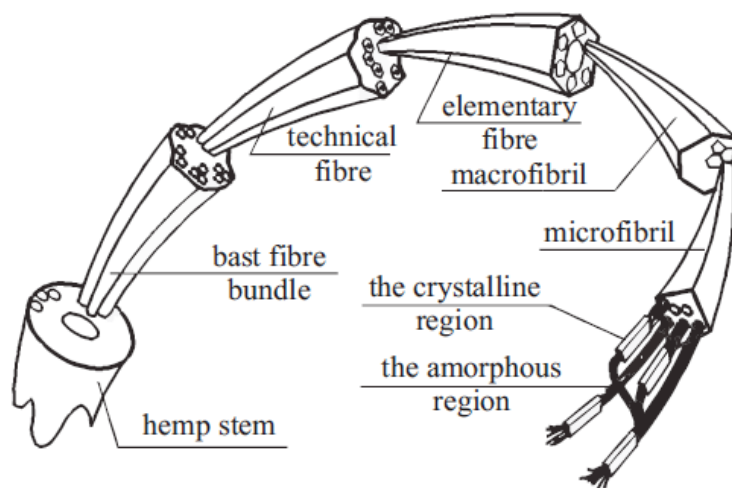


Figure 8. Hemp fiber hierarchical structure [25].

### 1.1.8 Nylon

Nylon is a high-performance synthetic fiber, belonging to the category of the organic fibers. These fibers are often similar to the natural textile fibers in appearance, but they are produced to enhance their mechanical performance [26]: the nylon fibers are more than twice stronger than the hemp fibers, but they have a 25% lower weight. They are also known as Polyamides (PA), being made up of repeating units linked together by amide bonds [27]. In fact, this synthetic material must firstly undergo a condensation polymerization, by linking monomers containing terminal carboxylic acid ( $-\text{COOH}$ ) and amine ( $-\text{NH}_2$ ) groups together to form a chain, as shown in fig. 9, and then it must be extruded into fibers [28], [29]. The nylon molecules are linear but not perfectly aligned parallel to the fiber axis, so they have a low Young's modulus. The fibers are composed of 5 nm-thick microfibrils, connected by well-ordered molecules, folded as in a concertina. In the remaining

regions, there are less well-ordered molecules with an overall semi-crystalline structure with a crystalline content of the order off 40%. The single fiber has a diameter of 30  $\mu\text{m}$  [26].

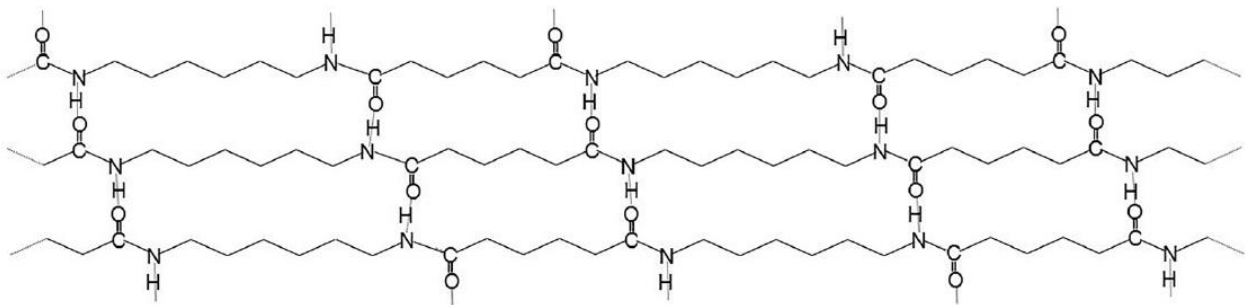
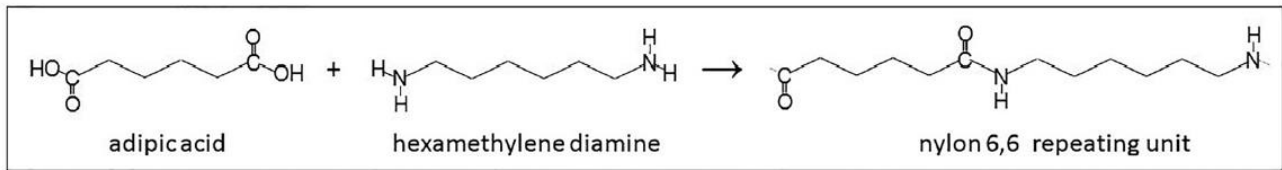


Figure 9. Condensation polymerization to form Nylon fibers [29].

## 1.2 Three-dimensional (3D) printing

### 1.2.1 Additive manufacturing different methods

Three-dimensional printing, also called additive manufacturing (AM), is a technology which includes methods that create 3D objects by building them layer by layer [30]. Therefore, this technique produces much less waste than subtractive manufacturing (bottom-up process). AM technology can be classified into seven categories [31], according to ASTM Standard F2792 [32]:

- *Binder jetting*: a powder-based 3D printing technique, in which droplets of a liquid binding agent are selectively deposited by an inkjet print head to join powder particles. After a consistent layer is created, the platform goes down and other powder is spread, so the process goes forward layer by layer. The amount of deposited binder has a strong influence on the printing accuracy and mechanical integrity of printed parts. The advantage of this technology is the versatility in the materials choice (everything in powder state), but it has a very limited resolution. However it is simple, fast and cheap, allowing the production of very large objects [31], [33]–[35].
- *Directed energy deposition*: it is commonly used to repair or add additional material to existing components. Its principles are similar to that of material extrusion technique, but the nozzle can move in multiple directions [33]. Focused thermal energy is used to fuse deposited materials by melting [36]. Examples are laser deposition and laser engineered net shaping (LENS) [33].
- *Materials extrusion*: this method can be used to print multi-materials and multi-colored objects [33]. The main example is fused deposition modelling (FDM), which is based on a material extrusion through a heated nozzle and deposition onto a platform layer by layer; it

uses thermoplastic filaments (PP, PMMA, PET, ABS and PLA), which undergo an instant phase transition from solid to liquid state. This method has some limitations in the available materials and in the resolution, but it is low-cost and fast, comparing to the other 3D printing techniques [30], [31], [37].

- *Materials jetting* [33]: this technology does not use ink, but the building material, a liquid photopolymer or other liquid materials, and the support material are simultaneously sprayed in the form of droplets by multiple print nozzles onto a build platform [31], [38]; the deposited layer is then flattened using a roller, to remove surplus material and to achieve the desired thickness. The droplets are solidified by a UV light, creating a bunch of ultra-thin layers to obtain the final 3D object [31], that does not need post-curing, but can be handled and used immediately [39]. The main example is Polyjet modeling (PJM), which is an advanced inkjet method [31].
- *Powder bed fusion* [33]: it includes methods like selective laser sintering (SLS) or selective laser melting (SLM), based on the use of a powder, which is rolled by a levelling drum to form a flattened thin layer and then sintered by the applications of a high-power directional heating source, such as a carbon dioxide laser beam. The powders are refill from the powder reserve chamber for every layer. This technology does not need structural support, allowing an easy printing of complex objects too, but it requires an expensive heating source and a long process time. The resolution of the printed objects, as for all the other technologies involving the use of a source of light, depends on the spots size of the laser beam [30], [31], [37].
- *Sheet lamination*: sheets material are bond together to produce a part of object [33]. The main example is laminated object manufacturing (LOM), widely used in the industry. The process consists of rolling a sheet material on a moving platform while a laser cuts the pattern to form the layer; then, a heated roller laminates it on a substrate [31].
- *Vat Photopolymerization*: it consists of the curing of photo-reactive polymers by using a laser. Stereolithography (SLA) is an example of this technology and is based on the solidification or curing of a liquid photopolymer, when exposed to UV light, the catalyst for the photopolymerization. A platform is submerged in a reservoir with a gradual depth increasing layer by layer. This approach is the earliest developed and the most used, because of its high resolution, low feature size [30], [31], [40], and low printer price. However, it is characterized by a limited material selection and a high price of the resin. Digital light processing (DLP) is similar to SLA technique in terms of principle and working concept [37], but it uses a different source of energy to solidify the resin, that is a scanning laser beam. It is faster than SLA, since the laser hits the entire layer at once, but it is characterized by a lower resolution and a worse surface finish [31].

Except for powder bed fusion technology, material cannot be deposited on empty space, but it requires filler or support material; therefore, a lattice structure is created to support the object, strengthen the structure during printing, and avoid distortions of the object during curing [41]. This

support structure is a mixture of propylene, polyethylene, acrylic monomer, and glycerin and needs to be removed [38]. It can be easily removed with a cutting tool, but it often needs an additional polishing for a good finish, using water jets [41].

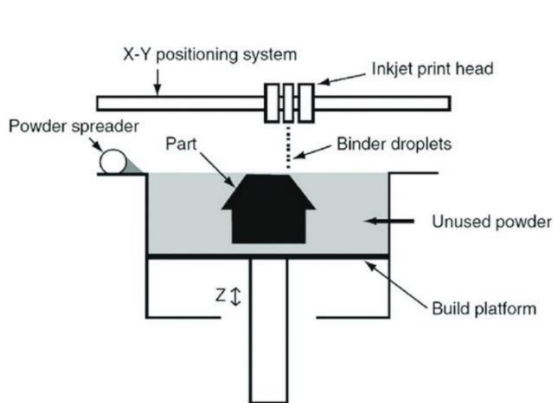


Figure 10. Binder jetting system [42].

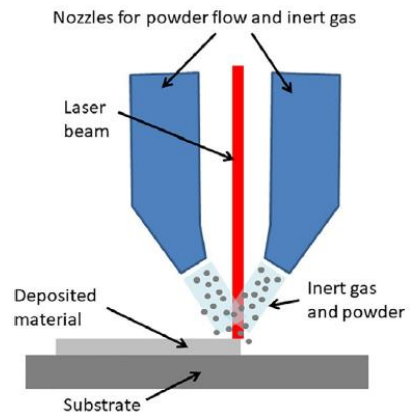


Figure 11. Example of directed energy deposition [43].

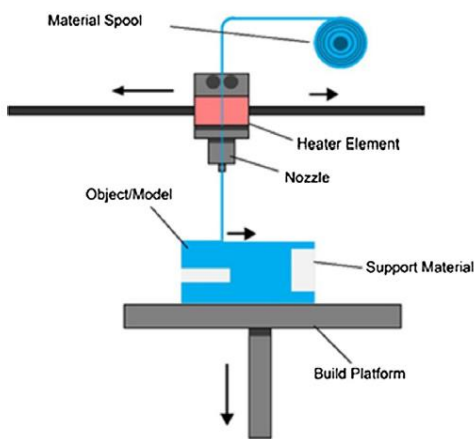


Figure 12. FDM: an example of materials extrusion technology [31].

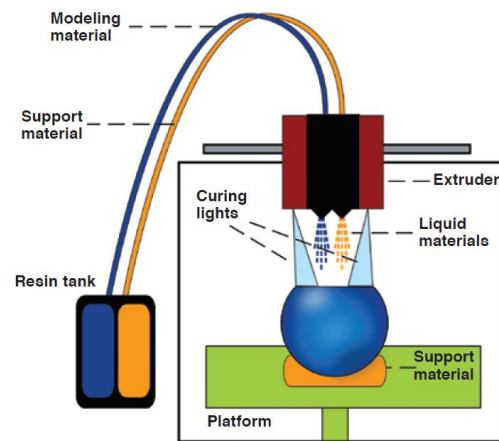


Figure 13. Polyjet modeling process [44].

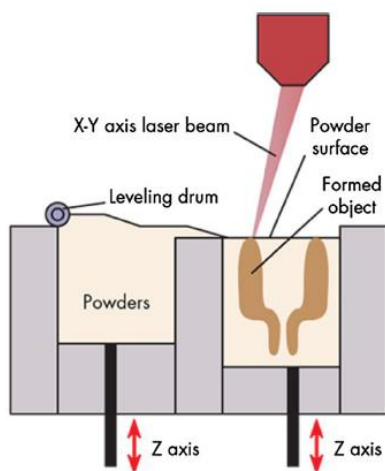


Figure 14. SLS: an example of powder bed fusion technology [31].

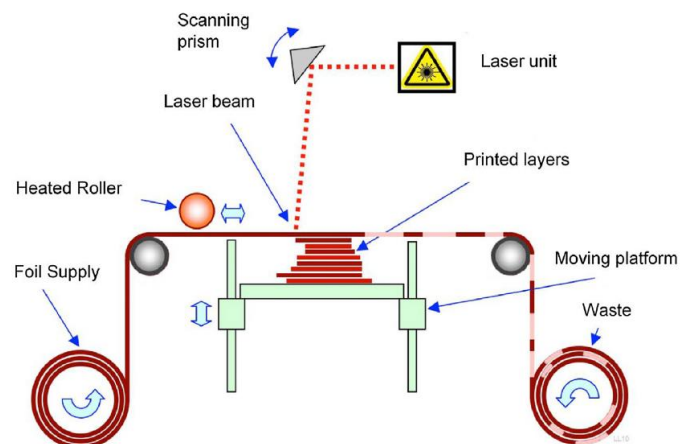


Figure 15. Schematic of LOM: a sheet lamination method [31].

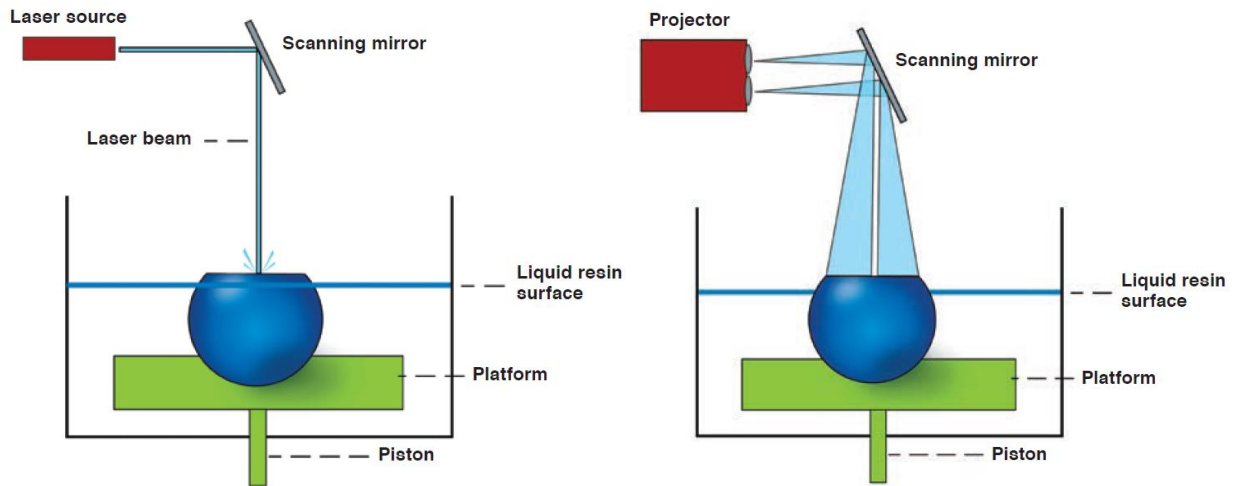


Figure 16. SLA vs DLP: two examples of vat polymerization technology [44].

### 1.2.2 General and medical applications

AM has been introduced in the late 1980s in Valencia, by Charles W. Hull, who printed the very first 3D objects, a small cup, using a stereolithography technology [45]. This process is still expanding, reaching its peak in the last 10 years, due to new technologies, materials, and methods. Initially, 3D printing technology was used for prototyping, to fix the system imprecisions and get the products to market earlier. Over the years, AM gradually spread to several fields of applications and commercial industries incorporate it in their real manufacturing strategy, allowing to increase the efficiency and the flexibility of their production. Today it is used in the aerospace, automotive, architecture, electronics, defense, business, industrial equipment, education, consumer-products markets, fashion, arts, and medicine. Particularly, in aerospace and automotive industry printing vehicles parts with AM is preferred to industrial production. The medicine field has been completely revolutionized with the introduction of 3D-printing [30], which can provide very specific and biocompatible materials for several applications [46]. Before the introduction of 3D printing, medical imaging was essential for many clinical disciplines. However, the flat screens were limiting factors for the visualization of three-dimensional imaging data. 3D objects overcome this limitation and are created basing on CT or MRI volumetric medical images. Images are acquired at ultra-high spatial resolution with good quality contrast, then segmented, processed using CAD software (e.g., Rhinoceros 3D, Autodesk Inventor), and finally sent to the 3D printer [37], [47]. The printer will print one layer (2D) on top of the other, and, after forming the 3D-object, it may need some post-processing (curing, annealing, painting, or others) depending on the desired property [31].

3D printing enables to produce custom-designed and patient-specific models with high complexity [48], allowing also to perform surgeries previously considered impossible [49]. Its medical applications are multiple, such as regenerative medicine, specifically in tissue engineering and organ bioprinting [48], [50], medical devices and surgical tools production [48], [49], [51], personalized medicine, designing smart drug and delivery systems [48], [51], [52], and high-fidelity physical tissue

models, as preclinical platforms or for education [48], [49], [51]. Its capability of proving materials specific to their intended purpose [46] is really useful, especially for planning and executing surgery, to improve the diagnostic quality and have successful surgical outcomes [30]. It has been applied in the fields of craniofacial and maxillofacial surgery, pelvic surgery, neurosurgery, spine surgery, cardiovascular surgery, orthopedic surgery, and visceral surgery. The ability of producing phantoms by rapid prototyping can be exploited to better understand physiological and pathological processes [47], reaching a really high level of detail [51]. A better confidence and understanding of complex pathologies and critical intraoperative procedures is, therefore, possible [53], since the surgeon can precisely guide the drilling system, estimate proper angulations, and evaluate the nerves' location [54]. He can visualize, plan, simulate and better explain the surgery, decreasing the cost, the operating and hospitalization time and enhancing doctor-patient communication [53], [55]. More importantly, this procedure decreases the complications, such as blood or patient loss, and the risks to the surrounding tissue and organs [56]. Thus, patient-specific implants lead to simplification, save time, and optimization of surgery procedures [53]. Medical education and training using 3D objects [47] minimize the use of animals and cadavers [57] and improve surgeon's abilities and results [47], [58]. However, there are several limitations associated to 3D printing technology, regarding the limited printing resolution, the long printing time, and a few available multi-materials [48], [49], characterized by a lack of versatility and diversity too [54]. Moreover, 3D printing is limited by its precision and usability and its price, both of the printer and the materials [56]. In addition, the majority of the AM techniques require a post-processing step, which complicates the workflow, increases the time and the cost of the procedure, and can also worsen the product quality [55].

### ***1.2.3 Stratasys 3D J750™ Digital Anatomy™ Printer (DAP) and available materials***

The Stratasys 3D J750™ Digital Anatomy™ Printer (DAP), a material jetting AM device [31], overcomes the limitations of the other 3D printers, providing parts, prototypes and models in multiple materials, colors and color textures, including blended transitions and transparency [58]. The use of multiple print heads and immediate curing allows for much greater control, leading to the development of several materials, which can be printed in the same part [36]. It has the advantages of high resolution and simultaneous multi-material printing. Due to the ability of fabricating multi-material objects, this technology allows to obtain high-performance composite materials, combining hard and soft polymeric filaments in a single process, without compromising the complexity of the design and enabling the printing of colors with properties of polymers similar to ABS, nylon, polypropylene, and rubber.

Thermosetting photopolymers are used in PJM. It is possible to check both the material properties and the apparent properties in the resulting parts by controlling, respectively molecular structure, molecular weight, additively, and orientation, density, and process states during 3D printing. In PJM 3D objects are characterized by a lower anisotropy, compared to the other techniques, and the low curing energies make the local volume uniformly cured [36]. In fact, liquid-based technologies tend to create more homogeneous material properties, that can be hard or elastic. Moreover, these techniques provide the best accuracy, producing high-quality printing with a high level of details [41]. Particularly, the J750 DAP allows to print parts with layer thickness down to 14 or 27 microns

and accuracy of up to 200 microns for full model size. It has the lowest estimated time, but it is a high-cost printer [59], [60], requiring an expensive technical support to avoid the clogging of the nozzles [41].

There are several materials of the Polyjet range available for the J750 DAP: full Vero™ family of opaque materials including neutral shades and vibrant VeroVivid™ colors; TangoPlus™, TangoBlackPlus™ and Agilus30™ (flexible materials); VeroClear™ and VeroUltraClear™ (transparent materials) [61]. In addition, GelMatrix™, TissueMatrix™, and BoneMatrix™ are three specific resins for the J750 DAP. These three innovative materials, and their combinations to make digital materials, perfectly match the anatomical applications; anyway, there are no studies in the literature on the mechanical characterization of these materials yet. TissueMatrix™ is ideal for reproducing the appearance and structure of heart tissue [62], because it is the softer material on market [63]. BoneMatrix™ is a robust and flexible material with shape memory, used for the production of musculoskeletal models, such as bone structures, fibrotic tissues, and ligament. GelMatrix™ is a gel-like support material used to print small and complex vascular models. Structural heart, blood vessels and other soft organs, and musculoskeletal models have been created as complex combinations of print materials, deposited by the nozzles: Agilus™, Vero™, BoneMatrix™, GelMatrix™, TissueMatrix™ [62].

Agilus30™ is a durable, rubber-like photopolymer, capable of withstanding repeated flexing and bending. It is available in clear, black and white colors [64]. It has improved mechanical properties, tactile quality and it is easier to use, compared to Tango™ family materials. It has a Shore A of 30-35, but it can be made harder combining it with rigid materials, such as Vero™, reaching a Shore A up to A95. For a hardness value of A30-35, it is characterized by an elongation at break of 220-240% and a tensile strength of 2.4-3.1 MPa [65]. Agilus30 White FLX935 differs from the others: it has a lower elongation at break (185-230%) and a lower tensile strength (2.1-2.6 MPa), reaching a higher hardness value (A30-40) [66]. Below the room temperature, all the elastomers exhibit an elastic stress-strain behavior with a high strain at break and a low tensile strength, as shown in fig. [67].

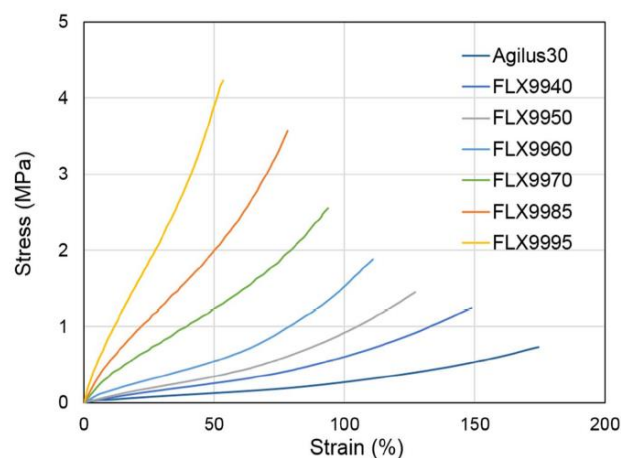


**Figure 17.** Stress-strain curves of Agilus30 and other elastomeric materials at room temperature [67].

Vero™ is a family of multi-purpose and multi-color photopolymers, which offer strength, stiffness, and versatility in blue, white, black, gray, cyan, magenta, and yellow: VeroBlue RGD840, Vero PureWhite™, VeroGray RGD850, VeroBlackPlus RGD875, VeroWhitePlus RGD835, Vero Blue RGD840, VeroYellow RGD836, VeroCyan RGD841, VeroMagenta RGD851, VeroMagentaV, VeroYellowV, VeroCyanV™. For multi-material versatility, it can be blended with other photopolymers to vary hardness, flexibility, translucency, or heat resistance. Vero™ materials are also offered in clear, flexible and dental [68], [69]. VeroClear™ is a transparent PolyJet photopolymer for clear acrylic simulation. It offers strength, stiffness, elongation and impact resistance, enabling visualization of internal components and features [70]. Vero™ family has an elongation at break of 10-25% and a tensile strength of 50-65 MPa, resulting in an elastic modulus of 2-3 GPa [69], with a Shore A of 83-86. VeroBlue RGD840, instead, has an elongation at break of 15-25% and a tensile strength of 50-60 MPa [66].

Tango™ material exhibits rubber-like behavior for applications requiring flexible characteristics. It is available in black, gray, and translucent colors. TangoBlackPlus FLX980 and TangoPlus FLX930, which can have a Shore A of 26-28, reach an elongation at break of 170-220% and a tensile strength of 0.8-1.5 MPa; TangoBlack FLX973, with a Shore A of 60-62, has an elongation at break of 45-55% and a tensile strength of 1.8-2.4 MPa; TangoGray FLX950 has an elongation at break of 45-55% and a tensile strength of 3-5 MPa, with an hardness value of A73-77 [66], [69], [71].

These polymers were combined and tested in several studies to evaluate their mechanical properties, being them potentially suitable for personalized prosthetic production [46], [72]–[75].

## **2. Mechanical theoretical background**

### **2.1 Standards for the mechanical characterization of the proposed pattern**

The measurement of the characteristics and behavior of substances under various conditions is named “materials testing”. The data obtained can be used in specifying the suitability of materials for various applications or in projecting mathematical models to predict their capabilities. Materials testing can be divided into five major categories: mechanical testing; testing for electrical properties; testing for thermal properties; testing for resistance to corrosion, radiation, and biological deterioration; and nondestructive testing. Standard test methods are regulated by International Organization for Standardization (ISO) and American Society for Testing and Materials (ASTM) [76]. Particularly, for the characterization of our printed specimens, the ASTM D638 – 14 and D412 – 16 were followed.

#### **2.1.1 ASTM D638 – 14**

Being the printed specimens made of rubber-like materials, the ASTM D638 – 14 (Standard Test Method for Tensile Properties of Plastics) [77] was chosen for their mechanical characterization. It was necessary to carefully control the environmental conditions and the speed of testing, since they could influence the tensile properties, as proved by *Abayazid et al.* [72]. The repeatability of the tests is one of the investigated parameters; therefore, all the specimens need to be identical and have the same preparation. This Standard gives the operator several recommendations about the preparation and the placing of the specimen and the parameters to be set on the testing machine. Moreover, it suggests how to compute the tensile properties, such as the tensile strength, the elongation at break, the strain, the modulus of elasticity, the tensile stress, and the Poisson’s ratio [77].

#### **2.1.2 ASTM D412 – 16**

A more detailed analysis of the testing method and a clearer definition of the previous tensile properties are given by the ASTM D412 – 16 (Standard Test Methods for Vulcanized Rubber and Thermoplastic Elastomers – Tension). Specifically, for the dumbbell specimens (our printed ones), it is needed to refer to Test Method A (page 4), in which every step of the mechanical tests is accurately described [78]. Tensile stress, yield point, and tensile strength are based on the original cross-sectional area of a uniform cross-section of the specimen. Method A can be performed using a universal testing machine capable of constant rate of extension (CRE) control [79].

## **2.2 Mechanical tests theory**

The mechanical tests, carried out experimentally, help to prevent the failure of the structures, indicating which materials may safely be employed for a specific application. There are eight different mechanical tests:

- Static tension and compression tests: the tension tests determine the breaking point of the material and its elongation, while the compression tests determine a material's response to crushing.
- Static shear and bending tests: to evaluate the deformation of a material to forces applied tangentially.
- Measures of ductility: the permanent deformation of a material in response to stress.
- Hardness testing: measuring the penetration of a load pressed at one small point of the material [76].
- Impact test: to evaluate the behavior of a material when it is hit by a load that causes the deformation, the fracture or the complete rupture of the specimen [80].
- Fracture toughness tests: to measure the material's capability to resist the growth or propagation of a crack [81].
- Creep test: to measure how the dimensions of a material slowly change during the application of a prolonged stress.
- Fatigue: phenomenon measured by repeatedly applying different values of stress, from maximum to minimum [76].

### **2.2.1 Tensile test**

The tension test, also called tensile test, is one of the most common types of mechanical testing, with the aim of characterizing several mechanical properties of a material. It is very simple, inexpensive, and fully standardized. Applying a pulling force to a specimen, it is possible to measure its mechanical response and to determine how strong that material is (tensile strength) and how much it elongates (strain). For 3D printing, the test provides information about the quality and the behavior of a 3D-printed material. During the test, we have to consider the variation in geometry of the specimen, especially when it exceeds the elastic limit. The loading rate, the environment, the temperature, the composition of material and its microstructures and the geometric effects influence the fracture toughness, that is the material's capacity to resist fracture [82]–[84]. The tensile bars are called “dog bones” because of their shape: they are designed with two opposing shoulders and a central narrower cross section, meant to be a predictable point of failure. The cross section can be rectangular or round in shape [84].

### **2.2.2 UTS tensile testing machine**

The basic principle of a tensile test is to place this specimen (or sample), of known dimensions (length and cross-sectional area), between two threaded or serrated pneumatic fixtures called “grips”, which clamp the material. One end is then moved in order to strain the dog bone and the other end remains fixed. The load (or force) is gradually increased at a uniform rate of speed while measuring the change in length of the sample until it breaks at its weakest point [85]. To do this, operators typically use electromechanical or universal (or tensile) testing machines (Fig. 18 and 19).

They are equipped with a load cell, testing software, grips, and accessories, such as extensometers. Basing on the material to be tested, different accessories are needed, and it is possible to test different materials simply by changing the fixturing. A wide range of grips and fixtures are available [82]. The load cell is a transducer which precisely measures tension applied to the specimen and the extensometer measures its elongation [84]. A tensile testing machine can have single or dual columns representing the load frame and this influences its force capacity. The machine used in this work is a MTS Insight 2, a single-column tabletop model, which provides low force (1 KN) testing of smaller specimens [82], [86]. An integrated digital controller allows to automate the load frame. In case of danger, the operator can also stop the testing by pressing the emergency button based on the structure. Every testing machine has a test software, where operators can configure test methods and output results. MTS Insight has the TestWorks software, which offers a variety of preset testing methods, optimizing the testing procedures. All MTS Insight models reliably perform standard tests such as peel, tear, shear, tensile, compression, and flex/bend; however, more advanced test, such as creep, multi-cycle and stress relaxation, can also be performed [86].

It allows the computation of several mechanical parameters:

- Peak load: the maximum value of the applied force.
- Elongation at break: the maximum value of the specimen extension.
- Tensile strength at break: the maximum value of the stress.
- Strain at break: the maximum value of deformation reached by the specimen.
- Modulus of elasticity (or Young's modulus).
- Stiffness: computed by multiplying the modulus of elasticity by the averaged original cross-sectional area and dividing by the original length of the constant region of the specimen ( $l_0=33$  mm).
- Strain at break (%): the maximum strain value in percentage.
- Final length, considering an initial length of 33 mm.
- Total length, considering an initial length of 65 mm.
- Pearson's coefficient ( $R^2$ ): to identify the linearity of the stress-strain curve.
- Coefficient of variation (CV): to determine the repeatability of the tests, by dividing the standard deviation by the mean of every parameter.

The "tensile strength at break", "strain at break" and "modulus of elasticity" parameters can be computed from the previous parameters following ASTM D638-14 [77]:

- *strain at break* ( $\epsilon$ ) =  $\Delta L/L$  , considering  $\Delta L$  as the maximum elongation value and  $L$  as the initial length of the narrow section ( $l_0=33$  mm);

- *tensile strength at break* ( $\sigma$ ) = *peak load*/*A*, considering *A* as the averaged original cross-sectional area in the constant part of the specimen in square meters, obtained by multiplying the width of the narrow section by the thickness;
- *modulus of elasticity* ( $E$ ) =  $\frac{y_M - y_B}{x_M - x_B}$ , that is by identifying the linear portion of the stress-strain curve and dividing the difference between the final and the initial stress values by the corresponding difference in strain.

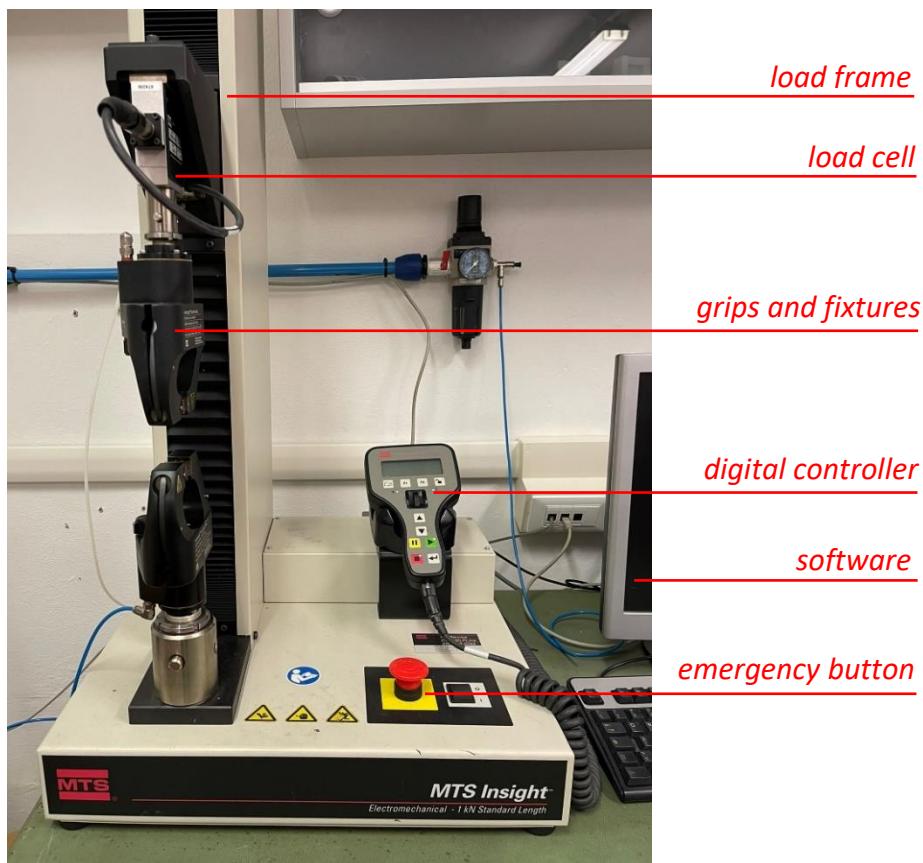
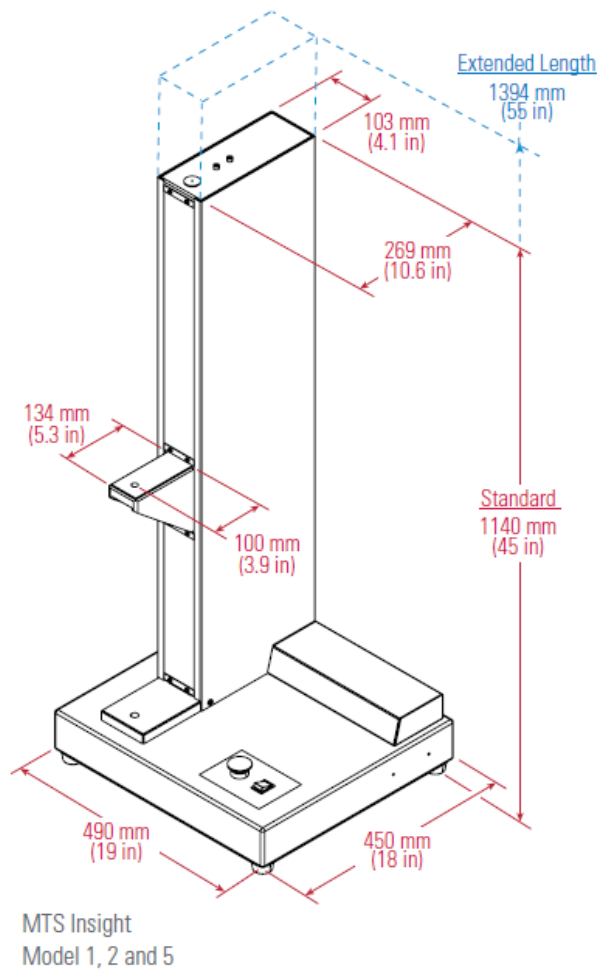


**Figure 18.** Identification of the testing machine components.



Column Configuration	Single
Force Capacity	2 kN (450 lbf)
Vertical Test Space	
Crosshead Travel	
Standard Length	750 mm (29.5 in)
Extended Length	1004 mm (39.5 in)
Maximum Test Speed	1000 mm/min (39 in/min)
Minimum Test Speed	0.001 mm/min (0.00004 in/min)
Height	
Standard Length	1140 mm (45 in)
Extended Length	1394 mm (55 in)
Width	490 mm (19 in)
Depth	450 mm (18 in)
Weight	
Standard Length	50 kg (110 lb)
Extended Length	55 kg (119 lb)
Clearance from Loading	100 mm (3.9 in)
Axis to Column Cover	
Space Between Columns	N/A
Power Requirements	
Power Supply	120 or 230 VAC (single phase)

Figure 19. Dimensions and technical specifications of MTS Insight 2.

### 2.2.3 Stress-strain curve

To perform the tensile test, it is needed to select the standard or custom test more appropriate. While the test is running, the graph is real-time auto-scaled on the digital display [86]. The resulting data, a graph of load versus extension (Fig. 20), shows the complete tensile profile of the material up to the breaking point [85]. The slope of this curve represents the stiffness of the specimen (N/mm), while the area under the entire curve is the energy absorbed at failure (N/mm), that is the maximum energy stored [87]. To analyze different materials, making their response independent of their size, we need to compute the stress-strain curve. The “load” is converted into “strength”, simply by dividing the force applied by the initial cross-sectional area:

$$\sigma = \frac{F}{A}$$

The “extension” is converted into “strain”, by dividing the displacement, that is the amount of movement, by the initial length of the specimen [85]:

$$\varepsilon = \frac{L - L_0}{L_0}$$

The area under the stress-strain curve represents the strain energy density (MPa) [87]. However, the greatest point of interest of this curve are usually the point of break or failure, modulus of elasticity, yield strength, and strain. The ultimate tensile strength is the maximum stress reached by the specimen during the test. It may or may not equate the tensile strength at break; for the rubber-like materials, tested in our work, these values are very similar, therefore we consider only one of these two parameters. The TestWorks software automatically identifies the linear region of the curve, by placing the point B, at the beginning, and M, at the end; it can usually be found in the initial portion of the test. In this region, the curve follows the Hooke's Law, according to which the slope of the line is constant and identifies E, the modulus of elasticity (or Young's modulus); it is computed by the ratio of stress to strain, which are proportional in this region:

$$\frac{\sigma}{\varepsilon} = E$$

The modulus of elasticity is a measure of the specimen's stiffness. In this region the material has an elastic behavior: if the load is removed, it returns exactly to the initial condition. When the curve is no longer linear, Hooke's Law no longer applies, and the specimen undergoes permanent deformation. The TestWorks software also identifies the point Y, which correspond to the material's yield strength, the value of stress at which plastic deformation begins to occur, usually coinciding with the point F (breaking point) [82].

## 2.3 Tendon/ligament mechanical behavior

Tendons and ligaments are flexible structures which play a significant role in providing the joint function and connecting muscle to bone [87]. They transmit and redirect musculoskeletal forces within the body, providing a wide range of joint motion by changing shape, due to their good flexibility. Ligaments act like passive joint stabilizers, while tendons allow to store and release elastic energy, due to their compliance, reducing the cost of muscle contraction. A second function is joint proprioception, which is better established in tendons than in ligaments: Golgi tendon organs are mechanoreceptors which alter muscle activity when resistance to movement is encountered. Tendons and ligaments behave both like crystalline and rubber materials, since their load-displacement curve shows both elastic and concave regions [6]. Visualizing the microstructure of a tendon/ligament using polarized light, collagen bundles appear aligned along its long axis, displaying a "waviness" or crimp. This feature allows the structure to elongate without undergoing damage [5]. The stretching-out of this "crimp-pattern" is identified by the initial toe region in the typical stress-strain curve of the tendon, where it is strained up to 2%. Initially minimal forces are needed for this elongation, then, when the fibers straighten, a greater force must be applied to lengthen them [6], [87]. Beyond this region, the tendon shows a linear behavior, where it is stretched less than 4%. Here, collagen fibers are no longer wavy, and it is possible to compute the elastic modulus, given by the slope of the curve. In general, the elastic modulus ranges between 1.0 and 2.0 GPa, which corresponds to a stiffness of 1.0-1.5 GPa [88]. If the tendon is stretched over 4%, it can never again return to its original length, because it undergoes plastic deformations. Beyond 8-10% strain, macroscopic failure occurs and further stretch causes its rupture (Fig. 21) [87]. Ligaments with unusually high elastin content can be strained to 30% or more without failure. They have an ultimate

tensile strength (UTS) ranging from 50 to 150 MPa, but they are likely subjected to damage [6], [88]. The mechanical behavior of tendon and ligament is viscoelastic; thus, their curves are rate dependent. Higher stress and strain are caused by higher strain rate and elastic modulus is slightly increased too [6]. Their non-linear viscoelasticity, reflected by their “J”-shaped stress-strain curve, is due to the collagen I fibrils, composing the structures, and their interactions with the non-collagenous proteins. The viscoelasticity of materials is defined by stress-relaxation, creep, and hysteresis. Because of this feature, tendons exhibit greater compliance in the first part of the curve than the other regions, enhancing their elastic energy absorption capacity at low stress levels. Ligaments often exhibit lower modulus and greater hysteresis than tendons, being more variable in composition and organization. Tendons provide more weight savings than ligaments, which are not as stiff or as strong along their longitudinal axis, as shown in fig. 22 [87], [88]. Ligaments increase their stiffness until a constant level, then, they continue to absorb energy until rupture. They can “load relax”, that is the decreasing of stresses within the ligament if they are pulled to constant deformations. They also “creep”: they wrap under a cyclically repetitive load [5].

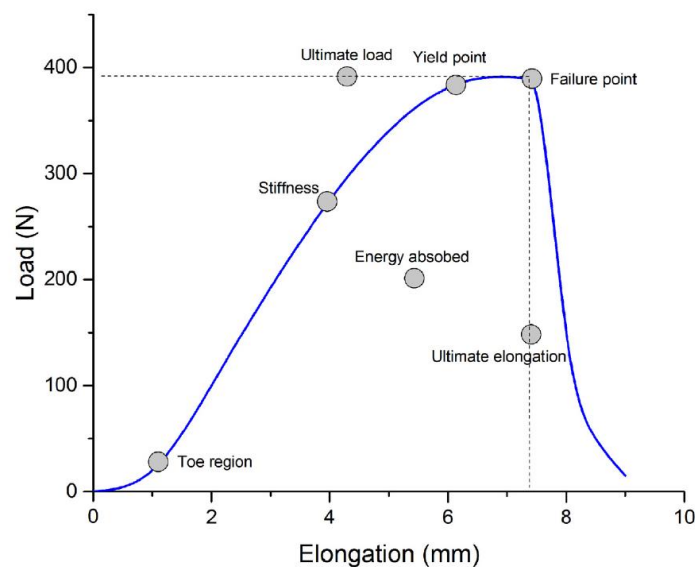


Figure 20. Load-elongation curve of a tendon/ligament [87].

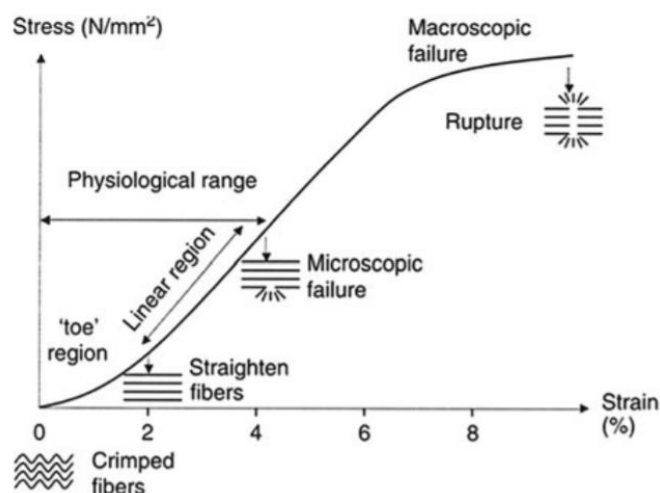


Figure 21. Stress-strain curve of a tendon/ligament [89].

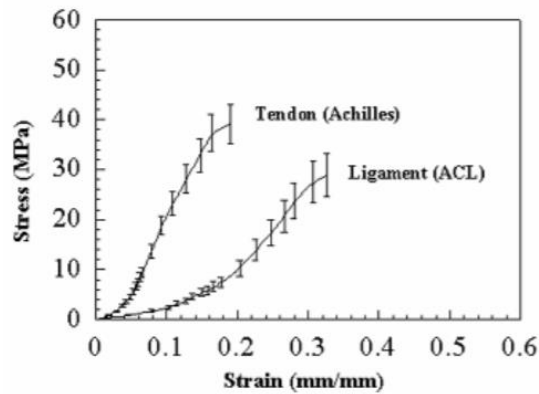


Figure 22. ACL and Achilles' tendon stress-strain behavior. Note how tendon's curve appears steeper than ACL's one.

### 2.3.1 Pathological conditions

Degenerative disorders of tendons are known as tendinopathies and are characterized by pain during activity, tissue degeneration, causing altered tendon morphology, and impaired functional performances. Indeed, in patients with tendinopathy, reduced mechanical properties accompany changes in tendon morphology [90]–[92]. Tendinopathic tendons seem to have greater CSA, lower tendon stiffness, and lower Young's modulus than healthy tendons. Actually, as shown in fig. 23, the pathological curve has a lower slope, that is the modulus of elasticity, than the physiological one. The enlargement of the CSA is due to an accumulation of water, hypercellularity, increased ground substance, and collagen fiber disruption. A larger tendon should be mechanically stronger, but the alterations in tissue composition and structure weakens the mechanical behavior, subjecting the tendon to higher strains [92]. Therefore, tissue degeneration impacts both the mechanical, morphological, and material properties of the tendon [93]. The patellar and Achilles tendons are the most commonly subjected to this pathology [90].

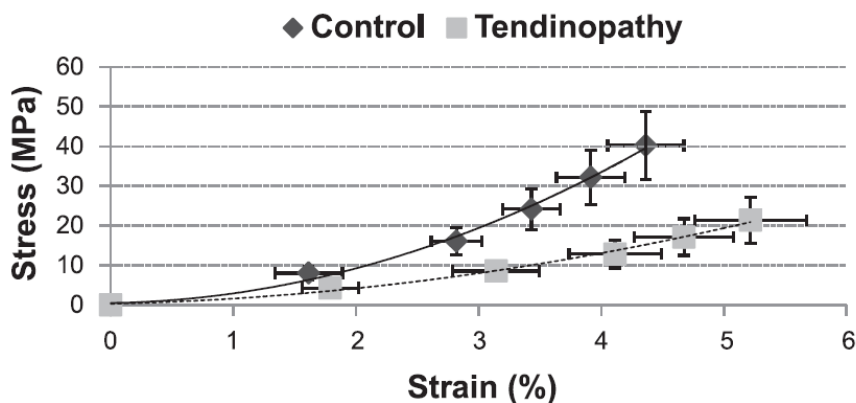


Figure 23. stress-strain curves of physiological (Control) and pathological (Tendinopathy) Achilles tendons [92].

## 3. Digital Image Correlation

### 3.1 Introduction

#### 3.1.1 *Basic principles of the Digital Image Correlation*

Digital Image Correlation (DIC) is a non-contact full-field optical-numerical technique for evaluating the features of almost any kind of material, measuring several parameters, such as shape, motion, and deformation, velocity, rotation, and curvature in the specimens with high accuracy [94]–[97]. The measurement consists of acquiring images of the specimen, storing these images in digital format (\*.tif or \*.tiff [98]), and analyzing them to extract the above-mentioned features of the object [99]. DIC is a statistical technique, since it contains the term “correlation”, aiming to compare two sections (subsets) taken from two different images of the same specimen to track the spots on its surface [94], [100]. The images are taken before and after the deformation process and are called, respectively, reference image and deformed image [94]. All the deformed images are compared to reference one [101]. This is a widely spread technique in biomechanical applications since it allows a reconstruction of the displacement and strain fields of biological materials, one of the main tasks in Biomechanics [94], [102].

#### 3.1.2 *History*

The first DIC system was developed by Peters and Ranson, two researchers at the University of South Carolina in the early 1980s, but it stems from photogrammetry, introduced about five centuries earlier [94], [99], [102]. Photogrammetry involved the extraction of the 3D shape of objects using a multi-view comparison of photographic records [94]. In the 90s DIC was first used in biomechanical applications, but initially it did not receive the attention it deserved because of its computational complexity. However, in the following decades, this technique was applied regularly in this sector and many different versions were introduced to improve its efficiency and performance, developing methods to digitally record images, algorithms to analyze them and approaches to automate the entire process [94], [99]. In recent years high-speed imaging systems have been developed and used in many contexts, such as biomechanics, structural dynamics, residual stress evaluation, and high temperature applications [94].

#### 3.1.3 *DIC vs traditional techniques*

The specimens, especially the biological ones, could be very inhomogeneous and anisotropic, therefore, full-field measurements are necessary to characterize them [102]. The deformation of a specimen, when applying a force (e.g., uniaxial tension), can be measured with different methods, like strain gauges, extensometers or DIC [101]. However, optical non-contact methods, like DIC, allow identifying crack initiation or propagation, stress concentrations, plastic instabilities, phase transformations and other localized material phenomena, which could not be visualized by strain gauges, for example [101], [102]. These techniques show several advantages over the traditional

ones [102]. First, a full-field measurement provides much more information for the specimen's behavior, allowing visualization of strain gradients and concentrations in all the directions; traditional technique (e.g., using marker bead arrays), instead, reported strains along the axis of loading, but not transverse or shear strains [95], [102]. Furthermore, DIC measures only the tissue-level response [95], avoiding the interference caused by contact measurement [103]. Lastly, this method needs a simpler preparation of the surface than traditional techniques [102] and an easy, even if time consuming, experimental setup [104]. However, to obtain good results optical techniques must be accurate and precise and DIC can overcome most limitations related to this kind of techniques [102].

## 3.2 DIC working principles

The implementation of the DIC technique requires three steps (shown in fig. 24):

1. *Speckle pattern preparation*: specimen surface must show a random pattern with enough contrast to allow good tracking [101], [104].
2. *Image acquisition*: one (2D-DIC) or more cameras (3D-DIC) capture some images of the specimen surface [104].
3. *Image analysis*: a matching algorithm compares the deformed images with the reference one to obtain displacement and strain fields [104].

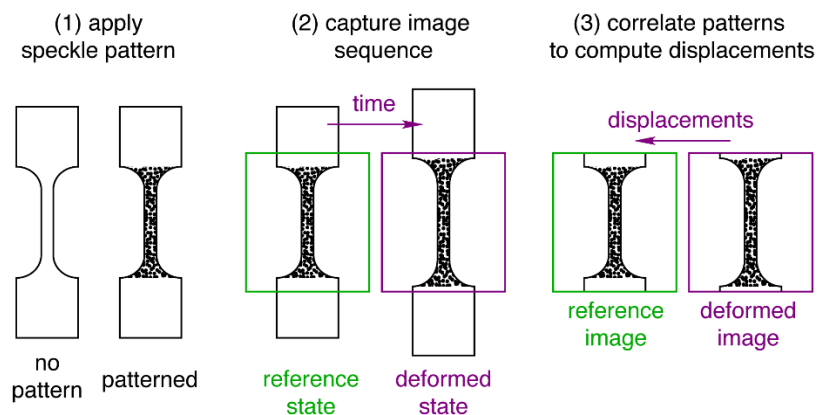


Figure 24. Different steps of DIC technique [101].

### 3.2.1 Speckle pattern preparation

The pattern on the surface highly influences correct solving of the correlation problem, consequently, DIC's performance too [94], [99]. This pattern should cover the area of interest of the surface [101] and have enough intensity variation in the subset selected; this is why a correct selection of subset size is essential [94]. A speckle pattern with more gradients usually generates a smaller number of bias and random errors [104]. The correct use of DIC requires a distribution of small dots on the surface of the specimen: in case of a natural random pattern, it is not necessary to generate it artificially; otherwise, it must be created [102]. To get precise and accurate measurements, the speckle pattern should have:

- Random distribution [102], [104], [105]: non-periodic because repeating textures could give problems in registration [99].
- Isotropy: not a preferred directionality [99], [104], [105].
- High contrast with the background [102] [106]: it is advisable to use black and white colours [105] to obtain a relatively large intensity gradient [104].
- Black/white ratio of 50:50 [102]: an equal distribution of black and white on the surface is required [105].
- Minimal roughness: it can alter the geometry of the specimen [102].
- Speckle dots of the right size, to the specimen size [102], and with a limited variability [106]: the dimension of the speckle should vary for each application [102] and condition [104]; a large measurement window allows larger speckle dots. The ideal size of the speckle dots is 3–5 pixels divided by  $M$ , where  $M$  represents the number of the pixels in the unit length of the examined object [99], [102]. A dimension smaller than 3 pixels can cause aliasing [105].
- Subset size: large enough to contain at least three speckles. Large size has both an advantage and a disadvantage: it improves the degree of similarity between the subsets, even if it damages spatial resolution and accuracy in measuring high displacement [106].
- Stability [104]: pattern tightly adheres to the specimen surface and follows its deformation, without showing important mechanical stress on the specimen [99], [101]; therefore, DIC can measure correctly large deformations too [99].

The choice of the DIC algorithm does not depend on the features listed above, but DIC's performance does. Therefore, before starting measuring it is always necessary to indicate the size of the measuring window, of the pixel and the speckle [106].

Speckle pattern can be obtained with constructive (e.g., spraying, airbrushing and spin coating) or destructive (e.g., scratching, chemical etching and FIB milling) methods [104]. The painting speckle pattern is a simple and well-known method, suitable to most engineering materials, allowing to quickly obtain high-quality results [101]. The most used techniques in macro-scale (millimeters to meters) are spraying and airbrushing, also because a laser speckle pattern can be subjected to decorrelation during rigid body movement of the specimen [104].

Speckle pattern can be black-on-white, with black dots on a white background, or white-on-black, with white dots on a black background (Fig. 25). The first method is more used because it provides better contrast. If the specimen has a light color surface, the first step (white background) can be avoided [102]. The generation of this pattern is usually made by spraying with an airbrush. This technique is cheap and easy, even if it does not provide a controlled and optimized pattern [104], [107]. Furthermore, its parameters must be previously determined [104]. If an airbrush is not available, the operator can also use a toothbrush, dipping its bristles into a small container of acrylic paint and flicking them on the surface of the specimen [108], [109].

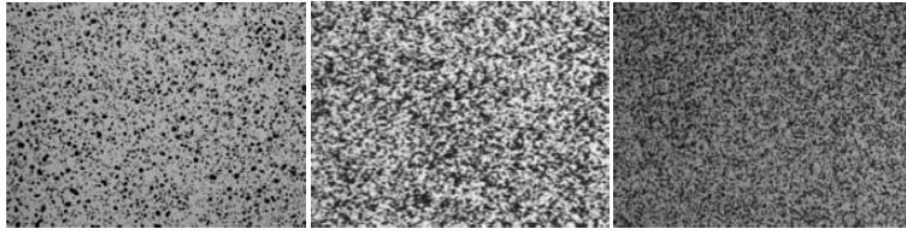


*Figure 25. Typical speckle patterns [99].*

### **3.2.2 Image acquisition**

With a single camera it is possible to perform 2D-DIC, while, implementing 3D-DIC and measuring deformation in three dimensions, the operator must use two or more cameras [94], [102]. 3D-DIC is based on 2D-DIC because it involves the analysis of images from each camera obtaining planar deformations. Afterwards, the combination of the results allows getting the deformation in the third direction [94].

#### **3.2.2.1 Description of the Hardware**

A camera is a multi-component device, consisting of optics (lens, optical filters, and shutters), camera hardware (e.g., charge-coupled device (CCD)) and digitation and storage process (discretization of CCD signal). Camera lenses can be thin or thick: a lens is considered thin when its thickness is much smaller than its focal length (distance between the lens and the sensor) and, therefore, it is negligible; in other cases, the lens should be considered thick. The thickness of the camera lenses influences image plane coordinates and, for this reason, it must be considered in the imaging equations [99]. CCD is an imaging detector consisting of an array of pixels that stores and transports charge packets, usually containing electrons, through the generation of potential wells. These packets are generated by incident photons or from internal dark signal through the photoelectric effect. Afterwards, an external device (e.g., computer) converts the output signal into a digital image [110]. In the acquired image, each intensity value can be identified as the average over a specified time, called image exposure time. This parameter has an important role during displacement measurements [99], because it represents the amount of time between two acquisitions, during which camera sensors gather light. If it is too long, image results really bright and this can generate blur in the acquired picture [105]. The lighting of the work plan must be stable and uniform to reduce noise and obtain better images. Moreover, cold light illumination (i.e., LED) produces better results [102].

#### **3.2.2.2 Calibration process**

The system must be calibrated before performing the measurements [99]. For 2D-DIC (Fig. 26A) only a line of standard length (like the horizontal field of view, or HFW) is used because a length scale conversion from the space coordinates to the image ones is required. For 3D-DIC (Fig. 26B) a line is no adequate anymore, because the system has two cameras; therefore, a target of known dimensions with uniformly spaced markers [99], [101], called calibration plate or calibration grid (shown in fig. 26C), is necessary. The plate has  $x \times x$  black points on a white background. The grid is titled and rotated into different orientations while images are captured by the cameras [103], because the target motions should represent the object to be measured [111]. The process requires

the acquisition of 25-50 images [101]; indeed, capturing too many images (about 500) can only slightly improve the results and it's mathematically time-consuming too [111]. Then, the clearest image is selected and the first point of the lower-left corner of the target is set as the center of the coordinates system [103].

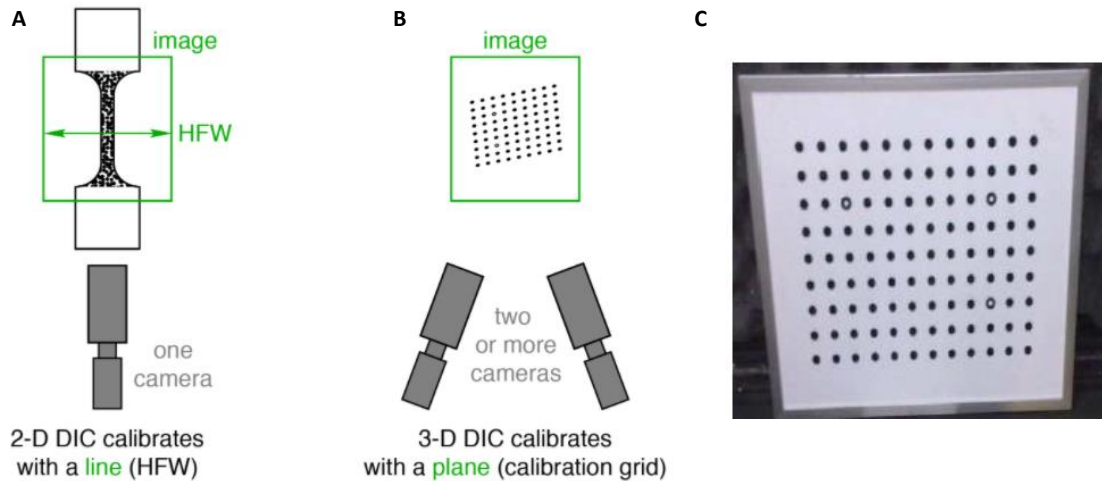


**Figure 26.** (a) 2D and (b) 3D DIC calibration [101]; (c) calibration plate or grid [103].

This step provides the calibration plate orientation and position during all the process. The position is usually deleted at the end of this procedure because it is not useful for the following steps. Through the calibration process, it is also possible to determine all the camera's intrinsic parameters and extrinsic parameters, helpful in the triangulation process [111]. The intrinsic parameters describe the internal camera geometric and optical characteristics: focal length ( $F_x, F_y$ ), image plane centre location in pixels ( $c_x, c_y$ ), skew (deviation from orthogonality between the row and the column directions in the sensor plane), and the radial distortion factors ( $\kappa_1, \kappa_2, \kappa_3$ ) [99], [112], [113]. The extrinsic parameters refer to the relationship between the two cameras inside the system: the relative orientations ( $\theta, \varphi, \psi$ ), the relative positions ( $T_x, T_y, T_z$ ) [114] and the pinhole location [99]. Before performing triangulation, radial distortion factors are used to correct all distortions within the matched image-points [115].

The calibration is an optimization process to find the above-listed parameters, using the extracted target points; therefore, more points mean better results. This can be done by increasing the number of extracted points, i.e., filling the field of view (FOV), or by acquiring more images: a bad distribution of these points into the volume can lead to poor calibration results [111]. The calibration quality is expressed by a number, the calibration residual, which indicates the uncertainty level of the point's calculated location. In fig. 27 the locations of the extracted pixels are indicated by the green crosshairs, while the black spots represent the same points calculated with the calibration parameters. The residual is given by the difference between the two numbers [111] and it is computed simultaneously with the calculation of the 3D point [115]. It is possible to obtain the residuals for all the images and then their standard deviation to have a calibration score, indicating the global quality of the procedure. High values denote problems during the process; hence, a good calibration needs a low calibration score [105], [111], [115].

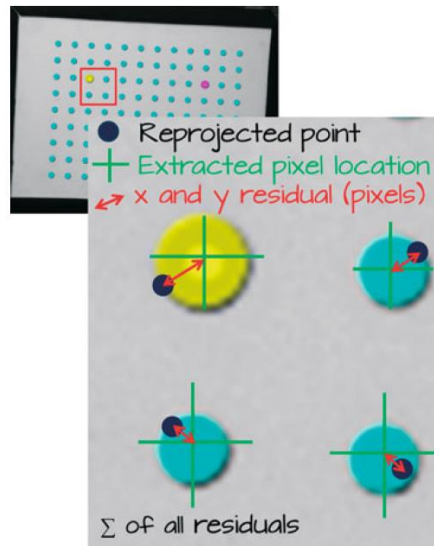


Figure 27. Computation of the residuals to determine the calibration quality [111].

### 3.2.2.3 Transformation of the coordinates

A perspective projection model or pinhole projection model (fig. 28) is used to describe the transformation from object coordinates  $M$ , in the three dimensions, to image coordinates  $M''$ , in-plane. The origin of the lens system is at  $C$ , while the center of the sensor plane system is  $O$ , and the direction of the optical axis is  $+z$  towards the specimen [99].

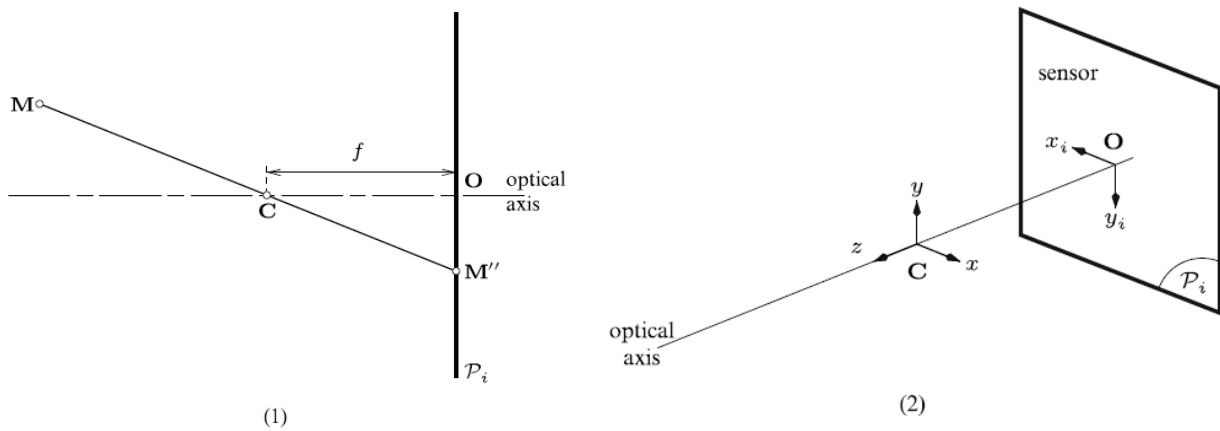
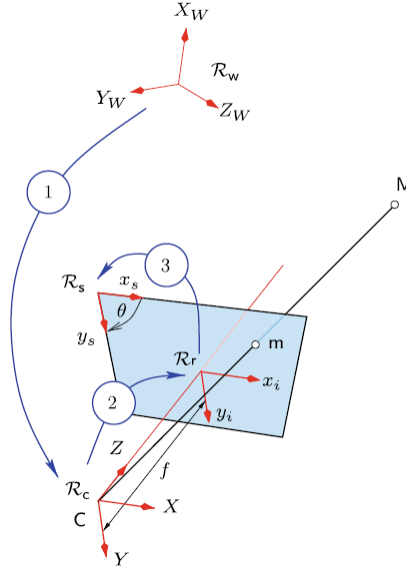


Figure 28. Perspective projection model or pinhole model [99].

The transformation from world system  $R_W$  ( $X_W, Y_W, Z_W$ ) to camera system  $R_C$  ( $x, y, z$ ) requires both rotation and translation as the first step of global transformation between object coordinates  $R_W$  and sensor coordinates  $R_s$ , shown in fig. 29. The second step is the transformation between  $R_C$  and  $R_r$ , the imaging system, with coordinates  $(x_i, y_i)$ ; this is a pure perspective projection. Finally, the third step describes the conversion of metric positions into pixel coordinates within the image  $(x_s, y_s)$ . This process can be mathematically represented as:

$$\tilde{\mathbf{m}} = \alpha \begin{Bmatrix} x_s \\ y_s \\ 1 \end{Bmatrix} = [\Lambda] \bullet \begin{Bmatrix} X_W \\ Y_W \\ Z_W \\ 1 \end{Bmatrix} \quad (1.1)$$

where the components of the matrix  $[A]$  are complex combinations of camera parameters, they are not a function of the global position of point  $M$ . Therefore, this is linear transformation to the sensor and world coordinates. Basing on equation (1.1), the pinhole camera model can be considered a projective transformation, where three-dimensional points become bidimensional points [99].



**Figure 29.** The transformation from the world coordinates to the sensor coordinates [99].

During the transformation of a 3D object into a 2D image, the third dimension is lost, but it is possible to recover it using two cameras capturing simultaneously images of the same specimen (shown in fig. 30) [99]. The 3D object is measured with the fundamentals of triangulation: the depth of the scene can be determined by calculating the parallax (apparent angular displacement of an object, when it is observed from two different points of view) in the images captured by the two cameras [103]. Using the cameras from different angles at the same time, the operator obtains 2D images of the same object from different points of view, after he calculates the 3D coordinates. To transform the 3D object, described by point  $P$ , into a 2D image-point, is used the pinhole camera model: a point  $P_1$ , in image 1, and a point  $P_2$ , in image 2, are obtained (shown in fig. 30).  $P$  is given by the intersection of the two projected rays. For a stereovision system, it is necessary to move from the image coordinates  $(u_i, v_i)$  to the world coordinates  $(x_w, y_w, z_w)$  of the point  $P$ . A 4x4 matrix is used for this transformation [115]:

$$s \begin{bmatrix} u_i \\ v_i \\ 1 \end{bmatrix} = \mathbf{A}_i \begin{bmatrix} \{R_i\}_{3 \times 3} & \{T_i\}_{3 \times 1} \\ \{0\}_{1 \times 3} & \{1\}_{1 \times 1} \end{bmatrix} \begin{bmatrix} x_w \\ y_w \\ z_w \\ 1 \end{bmatrix} \quad (1.2)$$

- $R_i$  is involved in the alignment of the world system with the  $i$ -th camera;
- Vectors  $T_i$  moves the world system to the origin of the  $i$ -th camera;
- $s$  is an arbitrary scale factor;
- $A_i$  is a camera calibration matrix.

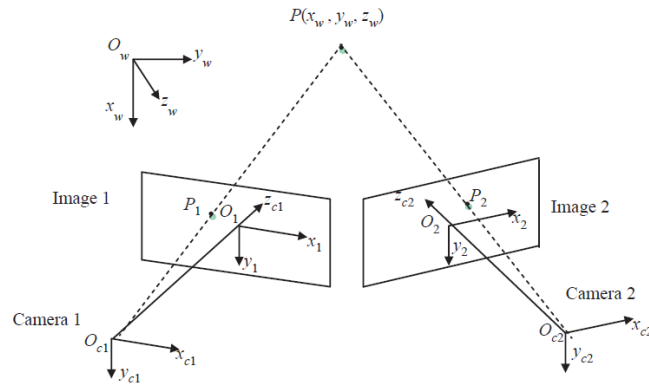


**Figure 30.** The basic principle of the 3D-DIC technique [115].

### 3.2.3 Image analysis

Images acquired, generally in grayscale, are divided into smaller images, called facets or subsets; the facets from reference and deformed images are compared by a matching algorithm [102]. This process can be considered the most important step in the DIC technique. In 2D-DIC the subset-based matching method is applied, that is comparing the same subset from two different images, captured by the camera before and after deformation. The stereovision matching is used in 3D-DIC and is based on the previous method, nevertheless, it requires two cameras, therefore, also the matching of four subsets from the same specimen surface captured before and after deformation (fig. 31) [115]. DIC technique searches for the target subset in the deformed image whose intensity pattern is more similar to the subset selected in the reference image. The differences between these subsets provide the subset center's displacement vector [116].

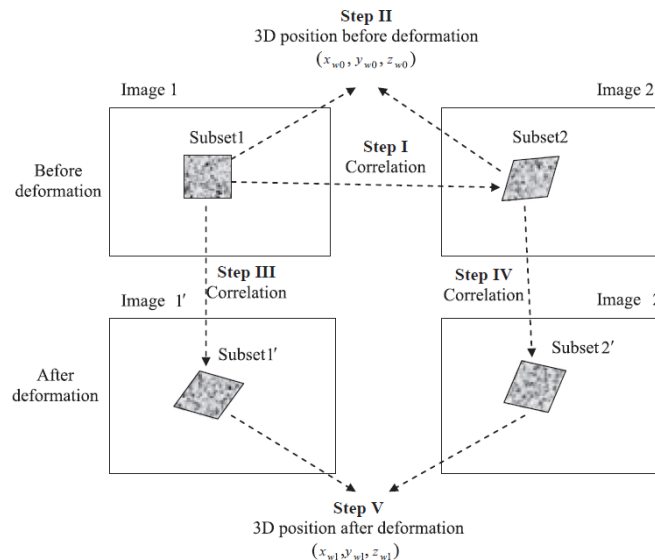


**Figure 31.** Matching and triangulation of a set of images acquired before and after deformation [115].

To obtain reliable and accurate matching, intensity must sufficiently vary on the surface of the specimen [116]. The grayscale distribution could not be appropriate in the images, therefore, during the measurement it must be interpolated many times (i.e., for each subset) to achieve subpixel accuracy, since the smallest element is one pixel [117]. Since spline curve functions are quite simple,

they are widely used to correct image distortions [99]. Bicubic spline (B-spline) is the most used fitting function and is a robust algorithm providing high accuracy at a low computational cost [117]. The bicubic spline interpolation implements a third-order polynomial in both reference and deformed images, to have approximately the same grayscale values in both of them [118]. Fig. 32 shows the block diagram of B-spline interpolation, where  $G$  is the gain factor, the pole  $z_k$  is the result of the derivation process, and  $K$  is the order of the function [117].

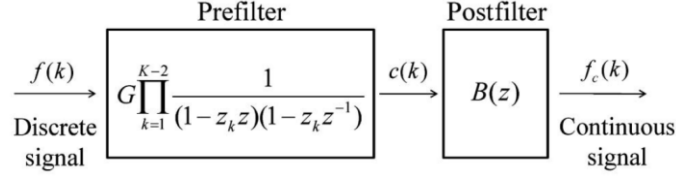


**Figure 32.** Block diagram of B-spline interpolation [117].

The matching between facets may consist in minimizing a function of different parameters [115] and can be evaluated with different methods: Zero Normalised Cross-Correlation criterion ( $C_{ZNCC}$ ), Zero Normalised Sum of Square Difference criterion ( $C_{ZNSSD}$ ) [94], [102], or a parametric sum of squared difference criterion ( $C_{PSSDab}$ ) [116]. Once a minimum value is reached, the software computes displacement and strain fields [102], [115]. These methods have the advantage to be insensitive to the potential scale and offset changes of the target subset intensity [116].

The  $C_{ZNCC}$  method is the most spread and is insensitive to light variation. It is calculated as [94]:

$$C_{ZNCC} = \sum_{i=-M}^M \sum_{j=-M}^M \left[ \frac{\{f(x_i, y_j) - f_m\} \{g(x'_i, y'_j) - g_m\}}{\Delta f \Delta g} \right] \quad (1.3)$$

$$f_m = \frac{1}{(2M+1)^2} \sum_{i=-M}^M \sum_{j=-M}^M f(x_i, y_j)$$

$$g_m = \frac{1}{(2M+1)^2} \sum_{i=-M}^M \sum_{j=-M}^M g(x'_i, y'_j)$$

(1.4)

$$\Delta f = \sqrt{\sum_{i=-M}^M \sum_{j=-M}^M [f(x_i, y_j) - f_m]^2}$$

$$\Delta g = \sqrt{\sum_{i=-M}^M \sum_{j=-M}^M [g(x'_i, y'_j) - g_m]^2}$$

$C_{ZNCC}$  can vary between 1 and  $-1$ , that is the highest and the lowest correlation of subsets considered [94].

It has been demonstrated that the  $C_{ZNSSD}$  function can compensate for unexpected intensity changes and it is calculated as [115]:

$$C_{ZNSSD} = \sum_{i=-M}^M \sum_{j=-M}^M \left[ \frac{f(x_i, y_j) - f_m}{\Delta f} - \frac{g(x'_i, y'_j) - g_m}{\Delta g} \right]^2 \quad (1.5)$$

The generalized PSSD<sub>ab</sub> coefficient is affected by any lighting changes [105]. It includes two unknown parameters  $a$  and  $b$  to represent, respectively, the offset and scale changes of the intensity of target subset, and it is calculated as [116]:

$$C_{PSSDab} = \sum (af_i + b - g_i)^2 \quad (1.6)$$

$f_m$  and  $g_m$  represent the mean of reference and deformed images selected subsets, while  $f()$  and  $g()$  (simplified as  $f_i$  and  $g_i$  in the last equation) represent the grey level intensity of the pixel of the two images, and  $2M + 1$  is the length of the subset [94], [116].

To optimize the process and improve accuracy, precision and spatial resolution, some parameters of the correlation algorithm (fig. 33) must be modified for each application:

- Facet size: the dimension of the subset making up every image; each facet is identified by a grey-level distribution, obtained after interpolation, and by its location in the image. This parameter must be defined according to specimen size, speckle size, strain gradients expected. The subset should be large enough to recognize small displacement, without losing resolution.
- Grid spacing: distance between consecutive facets; a small grid spacing indicates a large number of subsets, even if does not influence the precision and the accuracy of the results, while the overlap does.
- Strain computation window: strain field is computed by derivation of the displacements; therefore, it is necessary to choose the width of the computation window; a large window reduce the noise but can attenuate strain gradients too.
- Validity quote: minimum number of points necessary to calculate strain; software skips a certain area if the number of valid points is below this tolerance level.
- Filtering: strain field is usually affected by random error; software can apply filters of several type in different steps to reduce the noise, yet they involve loss of information [102].

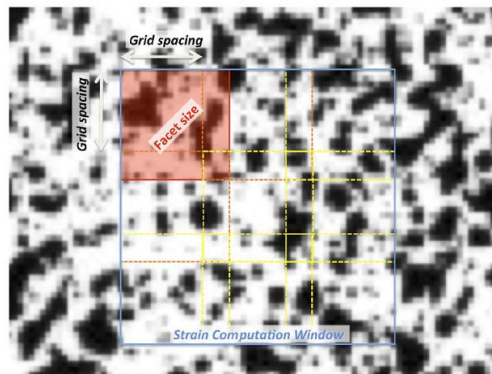


**Figure 33.** The surface of the specimen with the illustration of the correlation algorithm parameters [102].

After the definition of a correlation method, it can be optimized using different numerical algorithms to identify subpixel displacements. The iterative Least Square method (ILS) is an alternative technique to the conventional ones (e.g., Newton-Rapshon algorithm, of complicated implementation), easier and based on spatial gradient, for accurate subpixel motion detection. ILS is related to the intensity (variation of intensity of the deformed subset) and coordinate (changes in shape) correspondence of each point of the selected subset. The basic principle is to iteratively solve the desired parameter vector through the process and the equations shown in fig. 34.  $f(x_i, y_i)$  represents the grayscale intensity value at the  $i$ -th point of the reference image;  $g(x'_i, y'_i)$  is the grayscale intensity at the same point of the deformed image;  $a$  is the scale factor of the intensity change;  $b$  indicates the offset of the intensity change. Concerning displacement, there are shape functions of a different order, where the displacement components of the point in the two directions,  $u(x_i, y_i)$  and  $v(x_i, y_i)$ , can be seen [116].

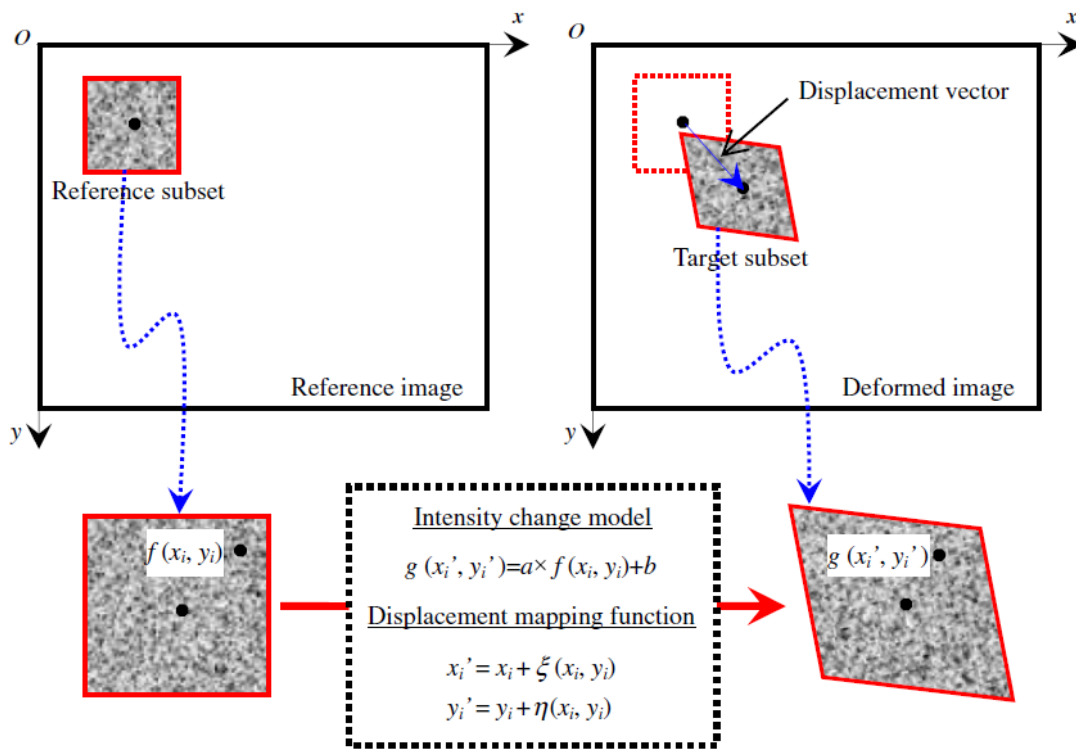


Figure 34. Diagram of the Iterative Least Square method (ILS) [116].

The subset-based method is the most spread, even if it has several limitations. First, having a good measurement of the points near the boundary could be a problem, since the selected subset could contain pixels from background image or other regions. Second, applying this technique to specimens with geometry discontinuities may lead to erroneous measurement. Fig. 35 shows the first described problem, where the subsets are indicated with a red square. To avoid decreasing in accuracy and reliability, these boundary points are excluded from the calculation or the results. Modified ZNSSD criterion, ZNCC criterion or PSSD<sub>ab</sub> criterion have been developed to easily identify the valid pixels in the boundary point and solve the first issue. Regarding the second question, an irregular ROI, rather than a rectangular one, is normally drawn in the reference image. This can bring

to a wrong computation; therefore, an automatic scanning strategy guided has been adopted to solve the errors [116].

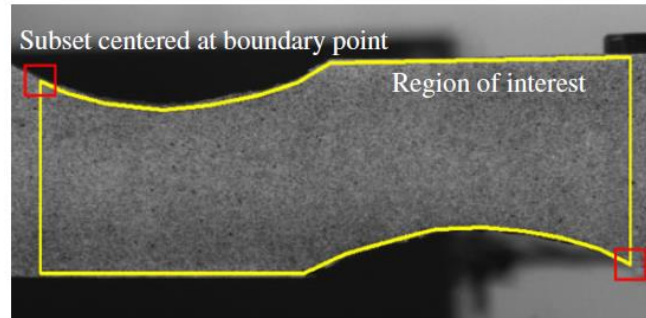


Figure 35. Representation of the first problem of subset-based method: points near the boundary [116].

### 3.3 VIC-3D System (VIC-EDU)

#### 3.3.1 Equipment

The DIC requires a simple equipment, involving light sources, to better capture images of the object’s surface, one or more cameras to get images and a computational device to process DIC on the images [94]. To carry out 3D-DIC, the operator must arrange one or more fixed cameras with the same performance and position to get the images of the specimen [103]. VIC-EDU system consists of two stereo cameras and a LED light source mounted in a single body (fig. 36a), which includes also a cooling fan, and an exterior USB & power connectors. There is also a tripod, tripod head, speckle roller, ink pad, calibration target, and a convenient carrying case. It is simply necessary a computer with one available USB3 port and a power source [119].



B

Camera Resolution	1920 x 1200 (2.3 Megapixels)
Frame Rate	20 Hz live, 0.5 Hz acquisition, 100 frames per capture
Exposure Time	19 $\mu$ s - 1 s
Field of View	Fixed: 150 x 200 mm
Displacement Resolution	In-plane: +/- 2 $\mu$ m; Out-of-plane: +/- 4 $\mu$ m
Strain Measurement Resolution	50 $\mu$ $\epsilon$
Strain Measurement Range	0.005% to >2000%
Analysis Licenses	Unlimited
Software Features	3D displacements, strains, graphing tools, etc.

Figure 36. (a) VIC-EDU system top and front view; (b) VIC-EDU system datasheet [119].

### **3.3.2 VIC-3D software**

VIC-EDU system needs two different software: VIC-Snap EDU and VIC-3D EDU [105]. VIC-Snap and VIC-3D software are employed to acquire and analyze data to obtain high-resolution measurements [120]. VIC-Snap EDU is applied to set the cameras features, avoiding images overexposure, and acquire calibration and test images. VIC-3D software, instead, calibrates the system and investigates the speckle images [105]. It analyses images captured by a stereo camera system and gives the measures of full-field displacements in the three directions (u, v, w). [121] It examines 3D surfaces and provides displacements at every point of the specimen surface. The 9<sup>th</sup> version of the software has been improved with new functionalities, allowing us to compare FE predictions and DIC measurements [120].

### **3.3.3 Testing guide**

To complete a test with VIC-3D EDU several steps must be followed [105]:

- Creation of the speckle pattern on the surface of the specimen
- Physical setup of the system
- Use of VIC-Snap EDU
- Acquisition of calibration images
- Acquisition of test images
- Calibration in VIC-3D EDU
- Analysis in VIC-3D EDU
- Visualization of the results

#### **3.3.3.1 Creation of the speckle pattern on the surface of the specimen**

Before starting the test, it is necessary to cover the surface of the specimen with a pattern with the above-listed characteristics. For the fixed field of view of this system, the better size of the dots should be at least 0.6 mm. It is optional to create a white background with a white spray paint and, after drying, it is needed to use the speckle roller supplied with the system to create the speckle pattern, even more than once if it is necessary [105].

#### **3.3.3.2 Physical setup of the system**

First, assembling the tripod, screwing the tripod head adjustment handles into the tripod head. The following step is to set the length of the legs, by moving the levers on the legs and clamping them back down when reaching the desired height. To rotate the tripod head, turning the adjustment handles counter-clockwise and then tightening them back to lock. There is a bubble level on both the tripod and the tripod head levelling the system.

Afterwards, to secure the system to the tripod, it is necessary to compress the small levers together to open the locking mechanism placed below the tripod head and then rotate it towards the outside. The baseplate is aligned with the tripod head and pushed into the position (fig. 37). The locking mechanism should close immediately to indicate the correct fixing.

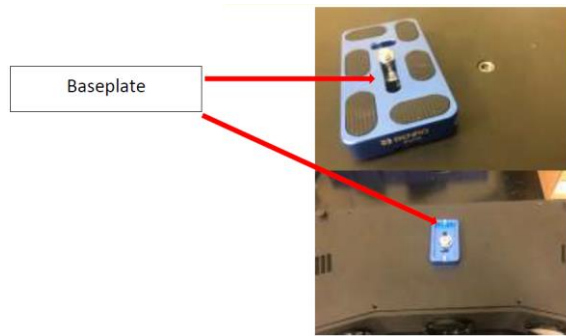


**Figure 37.** Fixing of the baseplate to the tripod head [105].

There are two cables, USB 3.0 type A to type B and a power supply. The two ends (A and B) of the first cable must be plugged, respectively, into the USB port of the computer and the back of the system. The second cable must be inserted into the back of the system too and the socket [105].

### 3.3.3.3 Use of VIC-Snap EDU

The following step is the acquisition of the specimen images and the software VIC-Snap EDU is required. If you can choose a camera system, select Point Grey, the builder of the cameras used. Four live images, two for each camera, should appear on the computer screen. It is possible to rotate images as shown in fig. 38 below.

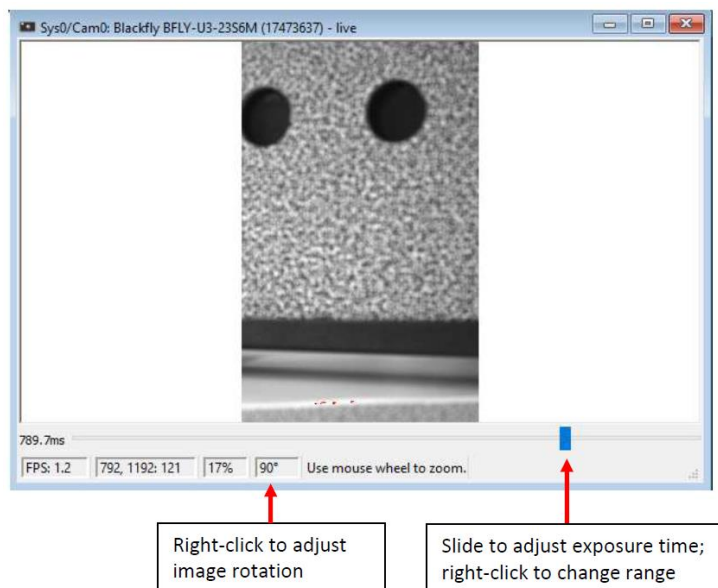


**Figure 38.** Commands to rotate images and set exposure time [105].

According to the geometry and the focal length of the system, the specimen should be placed at about 50 cm from the cameras. To verify the perfect alignment of the specimen, it is possible to activate the crosshairs overlay: they should be centered at the same point on the specimen.

To avoid problems in correlation caused by reflections from specimen surface, the system is equipped with polarizing lenses. The polarizers for the cameras should be oriented in the same direction and those for the light should be perpendicular to the previous orientation. Adjusting exposure time could help to reach the correct position (shown in fig. 38); when there is an

overexposure, indicated by the red spots (fig. 39), it is possible to rotate the polarizer of both cameras, one at a time, to minimize it. Images should appear darker [105].

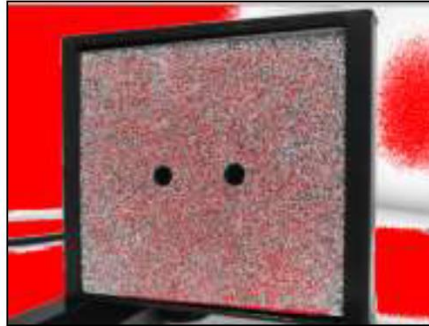


*Figure 39. Example of overexposed image (noticeable red spots) [105].*

#### **3.3.3.4 Acquisition of calibration images**

Before starting this procedure, be sure you can keep the system in the same position during all the measurement, after the calibration. It is only possible to change the exposure time. In this step the operator must take about 20 image pairs of the calibration grid in different position and orientation in the three axes, paying attention to cover the corners in some images. It is not necessary to put the calibration plate in the same location as the specimen, but it can be helpful to put it approximately in the same plane.

First, creating a directory for the project by clicking *Edit Files* in the menu or toolbar in VIC-Snap and choosing the name of the images (in this case “calibration”). After, it is possible to start the acquisition by pressing the spacebar or the *Capture* icon, considering that the calibration grid must be visible in both images. Optionally, the operator can check the system has been correctly calibrated by performing the system calibration in VIC-3D EDU [105].

#### **3.3.3.5 Acquisition of test images**

After the calibration procedure, it is possible to run the test. The operator must click *Edit Files* again and rename the images to indicate test images. Capture procedure can be manual or automatic:

- Manual Capture: pressing the *Capture* icon.
- Timed Capture: operator chooses the acquisition interval between two images and, in case, the length of the acquisition too, which can be made manually by pressing *Stop* [105].

#### **3.3.3.6 Calibration in VIC-3D EDU**

Once the acquisition is complete, it is needed to open VIC-3D EDU, import all the pairs (0, 1) of the calibration images (*Calibration images... Select the images... Open*) and calibrate the system (*Calibration... Calibrate stereo system*). With a coded grid, extraction is automatic, otherwise, the operator should click *Analyze* after selecting the grid used (Target menu). According to the overall error score displayed, it is possible to know if a good calibration has been done (green number) or not (red number). In the first case, the operator can press *Accept* to finish. In the second case, it is possible to remove some images (by clicking in the table of scores and then *Remove row*) or repeat the procedure to have a better calibration. Only one image per couple will be shown in the section “Calibration Images” of the Project window (by default, the 0 one, acquired by the left camera).

For each camera, the values shown are the following: type; center (x, y); focal length (x, y) in pixels; skew; distortion coefficient (Kappa 1 and Kappa 2); magnification. For the total system the values shown are: angles (angles between each camera); distances (distance between centers of the two cameras) [105].

### 3.3.3.7 Analysis in VIC-3D EDU

To analyze the specimen, importing the test images, by clicking *Speckle images*. It is advisable to check that only one pair of images shows the specimen when broken, not to do useless analysis. The image series can be visualized in the section “Speckle Images” of the Project window. Next, the operator must draw the area of interest (AOI) on the specimen, where shape and displacements will be analyzed. Using the Aoi tools it is possible to indicate this region in the reference image through a rectangle, a polygon, or a circle and remove the wrong figures if necessary (red cross). The operator can also define several AOIs. It is not necessary to accurately follow the specimen edges, because VIC-3D allows to set the confidence margin (distance from the boundary in pixels) and to exclude some regions of the specimen surface. The next step is setting the subset size for the AOI chosen; this can be done with the help of the software (pressing the red question mark) or manually by the operator and selecting *Apply to all*. A smaller subset size allows the software to consider more points (precision); a smaller step size makes the software more accurate but extends the computational time.

Now, the operator has to insert a start point and initial guess (*Create start point* from the Aoi tools); this point should be put in a region with low motion, which approximately maintains the same position during the test. Moving the mouse over it, the percentage of images, in which the software found that point, will be shown. Double-clicking on it causes the opening of a window (Initial Guess Editor), which shows the same point in all the deformed images framed in green (100%). If the frame is yellow or red, this point must be selected manually into all the images until the box becomes green. Otherwise, the operator can delete that image. Thus, this point should be easily recognizable also by the operator. The start points should be as many as the deformation stages.

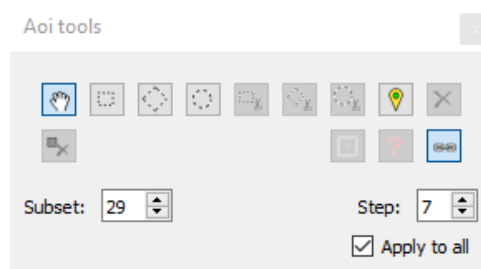


Figure 40. Aoi tools [105].

To start the process, the operator must click the green *Start Analysis* button in the toolbar or select *Data... Start Analysis*. A window will appear to allow him the control of correlation features [105].

In *Files* there is the list of the images, where the operator can deselect some of them. Then, he can choose the output directory; it is recommended to create it in the same directory of the acquired images [97].

In *Options*, the operator can choose: the weight of the pixels in the subset (Gaussian weights or Uniform weights); the interpolation of the grey value of the pixels (better a higher-order spline); the criterion of the correlation algorithm among the three above-mentioned; to compare each image to the previous one and not to the reference one, by selecting “Incremental correlation”; to insert a low-pass filter to reduce aliasing effects in images; the processor optimizations, by selecting the cores for this analysis. It is advisable not to modify these parameters.

In *Thresholding*, it is possible to set the limits beyond which data will be discarded to exclude some errors: inconsistent pixels; uncertainty due to defocus, highlights and pattern degradation; matches with poor contrast; matches that seem unrealistic.

In *Post-Processing* you can establish how data will be processed and also if calculate strain during correlation or after (*Strain computation*); then, you can choose the filter size and the tensor type (Lagrange, Hencky, Euler-Almansi, Log. Euler-Almansi, Biot, and Engineering).

Finally, operator can run the analysis by clicking the button *Run* to obtain the surface geometry and the displacement of each point. VIC-3D shows the Z value by default, but the operator can select other values, by right-clicking and selecting *Contour variable*. Some parameters are indicated at the bottom of the window; particularly, the projection error is really important, because it represents the difference between the location of a point according to calibration and its real position in the image (it must be shown in black, not in red); the number of the analyzed points is important too, to check how many of them are discarded by the software. If the analysis returns an error a manual start point must be created because the software did not determine an automatic one.

If the operator needs to calculate strain after computation, he should select *Data... Postprocessing tools... Calculate strain*. Strain values are filtered to remove the noise generated, but spatial resolution decreases too. Finally, he should click *Start* to calculate the selected values. By clicking *Preview* the effect on a single file can be seen. Now, new strain variables have been created. By default, strain in the x- and y-axes ( $e_{xx}$ ,  $e_{yy}$ ), shear strain ( $e_{xy}$ ), first and second principal strain ( $e_1$ ,  $e_2$ ), and principal strain angle ( $\gamma$ ) will be shown [105].

### 3.3.3.8 Visualization of the results

To see the data calculated, it is possible to double click on the desired file in the *Data tab* placed sideways. By clicking and dragging the operator can move the plot as he likes; with the mouse wheel or by approaching and pushing away his fingers on the touchpad he can zoom [105]. By right-clicking he can choose other display commands and see other variables, some of them always present, and some generated in post-processing (strain, velocity, curvature, and rotation variables) [97]:

- X [mm]: metric position along the X-axis (by default, the horizontal axis).
- Y [mm]: metric position along the Y-axis (by default, the vertical axis).
- Z [mm]: metric position along the Z-axis (by default, the out-of-plane axis).
- U [mm]: metric displacement along the X-axis, from the reference image. For the reference image, displacement values will always be 0.
- V [mm]: metric displacement along the Y-axis.

- W [mm]: metric displacement along the Z-axis.
- sigma [pixel]: this is the confidence interval for the match at this point, in pixels.
- x / y [pixel]: point location in the reference speckle image
- u / v / q / r [pixel]: internal raw disparity measures.
- exx [1]: strain in the X-direction. Positive numbers indicate tension; negative numbers indicate compression.
- eyy [1]: strain in the Y-direction.
- exy [1]: shear strain.
- e1 [1]: the major principal strain.
- e2 [1]: the minor principal strain.
- gamma [1]: the principal strain angle in radians, measure counterclockwise from the positive X-axis.

He can also compute additional strain variables: Tresca strain, von Mises strain, and/or Raw gradients. Von Mises strain is based on the distortion energy of a structure and is define as [122], [123]:

$$\varepsilon_{eq} = \frac{2}{3} \sqrt{\frac{3(e_{xx}^2 + e_{yy}^2 + e_{zz}^2)}{2} + \frac{3(\gamma_{xy}^2 + \gamma_{yz}^2 + \gamma_{zx}^2)}{4}} \quad (4.1)$$

where  $e_{xx}$ ,  $e_{yy}$ ,  $e_{zz}$  are the normal strains, plane strains and out-of-plane strain, and  $\gamma_{xy}$ ,  $\gamma_{yz}$ ,  $\gamma_{zx}$  are the shear strains.

- dU/dt [mm/s]: the rate of change of the U-displacement; that is, the velocity of a given point in the X direction.
- dV/dt [mm/s]: velocity in the Y direction.
- dW/dt [mm/s]: velocity in the Z direction.
- dExx/dt [1/s]: the rate of change of strain in X, or strain rate in X.
- dEyy/dt [1/s]: the strain rate in Y.
- dExy/dt [1/s]: the shear strain rate.
- cxx [1/mm]: curvature in the X-direction, equivalent to 1/(diameter of curvature).
- cyy [1/mm]: curvature in the Y-direction.
- c1 [1/mm]: the major principal curvature.
- c2 [1/mm]: the minor principal curvature.
- gamma [1]: the principal curvature angle in radians, measured counterclockwise from the positive X-axis.
- phi [1]: the in-plane rotation, in radians.

Using the *Animation toolbar*, he can see a video of the deformation process, which can be exported with the *Export* command in the plot.

By selecting *2D Plot* (icon in the top bar or *Plot... 2D Plot*), it is possible to reduce data using the *Inspector toolbar*, which appears on the top left. The *Inspect Point tools*, the *Inspect line tool*, the *Inspect Rectangle*, the *Inspect Disc tool*, or the *Inspect Polygon tool* allow the operator to see the results within a specific region. The *extensometer tool* can be used to emulate the behavior of placing an extensometer on the surface of the specimen, basically by clicking twice to place its two endpoints. The operator can visualize the strain or the deformation changes measured by the extensometer by right-clicking...*Inspector*. However, this tool shows only end to end distances. It is possible to take a screen capture, by clicking “Save” in the options menu (right-clicking).

By default, both axis and contour limits will auto-scale to the measured minimum and maximum values, but these values can be edited using *Plotting tools*, placed on the left of the screen.

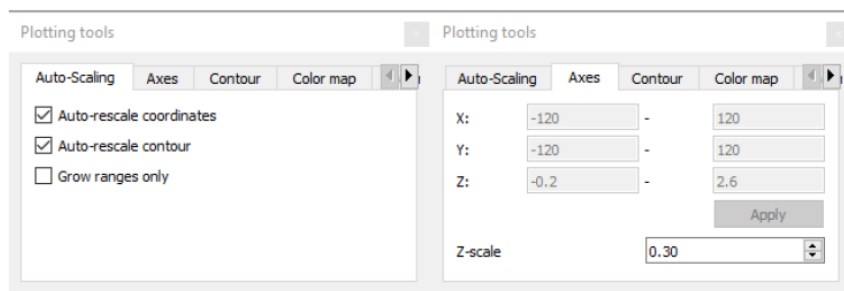


**Figure 41.** Plotting tools to set axis and contour limits [105].

In *Contour* the operator can choose the range of every variable; it is useful a preliminary data extraction to see these ranges in the extracted lines, by right-clicking in 2D Plot and then “Extraction”. *Plot extraction tool* shows data from any inspector tool or global average: it creates a line for the average and other lines for the previously placed tools (points, polygons etc.). To remove one or more tools, using the *Delete* command in the *Inspector toolbar*. To modify a line's variables, changing both the variables and the data source for the Y and X axes, as shown in fig. 41 [105].

In *Color map* the operator can select the map colors, the number of levels and labels. He can insert some iso-lines, to better distinct the levels on the images (a contour map will be shown), or white vectors in the main directions of the deformation [97].

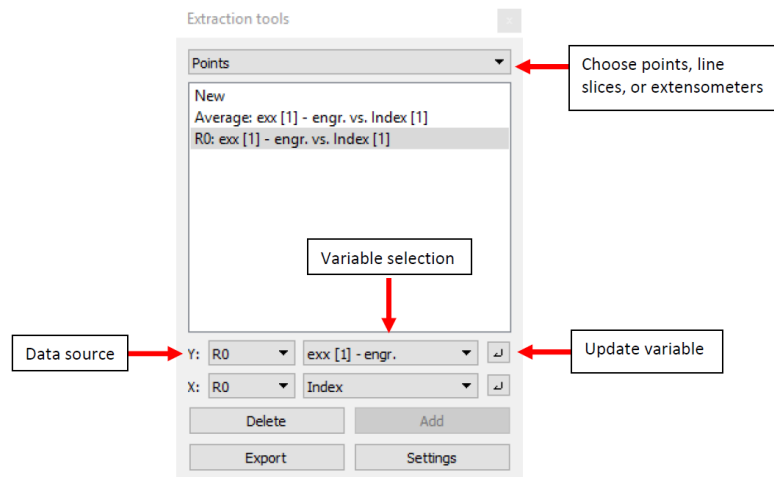


**Figure 42.** Extraction tools command windows to visualize different lines and modify the line's variable [105].

By clicking *New* (in fig. 42) and then *Add* after choosing its features, it is possible to create a new plot, where the operator will see several data, nevertheless the selected one will be plotted in red. Moving the mouse to see points coordinates on the plot and change its position by moving the mouse wheel and clicking and dragging; it is possible to fit the plot to the window by double-clicking.

By clicking *Export* in the *Extraction tools*, the operator can export the data of the extracted lines in Microsoft Office Excel® (\*.csv) and deselect the variables he does not need.

By clicking the eye-icon, the new *iris* visualization framework will replace the analysis workspace. Here the operator can create a presentation of the project: he can select the layout, start the editing using the top toolbar and, finally, export the slideshow in PDF format. The *iris* workspace contains [105]:

- Main toolbar: has controls for inserting new objects like plots and images; alignment controls; and buttons for exporting PDF and video.
- Page/template/report organizer: the left sidebar shows a graphical list of pages, templates, and backgrounds, selectable from the pulldown.
- Properties editor: the right sidebar has a list of adjustable properties for the currently selected item.
- Timeline: the timeline area at the bottom of the window shows all the timelines and keyframes in the project and allows scrolling through time.
- Main work area: where all objects/text/graphics will be placed and manipulated.

Furthermore, the operator can realize reports from template documents: the software will insert data such as calibration values, analysis settings, images, or plots in a document (OpenDocument or Word document, OpenDocument or PowerPoint presentation). This operation is possible after running the analysis, by clicking *File...Report* from the main menu. In the Report Options, the operator can choose the image resolution (*Print* generates better images than *Screen*), the scaling (*Nearest neighbor* for a faster creation or *Smooth* for a better quality), the video settings (encoder method, format and frame rate) [97].

## 4. Design and preparation of the specimens

### 4.1 Polymeric materials to mimic tendon/ligament behavior

The aim of the study is to design patterns which replicate the mechanical response of the tendon and ligament. Polymeric and composite materials are a valuable choice to reproduce the structure and the mechanical behavior of natural connective tissues since they allow the combination of a wide selection of material characteristics. Particularly, new design philosophy, such as “learning from nature” can be followed in designing new patterns, since the natural tissues are composites, and their properties reflect their microstructure. Natural tissue, in general, show non-linear and viscoelastic behavior, as shown in fig. 43 [124]. Hydrothane is a hydrophilic thermoplastic elastomer, which, in wet condition, when subjected to UTS tensile testing (ASTM D638), shows an elastic modulus of  $2.30 \pm 0.26$  MPa, a UTS of about 14 MPa and an ultimate elongation of 450-650% [124], [125]. Mechanical properties (elastic modulus and strength) of connective tissues appear higher than Hydrotane [124].

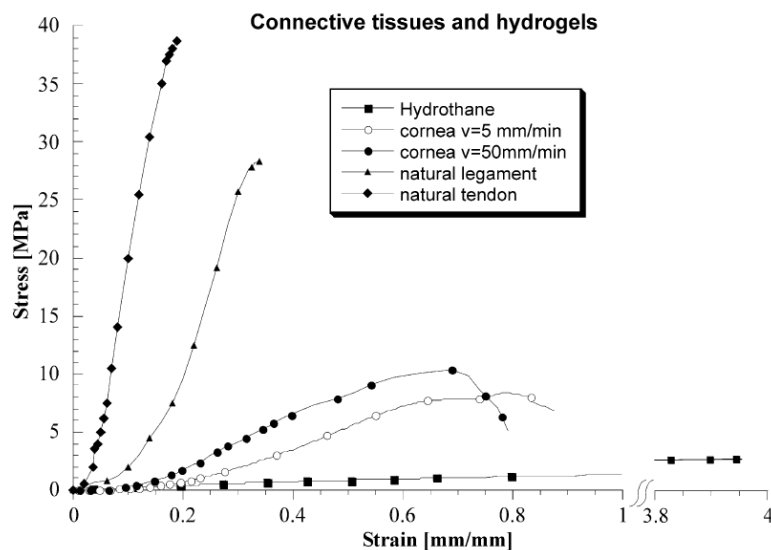


Figure 43. Stress-strain curves of connective tissues and Hydrotane [124].

These graphs show the tendon is a stronger and stiffer structure than the other two connective tissues, which are usually mimed using elastomers, rubber-like materials.

In the study of Wang *et al.* [126], high-performance nitrile rubber (NBR) elastomers, enriched with different content of  $Zn^{2+}$  and S, were designed. They obtained materials with different mechanical properties (Fig. 44), such as the elastic modulus, which represents the slope of the stress-strain curve.

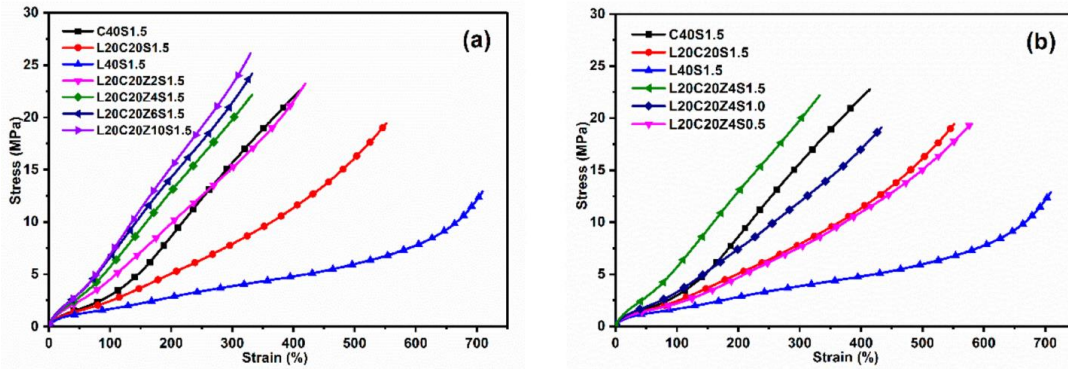


Figure 44. The engineering stress-strain curves of NBR elastomers with different slope, that is the elastic modulus [126].

In the study of *Bannych et al.*, it is demonstrated that the Young’s modulus of rubbers increases with increased multi-walled carbon nanotubes (MWCNT) concentration (Fig. 45), that stiffen the structure, raising the slope of the curve.

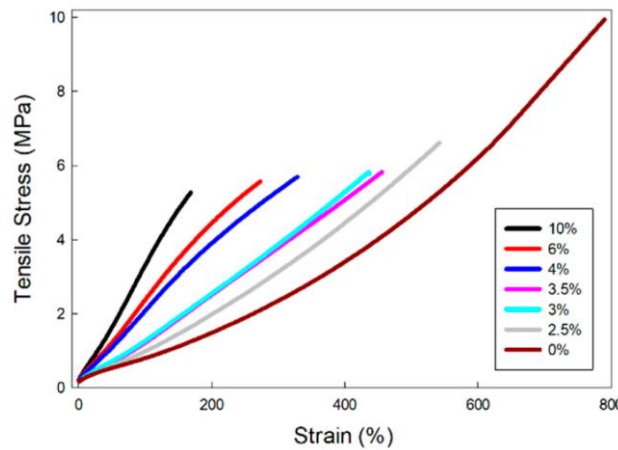


Figure 45. Stress-strain curves of vinyl methyl silicone rubber (VMQ) enriched with different percentages of MWCNTs [127].

Analyzing only the shape of the curves, it seems the tendon behavior could be better reproduced by a material with a higher elastic modulus. A more rigid polymer generates a steep curve with a high UTS. Moreover, a very resistant material is advisable since it must withstand high loads. Therefore, among the designed pattern, we will pick those with the highest mechanical properties (ultimate tensile strength and modulus of elasticity), being aware that the orders of magnitude of the polymers are not comparable to that of the tendon and ligament but based only on their qualitative behavior.

## 4.2 Pattern layouts

The pattern proposed have been designed in Rhinoceros (Rhino) 3D basing on two different natural hierarchical structures, the tendon and the bamboo. The pattern was placed within the CSA of the specimen, in order to have it only along the constant section of the specimen. The biomimetic approach allowed the design of multi-hardness specimens, compared to the fiber-matrix patterns, which produce only bi-hardness structures. The patterns designed are tendon-like (TL) and tendon-mimic (TM), based on the hierarchical structure of the tendon, and bamboo-like (BL) and helix bamboo-like (HB), based on the hierarchical structure of bamboo.

### 4.2.1 Tendon-like (TL) pattern

The TL pattern is made of fibers with concentric layers arranged to mimic the internal structure of tendon and ligament at the micro- and mesoscopic scale (Fig. 46). The inner layer represents the fiber at the microscopic level, that is the collagen fibril. The middle layer surrounds the inner one and aims to simulate the collagen fiber, the primary fiber bundle. The outer layer represents the tendon fascicle (secondary fiber bundle) and, as in the natural structure, it contains a cluster of collagen fibers (three in our pattern). Finally, the matrix surrounds all the fibers as the endotenon in the natural tendon. The structure of the TL pattern in details is shown in the fig. 47. The TL pattern's design specifications are shown in the following table (Tab. 1).

**Table 1.** TL pattern's design specifications: radius value and transversal area percentages in the CSA.

Tendon-like (TL) pattern		
Layers	Radius (mm)	Area%
Inner layer (collagen fibril)	0.08	3.42
Middle layer (collagen fiber)	0.18	15.27
Outer layer (tendon fascicle)	0.54	39.53
Matrix (endotenon)	-	41.78

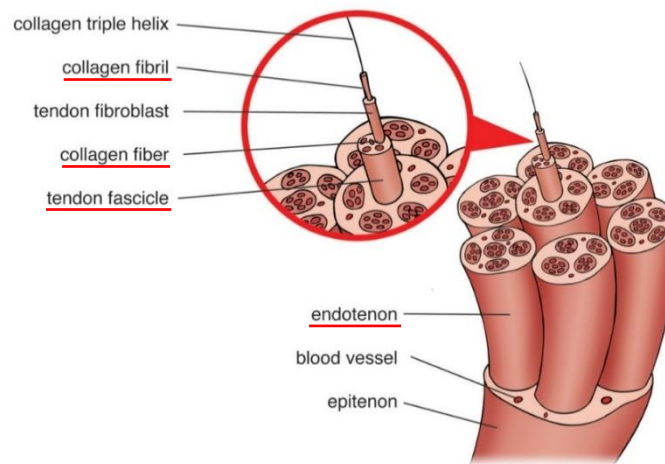


**Figure 46.** Hierarchical structure of the tendon with the substructures involved in the TL pattern underlined in red [128].

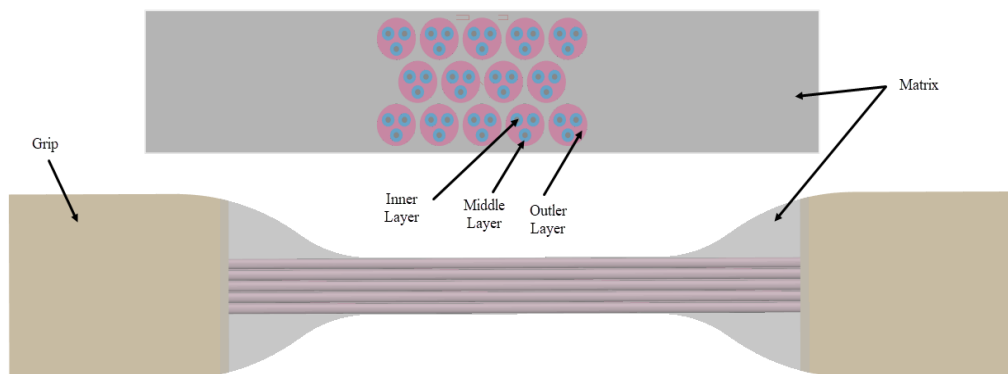


**Figure 47.** Different views of the tendon-like (TL) pattern: top view and CSA.

### 4.2.2 Tendon-mimic (TM) pattern

The TM pattern is composed of random fibers scattered in a matrix. The fibers represent the fibrous bundles typical of tendons and ligaments. A microscopic image of a deep equine tendon, available in the “Bio-inspired Nanomechanics Giuseppe Maria Pugno Laboratory” (DISEG, Politecnico di Torino), was used as a template for the segmentation process of the fibrous bundles. The tendon CSA is shown in the fig. 48A, where the irregular geometrical shapes of the fascicles can be noted.

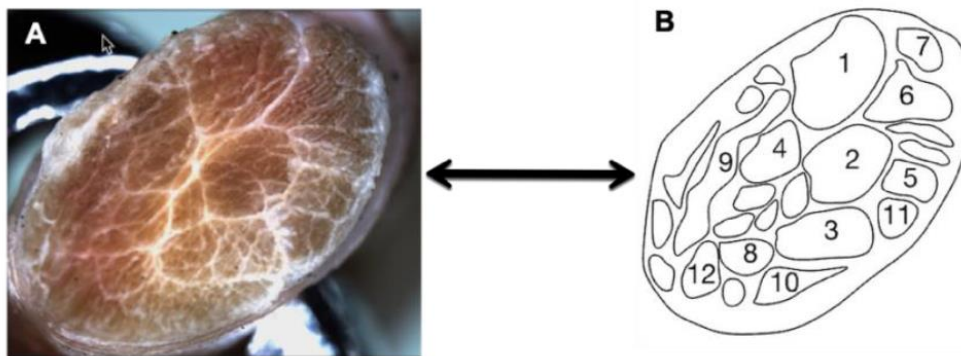


**Figure 48.** A) Deep equine tendon CSA and B) segmented fiber bundles.

The microscope image was imported in Rhino 3D, where the random shape borders of the fibers were segmented, as shown in fig. 48B. The areas of the different bundles were measured, obtaining the values reported in tab. 2. The average area of the fascicles was computed and the three fibers whose area most closely approximated the average one were chosen for creating the equine tendon-mimic pattern’s design. These fibers are highlighted in yellow in the tab. 2 and are marked with numbers 4, 6, 10 in fig. 48B.

**Table 2.** Areas of segment fiber bundles and their mean value. Picked fiber bundles marked in yellow.

Fiber bundles in equine tendon	
Section number	Area (mm <sup>2</sup> )
1	0.780
2	0.531
3	0.434
4	0.263
5	0.173
6	0.339
7	0.150
8	0.164
9	0.438
10	0.189
11	0.130
12	0.167
Mean	0.285

Three pattern variations (Fig. 49) have been designed to evaluate how much the percentage of fibers in the matrix influences the mechanical behavior of the specimens subjected to tensile test: variation A, variation B, variation C (Fig. 50). In variation A the fibers have a medium size and four different geometries. They occupy the 50% of the CSA, like the matrix. In variation B, the fibers are larger and have two different shapes. The percentage of fibers is higher (60%) than the percentage of matrix (40%). The variation C has 9 types of small fibers, which occupy 1/3 (33%) of the CSA, while the matrix is 67% of the CSA.

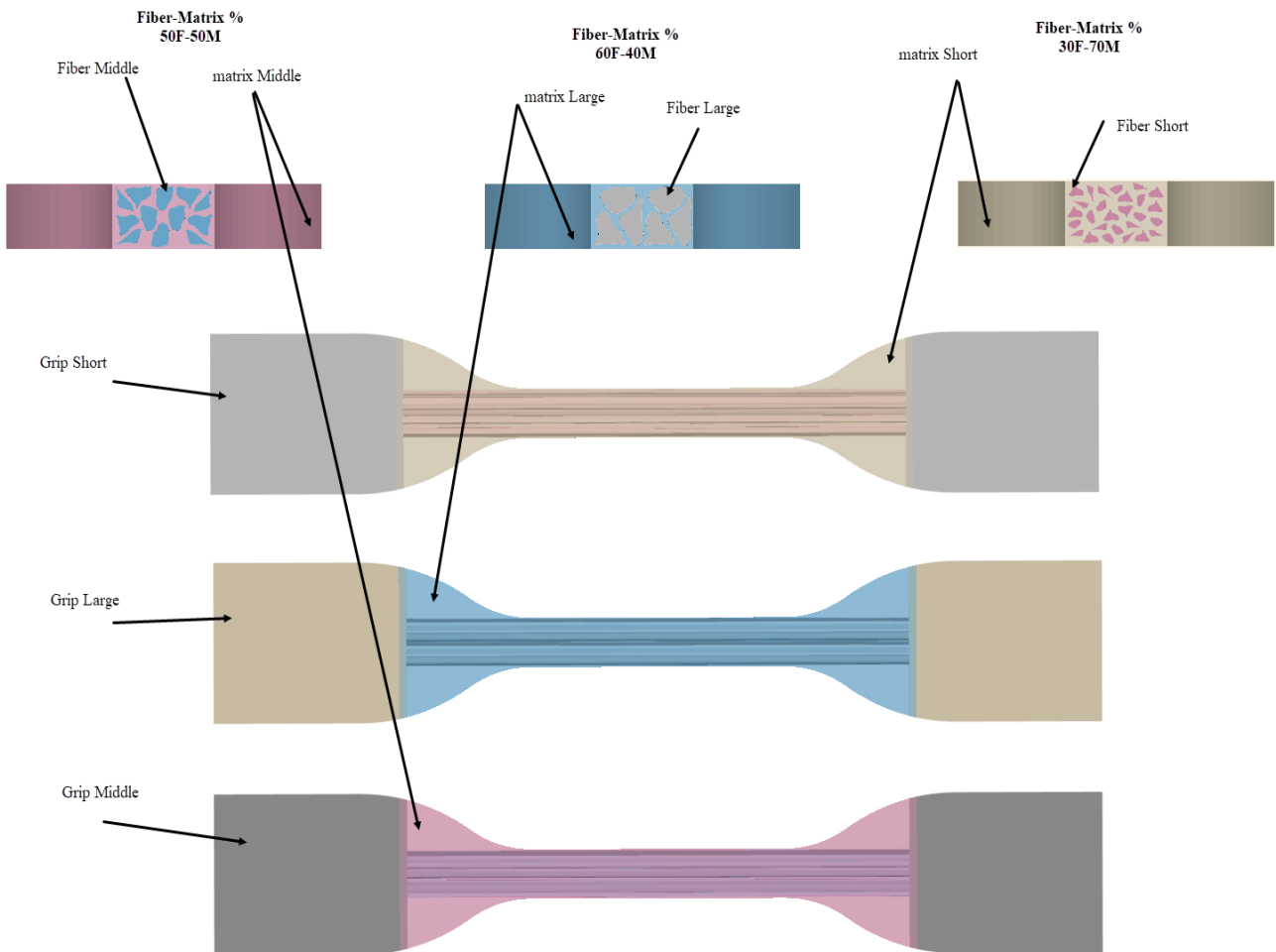


**Figure 49.** Different views of the three variations of tendon-mimic (TM) pattern: top view and CSA.

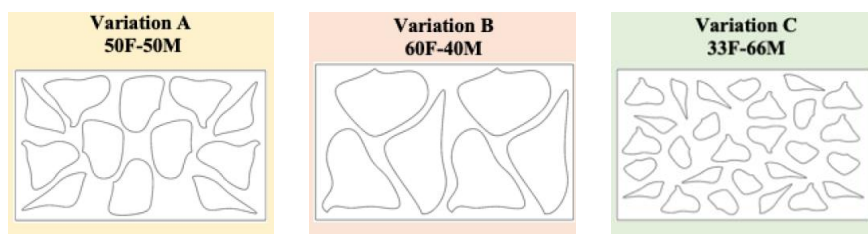


**Figure 50.** Detailed structure of the three variations of the TM pattern.

### 4.2.3 Bamboo-like (BL) pattern

The BL pattern mimics the concentric layers of the bamboo fibers, being composed of 13 circular structures, made of three different materials, as shown in fig. 51. This multi-layered organization

could excellently simulate the hierarchical structure of tendon/ligament collagen fibers and their mechanical behavior. The percentages of area of the different BL pattern's layers are shown in the following table 3. As shown, the inner layer occupies proportionally less surface area in the CSA and the matrix a bigger surface area than the other components, just like in the TL pattern.

**Table 3.** BL pattern's design specifications: radius value and transversal area percentages in the CSA.

Bamboo-like (BL) pattern		
Layers	Radius (mm)	Area%
Inner layer	0.26	4.20
Middle layer	0.46	12.77
Outer layer	0.71	30.27
Matrix	-	52.73

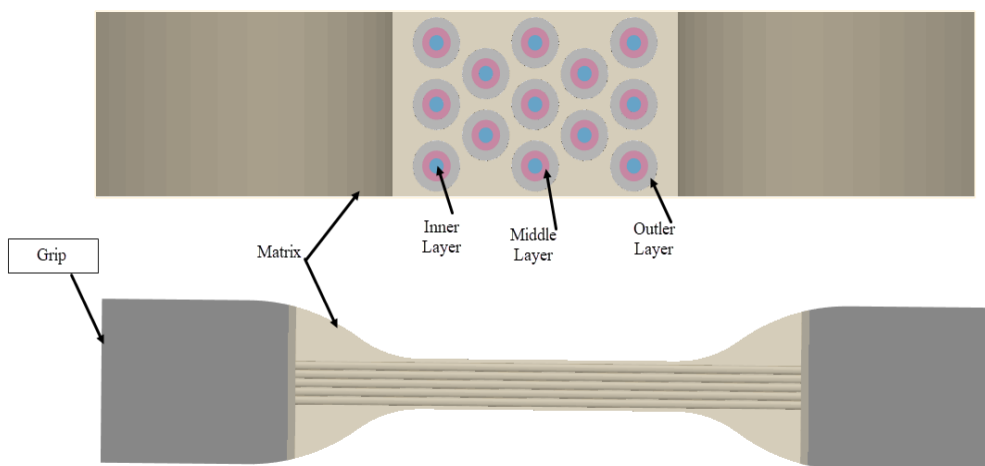


**Figure 51.** Different views of the three variations of bamboo-like (BL) pattern: top view and CSA.

#### 4.2.4 Helix bamboo-like (HB) pattern

The HB pattern represents a single bamboo fiber, mimicking the multi-layered structure and the microfibrils inside each layer, as shown in fig. 52. The microfibrils in the outer and middle layer were designed as double helices, while in the inner layer there is only a linear fiber. The fibers have a lower helix pitch (2.5) in the outermost layer than in the middle one (3.5), as shown in fig. 53. Moreover, the outer layer's fibers are at a 45-degree angle to the cross-sectional axis, while the middle layer's ones are parallel to this axis. This pattern aims to mimic the different orientations to which the bamboo's microfibrils are helically wound. It appears of particular interest, since the combination of concentric layers and double helices fibers enhances the choice of hardness values. The percentages of area occupied by the different HB pattern's layers and fibers is shown in the following table 4. As illustrated, the matrix is the component which occupies the larger area in the CSA (53%). In the pattern were designed 45 fibers, which occupy only 6.5% of CSA and have a diameter of 0.2 mm, that is large enough to allow the 3D printing (0.1 mm resolution).

**Table 4.** HB pattern's design specifications: radius value and transversal area percentages in the CSA.

Helix Bamboo-like (HB) pattern		
Layers	Radius (mm)	Area%
Inner layer	2.58	1.15
Middle layer	1.79	13.13
Outer layer	0.53	26.22
Fibers	0.10	6.50
Matrix	-	53.00

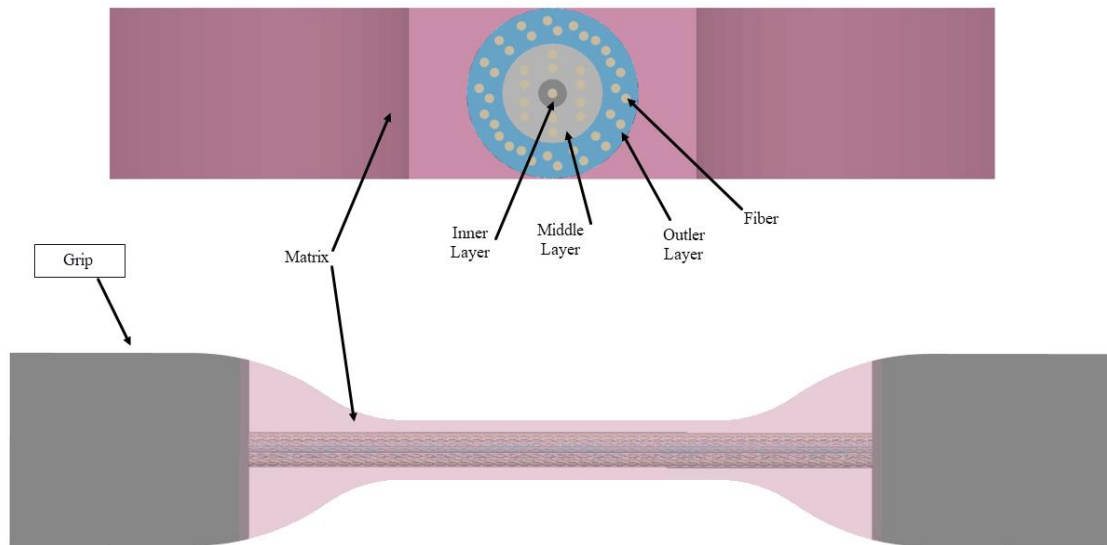


**Figure 52.** Different views of the three variations of helix bamboo-like (HB) pattern: top view and CSA.

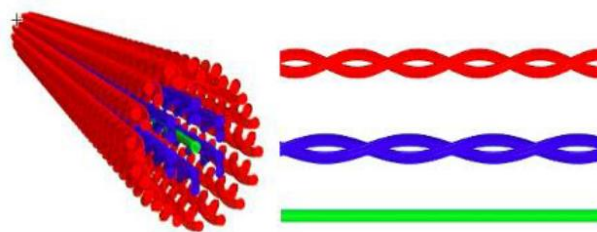


**Figure 53.** Different arrangements of the microfibrils inside the concentric layers: double helices in red (outer layer) and blue (middle layer) and linear fibril in green (inner layer).

### 4.3 Shore A values combinations

All the specimens were made of Agilus30, using three different hardness values, A50, A60, and A70. The TL pattern was placed in 6 specimens, the TM pattern in 18 specimens, the BL pattern in 6 specimens and the HB pattern in 14 specimens. No specimen is like another, since their layers are a combination of the three different Shore A values.

### 4.3.1 TL pattern hardness values

This pattern is composed of concentric layers; therefore, it is possible to combine the three Shore A values and obtain different specimens. Keeping the hardness of the matrix fixed, different combinations were thought by alternating the Shore A values of the three layers, as shown in tab. 5. The specimens A-D have a matrix with a Shore A60. The specimens A and B have, respectively, a growing and declining trend of the layers' hardness values. In the other four specimens the adjacent layers have an alternating configuration (soft and hard). In the specimens C and D, the middle layer is kept to A60 and the other two layers have a Shore A70 (in C) and A50 (in D). The specimen C will surely appear harder than the specimen D. In the specimens E and F the alternating Shore A values are A50 and A70, starting, respectively, with A70 and A50; thus, the matrix of E is softer than the matrix of F. Specimens E and F show a greater hardness gradient between the adjacent layers.

**Table 5.** Shore A hardness values of the specimens with TL pattern.

Tendon-like (TL) pattern				
Specimens	Inner layer	Middle layer	Outer layer	Matrix
A	50	60	70	60
B	70	60	50	
C	70	60	70	
D	50	60	50	
E	70	50	70	50
F	50	70	50	70

### 4.3.2 TM pattern hardness values

Six hardness values combinations were proposed for each TM pattern variation, as shown in tab. 6. Specimens with harder fibers in softer matrix and softer fibers in harder matrix were designed: two soft configurations (fibers A50 – matrix A60, and vice versa), two hard configurations (fibers A70 – matrix A60, and vice versa), and two maximized gradient configurations (fibers A70 – matrix A50, and vice versa).

**Table 6.** Shore A hardness values of the specimens with TM pattern.

Tendon-mimic (TM) pattern			
Specimens	Fiber	Matrix	Fiber-Matrix %
G	50	60	33F-67M
H	60	50	
I	50	70	
J	70	50	
K	60	70	
L	70	60	
M	50	60	50F-50M

N	60	50	
O	50	70	
P	70	50	
Q	60	70	
R	70	60	
S	50	60	60F-40M
T	60	50	
U	50	70	
V	70	50	
W	60	70	
X	70	60	

### 4.3.3 BL pattern hardness values

Each fiber of the BL pattern has different levels of hardness for each proposed combination, following the same criteria of the TL pattern, since the two patterns consist of the same number of concentric layers. Six different specimens were therefore designed. This approach permits to evaluate which of these two concentric-layered patterns leads to the best tensile mechanical results, having eliminated the variability of durometer choice.

*Table 7. Shore A hardness values of the specimens with BL pattern.*

Bamboo-like (BL) pattern				
Specimens	Inner layer	Middle layer	Outer layer	Matrix
Y	50	60	70	60
Z	70	60	50	
A1	70	60	70	
B1	50	60	50	
C1	70	50	70	50
D1	50	70	50	70

### 4.3.4 HB pattern hardness values

In the HB pattern there is another variability factor, having introduced little fibers within the concentric layers of the single bamboo fiber. Never coming into contact, it is possible to choose a single Shore A both for the little fibers and for the matrix. Thus, keeping the hardness value of these two substructures fixed, the same approach as for TL and BL (concentric layered) patterns was followed. When the Shore of the fibers and the matrix is A60, the increasing and decreasing trend of the durometer could be applied to the layers (specimens J1 and K1). In all the other specimens, the adjacent layers have an alternating configuration of two hardness values.

**Table 8.** Shore A hardness values of the specimens with HB pattern.

Helix-bamboo (HB) pattern					
Specimens	Inner layer	Middle layer	Outer layer	Matrix	Fibers
E1	60	50	60	50	50
F1	60	70	60		
G1	70	50	70		
H1	70	60	70		
J1	50	60	70	60	60
K1	70	60	50		
L1	50	60	50		
M1	70	50	70		
N1	50	70	50		
O1	70	60	70		
P1	50	60	50	70	70
Q1	50	70	50		
R1	60	50	60		
S1	60	70	60		

### 4.3.5 Base materials

These are the base materials of Agilus30 of the three different Shore A values, A50, A60, and A70. They were also 3D printed and tested, to compare the mechanical response of the specimens with the pattern to the specimens without any pattern. We also tested the TissueMatrix, a soft and contractile material typical of the J750 DAP [129].

**Table 9.** Shore A hardness values of base materials.

without Pattern (Base Agilus30 materials)	
Specimens	Durometer
T1	50
U1	60
V1	70
without Pattern TissueMatrix material	
W1	

## 4.4 3D Printing of the specimens

The different designed patterns in \*.3dm format were converted into \*.STL format and sent to the GrabCAD™ Print Software of the J750 DAP [61]. The 44 different combinations of the four proposed patterns and four base materials (Agilus A30 with Shore A of 50, 60, and 70 and TissueMatrix) were 3D printed at the Stratasys headquarters (Rehovot, Israel) using the J750 DAP. The type IV dog bone

was chosen as specimen shape (Fig. 54), according to the ASTM D638-14 [77] and the work of *Severseike et al.* [73]. The specimen grips were made of Digital ABS, a rigid material, with the aim to absorb the pressure of the clamping jaws during the tensile test. Moreover, there was a 1 mm overlapping between the material of the grips and that of the test region, to avoid a discontinuity at the interface which could cause high stress values. The test specimens were printed along the X-axis, that is the longitudinal direction of the specimen, and the Y-axis, the transversal direction (Fig. 55). The build orientation influences the anisotropy in the elastomers; therefore, the effect of orientation on the mechanical properties of Polyjet plastics was investigated in several works, concluding that parts printed along X-Y plane showed the highest elastic modulus and that Z-specimens had the poorest mechanical properties [72], [130]–[133].

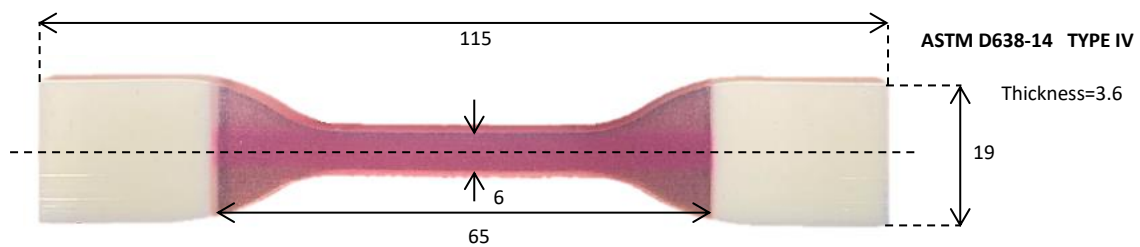


**Figure 54.** ASTM 638-14 Type IV specimen, dimensions in millimeters.

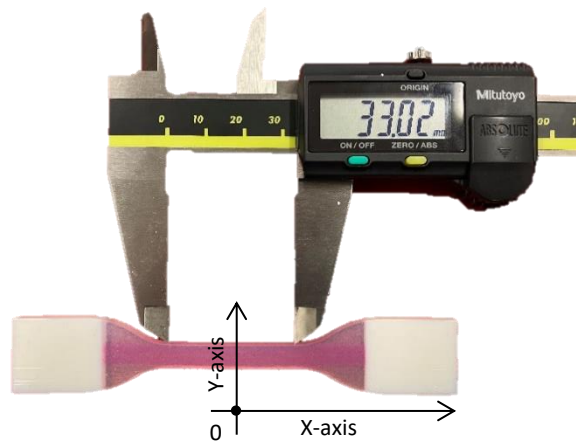


**Figure 55.** Length of the constant region of the specimen and build orientation.

## 5. Mechanical tests and results

### 5.1 Experimental setup

The specimens were then tested for tensile using an MTS Insight® Electromechanical Testing System [86] at the Bio-inspired Nanomechanics Giuseppe Maria Pugno laboratory (Turin, Italy) and, simultaneously, several images of the specimens were captured by a VIC-EDU system (Fig. 56).



**Figure 56.** Experimental setup: UTS testing machine and DIC system.

### **5.1.1 Setup of the UTS (Ultimate Tensile Stress) testing machine and output**

The trials lasted four days. For every specimen type three samples were tested, to obtain a mean and a standard deviation (std). The testing machine available, the MTS Insight 2, was equipped with Advantage™ Pneumatic Grips, with a static force capacity of 200 N, a range of supported temperature between -40°C and 200°C and a maximum operating pressure of 5.5 Bar. The specimens were gripped at the distal parts appearing with their X-axis along the vertical direction of the space.

The tensile machine needed these input parameters:

- Data acquisition rate: 60 Hz;
- Grip separation: 65 mm;
- Speed of testing: 50 mm/min.

Following the ASTM D638-14 [77], this speed was chosen between the available speeds for the type IV specimen:  $5\pm 25\%$ ,  $50\pm 10\%$ ,  $500\pm 10\%$ . According to the work of *Abayazid et al.* [72], increasing the speed of testing (or strain rate), the stress-strain curve would be S-shaped and with an initial stiff region, showing a nonlinear behavior. Moreover, the extension and the tensile strength at break increased with the strain rate. Since an almost linear curve was desired, a fairly low velocity was chosen.

It is also possible to provide the width and the thickness of the specimen to the testing machine to compute the stress and strain vectors, but it was preferred doing this operation in Microsoft Office Excel® and considering only the elongation (L, in mm) and the load vectors (F, in N). Before starting the mechanical test, it is important to zero the load cell and crosshead channels and avoiding leaning on the table during the analysis, not to distort the results. In the displayed curve, the coordinates of B and M points, which represents the linear region of the curve, were written on a tab in an Excel spreadsheet and the test result was exported as a \*.txt file.

### **5.1.2 DIC setup and calibration**

Before starting the mechanical tests, the specimens underwent a washing and a preparation. They were cleaned using a bowl of water and a toothbrush, to remove the support material on the surface. It was necessary to wait at least 72 hours before testing the specimens, to ensure a good drying and avoid the presence of residual moisture. In the first day of tests, considering the light color of the specimens, the specimens were only covered by a black speckle pattern, without any artificial background (Fig. 58A). The speckle pattern was generated as random as possible using a toothbrush, flicking it on the specimen surface, as shown in fig. 57. Nevertheless, analyzing the first images acquired by the DIC cameras, the contrast was not optimal, so it was decided to create first a white background with a spray can and then the black dots after drying (Fig. 58B). It was noted that too long time between the drying of the background and the testing made the DIC analysis unfeasible, since the paint peeled off during the pulling. Therefore, the pattern on the surface was generated just a minute before the testing.

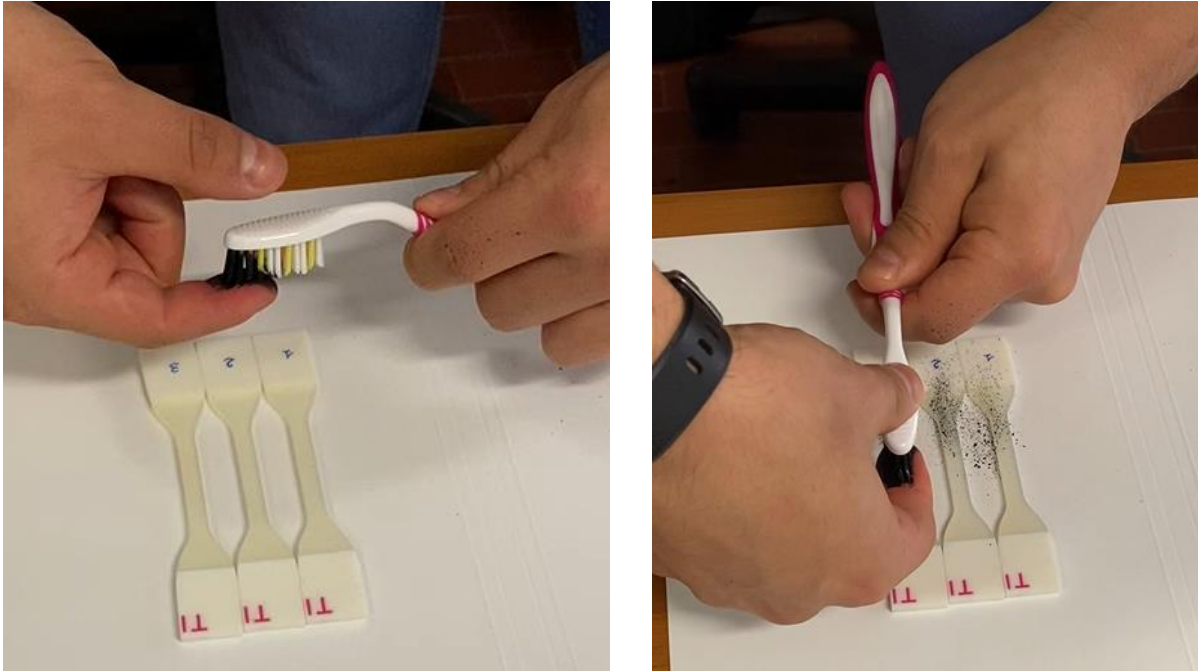


**Figure 57.** Creation of the black speckle pattern on the specimens using a toothbrush.

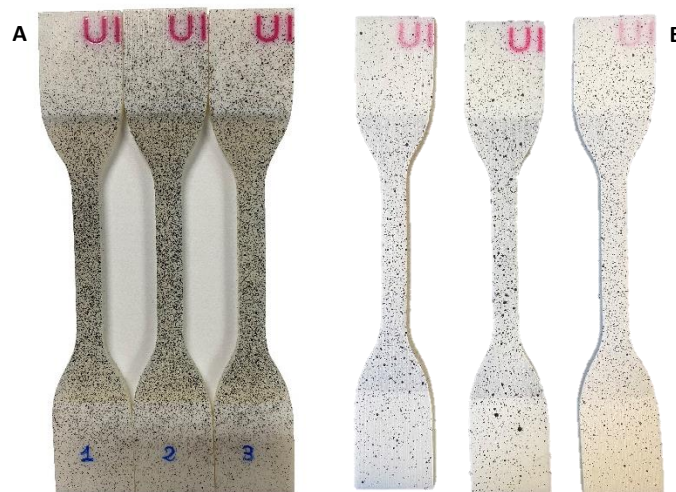


**Figure 58.** Specimens U1 covered with black pattern: a) without the background and b) with the background.

The VIC EDU system was assembled in front of the testing system to capture images simultaneously with the deformation of the specimens. In the first day of tests (March 30), the tripod was placed at 54.5 cm away from the specimen, and at 117 cm off the ground to capture the complete process of deformation (Fig. 59). The tripod plus tripod head complex is overall 126 cm off the ground. For a better lighting of the specimen surface, two lights were added to the LED light of the system.



**Figure 59.** Physical setup of the VIC EDU system.

The software VIC-Snap was used to monitor the field of view of the cameras and verify the good placement of the specimen and the optimal lighting. The position of the lights had been changed until the software showed a blue or violet color on the specimen surface in both the mirror images (Fig. 60); a blue color is better to avoid overexposure during the test. This process was repeated for all the tested specimens.

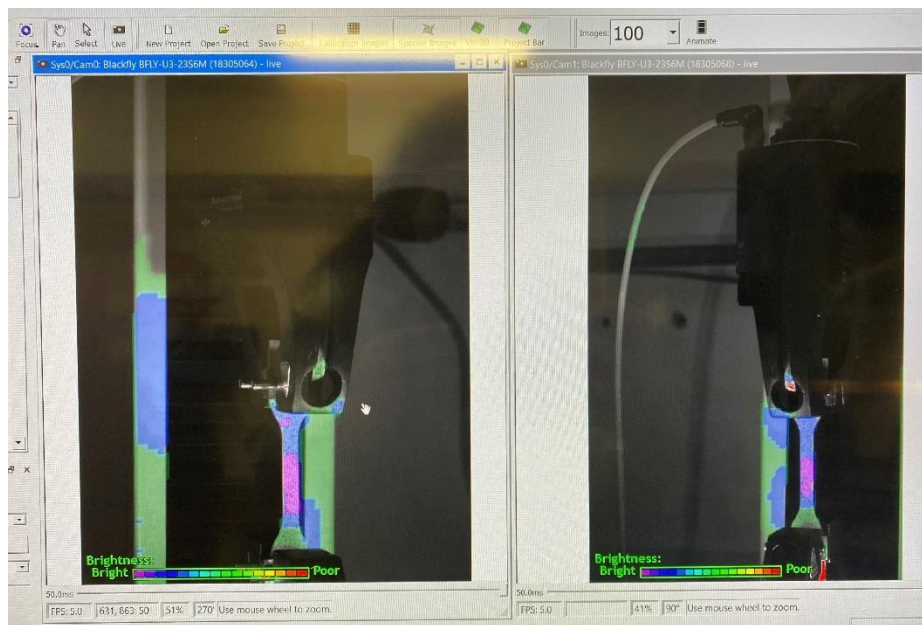


**Figure 60.** Regulation of the brightness of a specimen using VIC-Snap.

The acquisition time was set considering the deformation time of the specimen, that is about 204 seconds. Thus, the cameras would capture a pair of images every 2 seconds; a total of 100 images were acquired for each specimen. The eventual extra images after the breaking were deleted before examining the results, obtaining 30/40 images per specimen. The exposure time was 50 ms.

To calibrate the system, a calibration plate (Fig. 61B) was placed in front of the cameras before the specimen and was moved and rotated while acquiring about 30 images. It is not important to catch all the points of the plate, but only the different ones, reference points for the system. During the acquisition process the images which displayed “0,0” values were discarded. The calibration process must be done every time the system is moved; therefore, it was repeated every day of tests. The final calibration score, displayed in green, were 0.034.

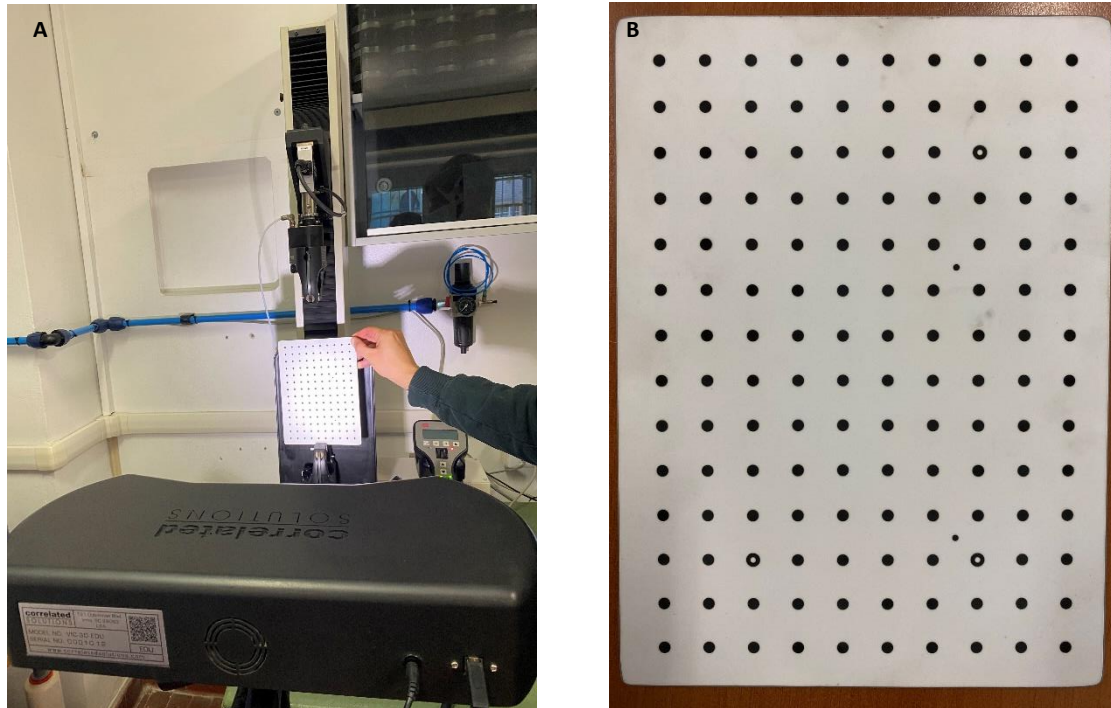


**Figure 61.** a) carrying out the calibration process; b) calibration plate or grid.

Finally, the specimen was placed between the grips and the test started. The specimens tested on the first day were T1, U1, V1, W1, Y, Z, A1, B1, C1, D1. The white background was initially created only on the specimen W1 because of its transparency. However, analyzing the images later, it was found that, without a white background, there was a bad contrast. Moreover, the cameras were too far from the specimen to optimally focus it. Therefore, these specimens were tested again in the final day (April 30).

In the second day of tests (April 2) the DIC system was moved 4 cm closer to the testing machine to better focus the specimen. In the images previously acquired, indeed, the specimens appeared slightly blurred, because of their distance from the cameras. This is because the calibration plate must be placed on the same plan of the specimen to have higher quality images, not before it. The calibration process was repeated, obtaining a score of 0.045, and the specimens G, H, I, J, K, L, M, N, O, P, Q, R, S, T, U, V, W, X, P1, Q1, R1, S1 were tested.

In the third day of test (April 22) the specimens A, B, C, D, E, F, G, E1, F1, G1, H1, J1, K1 were tested. The DIC system was repositioned 2 cm closer to the specimen and recalibrated (score: 0.052). These specimens appeared perfectly focused, which meant there would not be noise into the images.

In the fourth and last day of tests (April 30) the specimens L1, M1, N1, O1 were first-time tested and the specimens T1, U1, V1, W1, Y, Z, A1, B1, C1, D1 were retested. The DIC system was placed in the same position as the previous time and recalibrated (0.056).

## 5.2 Post processing

### 5.2.1 Processing of the mechanical data

To process all the data a Matlab code has been developed, in which B and M coordinates need to be manually inserted and the three txt files are loaded through a command. The code computes the stress and the strain vectors, finds the corresponding B and M points in the stress-strain curve and plots it. Then, several mechanical parameters (mean and std) were computed: peak load; elongation at break; tensile strength at break; strain at break; modulus of elasticity; stiffness; strain at break (%)\*; final length\*; complete elongation\*; Pearson's coefficient ( $R^2$ )\*; coefficient of variation (CV)\*.

\*without standard deviation

The Pearson's coefficient was computed using the following Matlab routine:

```
%Pearson's coefficient computation
indmax=find(stress==max(stress));
stress_peak=stress(1:indmax);
strain_peak=strain(1:indmax);
mdl=fitlm(strain_peak, stress_peak); %linear regression
r2=mdl.Rsquared.Ordinary;
```

Considering `stress` and `strain` as the stress and strain vectors.

CV was computed only for the first six mechanical parameters.

#### 5.2.1.1 Analysis of the mechanical parameters

For every pattern elastic modulus (Fig. 62), tensile strength at break (Fig. 63), and strain at break (Fig. 64) were graphed to identify the best specimen for every pattern, according to these parameters, and then compared them to the base materials. Particularly, we want to detect the strongest specimens, being the tendon an extremely resistant material, and the stiffest ones, since the other connective tissues appear definitely softer than it; therefore, the chosen ones will show the highest tensile strength at break and elastic modulus. The elongation at break must not be overlooked, since the tendon is an elastic structure too, thus its value should not be too low. At the end of the analysis, among the best specimens, those whose stress-strain curve more closely resembles that of tendon and ligament will be chosen as potential candidates.

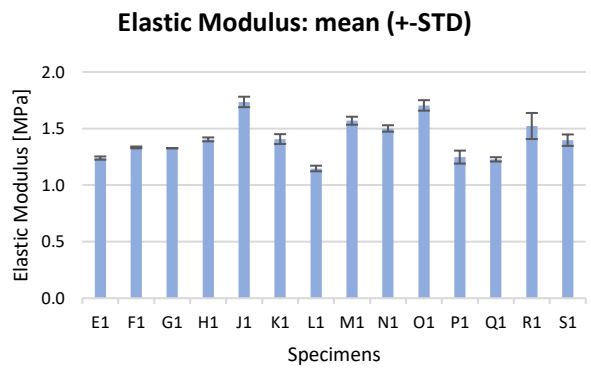
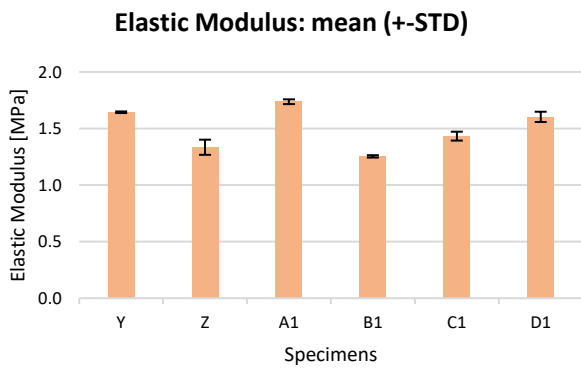
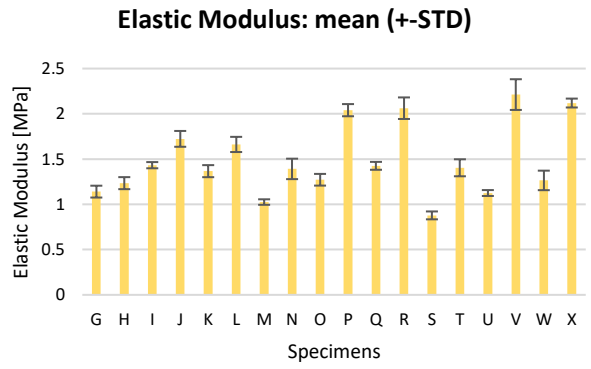
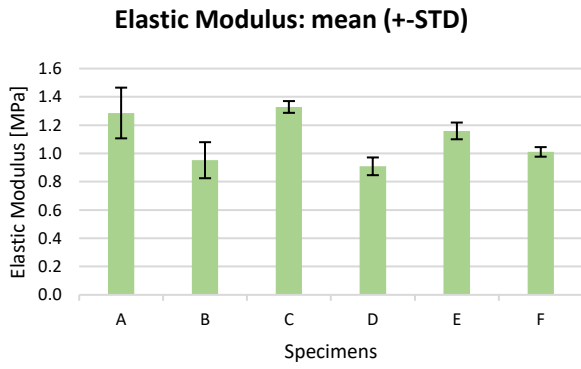


**Figure 62.** Modulus of elasticity of the 44 specimens, according to the four patterns (TL, TM, BL, HB).

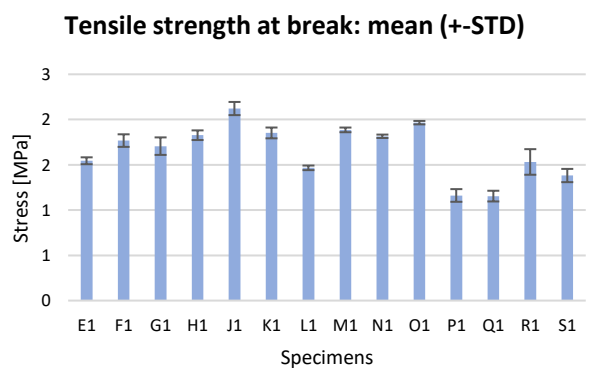
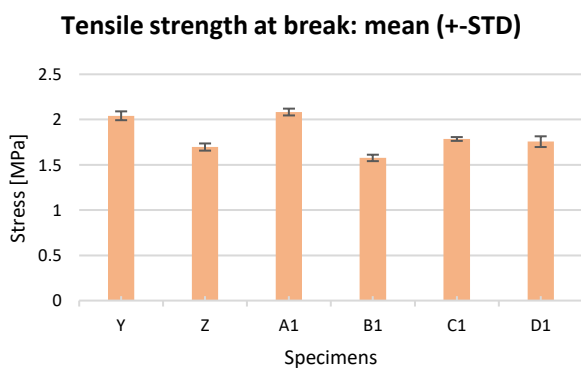
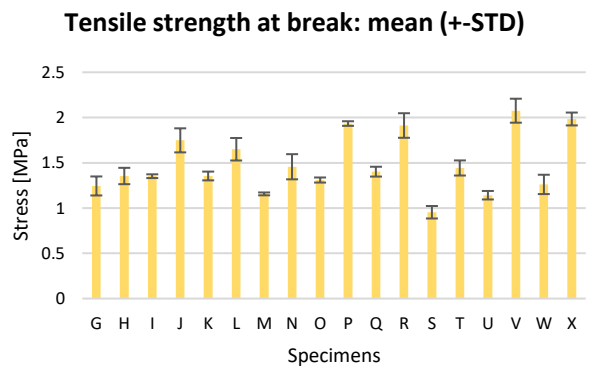
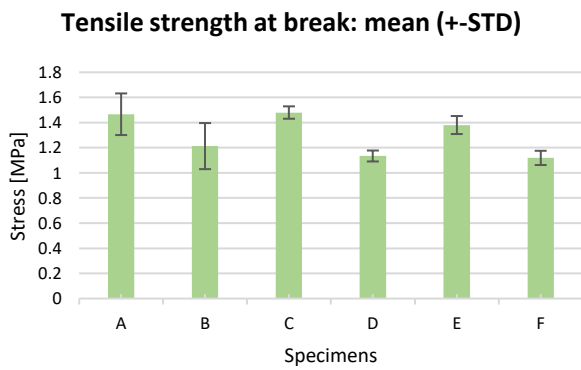


**Figure 63.** Tensile strength at break of the 44 specimens, according to the four patterns (TL, TM, BL, HB).

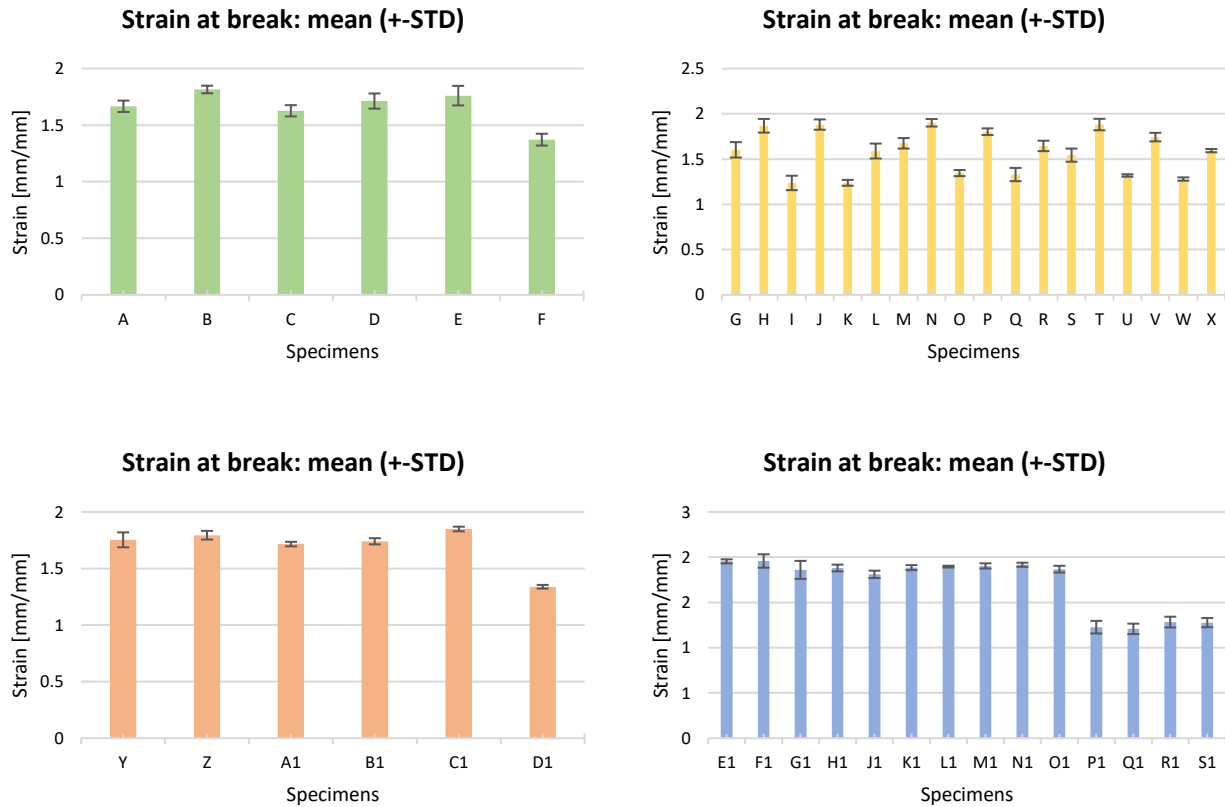


**Figure 64.** Strain at break of the 44 specimens, according to the four patterns (TL, TM, BL, HB).

The specimen A1 was chosen as best BL pattern, since it reached the highest tensile strength at break (2.08 MPa) and was characterized by the greatest elastic modulus (1.74 MPa). Among the TL pattern category, the specimen C was the most performing, with a tensile strength at break of 1.48 MPa, similar to the specimen A (1.47 MPa), but the elastic modulus of C was higher than A one (1.33 MPa vs 1.29 MPa). For the HB pattern the specimen J1 reached the highest tensile strength at break (2.12 MPa) and the better elastic modulus (1.73 MPa). Concerning the TM pattern, the specimen V showed clearly superior mechanical properties than the other specimens belonging to its category, being characterized by a tensile strength at break of 2.08 MPa and an elastic modulus of 2.21 MPa. The computed strain at break ranged between 163-181% for all the bioinspired chosen specimens.

Analyzing the base materials, the elastic modulus showed a growing trend as the hardness value of the materials increased (T1, U1, V1); the same happened to the tensile strength at break; instead, the strain at break had a decreasing trend. This what it was expected, since a higher Shore A refers to a harder material and, therefore, less deformable. Concerning the TissueMatrix, this resin appeared extremely soft, as shown by the value of the elastic modulus and of the tensile strength at break. However, its strain at break was not as high as expected, since it had about the same value as the specimen U1 (1.723 vs 1.725 mm/mm), but the other two parameters were definitely lower compared to U1 ones (E: 0.240 vs 1.444 MPa,  $\sigma$ : 0.331 vs 1.596 MPa); this could be due to the extreme fragility of this material. The results obtained are comparable to the study of *Severseike et al.* [73].

Since the aim of this study was to evaluate the pattern influence on the mechanical behavior of the specimens, the four best patterns (C, V, A1, J1) were compared to the base materials made of Agilus30 with different Shore A values (T1, U1, V1). The comparison was done adopting the following criterion, as shown in the workflow in fig. 67: the specimens C and A1, made of parts with SH\_A60 and SH\_A70 (Tab. 1 and 3), were compared to the specimen U1 and V1 (base material with SH\_A60 and SH\_A70), while the specimens V and J1, which have a high hardness variability, were compared to all the base materials.

A1 underwent almost the same deformation as U1, while had higher tensile strength at break (by 30%) and elastic modulus (by 20.8%) values; however, the mechanical properties of specimen A1 were lower, apart from the strain at break that was higher, compared to the base material V1 (by 8.8%, 22.7% and 21.9%, respectively). This allows us to state that the BL pattern does not influence the mechanical tensile behavior of the specimens, but the improved mechanical properties observed, compared to specimen U1, are due to the parts with SH\_A70 contained in the specimen; indeed, the specimen with the highest mechanical parameters is the one with the highest hardness values combination (70-60-70-M60).

C reached a shorter value of strain at break (by 5.2%) and had lower tensile strength at break (by 7.5%) and elastic modulus (by 7.6%), compared to U1. Comparing C to V1, instead, it had clearly lower mechanical properties, since its elastic modulus and its tensile strength at break differed by 39.6% and by 35.2% from the V1 ones; the strain at break, instead, was higher by 15.5%. Since C has the same hardness values combination as A1 (70-60-70-M60), it can be stated that the TL pattern worsens the mechanical behavior of the specimens, according to the lower values of its mechanical parameters, compared to the specimen U1.

J1 had a strain at break slightly higher than U1 (by 5.2%), but lower than T1 (by 13.4%); its tensile strength at break was lower by 7% than V1, but higher by 32.5% than U1; its elastic modulus was lower by 21.3% than V1, but higher by 20.1% than U1. Surely, adding double helixes into the concentric pattern (HB) enhances the strain at break of the specimen, since it reached the highest value of deformation (59.735 mm) among all the best bioinspired specimens, considering that the other two parameters are comparable to the A1 ones (Fig. 65). Anyway, the other mechanical parameters did not show a considerable improvement, compared to the base materials.

V showed a strain at break higher by 1.2% than U1, but lower by 16.8% than T1; its tensile strength at break was lower by 8.8% than V1, but higher by 30% than U1; its elastic modulus was comparable to V1 (by 0.4%), the hardest base material. The TM pattern improves the mechanical properties of the specimens, because of the high elastic modulus of the best specimen of the category (V), even if it is composed of a matrix (40% of CSA) with SH\_A50 and fibers (60% of CSA) of SH\_A70. Moreover, its strain at break is comparable to U1, although it is composed most of fibers with SH\_A70.

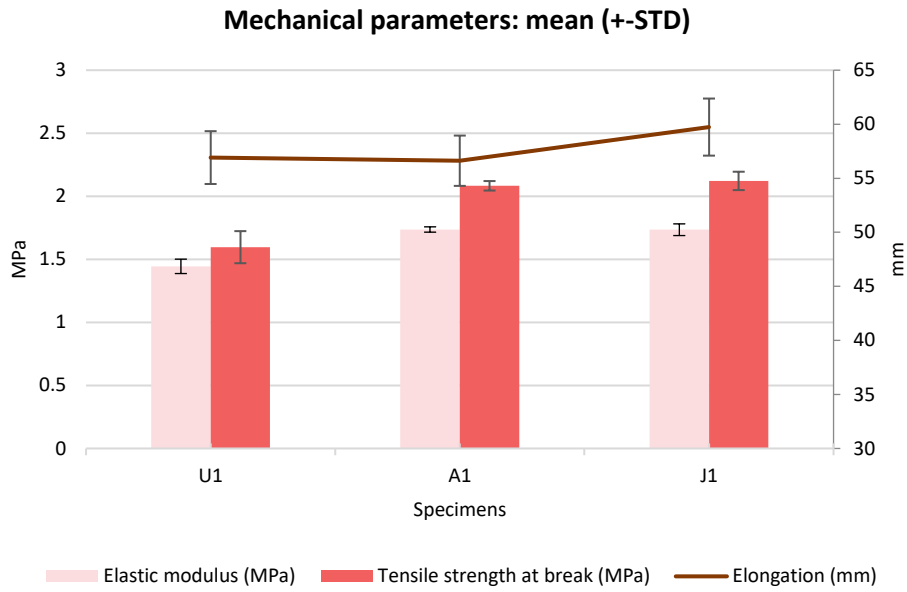


**Figure 65.** Comparison between the mechanical parameters (elastic modulus, tensile strength at break and elongation at break) of the specimens U1, A1 and J1.

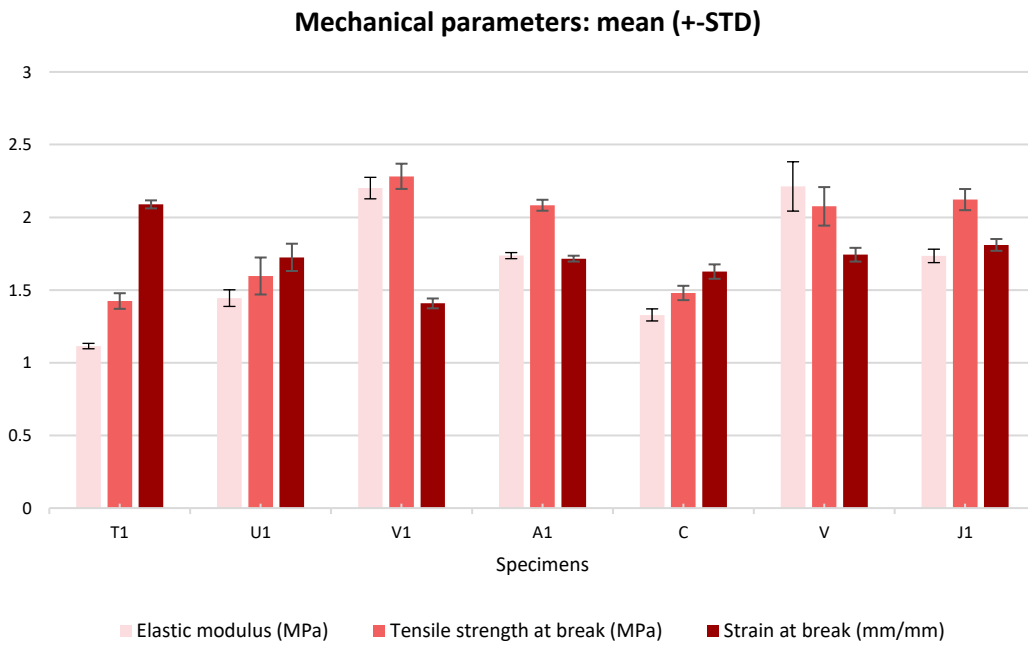


**Figure 66.** Comparison between the mechanical properties of the best specimens and the base materials.

At the end of the analysis, the configuration V was picked as the strongest one, since it has the greatest elastic modulus value, a high tensile strength at break and a good strain at break.

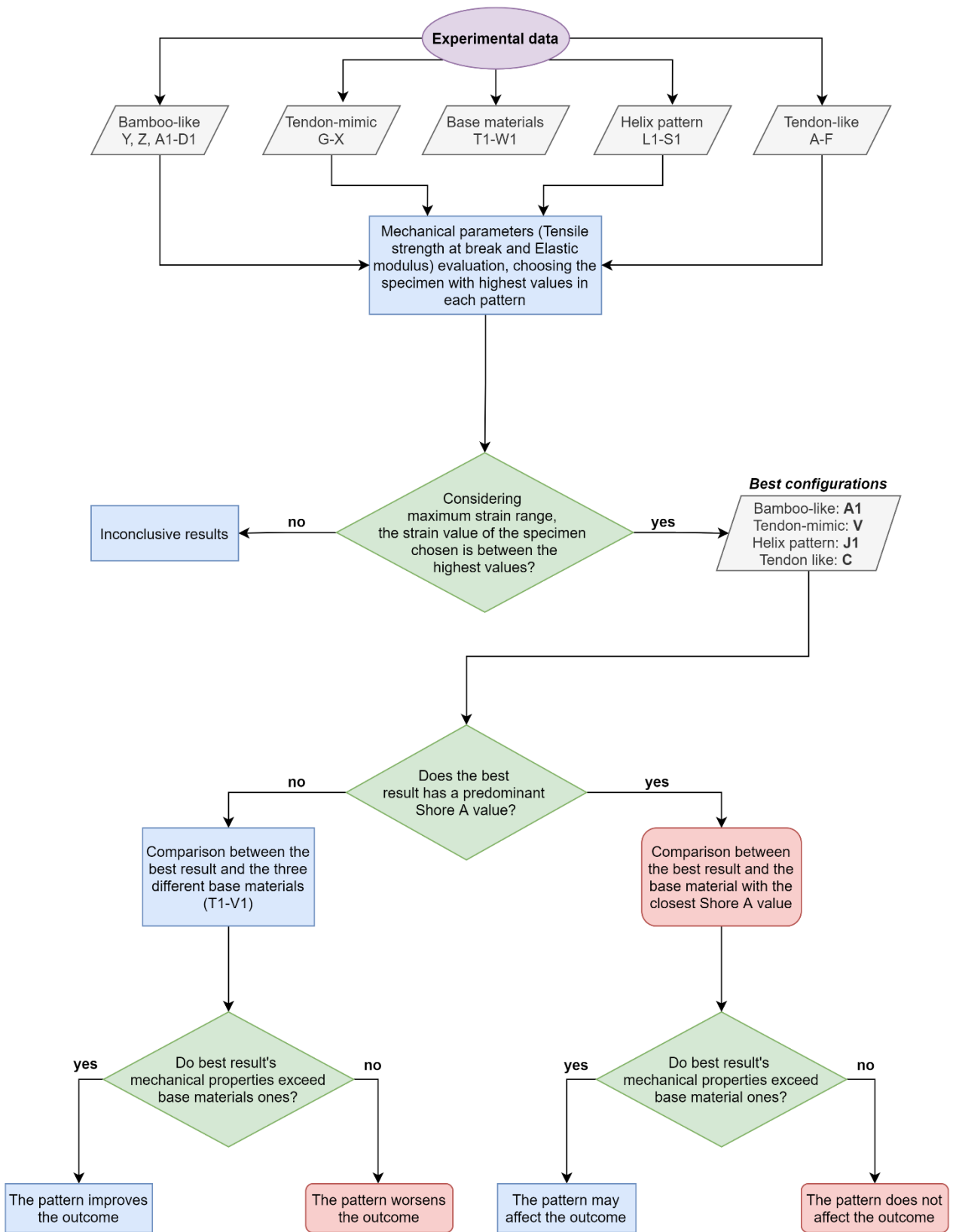


Figure 67. Flow chart of the mechanical data processing.

### 5.2.1.2 Stress-strain curve and related parameters

All the stress-strain curves of the picked specimens (Fig. 68) did not show a toe region, typical of the tendon/ligament [87], [88], whose fibers are initially wavy and, applying a tensile load, become highly stretch, showing a crimp pattern [5]. However, the linear region is common both for our specimens and for the tendon/ligament. As could be deduced looking the curves and as shown in the Table 10, the Pearson's coefficient results just under 1 for all the analyzed specimens, proving the linearity of the curves.

Moreover, the tests were found highly repeatable, having all the mechanical parameters a CV below 8% for all the best specimens (Tab. 10). In anatomical tissues, instead, the tests showed an high variability, due to the non-homogeneous fascicles organization [134]. The repeatability of the tests could be an advantage of the 3D printing for the surgeons' training and presurgical planning, comparing to the high variability related to the cadaveric tissue [48], [135].

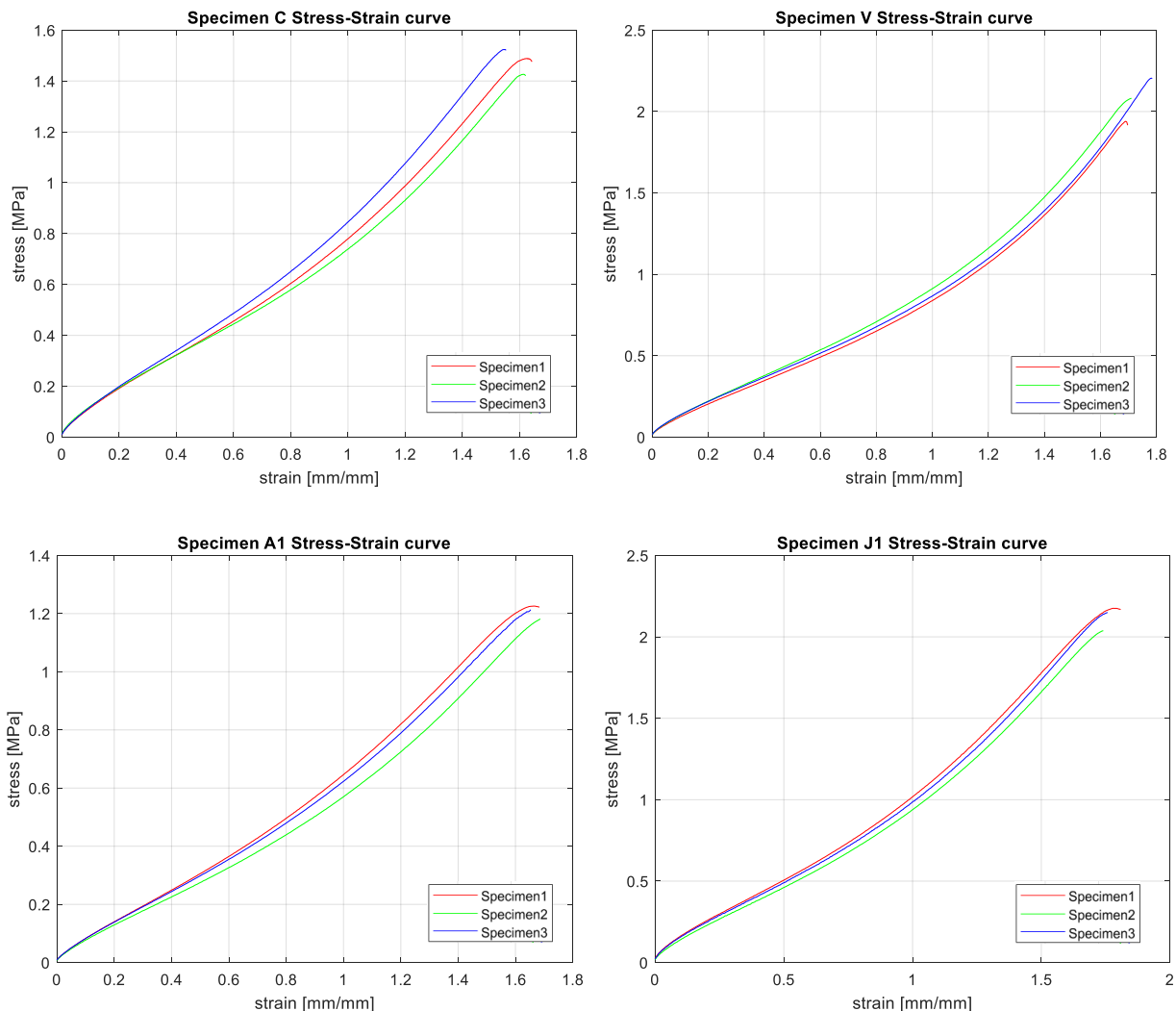


Figure 68. Stress-strain curves of the picked specimens.

**Table 10.** Pearson's coefficient and coefficient of variation (CV) for all the specimens. The yellow highlighted rows represent the best specimen of every pattern, while the green one represents the chosen specimen.

Specimens	Pearson's coefficient=R <sup>2</sup>				Coefficient of variation (CV)					
	1	2	3	mean	F (N)	L (mm)	σ (MPa)	ε (MPa)	E (MPa)	Stiff (N/mm)
A	0.9813	0.9832	0.9826	0.9824	0.1129	0.0301	0.1129	0.0301	0.1394	0.0007
B	0.9829	0.9832	0.9838	0.9833	0.1512	0.0185	0.1512	0.0185	0.1339	0.0005
C	0.9832	0.9810	0.9844	0.9829	0.0333	0.0305	0.0333	0.0305	0.0313	0.0002
D	0.9884	0.9857	0.9880	0.9874	0.0383	0.0392	0.0383	0.0392	0.0691	0.0002
E	0.9837	0.9865	0.9769	0.9824	0.0519	0.0490	0.0519	0.0490	0.0510	0.0002
F	0.9952	0.9938	0.9941	0.9944	0.0507	0.0381	0.0507	0.0381	0.0336	0.0002
G	0.9821	0.9819	0.9863	0.9834	0.0844	0.0298	0.0845	0.0531	0.0573	0.0573
H	0.9655	0.9683	0.9740	0.9693	0.0667	0.0141	0.0668	0.0404	0.0539	0.0539
I	0.9945	0.9921	0.9909	0.9925	0.0154	0.0343	0.0154	0.0644	0.0239	0.0239
J	0.9543	0.9595	0.9585	0.9574	0.0760	0.0312	0.0760	0.0303	0.0507	0.0507
K	0.9936	0.9952	0.9942	0.9943	0.0358	0.0410	0.0358	0.0263	0.0487	0.0487
L	0.9724	0.9799	0.9780	0.9768	0.0754	0.0204	0.0754	0.0519	0.0504	0.0504
M	0.9850	0.9806	0.9834	0.9830	0.0138	0.0195	0.0137	0.0345	0.0296	0.0296
N	0.9623	0.9685	0.9638	0.9649	0.0955	0.0135	0.0955	0.0219	0.0812	0.0812
O	0.9954	0.9942	0.9949	0.9948	0.0215	0.0339	0.0215	0.0251	0.0508	0.0508
P	0.9618	0.9539	0.9538	0.9565	0.0131	0.0163	0.0131	0.0204	0.0329	0.0329
Q	0.9935	0.9903	0.9907	0.9915	0.0395	0.0241	0.0388	0.0550	0.0306	0.0306
R	0.9627	0.9719	0.9677	0.9674	0.0710	0.0115	0.0710	0.0350	0.0577	0.0577
S	0.9887	0.9879	0.9856	0.9874	0.0723	0.0471	0.0723	0.0472	0.0497	0.0496
T	0.9593	0.9624	0.9701	0.9639	0.0578	0.0338	0.0578	0.0338	0.0669	0.0668
U	0.9935	0.9949	0.9949	0.9944	0.0410	0.0103	0.0411	0.0102	0.0289	0.0288
V	0.9647	0.9676	0.9584	0.9636	0.0639	0.0272	0.0638	0.0271	0.0766	0.0766
W	0.9937	0.9936	0.9932	0.9935	0.0847	0.0145	0.0847	0.0145	0.0853	0.0853
X	0.9770	0.9714	0.9712	0.9732	0.0358	0.0115	0.0358	0.0115	0.0232	0.0232
Y	0.9892	0.9857	0.9866	0.9872	0.0239	0.0452	0.0239	0.0376	0.0043	0.0144
Z	0.9870	0.9820	0.9848	0.9846	0.0234	0.0330	0.0234	0.0214	0.0502	0.0631
A1	0.9874	0.9805	0.9852	0.9844	0.0181	0.0411	0.0181	0.0117	0.0121	0.0425
B1	0.9857	0.9855	0.9871	0.9861	0.0225	0.0101	0.0225	0.0158	0.0084	0.0101
C1	0.9857	0.9821	0.9836	0.9838	0.0118	0.0128	0.0118	0.0112	0.0274	0.0185
D1	0.9978	0.9971	0.9963	0.9971	0.0338	0.0187	0.0338	0.0121	0.0282	0.0039
E1	0.9740	0.9743	0.9735	0.9739	0.0247	0.0133	0.0247	0.0116	0.0116	0.0116
F1	0.9857	0.9781	0.9807	0.9815	0.0392	0.0564	0.0392	0.0379	0.0060	0.0060
G1	0.9861	0.9823	0.9807	0.9830	0.0566	0.0841	0.0566	0.0535	0.0014	0.0014
H1	0.9822	0.9827	0.9818	0.9822	0.0293	0.0214	0.0293	0.0198	0.0123	0.0123
J1	0.9814	0.9777	0.9776	0.9789	0.0343	0.0442	0.0343	0.0225	0.0267	0.0267
K1	0.9801	0.9803	0.9813	0.9806	0.0322	0.0109	0.0322	0.0147	0.0309	0.0309
L1	0.9797	0.9813	0.9797	0.9802	0.0172	0.0127	0.0172	0.0053	0.0217	0.0217
M1	0.9713	0.9733	0.9717	0.9721	0.0136	0.0143	0.0136	0.0151	0.0226	0.0226
N1	0.9733	0.9712	0.9728	0.9724	0.0103	0.0156	0.0103	0.0119	0.0189	0.0189
O1	0.9700	0.9706	0.9694	0.9700	0.0097	0.0256	0.0097	0.0198	0.0273	0.0273
P1	0.9939	0.9938	0.9943	0.9940	0.0603	0.0567	0.0604	0.0567	0.0461	0.0461
Q1	0.9943	0.9947	0.9956	0.9949	0.0511	0.0475	0.0511	0.0475	0.0156	0.0156
R1	0.9921	0.9930	0.9953	0.9935	0.0923	0.0461	0.0923	0.0461	0.0758	0.0758
S1	0.9943	0.9934	0.9921	0.9933	0.0530	0.0398	0.0530	0.0398	0.0362	0.0362

### 5.2.2 Processing of the DIC data

During the test all the images of the calibration process and of the specimens' deformation were collected in specific folders to be processed using the software Vic-3D 9 [121].

For every specimen, the calibration and the speckle images were imported in the software; the system was calibrated using the calibration images and a polygon was printed on the picture representing the undeformed specimen (Fig. 69), following its boundaries, with the Aoi tools. Finally, the start point was placed at the bottom of the specimen's surface (as shown in fig. 69) in most of the cases and sometimes at the top, regions characterized by almost zero displacement during the tensile. The subset was initially set at 9 and the step at 1 for all the specimens, then, if the points captured were too few or the projection error appeared in red, these values were increased until the results were satisfactory.

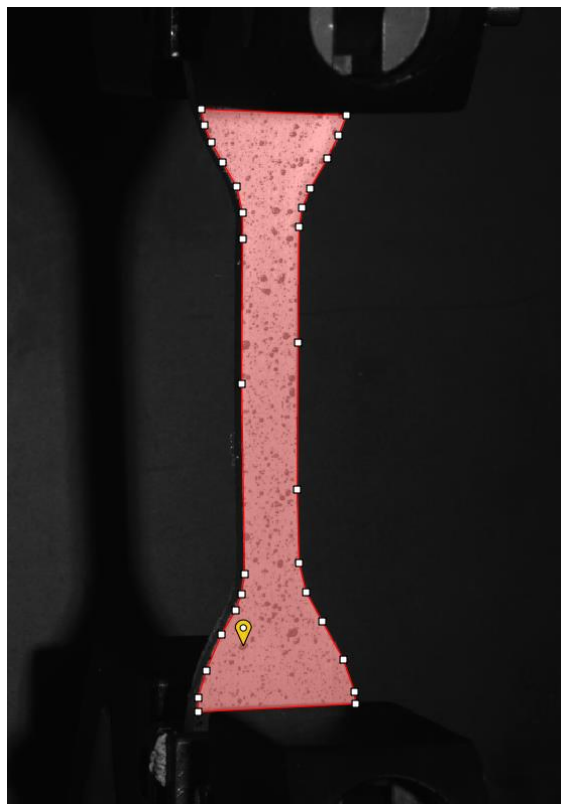


*Figure 69. Area of interest printed on the specimen's surface and start point placed at the bottom of it.*

The displacements were computed by starting the analysis and the deformations were calculated at a later time. Several images showing the deformation process until the break were obtained; the map of colors was set at "Rainbow" and the levels at 20, adding the isolines to better identify the level shifts.

Comparing the images acquired by DIC system, specifically the one representing the specimen at the beginning and the one representing it just before the failure, it appeared that the distal parts, considered non-deformable during the mechanical analysis, underwent a high strain too. During post-processing, two virtual extensometers were placed along the y-axis of the specimen to calculate the local longitudinal strain: E0 was placed along the central constant length ( $l_0=33$  mm);

E1 was placed along one of the distal parts. Another extensometer (E2) was placed perpendicularly to the previous ones to compute the local transversal strain (Fig. 70-73). E0 and E2 were used to calculate the Poisson's ratio, while E1 and E0 to compare the strain values of the different sections.

For every specimen, three series of images were acquired and the parameters  $\epsilon_{xx}$ ,  $\epsilon_{yy}$  and Von Mises strain were analyzed; the following images represent the values distribution of the three selected parameters just before the break, for the four picked specimens (C, V, A1, J1).

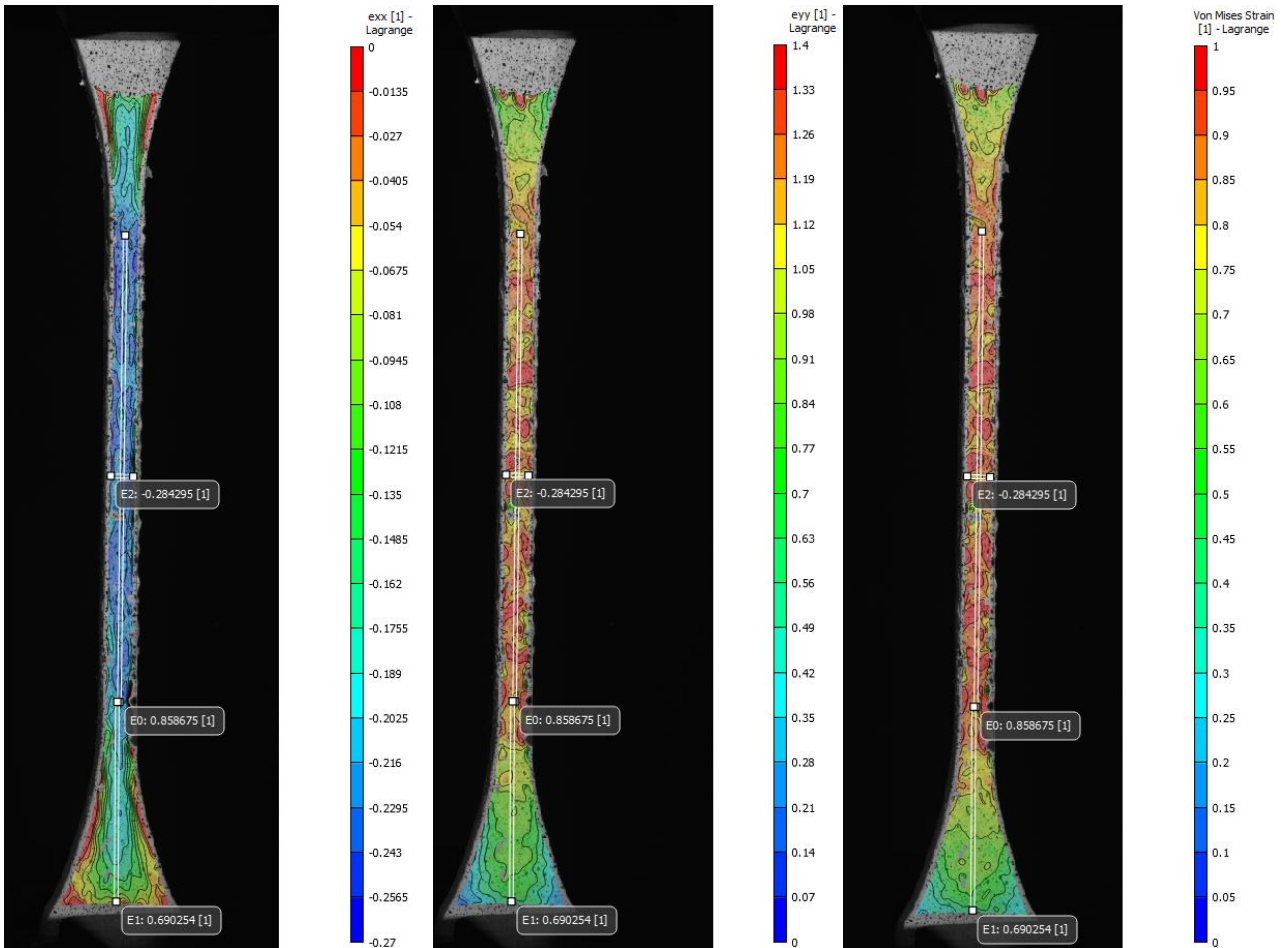


**Figure 70.** Deformation parameters ( $\epsilon_{xx}$ ,  $\epsilon_{yy}$ , Von Mises strain) of the specimen C. Please notice the position and orientation of E0, E1, and E2 (superimposed to the strain field in the images).

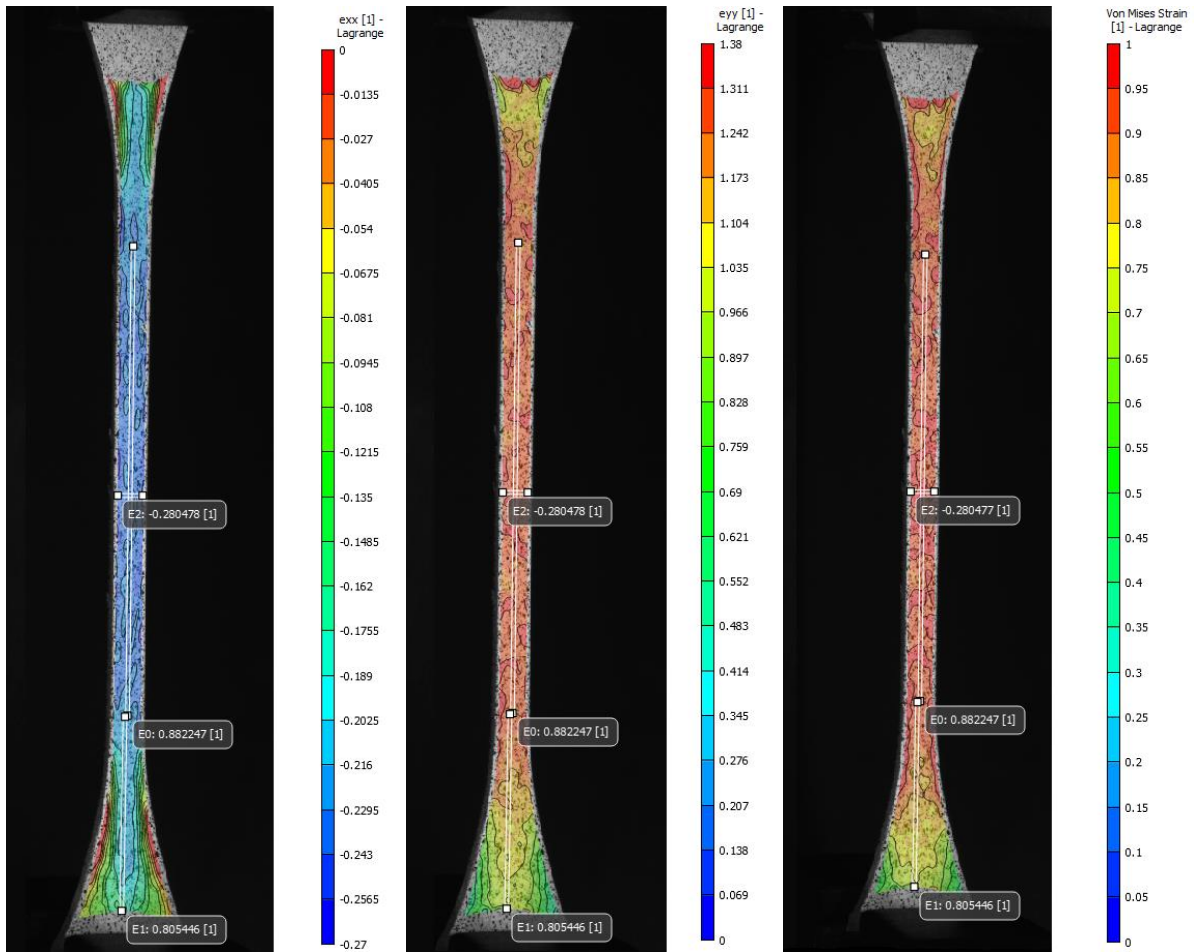


Figure 71. Deformation parameters ( $exx$ ,  $eyy$ , Von Mises strain) of the specimen V.

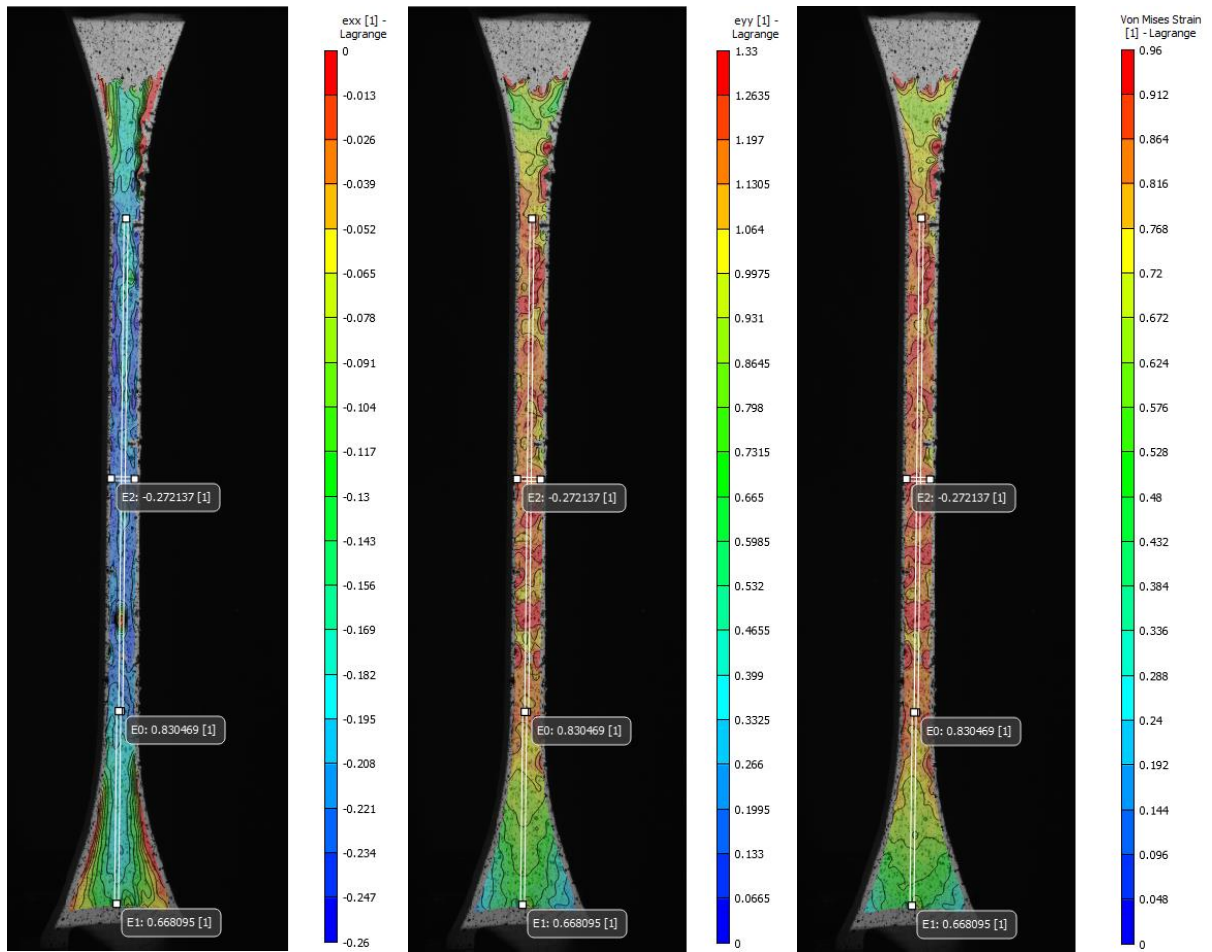
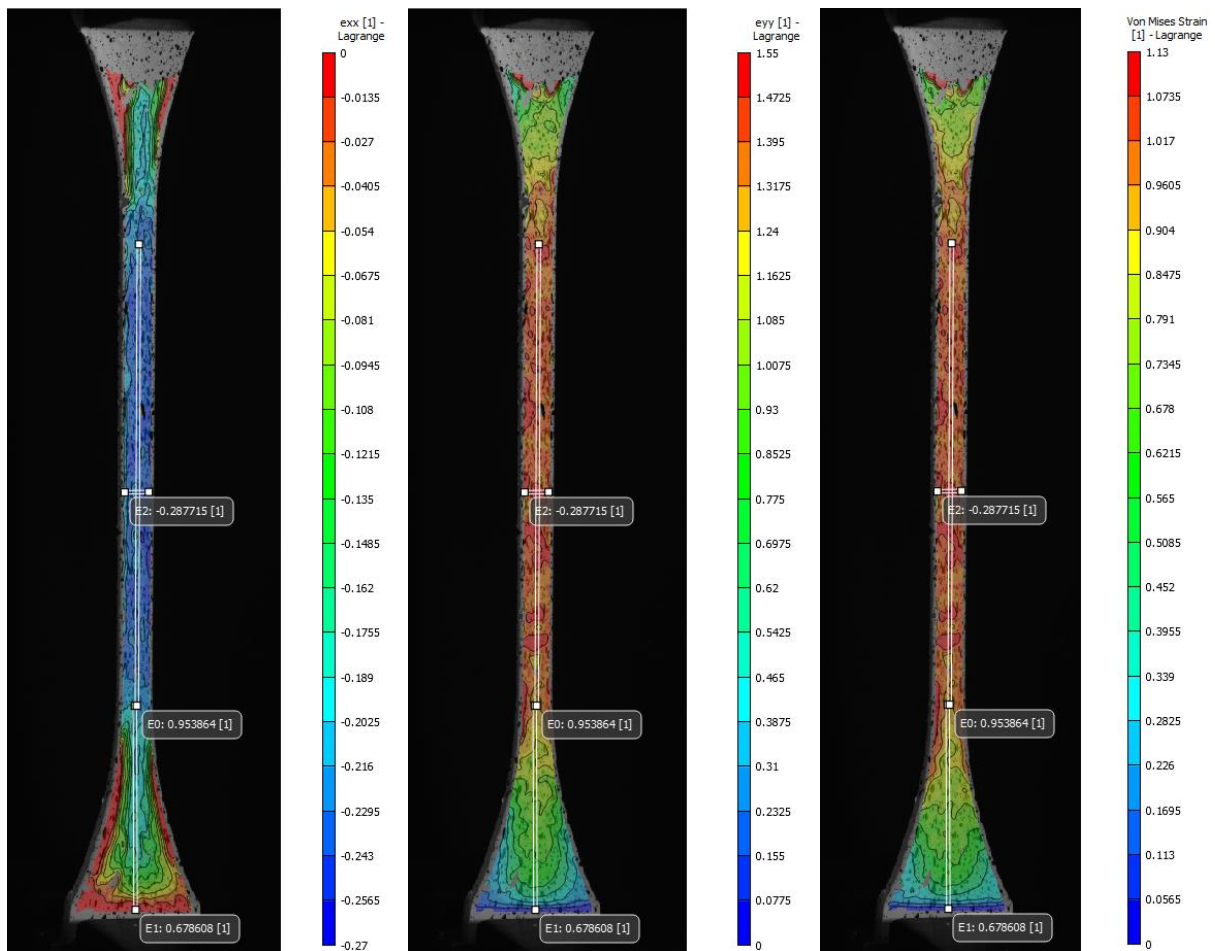


Figure 72. Deformation parameters ( $exx$ ,  $eyy$ , Von Mises strain) of the specimen A1.



**Figure 73.** Deformation parameters (*exx*, *eyy*, Von Mises strain) of the specimen J1.

As proved by these images and by the extensometers E1, the value of the deformation on the distal parts was not zero, showing them colors which ranged from cyan to orange for *eyy* and Von Mises strain. However, they underwent a lower deformation than the constant region because the peak of strain was always in the middle of the specimen.

The parameters of the deformation and of the three extensometers were exported as \*.csv files and processed using a Matlab code. The Poisson's ratio (Tab. 11) was computed by dividing the maximum values of strain detected by the extensometers E2 and E0, respectively. The specimens U and W could not be processed, since their inner pattern was visible on the surface (probably too little paint) making it inhomogeneous (Fig. 74 and 75) and this misleads the DIC cameras; therefore, their Poisson's ratio could not be computed.

**Table 11.** Poisson's ratio for all the specimens. At the bottom, in yellow the best specimen of every pattern and in green the chosen specimen.

<b>A</b>	<b>B</b>	<b>D</b>	<b>E</b>	<b>F</b>	<b>G</b>	<b>H</b>	<b>I</b>	<b>J</b>	<b>K</b>	<b>L</b>
0.3300	0.3021	0.3077	0.2805	0.3405	0.3147	0.3007	0.3490	0.3019	0.3419	0.3204
<b>M</b>	<b>N</b>	<b>O</b>	<b>P</b>	<b>Q</b>	<b>R</b>	<b>S</b>	<b>T</b>	<b>U</b>	<b>W</b>	<b>X</b>
0.3145	0.3003	0.3396	0.3067	0.3399	0.3341	0.3200	0.3021	-	-	0.3274
<b>Y</b>	<b>Z</b>	<b>B1</b>	<b>C1</b>	<b>D1</b>	<b>E1</b>	<b>F1</b>	<b>G1</b>	<b>H1</b>	<b>K1</b>	<b>L1</b>
0.2973	0.2948	0.2988	0.2790	0.3339	0.2869	0.2751	0.2778	0.2913	0.2931	0.2856
<b>M1</b>	<b>N1</b>	<b>O1</b>	<b>P1</b>	<b>Q1</b>	<b>R1</b>	<b>S1</b>	<b>T1</b>	<b>U1</b>	<b>V1</b>	<b>W1</b>
0.3023	0.2928	0.2884	0.3522	0.3499	0.3493	0.3566	0.2751	0.3006	0.3326	0.2958
				<b>C</b>	<b>V</b>	<b>J1</b>	<b>A1</b>			
				0.3128	0.3187	0.3060	0.3006			

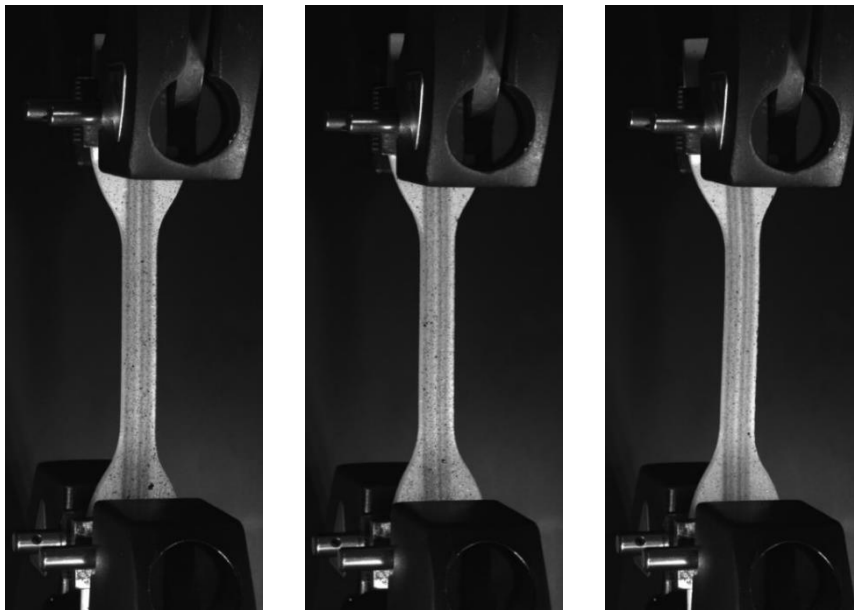


**Figure 74.** First image (before starting the tensile test) of the three samples of specimen U, as acquired by the DIC system.

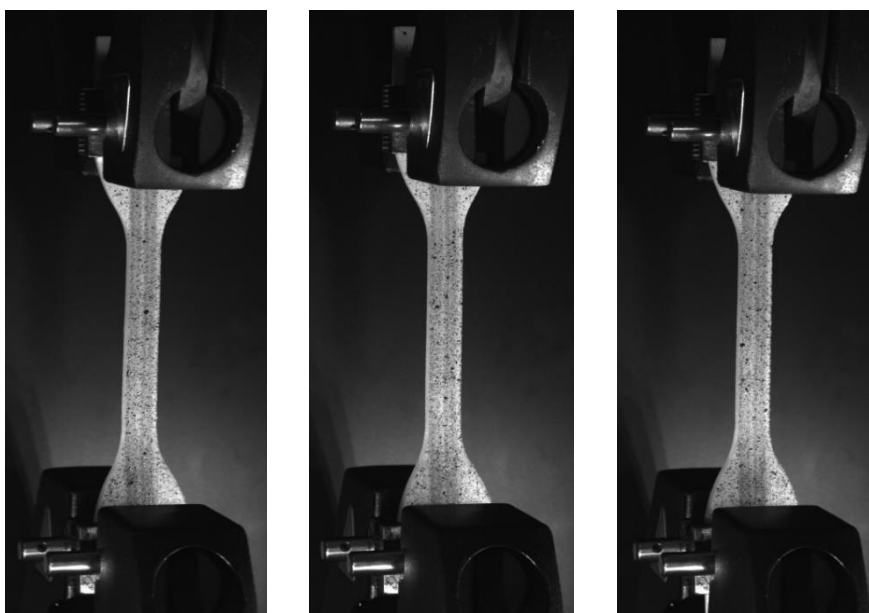


**Figure 75.** First image (before starting the tensile test) of the three samples of specimen W, as acquired by the DIC system.

### 5.2.3 Direct measurements vs DIC system

Looking at the following bar charts, we could make a comparison between values of deformation measured with different methods. The first two bars represent the strain measured by the testing machine, while the latter ones represent the strain computed with the DIC system (Fig. 76). It can be noted that, following the ASTM D638-14 [77], the strain is overestimated (first bar), since this method omits the distal parts' deformation, considering them unchanging. Otherwise, dividing by the entire length of the specimen ( $l_0=65$  mm), you get an average between the strain of the constant section and of the distal parts (Fig. 76, second bar). According to the different hardness values of the specimens, the deformation of the distal parts may or not be comparable to that of the constant region: for the specimen V, picked as the best one, these values are not that different, as shown in Fig. 76, therefore the averaged strain and the DIC strain look the same. The DIC strain represents the output of the extensometer E0, placed on the constant section of the specimen. Von Mises strain takes into account all the directions of deformation and appears comparable to the averaged strain computed for  $l_0=65$  mm.  $\epsilon_{yy}$  is, instead, an averaged value of the deformation along the y-axis (longitudinal) of the entire Aoi selected, considering the displacement of every point of the region. Surely, the measurements made using the extensometers are more accurate than this parameter, that overestimates the value of deformation.

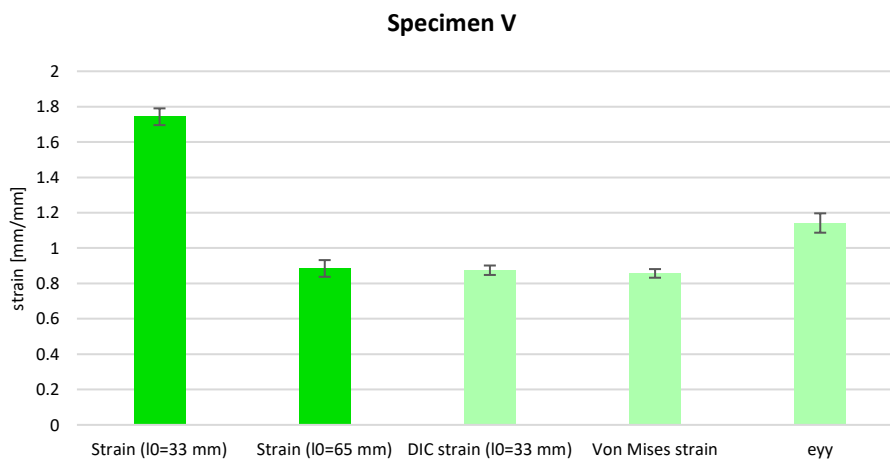
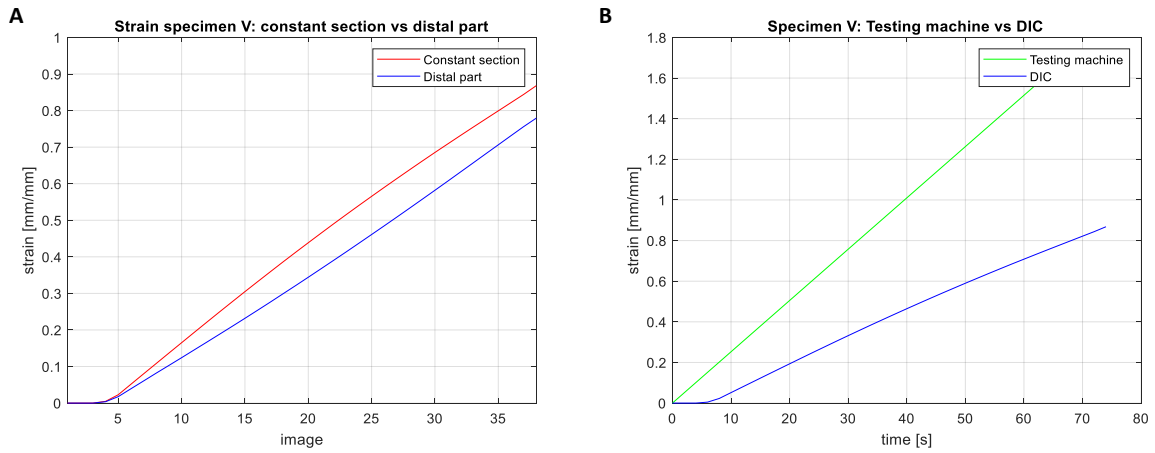


Figure 76. Comparison between strains measured with different methods.

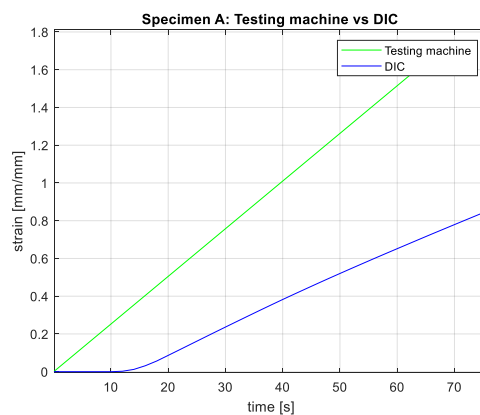
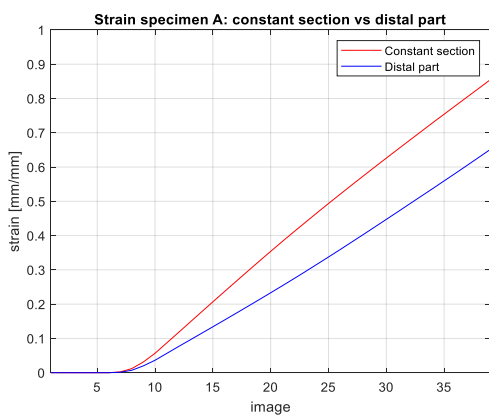
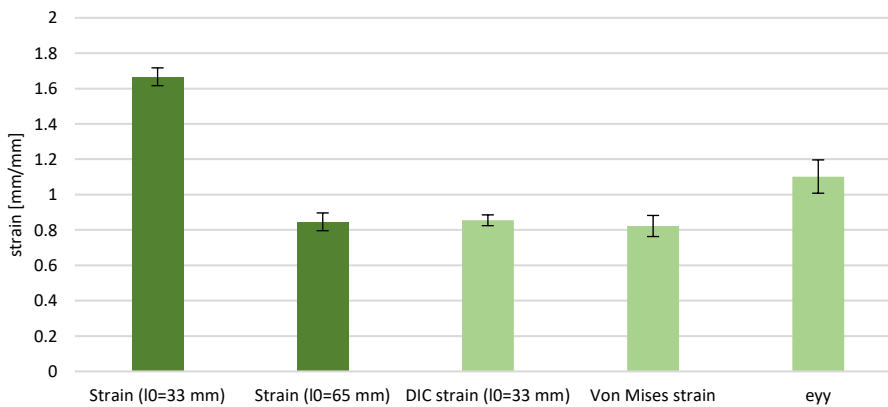
Therefore, the charts given by the Matlab code suggest that both the constant section and the distal parts underwent a not negligible deformation, even if the strain of the first is higher than the other one (Fig. 77A). The strain obtained according to ASTM D638-14 should be comparable to the value given by the extensometer E0 (DIC strain), which refers to the strain of the constant region, since this part is supposed to be the one which changes shape; however, the Fig. 77B proves this is wrong, because the two values are very different from each other.



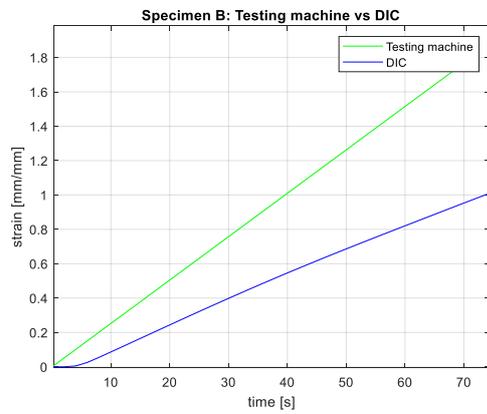
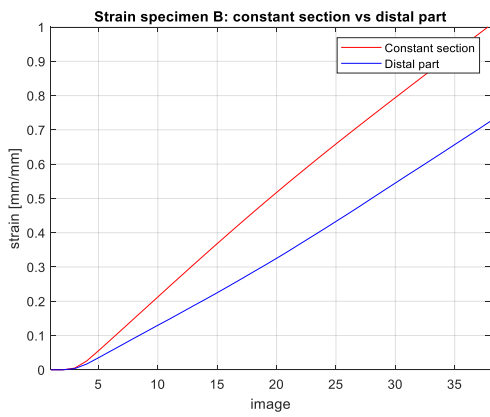
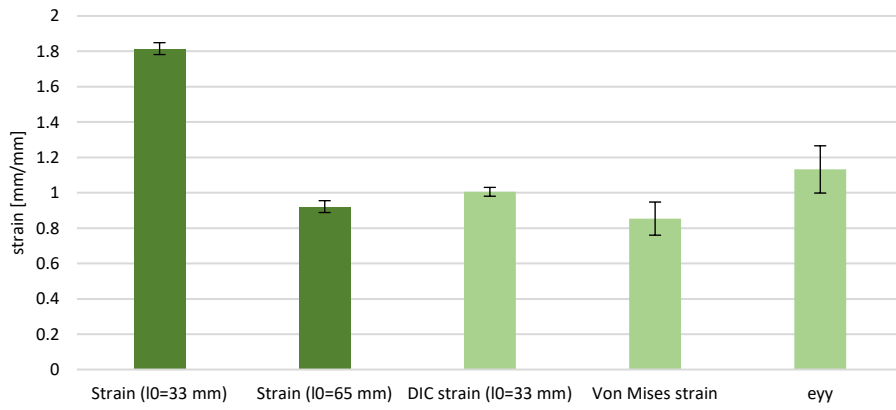
**Figure 77.** A) Strains of the different parts of the specimen, measured with DIC system; B) Strains of the constant region of the specimen measured with the testing machine and the DIC system.

The following figures represent the bar chart and the graphs relative to the specimens characterized by the TL pattern.

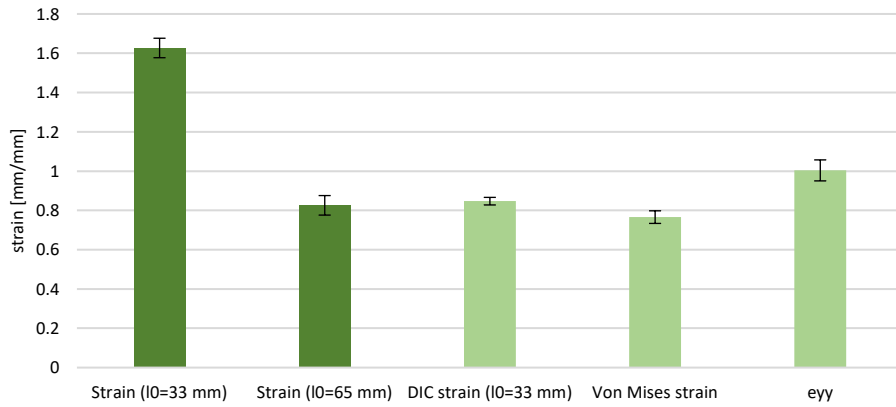
**Specimen A**

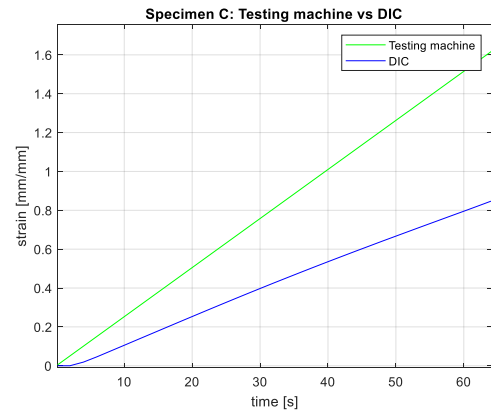
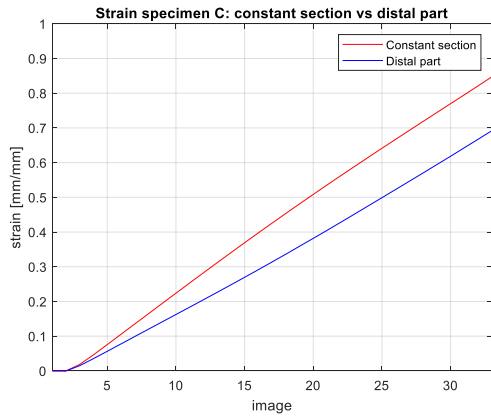


### Specimen B

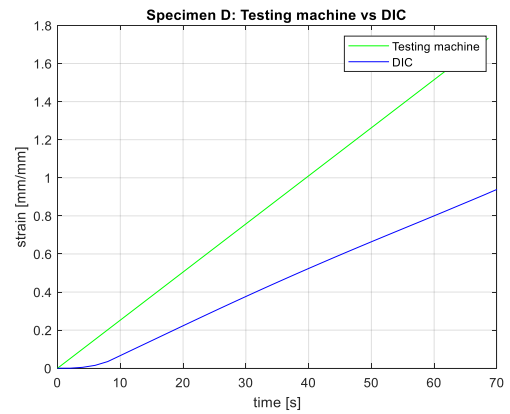
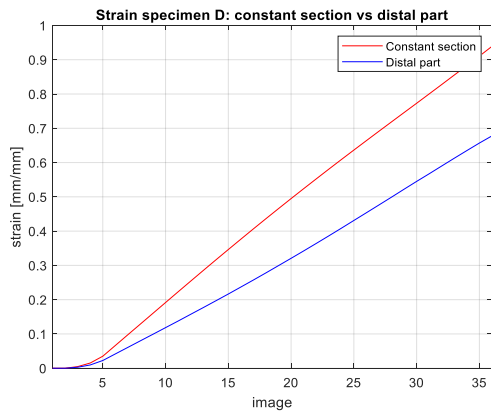
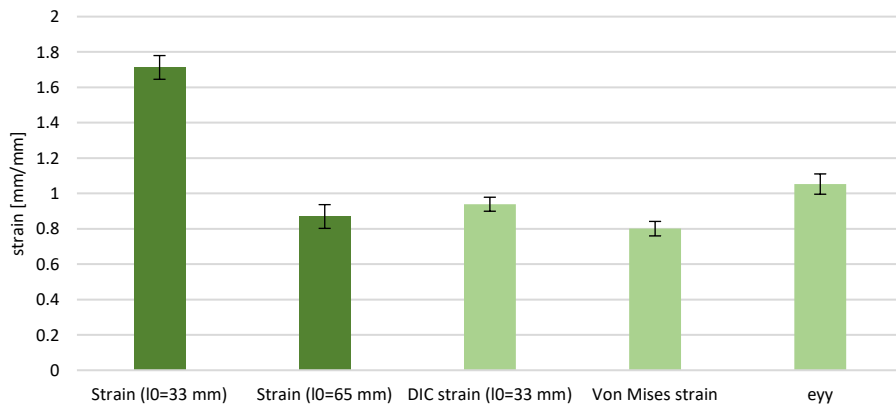


### Specimen C

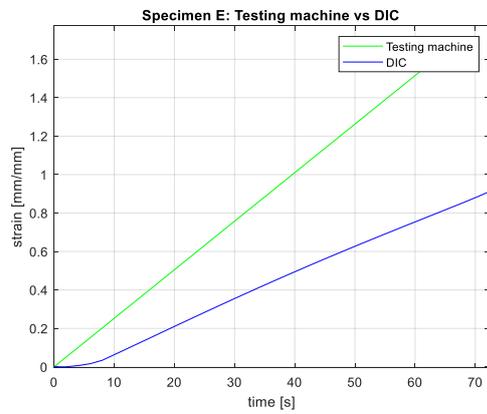
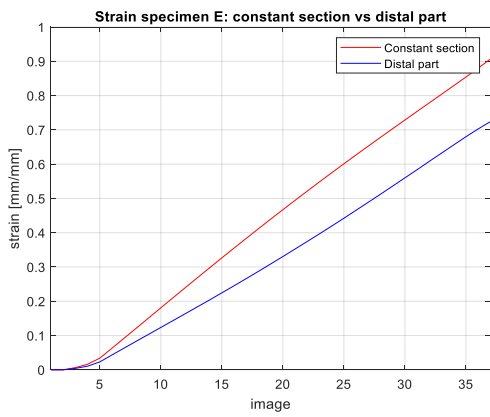
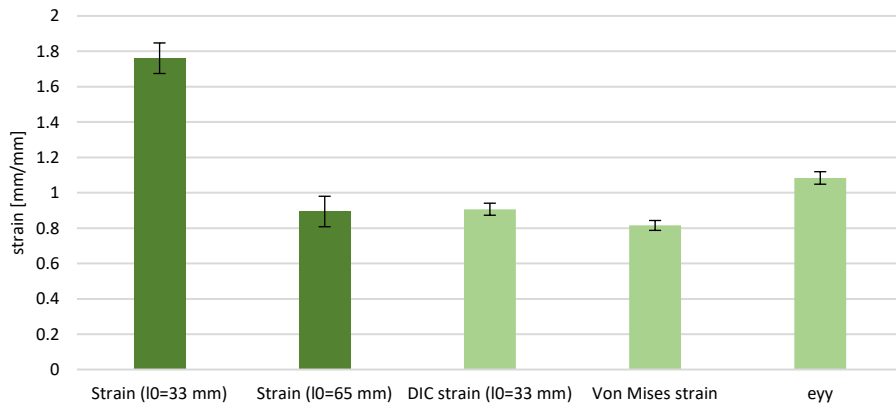




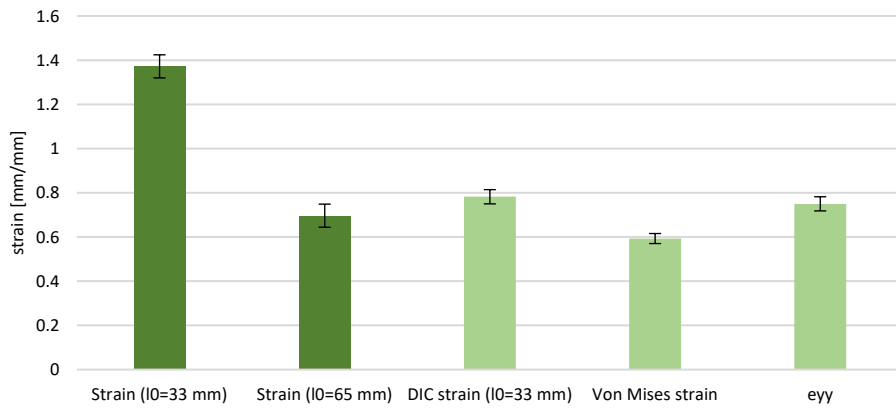
**Specimen D**

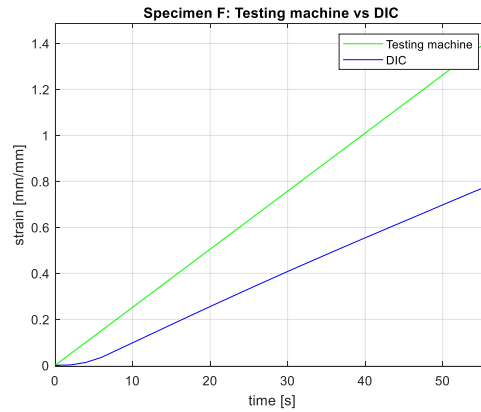
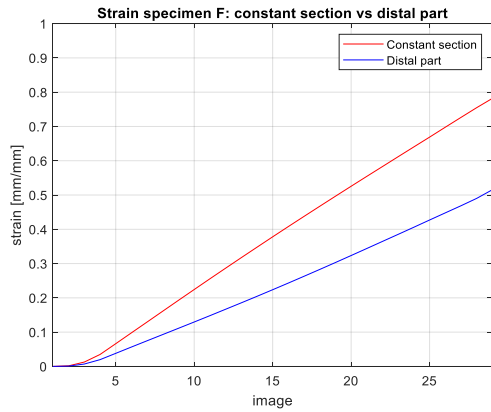


### Specimen E



### Specimen F

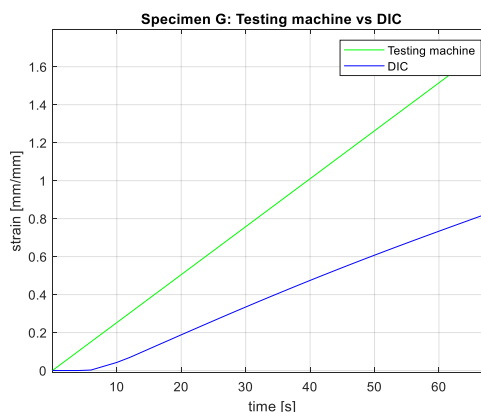
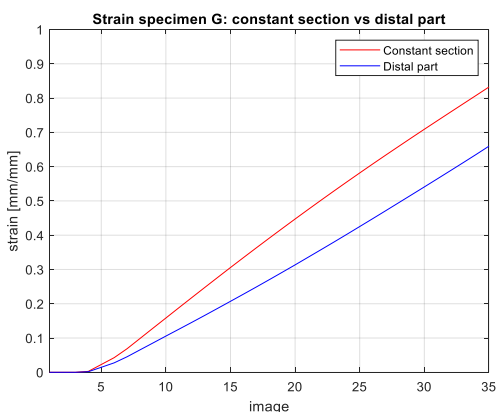
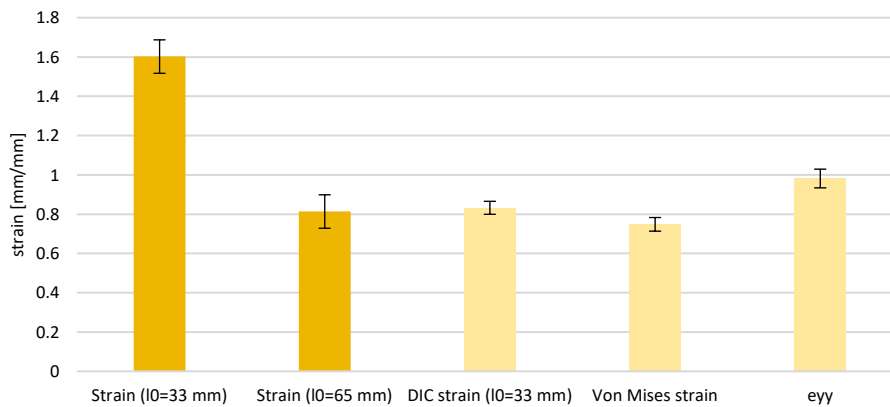




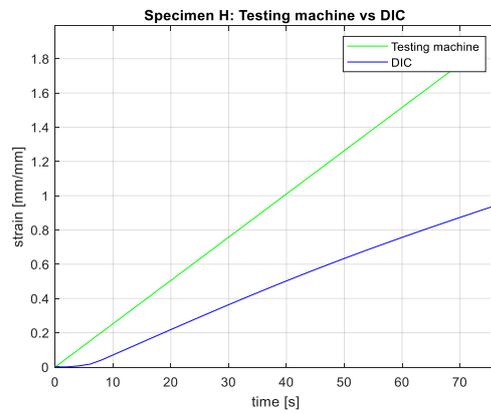
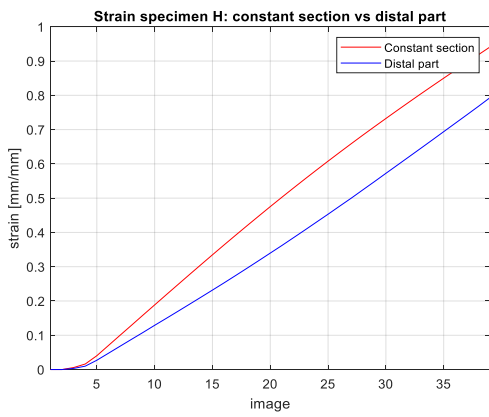
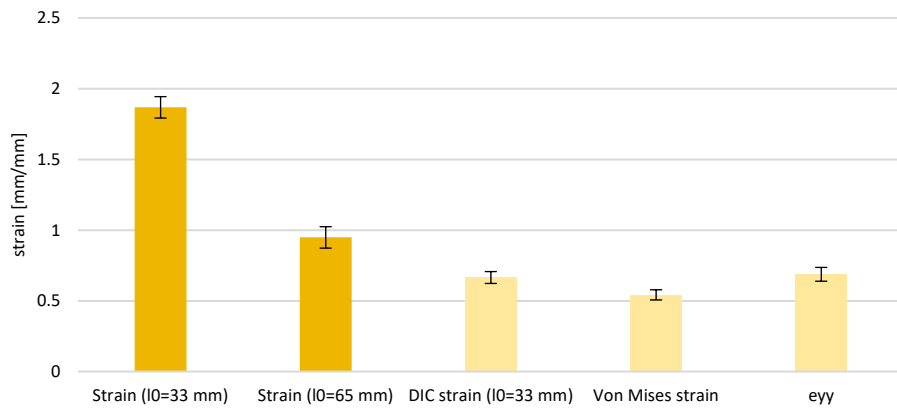
It could be noted that the constant section of the specimens B, D and F is much more deformable than the distal parts (1.005 vs 0.725, 0.939 vs 0.678 and 0.782 vs 0.515), compared to the other specimens with the same pattern. Since the pattern was placed only in the CSA, the distal parts are characterized by a larger amount of matrix than the constant region and these three specimens are characterized by softer fibers in harder matrix. This pattern does not influence the mechanical behavior of the specimens; therefore, this feature could be due to the higher density of hard materials in the distal parts, which causes a lower deformation.

The following figures represent the bar chart and the graphs relative to the specimens characterized by the TM pattern.

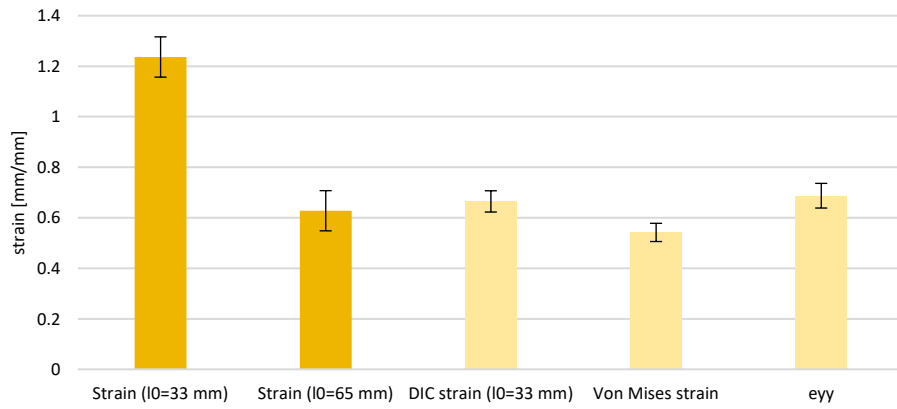
### Specimen G

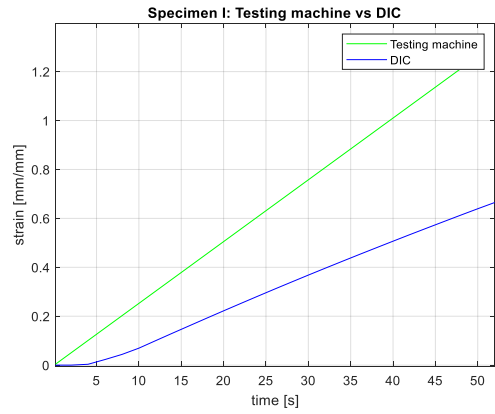
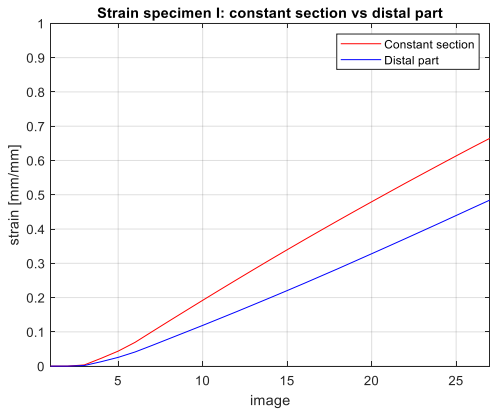


### Specimen H

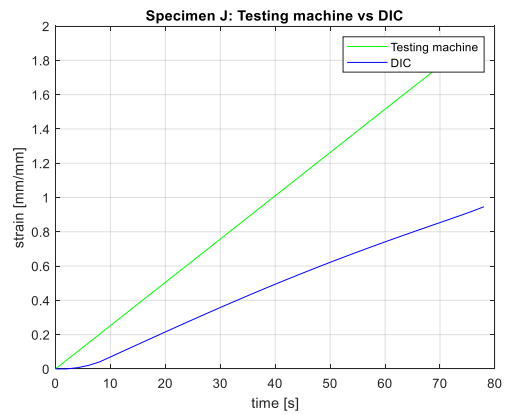
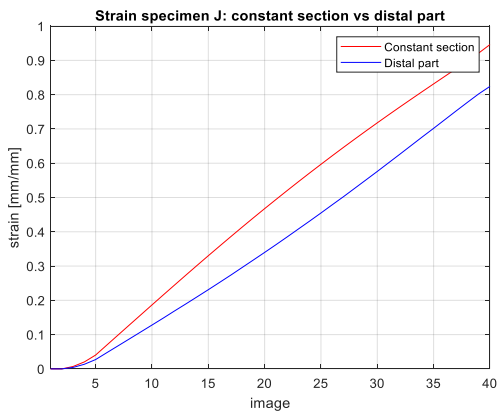
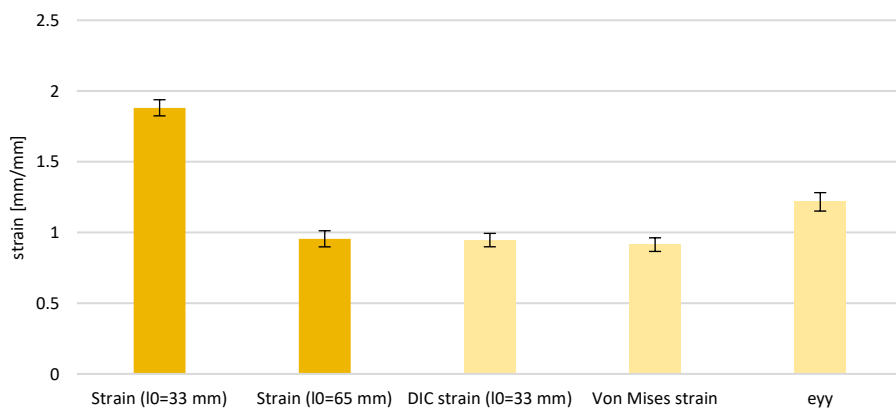


### Specimen I

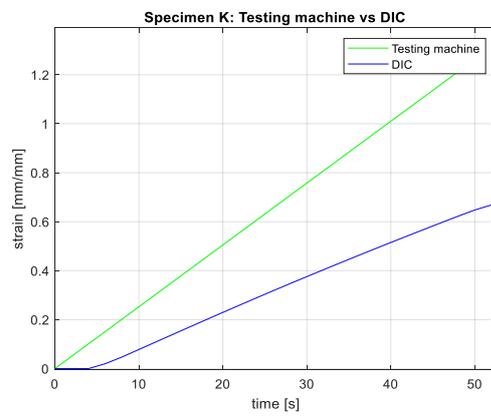
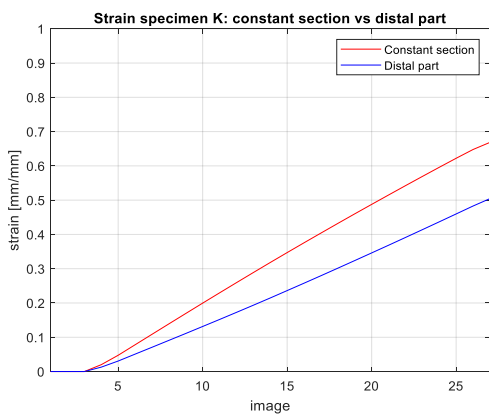
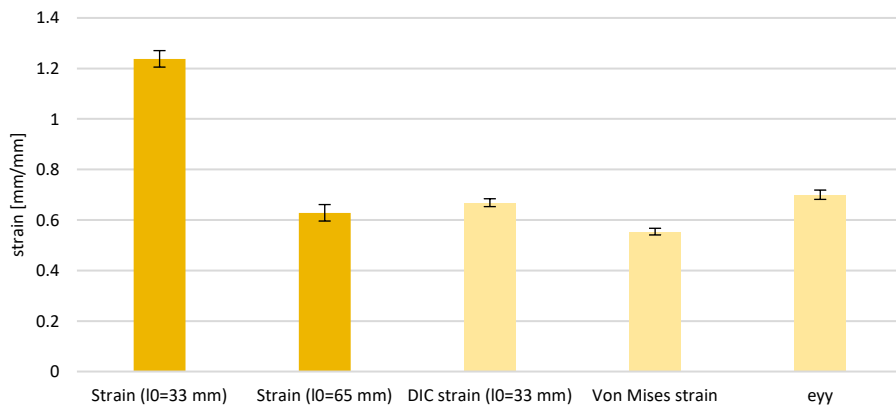




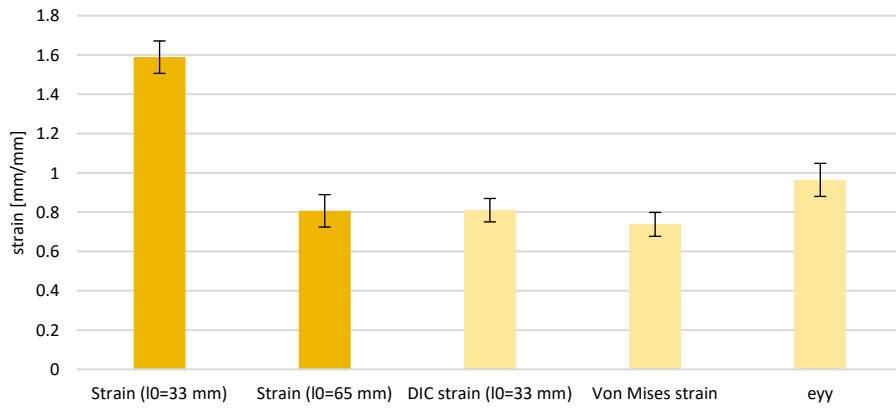
## Specimen J

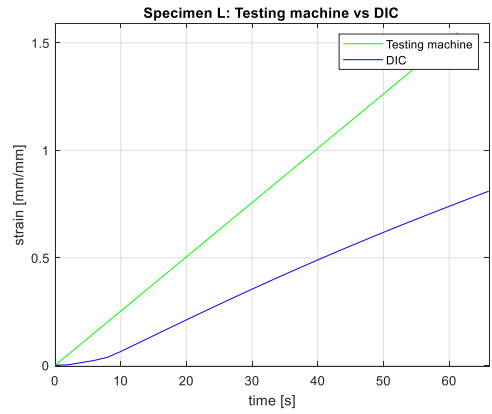
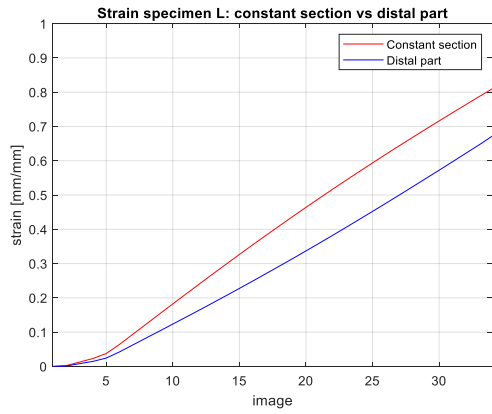


### Specimen K

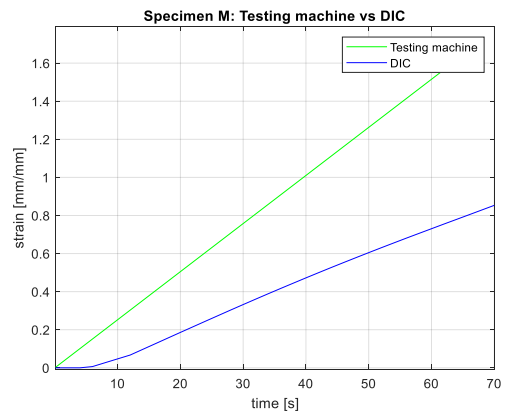
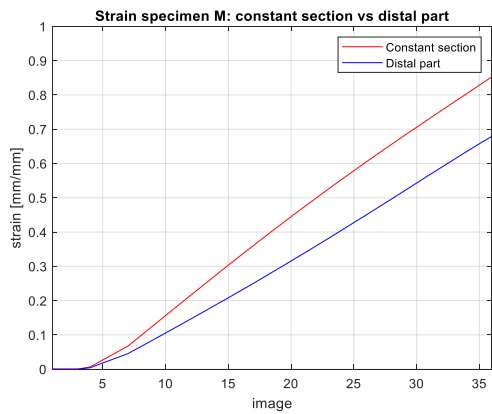
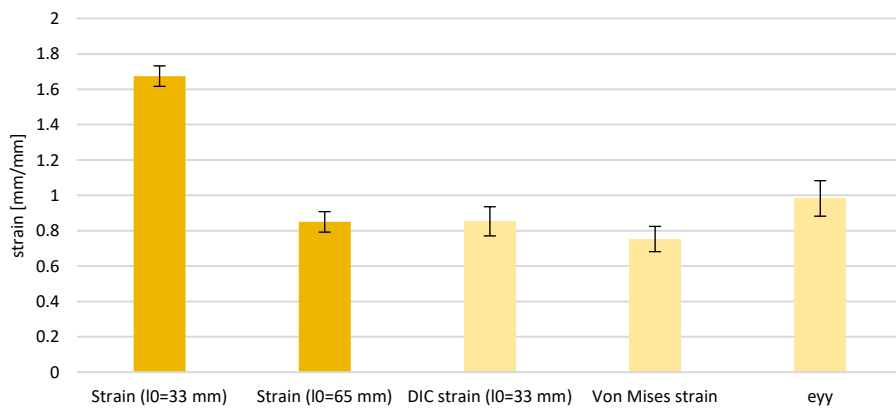


### Specimen L

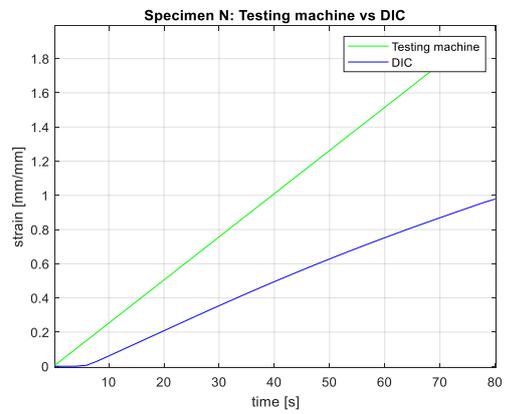
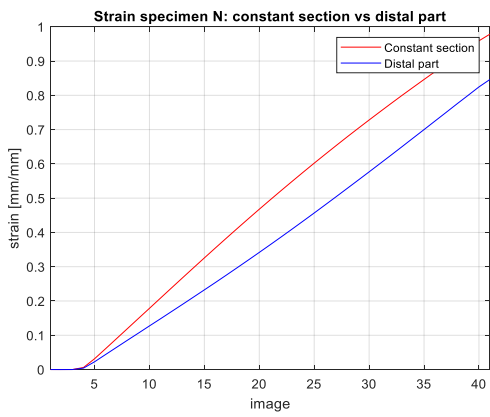
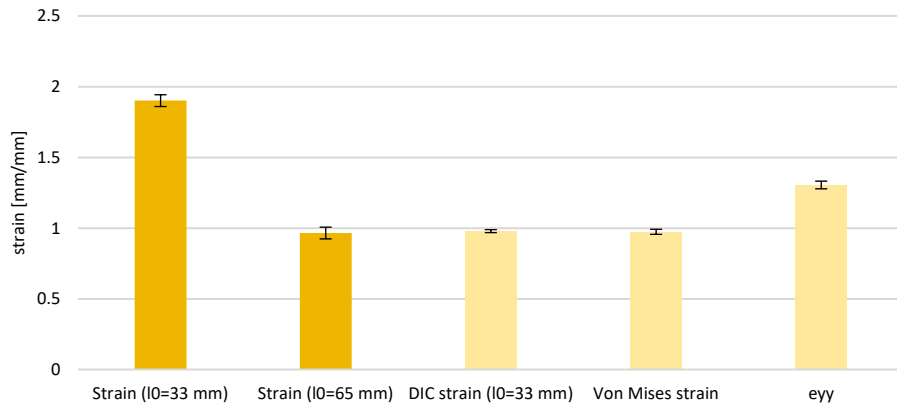




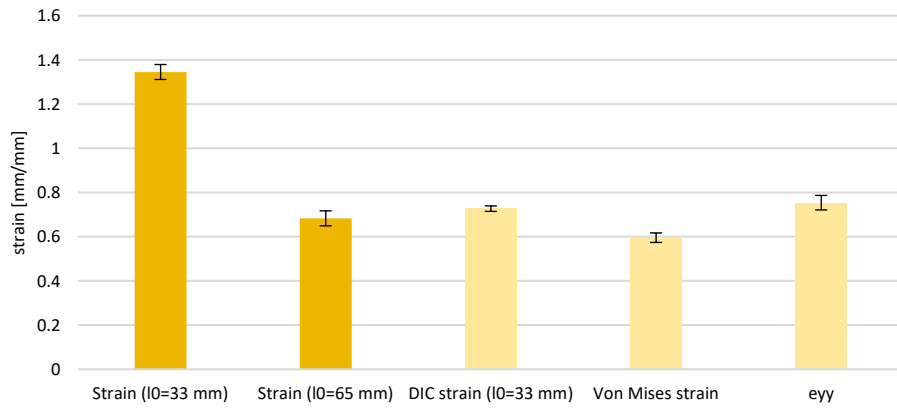
**Specimen M**

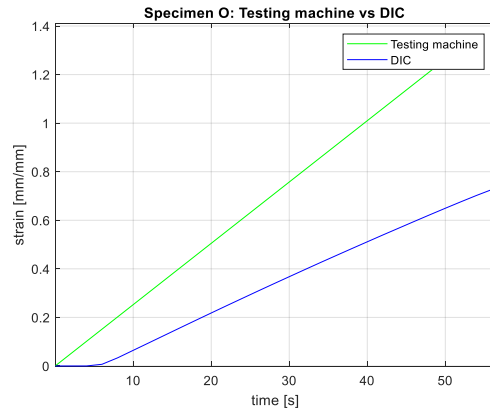
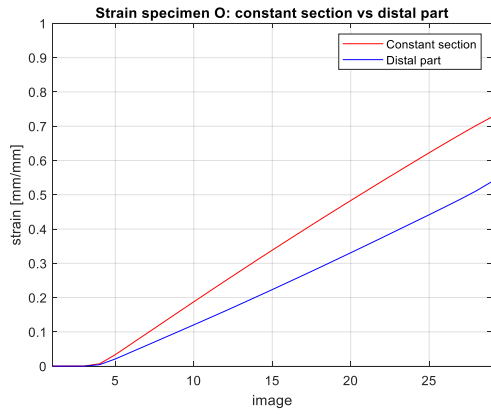


### Specimen N

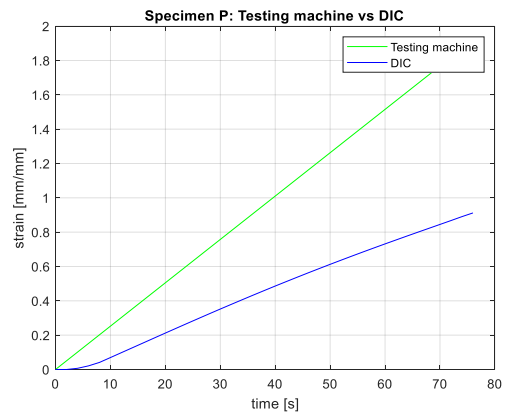
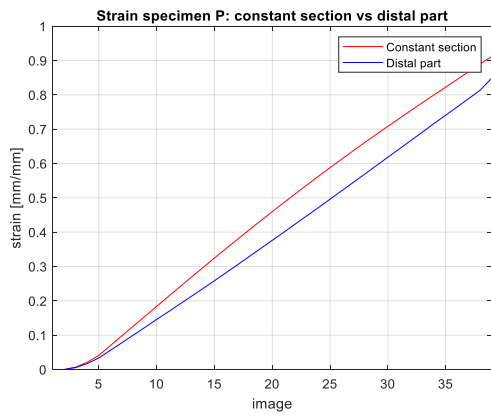
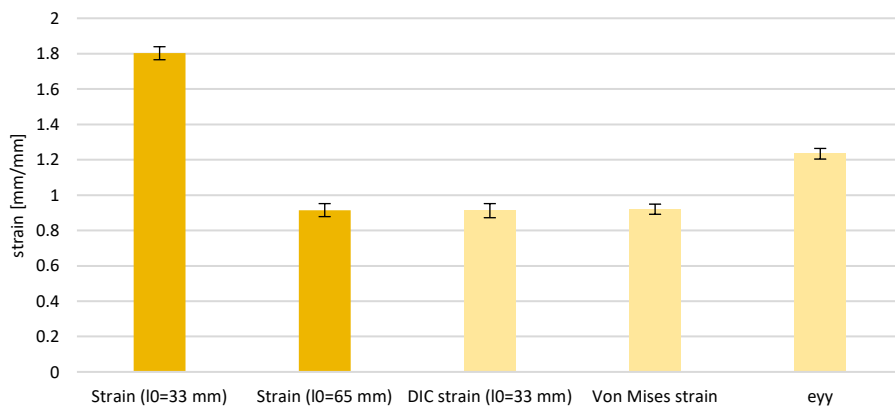


### Specimen O

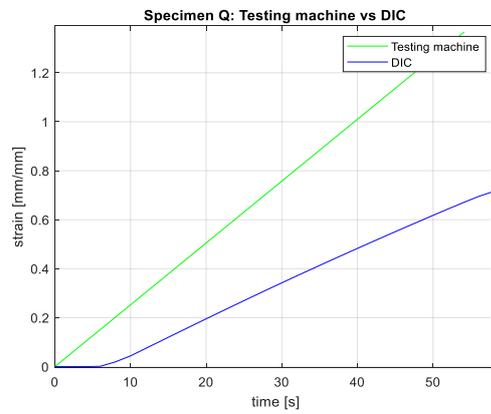
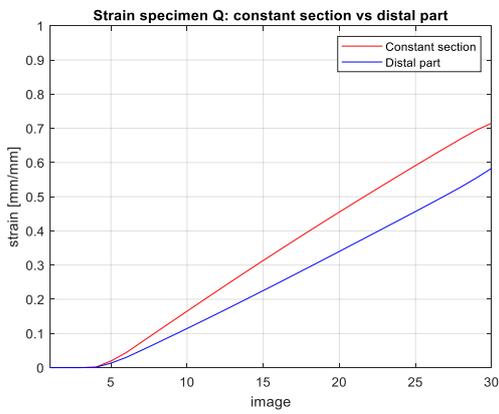
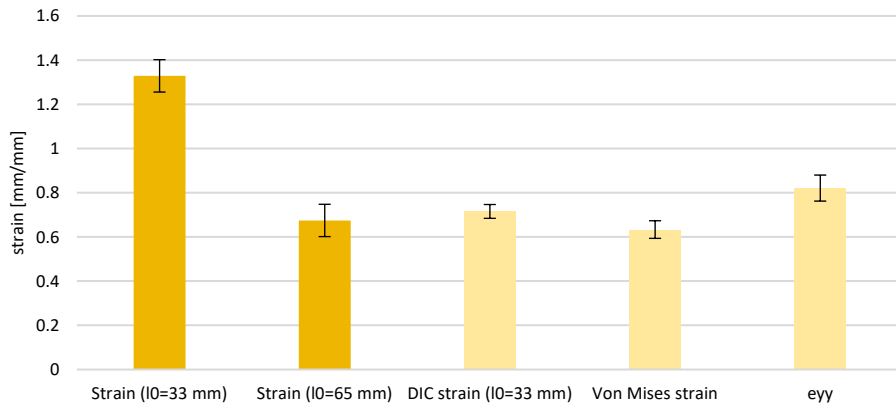




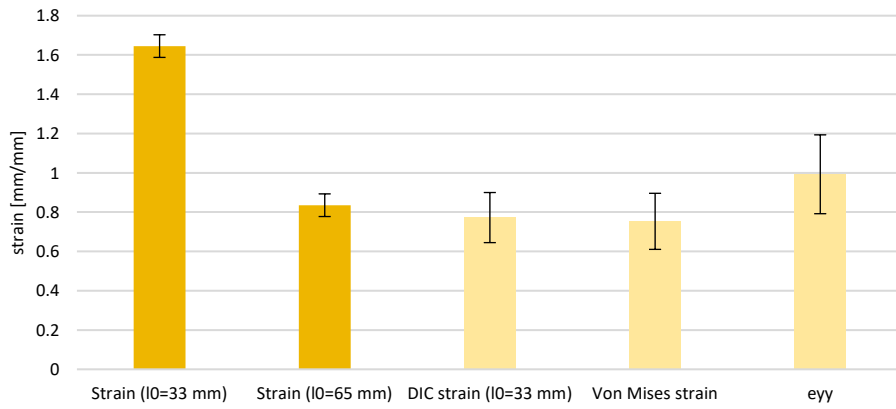
**Specimen P**

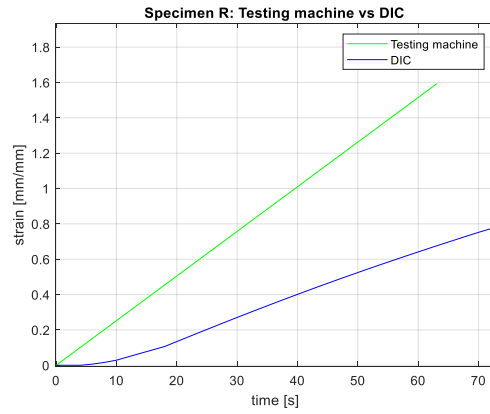
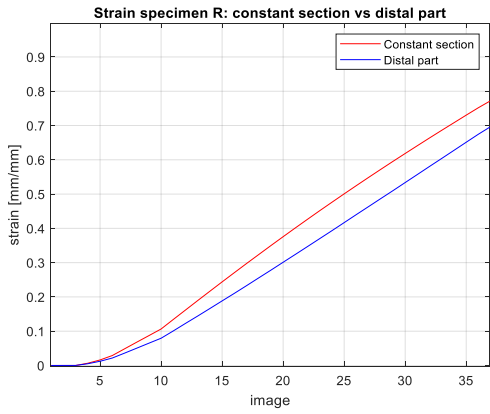


### Specimen Q

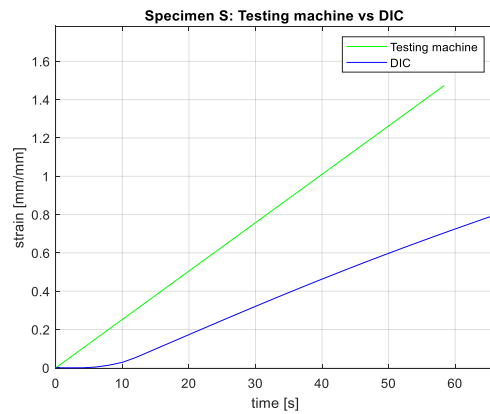
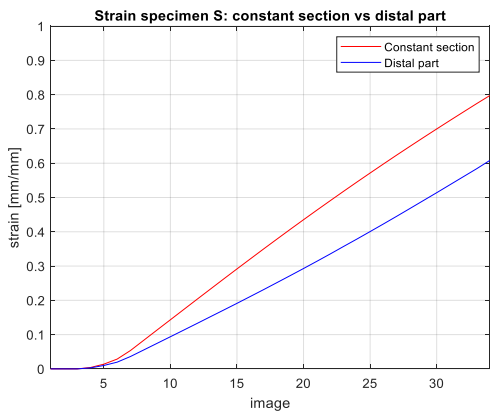
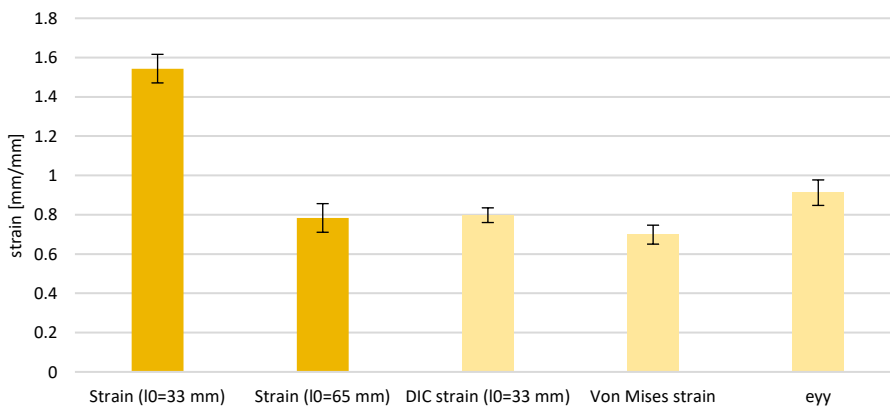


### Specimen R

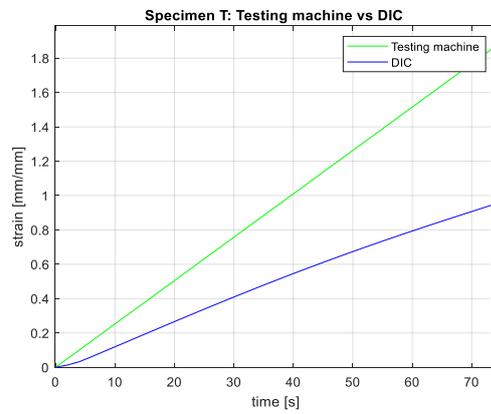
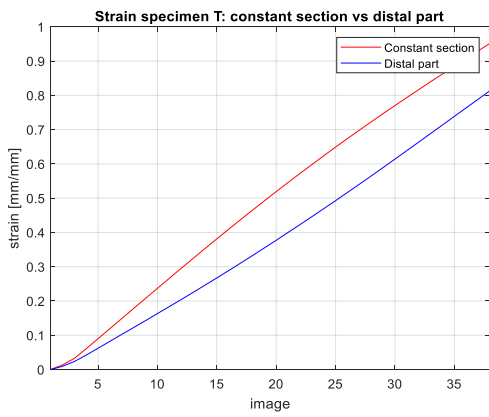
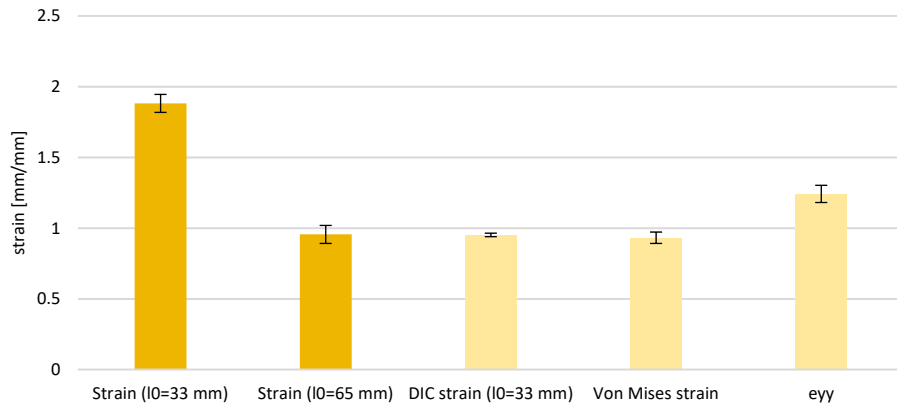




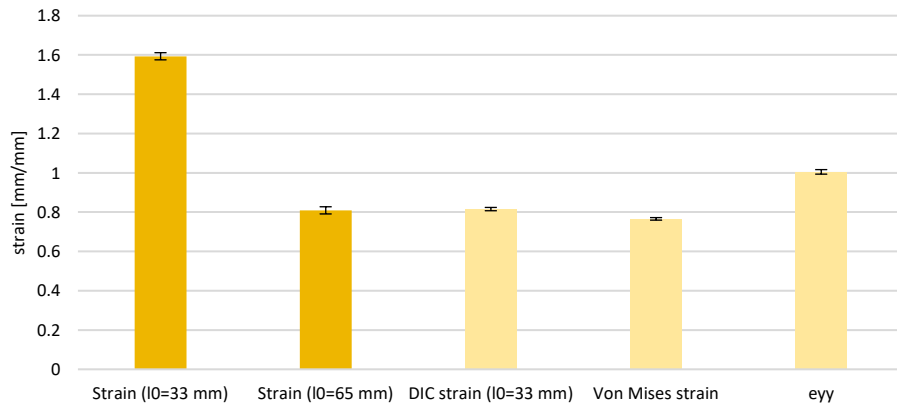
**Specimen S**

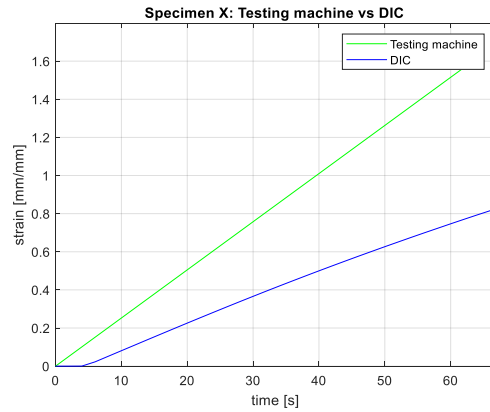
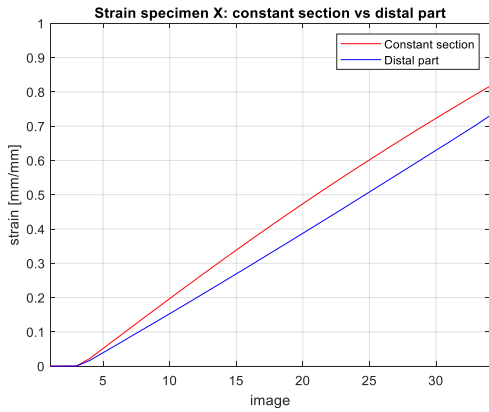


### Specimen T



### Specimen X

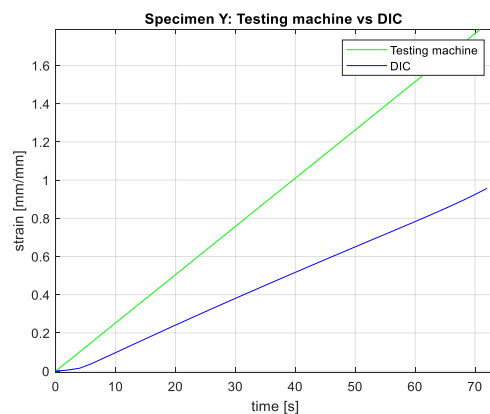
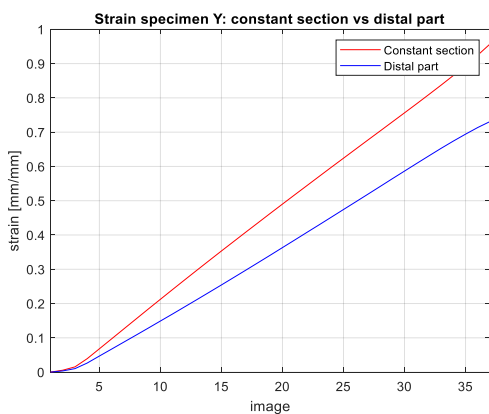
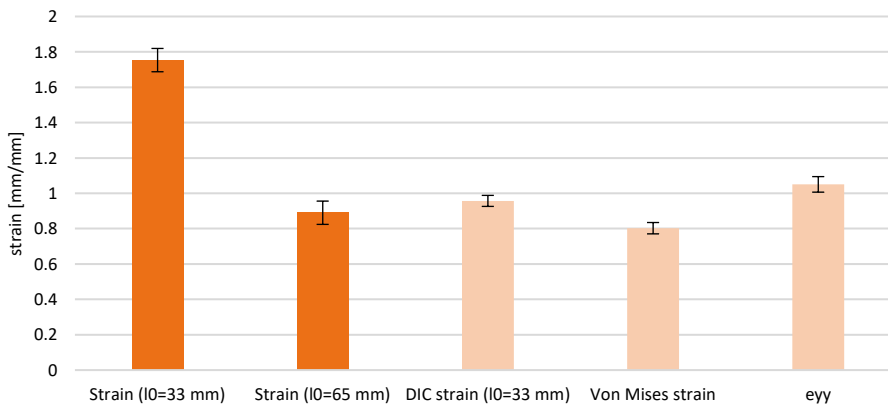




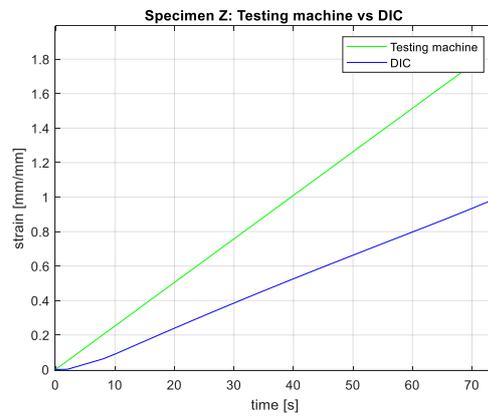
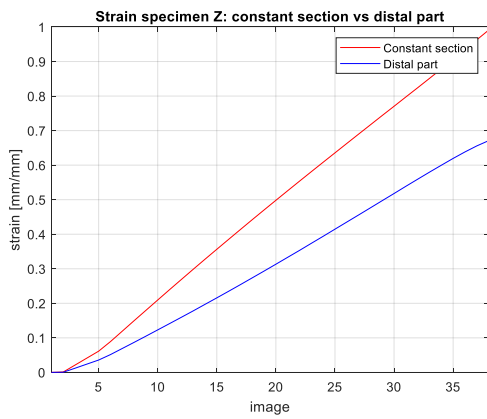
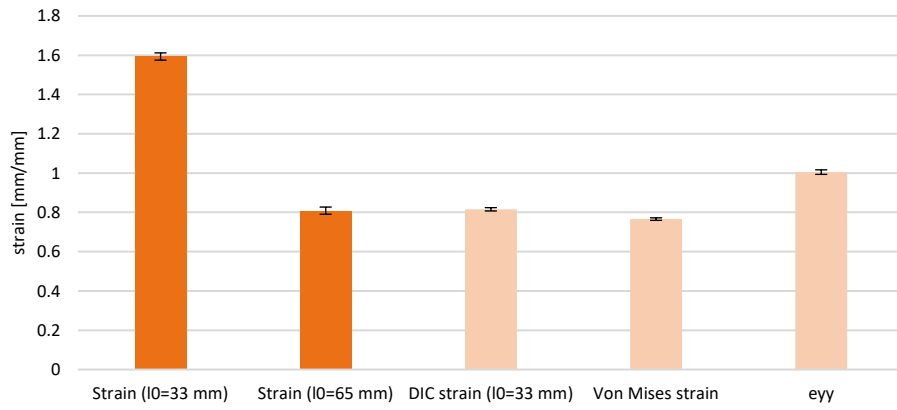
As said before about the Poisson's coefficient, the bar charts and the graphs related to the specimens U and W could not be obtained, since their surface did not allow the DIC analysis. This pattern influences all the mechanical properties of the specimens. Generally, for this category, the DIC strain is always comparable to the averaged strain ( $l_0=65$  mm), apart from the specimens H. This could be due to some anomalies on the constant region of the specimen's surface during the deformation, which prevented the extensometer E0 to measure the deformation on the last images.

The following figures represent the bar charts and the graphs relative to the specimens characterized by the BL pattern.

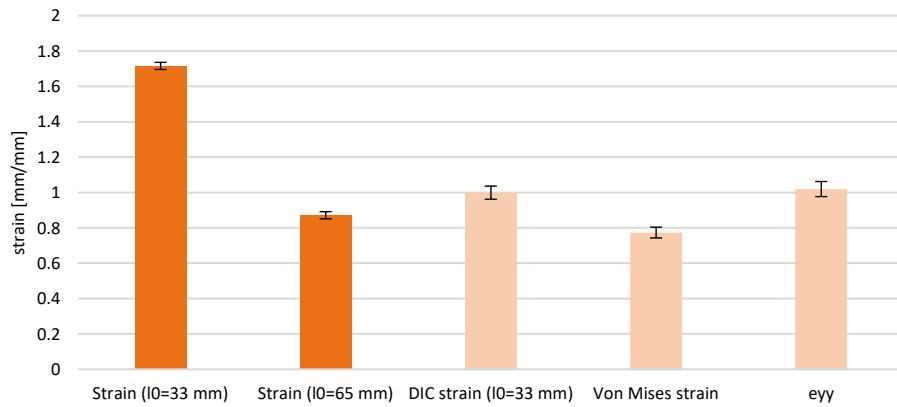
### Specimen Y

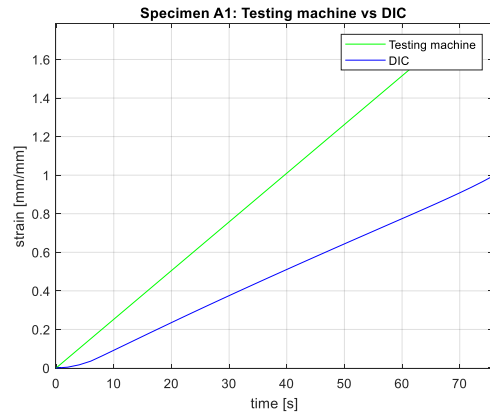
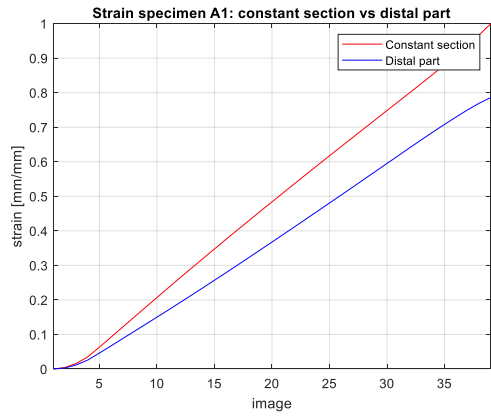


### Specimen Z

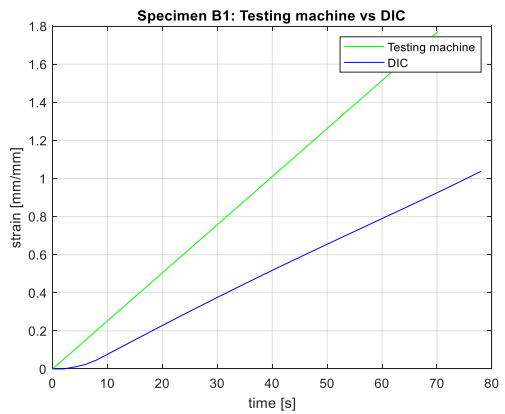
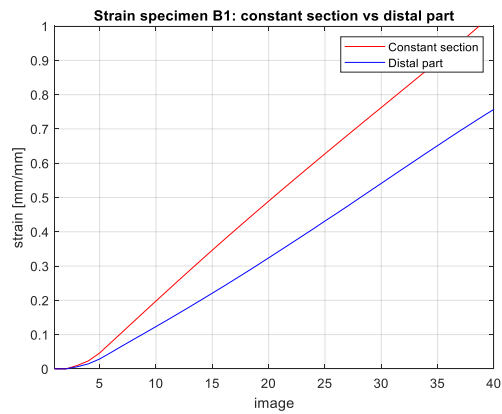
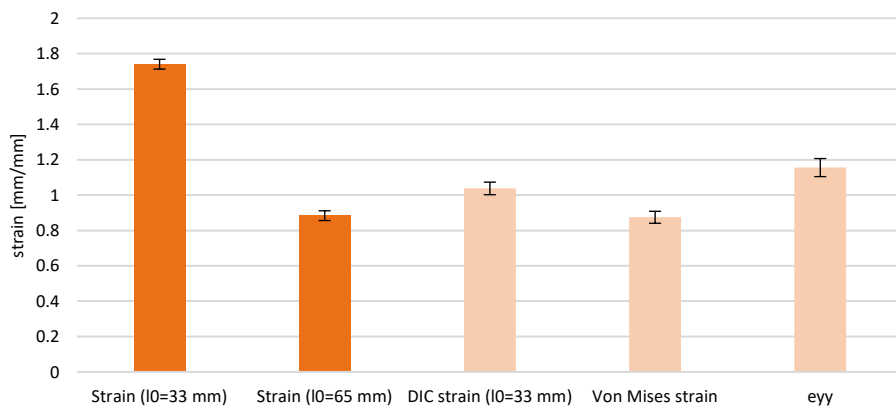


### Specimen A1

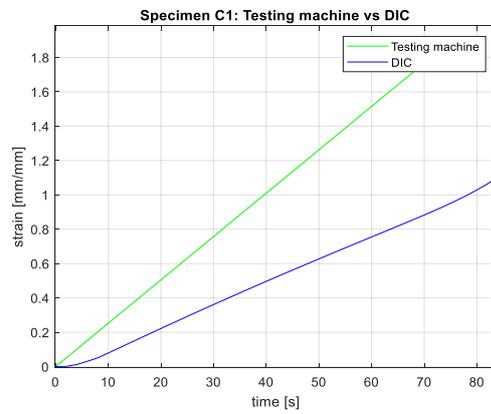
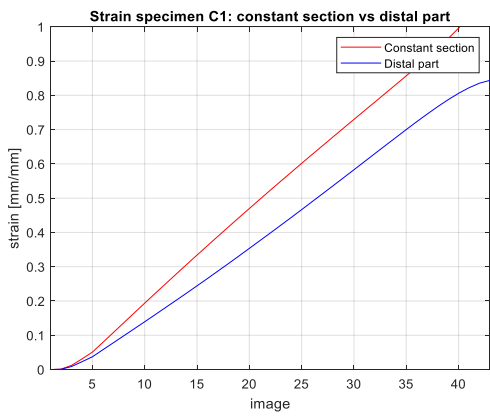
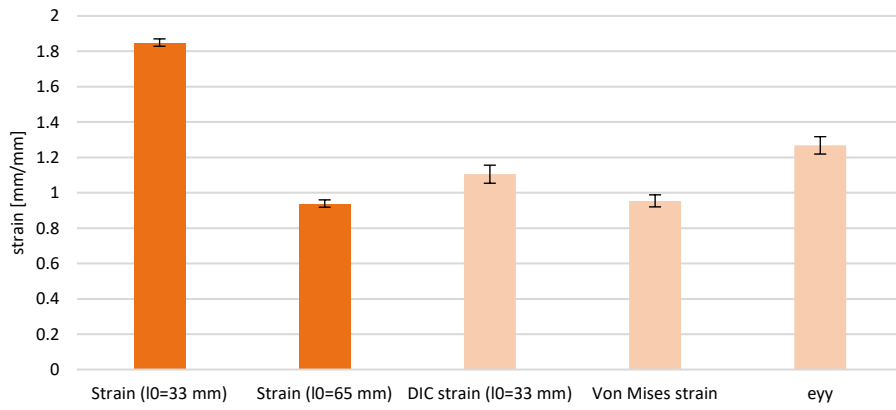




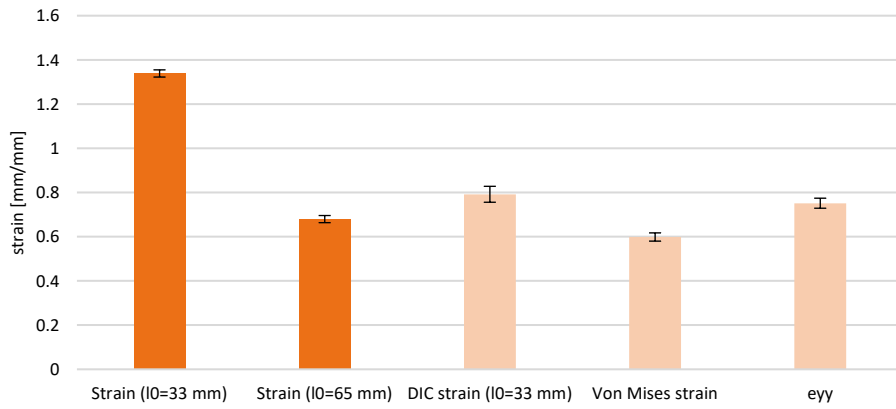
**Specimen B1**

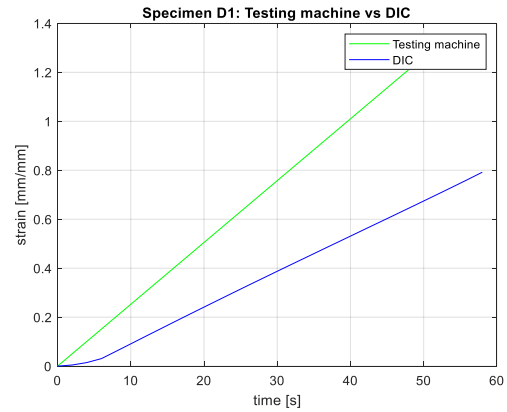
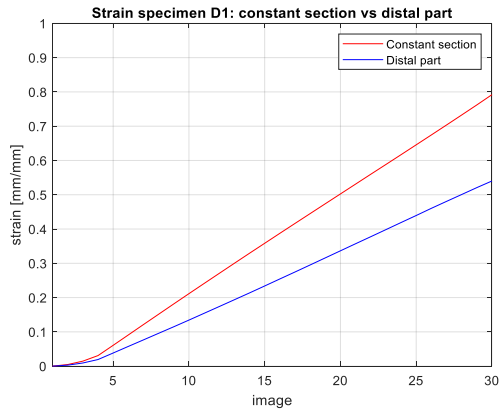


### Specimen C1



### Specimen D1





This pattern does not influence the mechanical properties of the specimens. In most of the cases the DIC strain is not comparable to the averaged mechanical strain ( $l_0=65$  mm) and the constant region undergoes a much higher deformation than the distal parts.

These specimens were tested twice, since the images of the first day were blur. However, analyzing the mechanical data obtained using the testing machine, it resulted a lower peak load, and hence a tensile strength at break too (Fig. 78), and a lower elongation at break, and hence a strain at break too (Fig. 79); the elastic modulus, instead, was found higher than to the one computed on the day 1 (Fig. 80). This phenomenon may be justified by the aging of the specimens: one month has passed between the two tests. The specimens appeared harder, since they have a higher elastic modulus, but their mechanical performances have generally worsened. They reached a lower peak load, showing a greater fragility and a stiffening, due to the aging.

The variation of the mechanical properties (Tab. 12) was computed according to the following formula:

$$Variation(\%) = \frac{MP_{day\ 31} - MP_{day\ 1}}{MP_{day\ 1}} * 100 \quad (4.2)$$

where MP is the corresponding mechanical parameter (tensile strength at break, strain at break and elastic modulus).

**Table 12.** Variation (%) of the mechanical parameters of the BL specimens.

Specimens	Mechanical parameter (MP)		
	Tensile strength at break	Strain at break	Elastic modulus
Y	-35.05	-46.91	21.64
Z	-35.74	-47.26	20.62
A1	-29.27	-43.87	25.75
B1	-31.26	-43.43	24.75
C1	-31.03	-42.52	22.92
D1	-31.49	-43.83	22.96

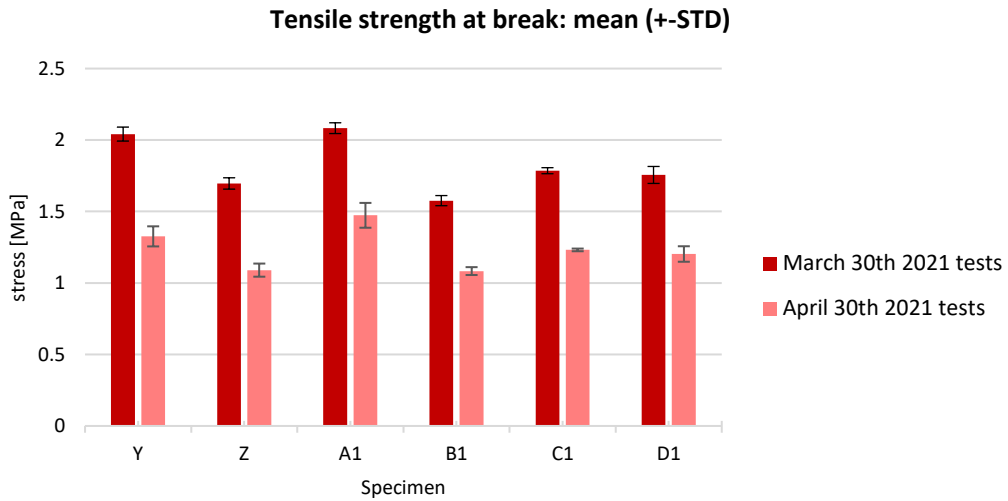


**Figure 78.** Day 1 vs day 31: decrease of the tensile strength at break of the specimens.

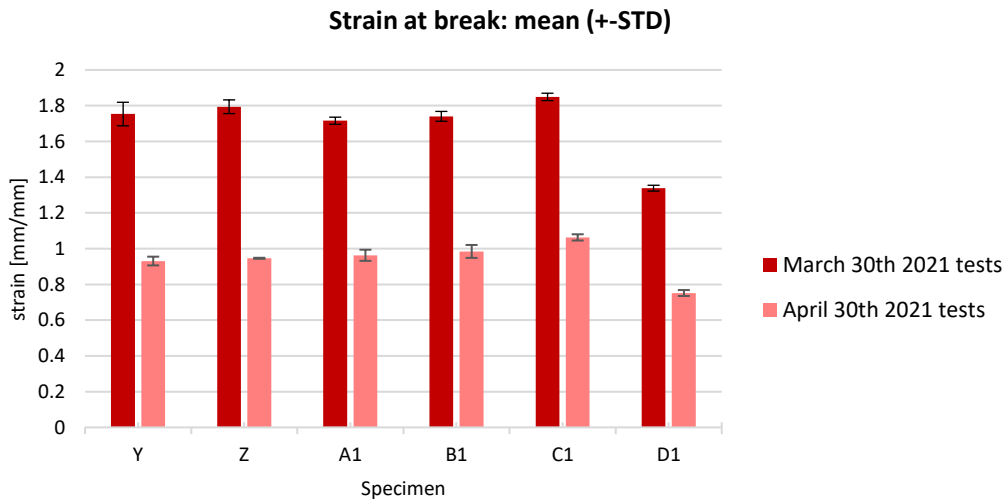


**Figure 79.** Day 1 vs day 31: decrease of the strain at break of the specimens.

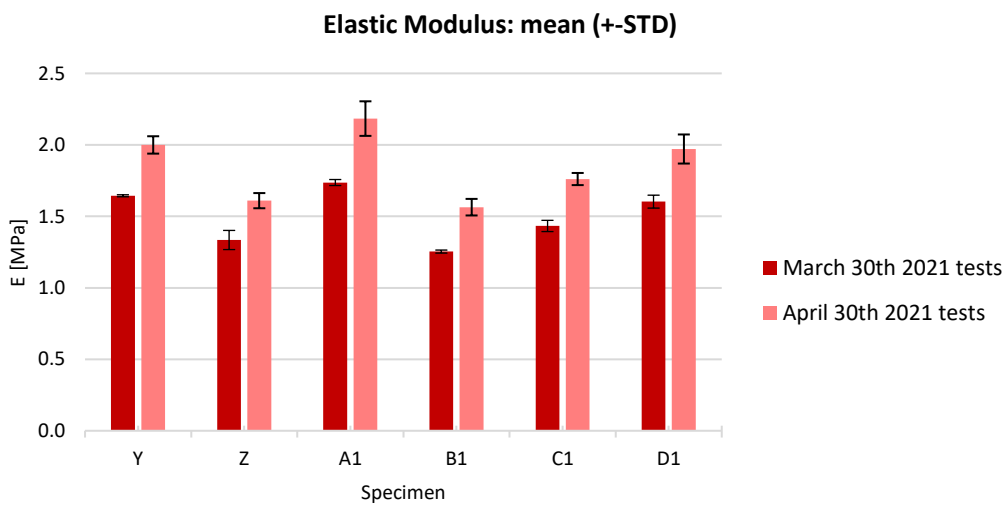


**Figure 80.** Day 1 vs day 31: increase of the elastic modulus of the specimens.

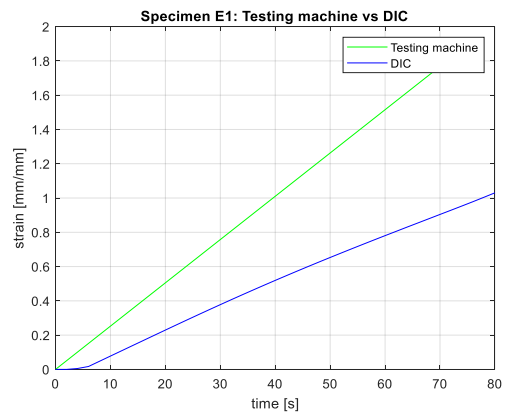
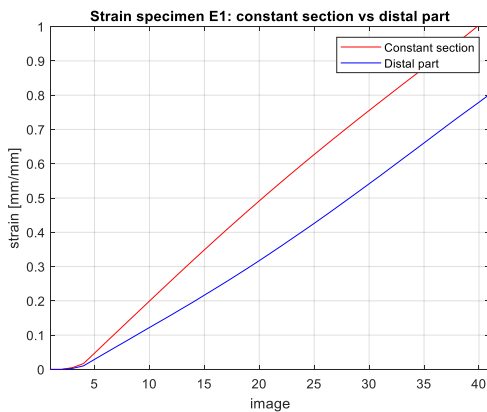
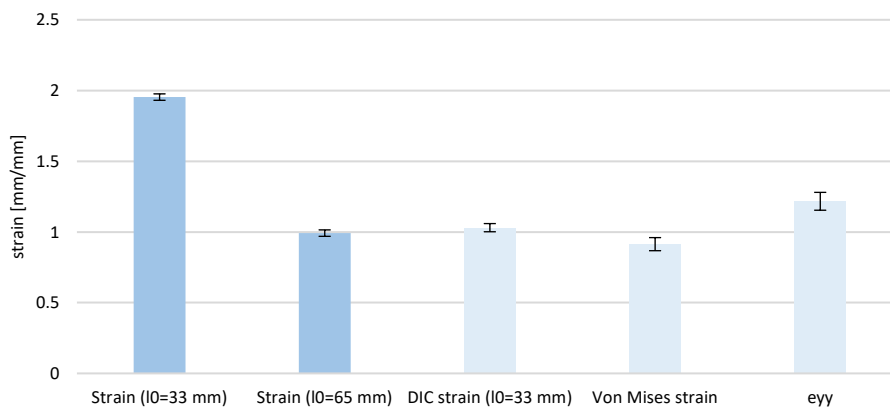
On the day 1, March 30th, of the test the acquired images showed a bad focus, which impeded the DIC analysis. On April 30th they were tested using the testing machine and the DIC system, but their mechanical properties appeared modified after one month. Therefore, the following proportion was done to obtain an approximation of the DIC strain related to the specimens tested on the day 1 ( $x$ ):

$$\varepsilon_{MAC,day 1} : \varepsilon_{MAC,day 31} = x : \varepsilon_{DIC,day 31} \rightarrow x = \frac{\varepsilon_{MAC,day 1}}{\varepsilon_{MAC,day 31}} \varepsilon_{DIC,day 31}$$

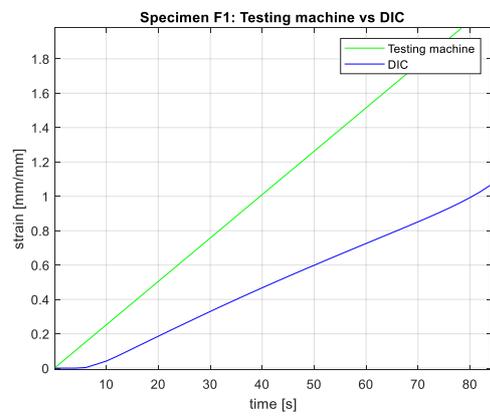
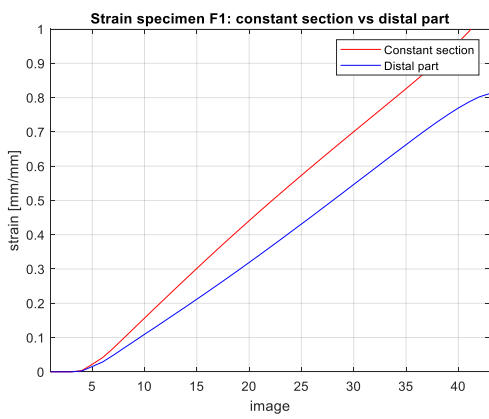
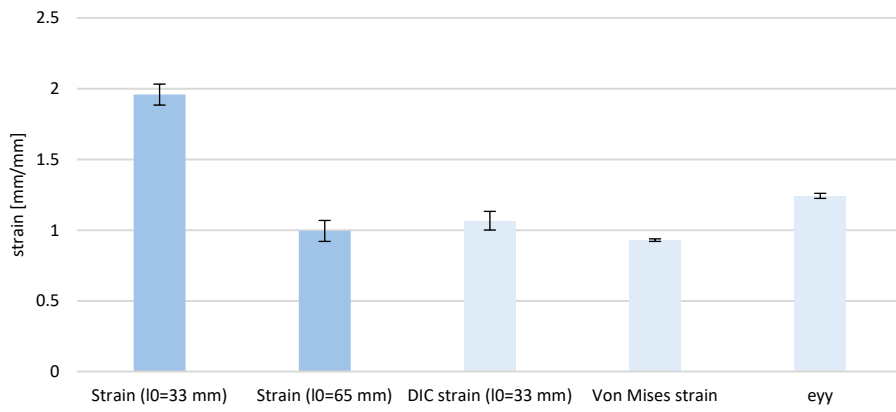
This formula has proved effective since the computed values are comparable to those obtained through the DIC analysis of the specimens belonging to the other categories.

The following figures represent the bar charts and the graphs relative to the specimens characterized by the HB pattern.

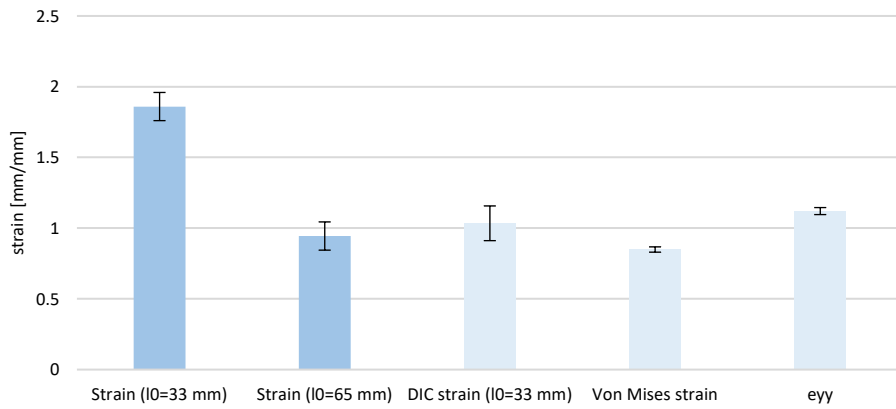
### Specimen E1

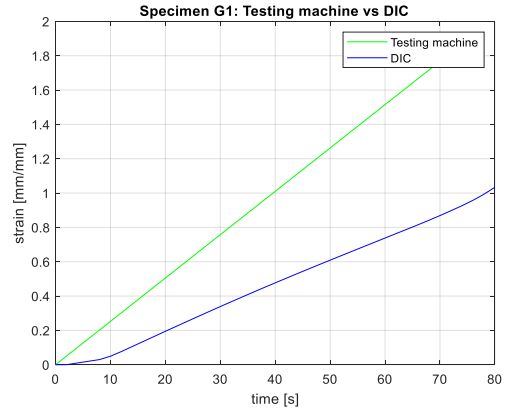
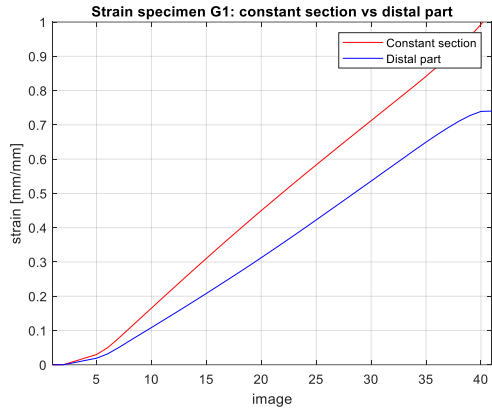


### Specimen F1

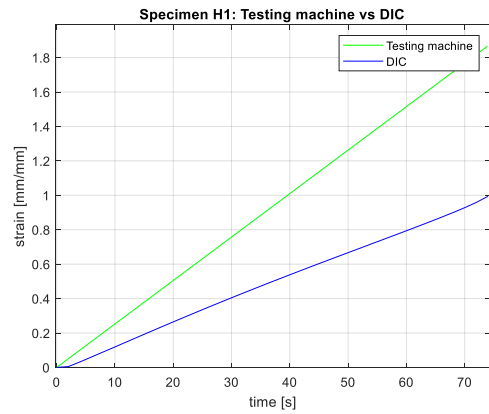
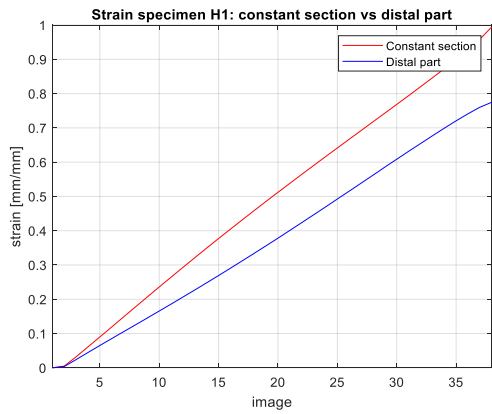
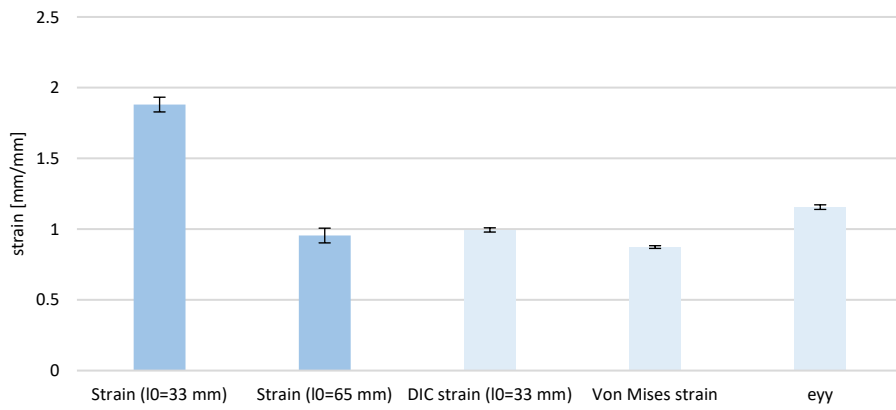


### Specimen G1

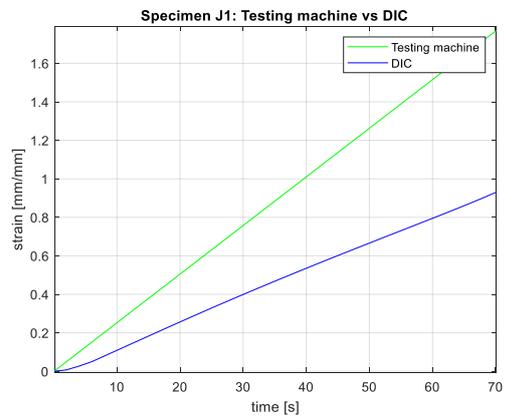
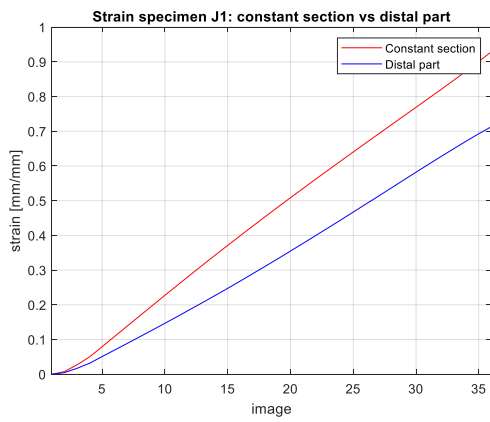
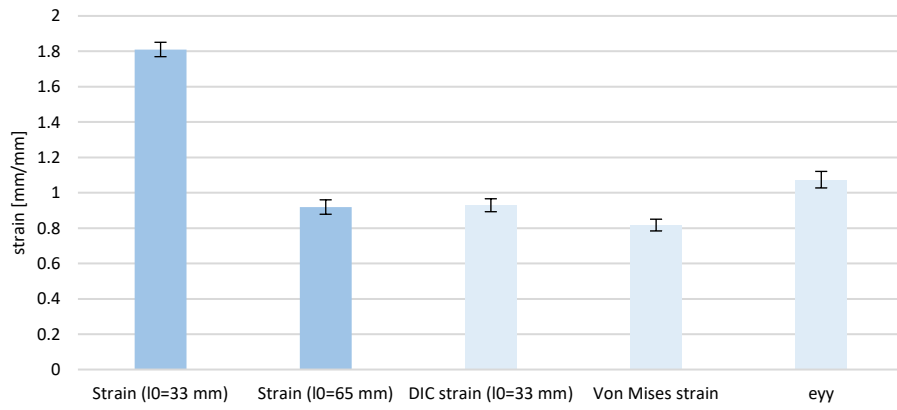




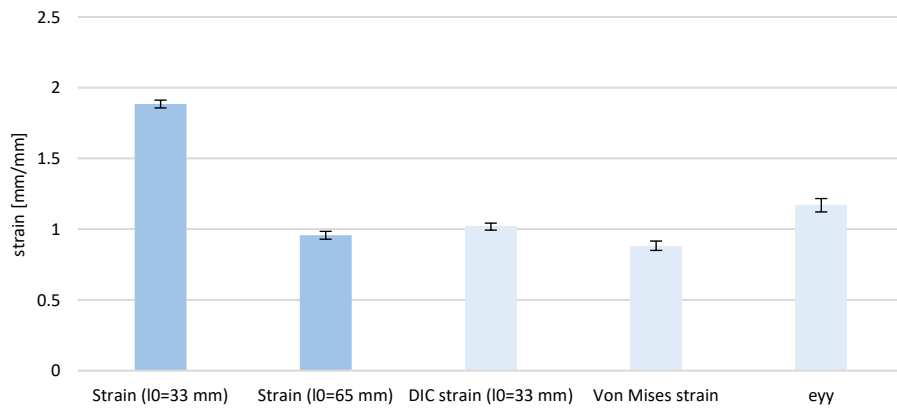
**Specimen H1**

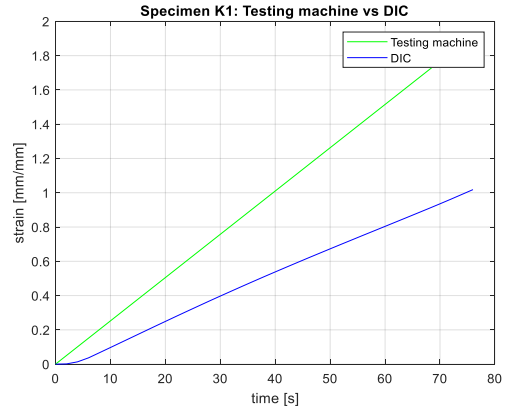
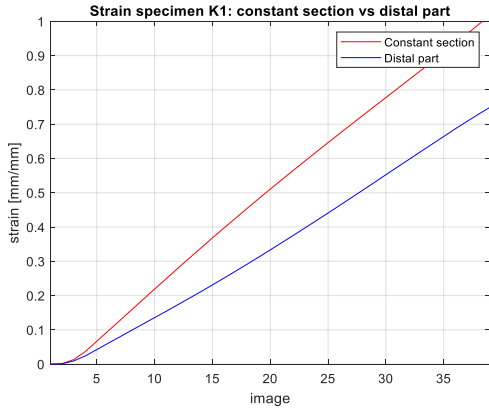


### Specimen J1

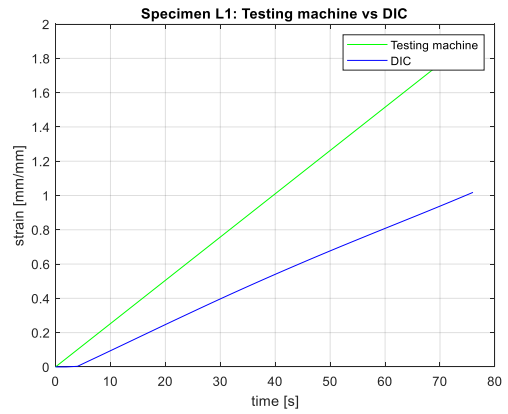
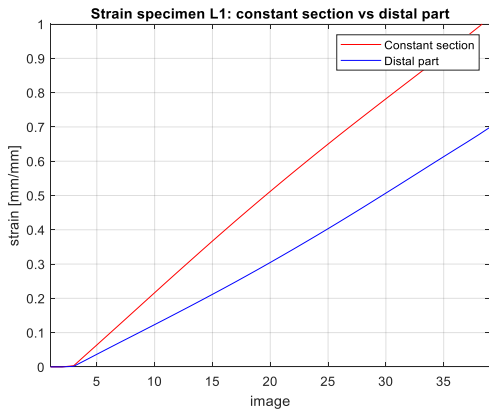
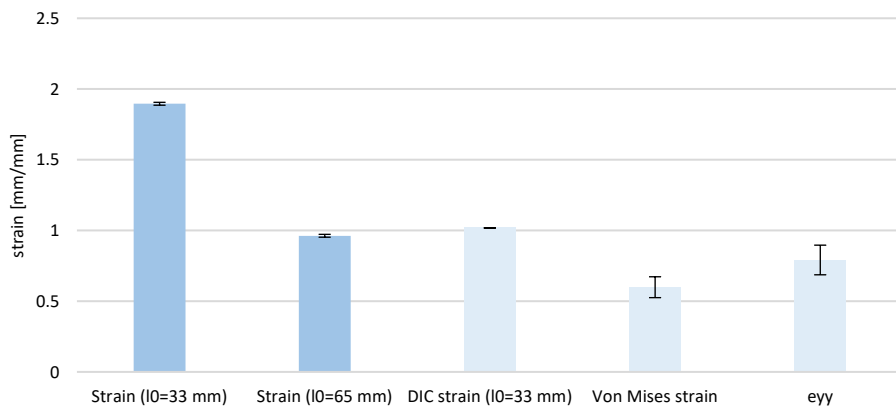


### Specimen K1

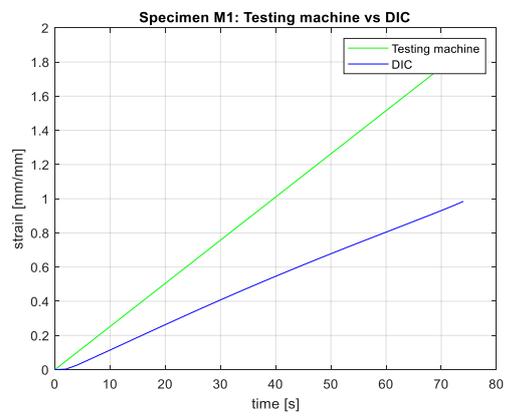
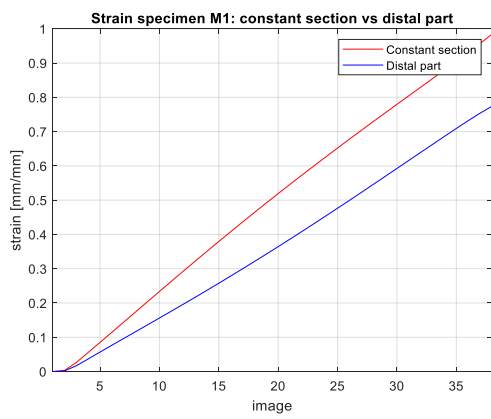
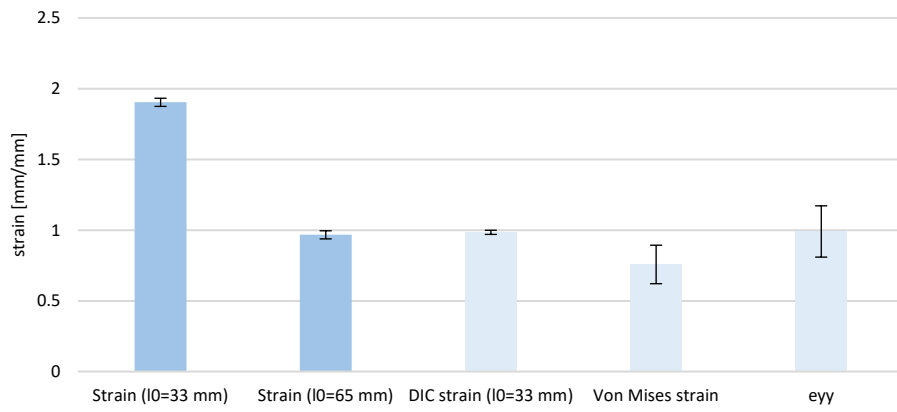




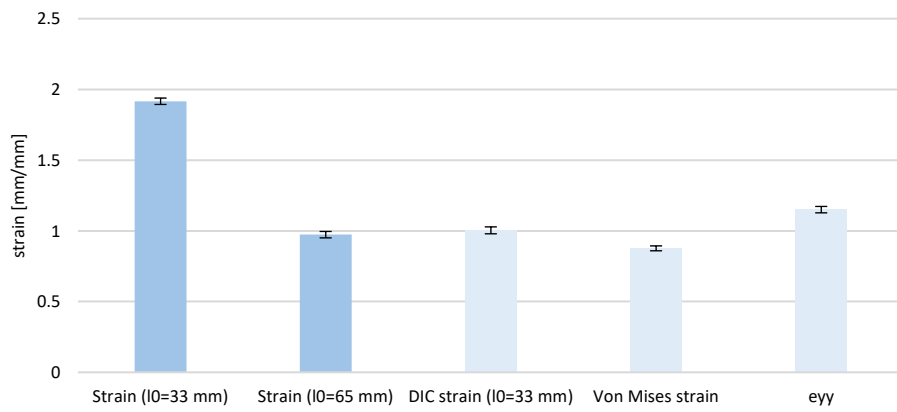
**Specimen L1**

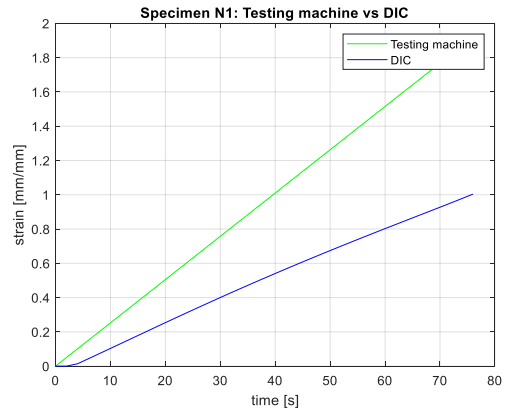
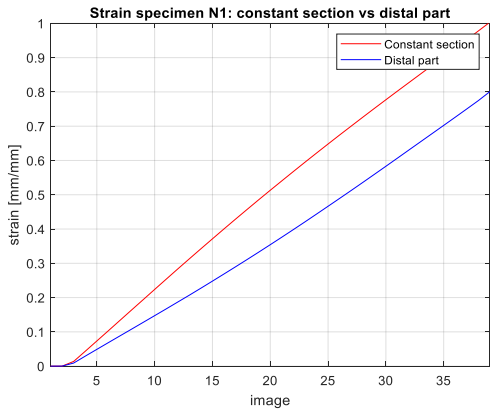


### Specimen M1

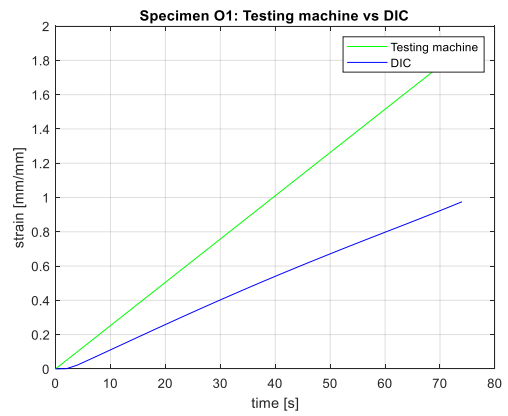
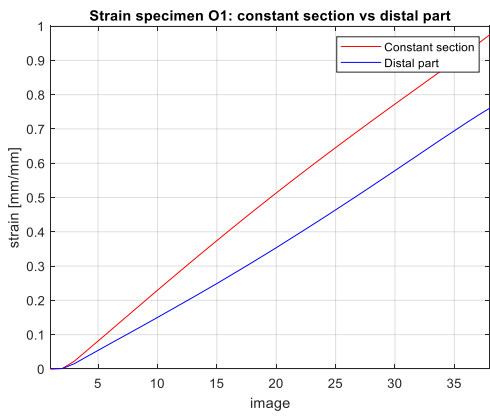
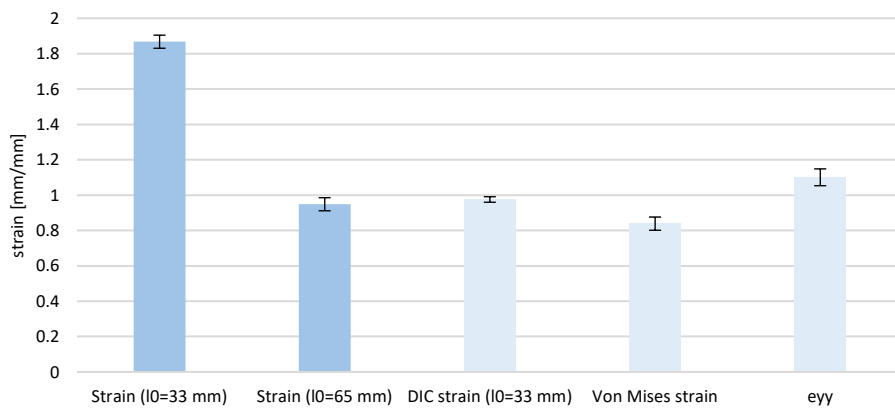


### Specimen N1

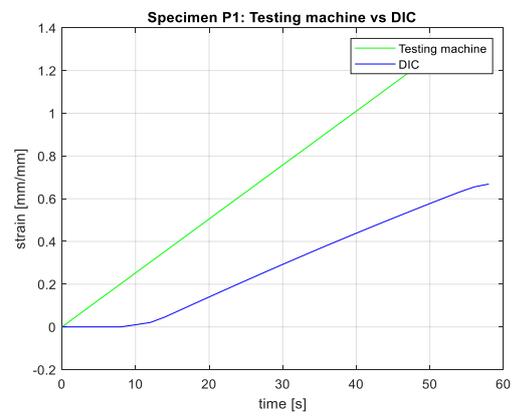
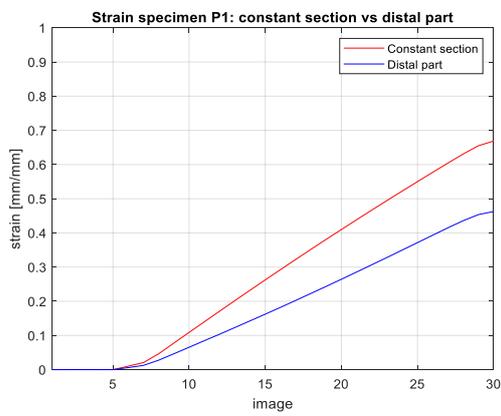
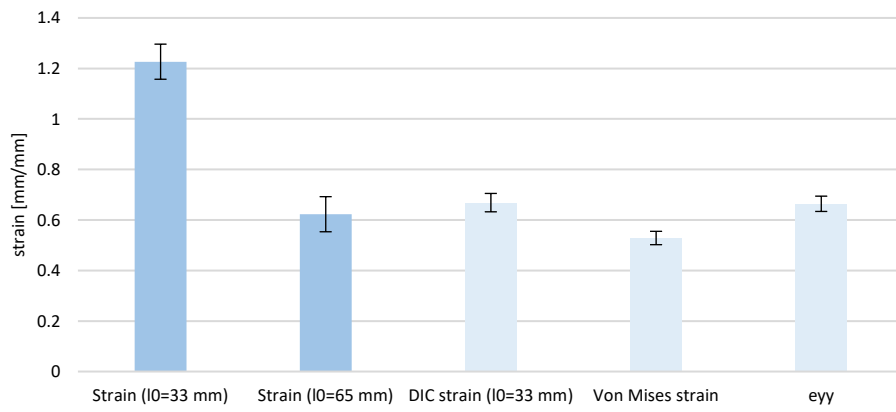




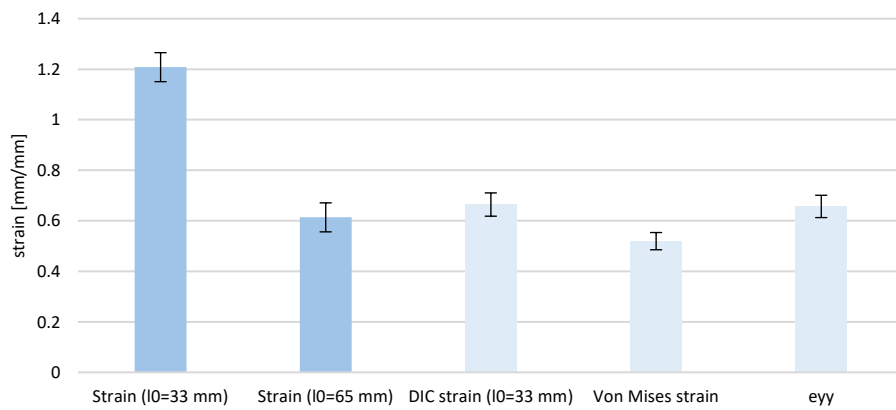
**Specimen O1**

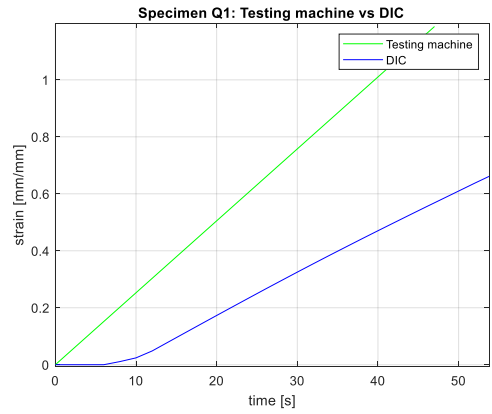
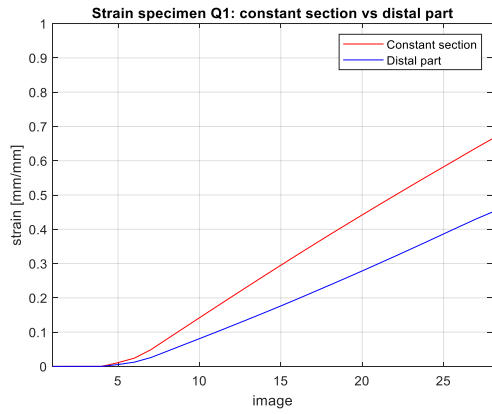


### Specimen P1

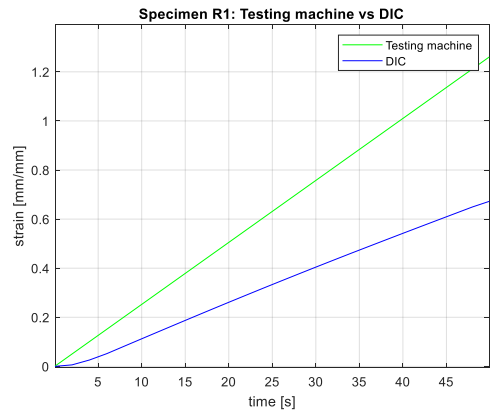
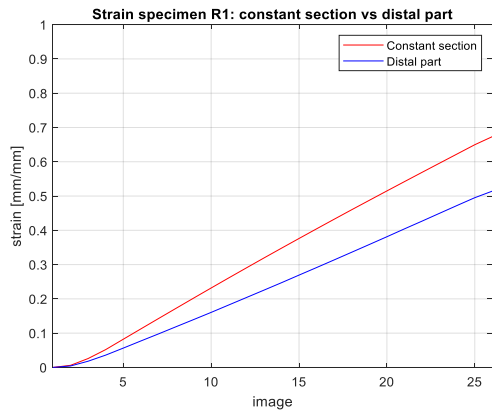
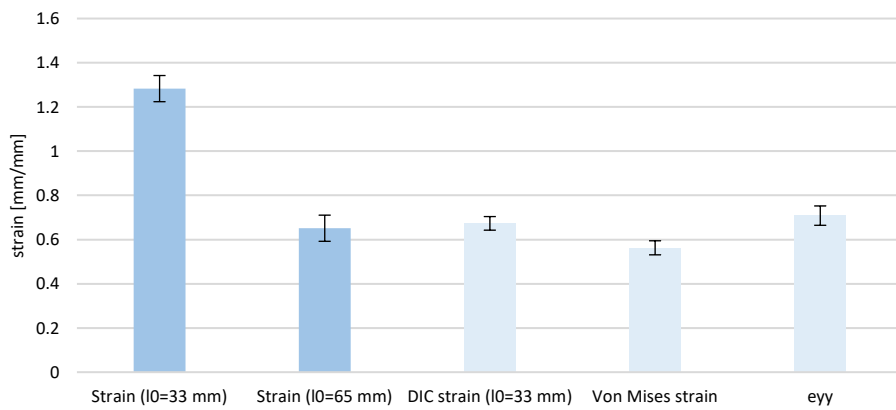


### Specimen Q1

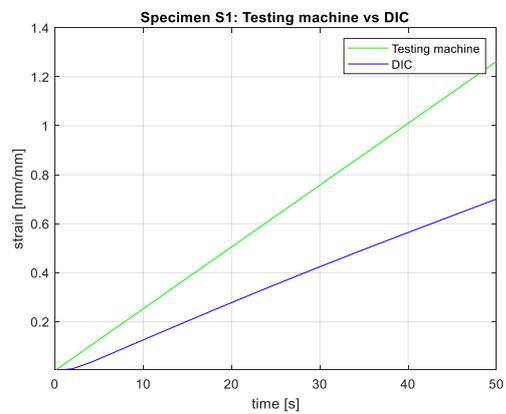
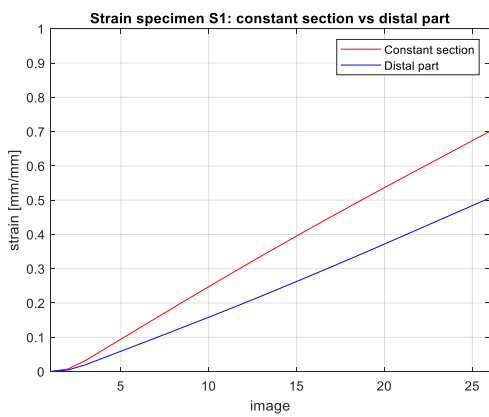
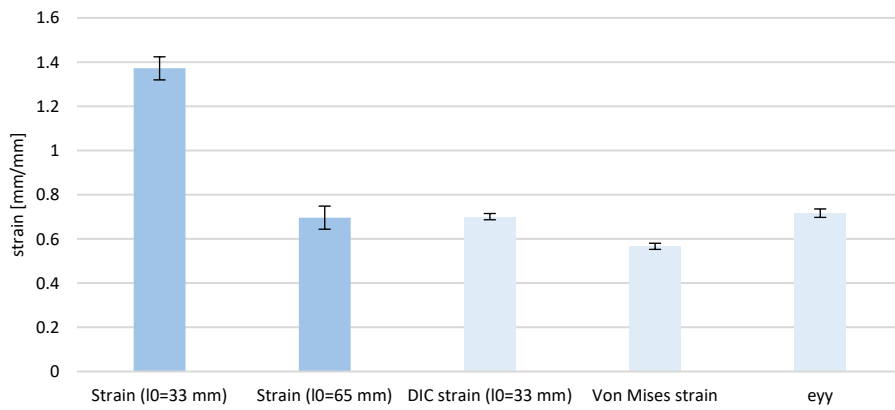




**Specimen R1**



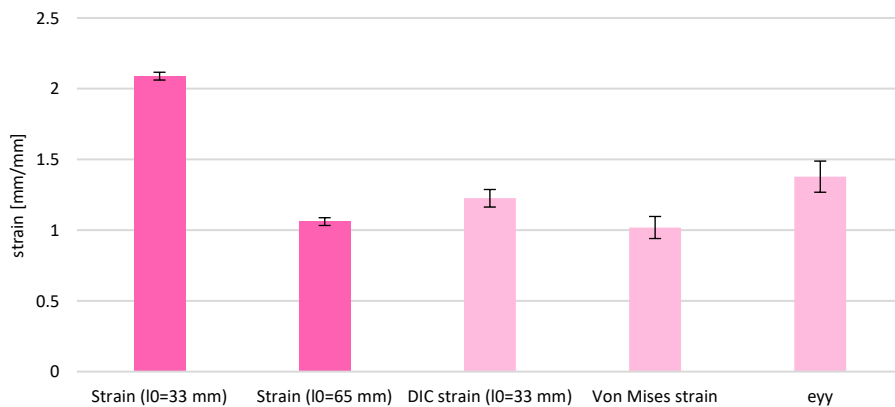
### Specimen S1

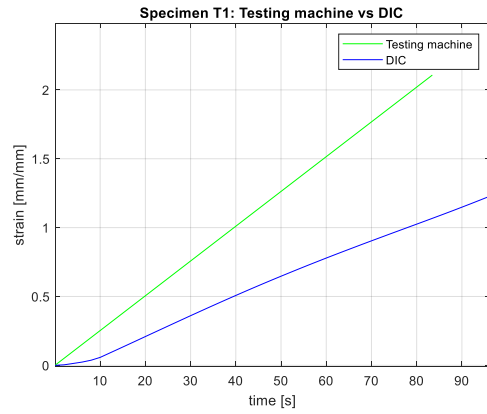
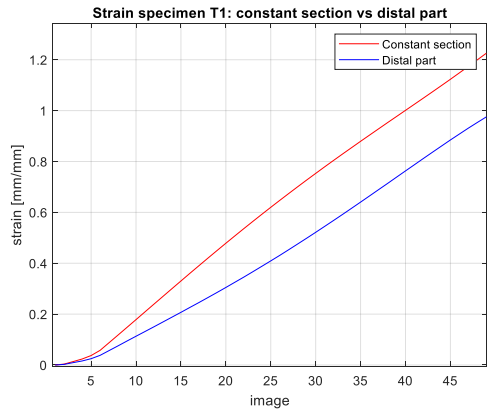


This pattern influences only the strain at break, causing low elastic modulus for all the specimens in general. The DIC strain is comparable or slightly higher than the averaged mechanical strain. Therefore, in most of the cases, the constant region underwent a much higher deformation than the distal parts.

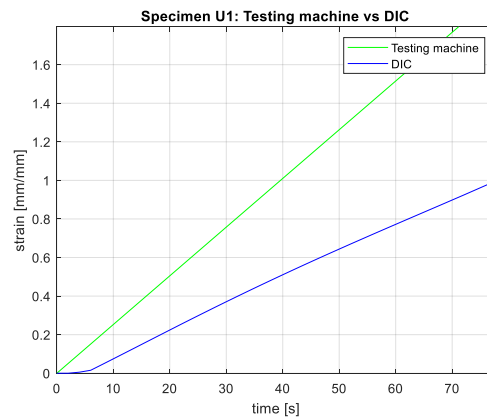
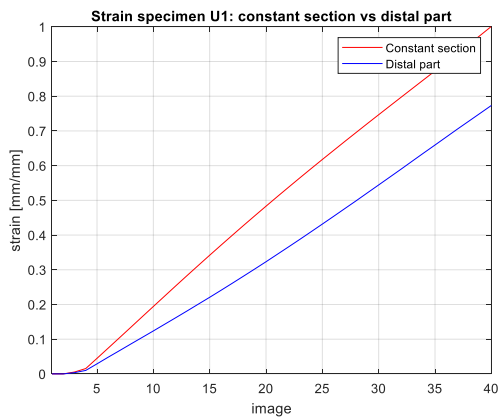
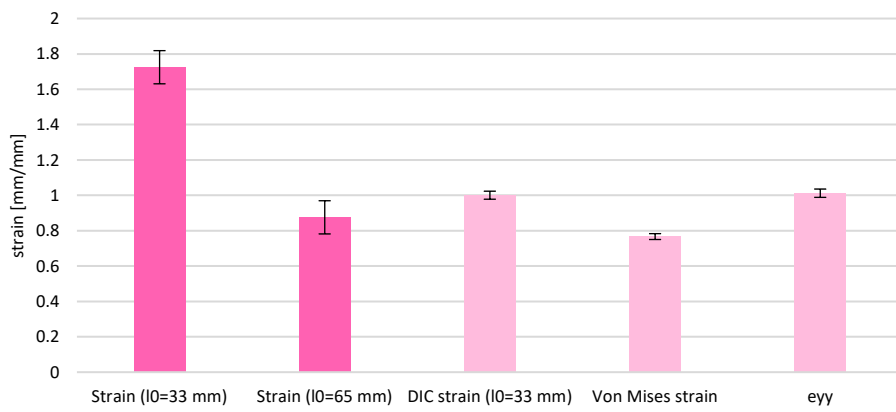
The following figures represent the bar charts and the graphs relative to the specimens made of the base materials, without any pattern: Agilus30\_50, Agilus30\_60, Agilus30\_70 and TissueMatrix.

### Specimen T1

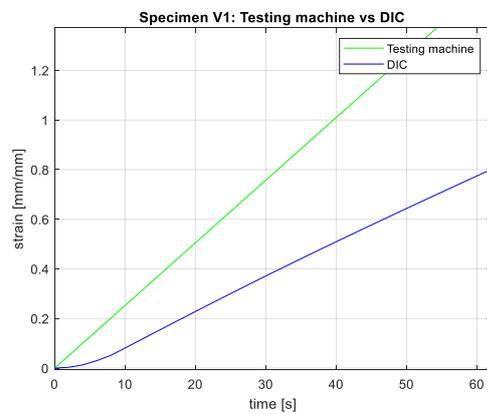
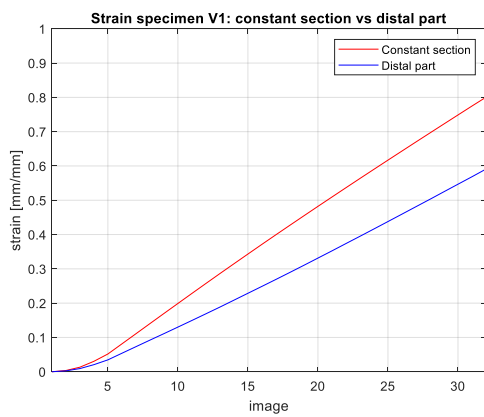
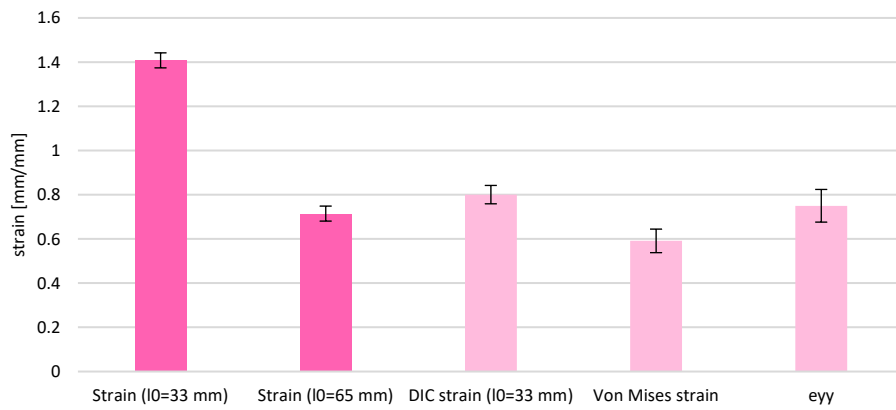




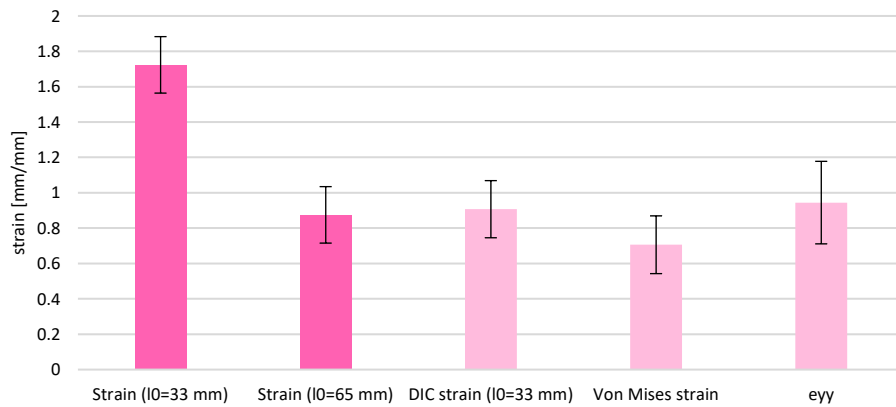
**Specimen U1**

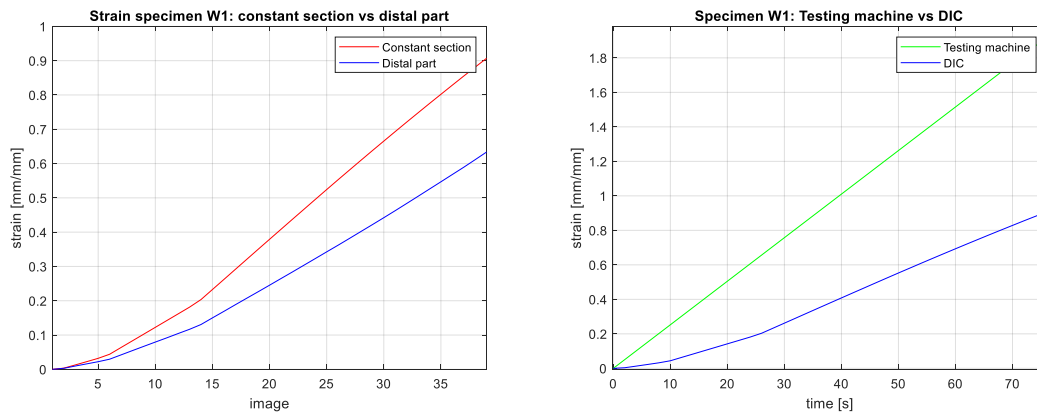


### Specimen V1



### Specimen W1





Since the specimens T1, U1, V1 do not have any pattern, the ratios between the maximum deformation values of the constant section and the distal parts (strain constant region/strain distal part\*100) are all about the same: 125,7%, 129,5%, 135,5%, respectively. They have a slight upward trend, maybe due to the progressive hardening of the materials with the increasing of the Shore A value: the harder the material is the more non-deformable are the distal parts, which have a larger width. Concerning the TissueMatrix (W1), it is a special resin, highly irregular, as the high standard deviation suggests, and fragile. The trend of the deformation is less linear compared to the other specimens, as shown in the first chart; this could be due to the inhomogeneity of the materials making up the resin.

The base materials belonged to the group of specimens tested on the first day, thus they were retested. As the previous category, they showed different mechanical properties after a month, as shown in the following bar charts.

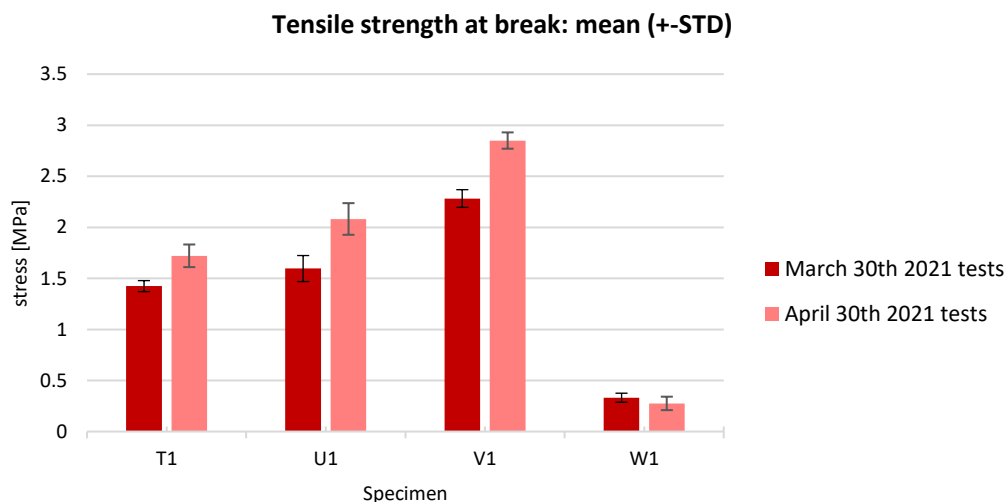


**Figure 81.** Day 1 vs day 31: tensile strength at break of the specimens.

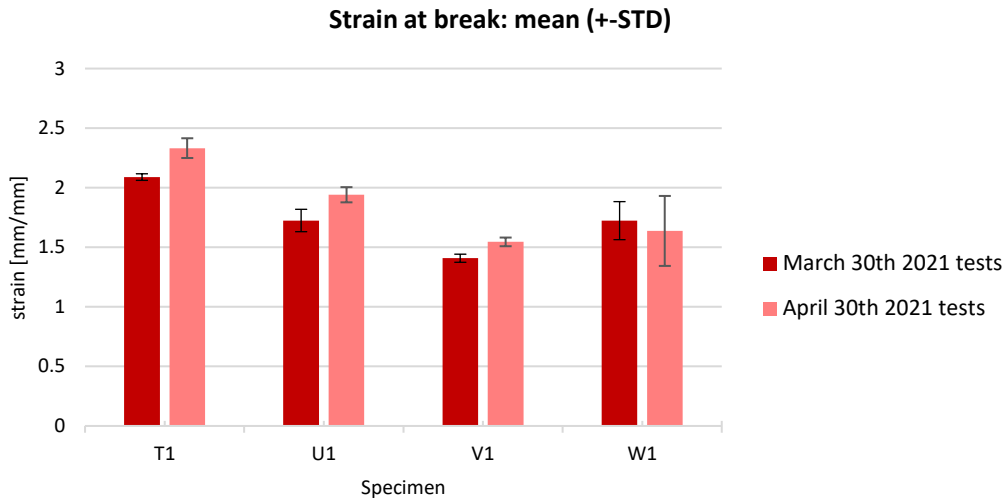


Figure 82. Day 1 vs day 31: strain at break of the specimens.

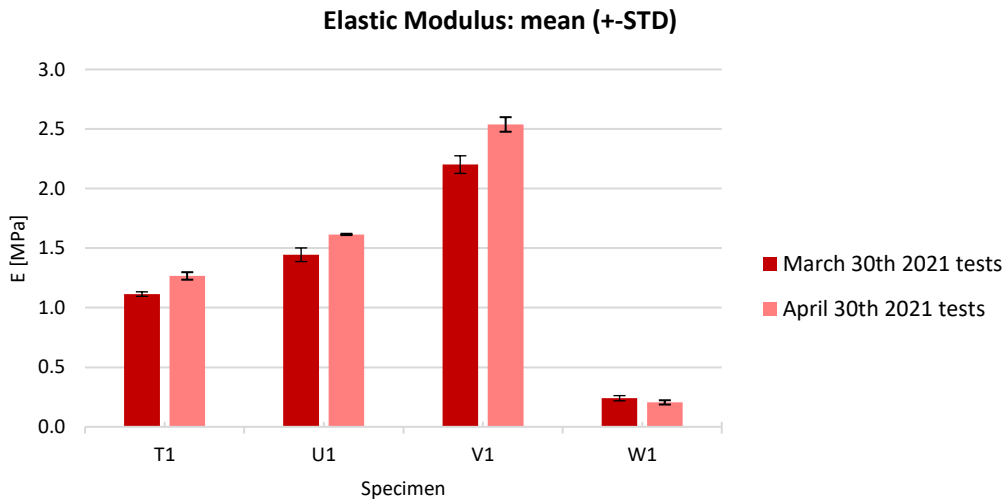


Figure 83. Day 1 vs day 31: elastic modulus of the specimens.

The tensile strength at break has an increasing trend for the base materials made of Agilus30, while it is almost the same for the TissueMatrix. However, having the strength at break of the day 1 a very low value, the percentage variation results pretty high (Tab. 13), and the value appears decreased. The same considerations could be done for the elastic modulus and the strain at break, but with smaller variations.

Table 13. Variation (%) of the mechanical parameters of the BL specimens.

Specimens	Mechanical parameters		
	Tensile strength at break	Strain at break	Elastic modulus
T1	20.85	11.63	13.67
U1	30.41	12.53	11.83
V1	24.88	9.75	15.32
W1	-16.85	-5.01	-14.62

### 5.3 Discussion and conclusion

It could be stated that, for the TM and HP materials, the pattern and the hardness values influence the specimens' properties, while, for the BL and TL patterns, the percentage of area occupied by each component is more relevant than the pattern itself. Among the TM pattern category, analyzing the specimens 50F-50M and 60F-40M, it can be noted that all the specimens characterized by fibers with SH\_A 70 in a softer matrix – SH\_A60 or SH\_A50 – (P, R, V, X) have superior mechanical performance than the others. Thus, first, to improve the mechanical properties of the material, the amount of fibers should be greater or comparable to the amount of matrix. Then, the presence of very hard non-uniform shaped fibers in a softer matrix enhances the tensile response of the specimen.

Further considerations about the two concentric-layered patterns (TL and BL) can be offered. They were, in fact, thought to be compared, since the same approach was followed in the assignment of their hardness values. Looking at the percentages of area occupied by the different components, they are not the same (Fig. 84), but we can do a qualitative comparison between their mechanical properties, since the percentages of the inner and the middle layers are very similar. Overall, the BL pattern seems to give better mechanical results, showing always greater tensile strength at break (Fig. 85) and elastic modulus (Fig. 87); regarding the strain at break, the values are comparable (Fig. 86). This happens even if the matrix's Shore A value is lower than that of the outer layer (Y, A1, C1) and hence the amount of harder material is less than that of softer material, since in the BL pattern the matrix occupies the largest volume. As for the TM pattern, the specimens with hard fibers in a softer matrix show better properties than the others, both for the TL and the BL pattern. It can therefore be concluded that concentric-rings fibers have a better mechanical tensile behavior than fibers containing concentric little wires; thus, to enhance the mechanical response of the materials, considering the two design strategies, the former should be followed. Moreover, as above, specimens with harder fibers in a softer matrix are preferable.

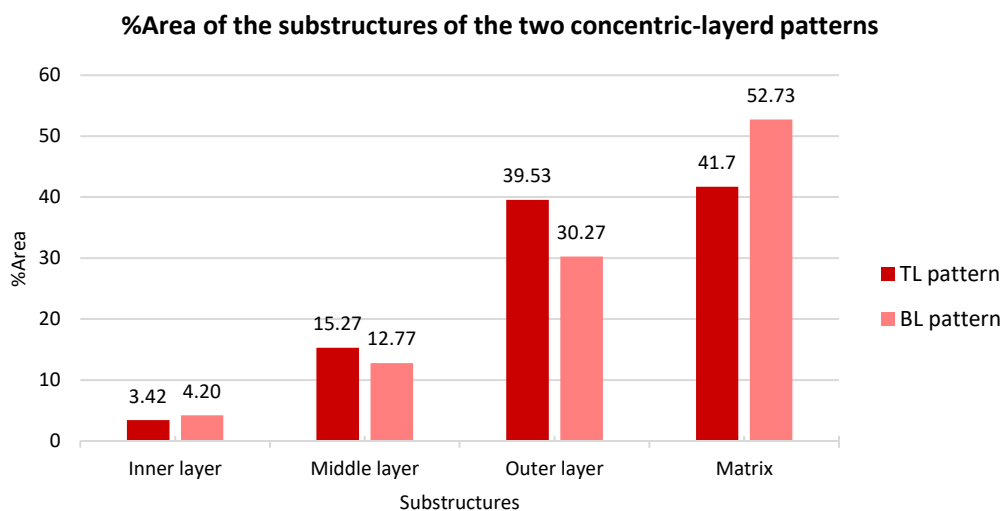
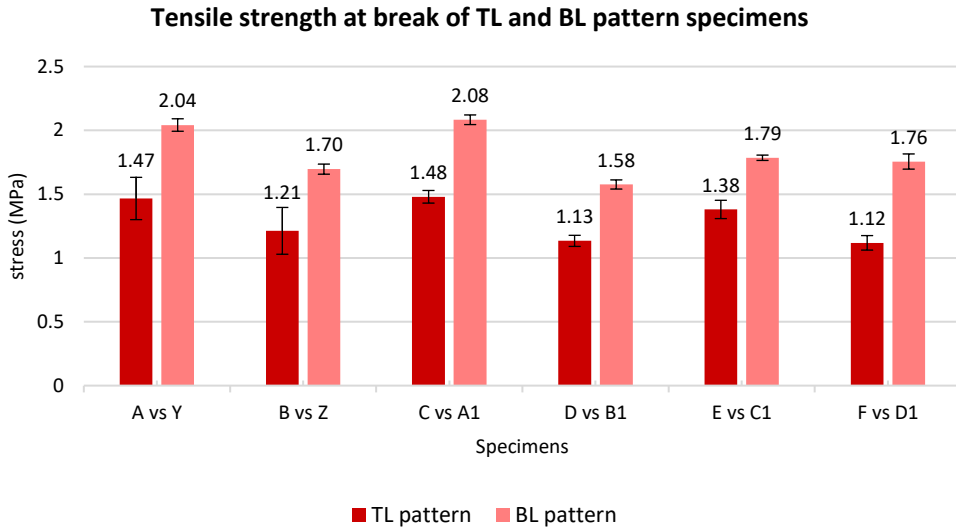
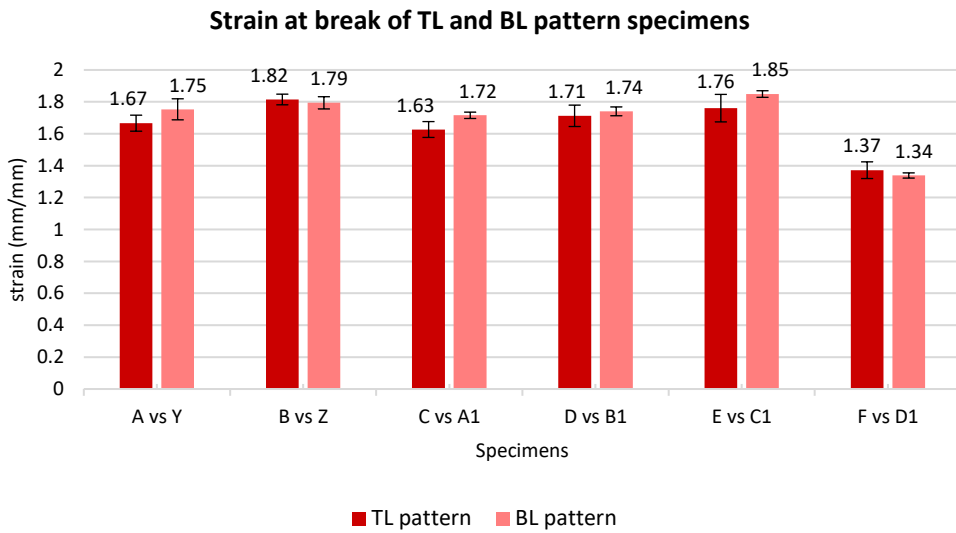


Figure 84. Comparison between the percentage area of the two patterns' substructures.



**Figure 85.** Comparison between the mechanical properties of the TL and BL pattern specimens: tensile strength at break.



**Figure 86.** Comparison between the mechanical properties of the TL and BL pattern specimens: strain at break.

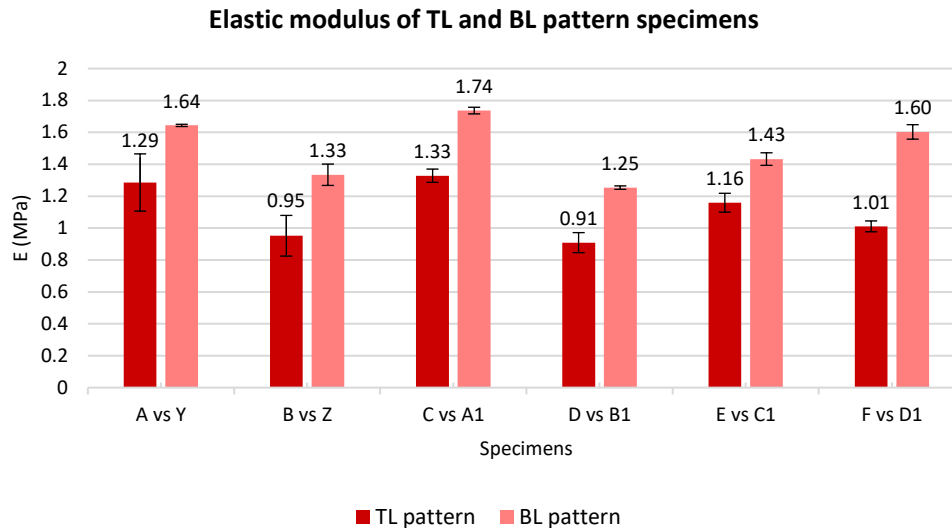


**Figure 87.** Comparison between the mechanical properties of the TL and BL pattern specimens: elastic modulus.

According to the obtained results, following the ASTM D638 to compute the deformation of the specimen leads to an incorrect result. As a consequence, this could give rise to doubts about the values of the tensile strength at break and of the modulus of elasticity. The values of the Young’s modulus of rubber and plastic materials can be also computed by using the following empirical formula, postulated by Ruess, by leveraging the correlation of durometer values to modulus of elasticity:

$$\log_{10} E = 0.0235 * S - 0.6403$$

where E is the Young’s modulus (in MPa) and S the ShoreA value of the material. However, this equation suffers from a significant scatter in whatever data sets it works with, since the Shore values are only an indication of the material’s ability to respond to a small and localized force on the surface, while the Young’s modulus is the ability of the entire material to respond to a load. Thus, the physical test data cannot be replaced by this equation [136], [137]. Moreover, this correlation can be applied only to the base materials, which have a single ShoreA value, not to the specimens with pattern, which are a combination of different hardness values. Anyway, even if the values appear very different (Tab. 14), we can verify the trend of the modulus of elasticity of the specimens T1, U1, and V1.

**Table 14.** Measured elastic modulus vs empirical elastic modulus of the base materials: values.

Specimens	Mechanical parameters		
	ShoreA	Measured E	Empirical E
T1	50	1.11	1.71
U1	60	1.44	2.16
V1	70	2.20	2.73

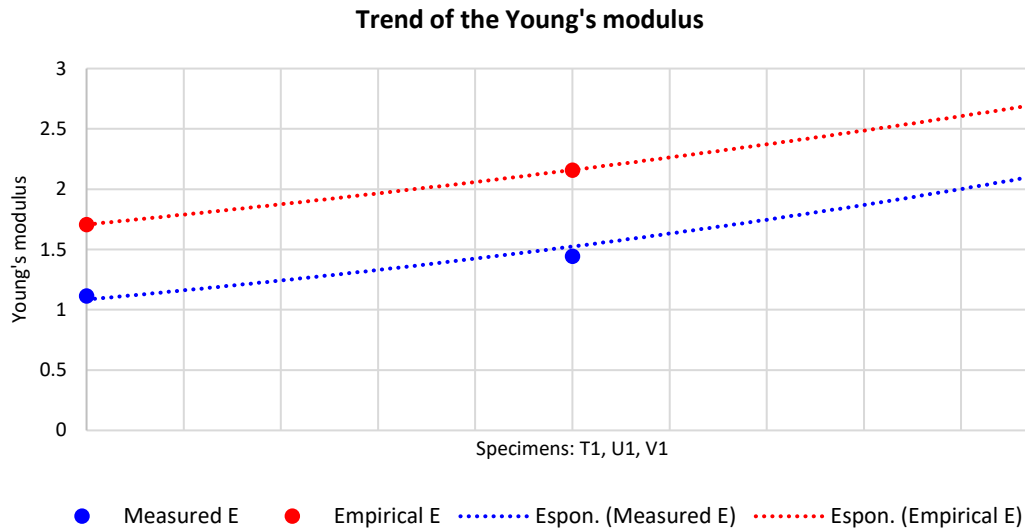


**Figure 88.** Measured elastic modulus vs empirical elastic modulus of the base materials: trend of the values.

The two curves show the same exponential growth, as shown in fig. 88; thus, even if the Empirical values differ from the Measured ones, the trend is the same. These computed values are, indeed, only an estimate of the actual values, but they are useful to validate the resulting data of the Young's modulus. We can, therefore, use the ASTM D638 to compute the modulus of elasticity, but this Standard cannot be used for the computation of the strain, which should be measured using the DIC, to obtain an accurate result. The same goes for the tensile strength at break, which could be estimated by simulation.

The tensile strength at break should be measured only in the constant section of the specimen, since the distal parts probably would show a higher strength, thus a lower stress concentration, having a greater area. Moreover, at the connecting point, the curvature could be subjected to a high stress concentration, which could influence the obtained data. Unfortunately, we are unable to obtain the stress field as DIC's output, except by applying the following equation to the field of deformation:

$$\sigma = E \cdot \varepsilon$$

However, we would like to verify both the tensile strength at break and the modulus of elasticity; therefore, applying this formula would be futile.

The Young's modulus of the Agilus30 seems unavailable in literature, while the tensile strength at break is given in Agilus30's datasheet and ranged from 2.1 to 3.1 MPa. However, being referred only to the constant section of the specimen, it cannot be compared to our results, in which the tensile strength at break appears smaller. The strain at break ranged from 185% to 270%, but these values are related to a material with a ShoreA of 30-40 [64].

In conclusion, since the Agilus30 was tested only in lower Shore hardness than 50, 60 and 70 [138]–[144], our results cannot be found in literature.

The Poisson's ratio of the tested specimens ranged from 0.275 to 0.356 and it is closer to that of stiff plastics (PAMS:  $\nu=0.32$ ; PPMS:  $\nu=0.33$ ; PMMA:  $\nu=0.36$ ) rather than that of the natural rubber,

which appears softer ( $\nu=0.5$ ) [142], [145]. Indeed, in the rubbers, the bulk modulus ( $E$ ) is much higher than the shear modulus ( $G$ ) and for this reason the Poisson's ratio has this value; this indicates that the rubbers are perfectly incompressible isotropic materials which deformed elastically at small strains [146].

Comparing the stress-strain curves obtained for the chosen specimens and that of the tendon and ligament, they appear very similar in shape. However, the tendon curve is steeper than the ligament one, as shown in fig. 89. Therefore, the tendon could be better mimicked by specimens which present an almost linear curve, that is with a higher Pearson's coefficient. On the other hand, the ligament shows a gentler curve; therefore, it could be better replaced by a material characterized by a lower Pearson's coefficient.

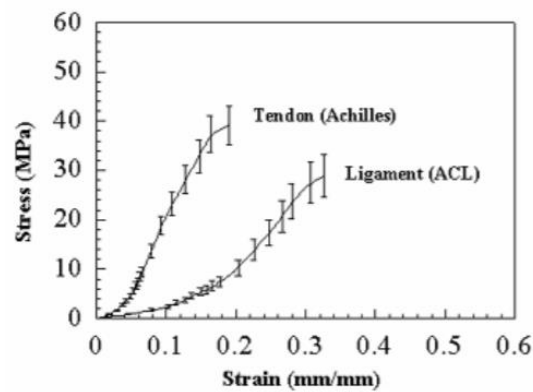


Figure 89. Tendon vs ligament stress strain curves.

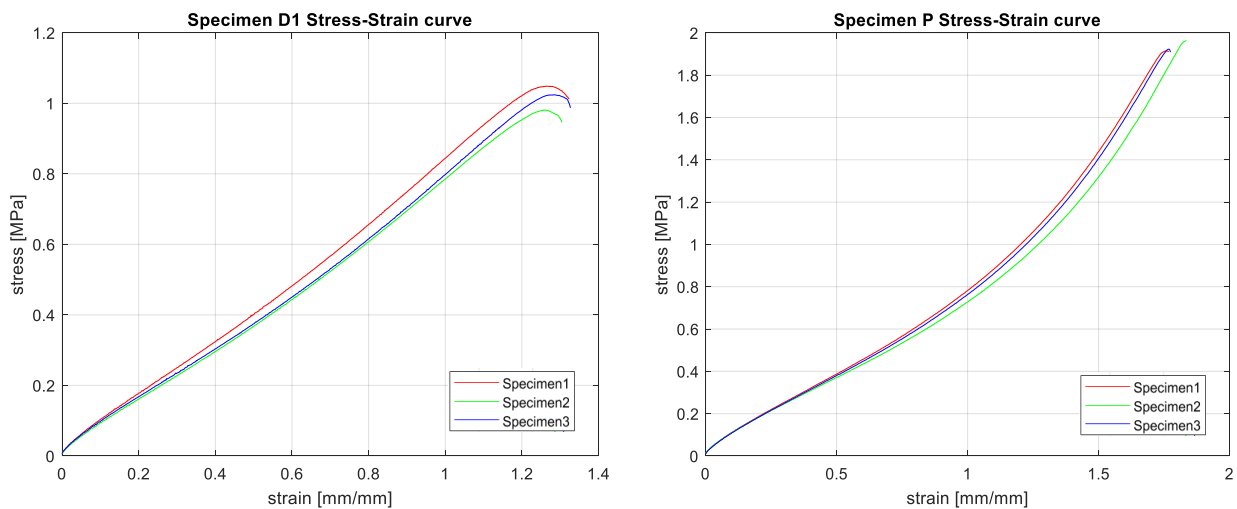
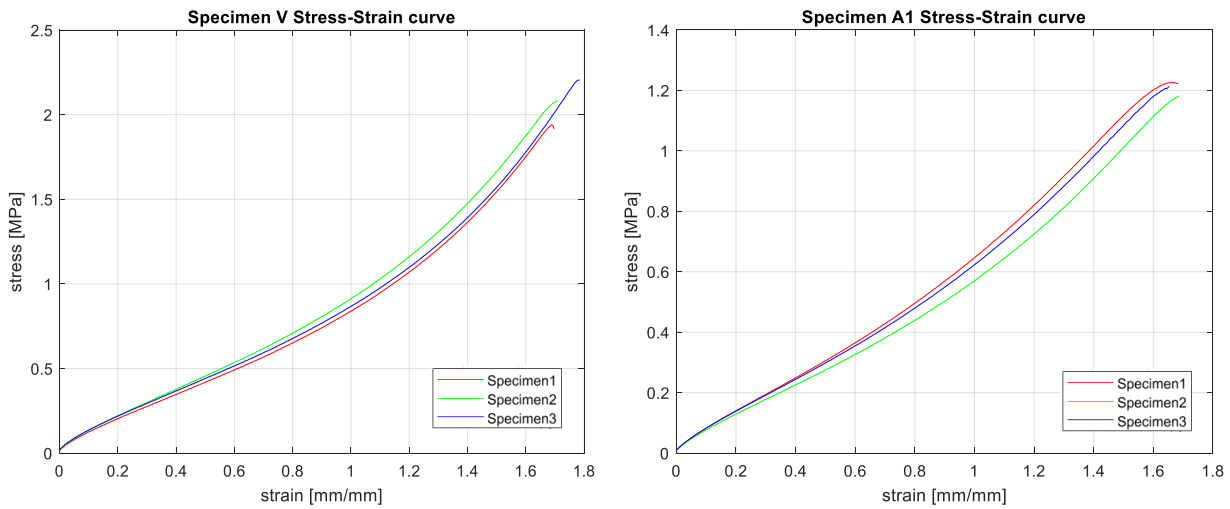


Figure 90. Stress-strain curves with the highest (specimen D1: 0.997) and the lowest Pearson's coefficient (specimen P: 0.956).

In fig. 90 the specimens with the highest and the lowest Pearson's coefficient are represented. The specimen P could well replicate the qualitative tensile behavior of the ligament, since the shape of the curves are very similar, except for the toe region, which is missing in our specimens' curve. Among the picked specimens, V is the one which most resembles the specimen P's behavior; therefore, it could be chosen to simulate the ligament in the final 3D multi-material model. The specimen D1 has a curve too straight to represent the tendon behavior. However, the chosen

specimens showed a curve less linear than this one, such as the specimen A1, which could well mimic the tendon's behavior, being very resistant and deformable too.



**Figure 91.** Stress-strain curve of the specimens V (Pearson's coefficient: 0.963) and A1 (Pearson's coefficient: 0.979), which could resemble the ligament and tendon mechanical behavior.

Considering the tendon in pathological conditions suffers a worsening of the mechanical properties (Fig. 92), having a lower Young's modulus and a higher strain at break [91]–[93], it is necessary to choose a specimen with a less steep and longer stress-stain curve. Compared to the specimen A1, among the same pattern category, specimen C1 (Fig. 93A) could simulate a tendinopathic tendon, since it has a lower elastic modulus (1.43 vs 1.73) and a higher strain at break (1.85 vs 1.71) (Fig. 93B).

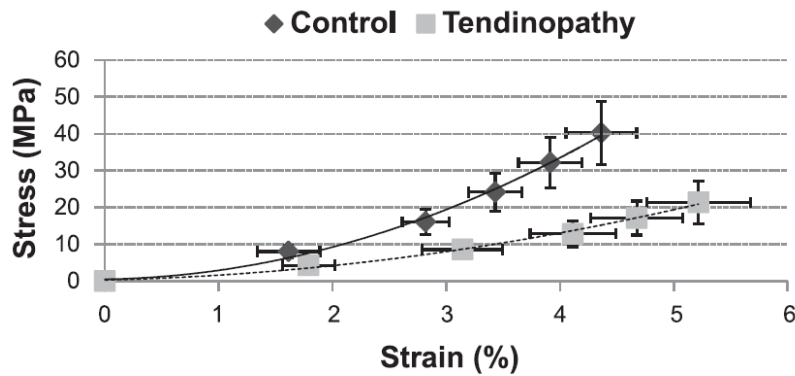


**Figure 92.** stress-strain curves of physiological (Control) and pathological (Tendinopathy) Achilles tendons [92].

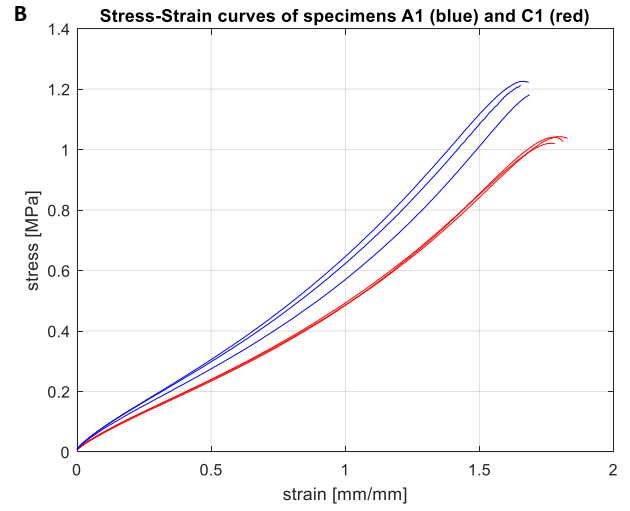
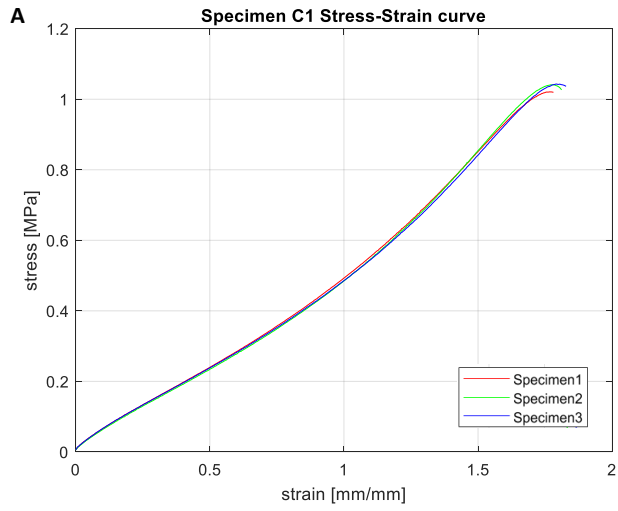


**Figure 93.** A) stress-strain curves of the specimens C1 and B) comparison between the stress-strain curves of the specimens A1 and C1.

## 6. Design and testing simulation of the new patterns

### 6.1 YS and JF: new bioinspired pattern

The obtained mechanical results revealed that the specimen V, belonged to the variation B of the pattern TM, showed the best mechanical performances. This category was characterized by random fibers within the matrix with a fibers' percentage of 60% (and hence 40% of matrix) of the CSA. Particularly, in this specimen the fibers were made of a hard material (Agilus A70) within a slightly softer matrix (Agilus A60). Based on these observations, it was decided to design two patterns with the same fiber/matrix ratio, to examine how the shape of the fibers might affect the mechanical behavior of the specimens. The two patterns were first hand-drawn and then designed in Rhino 3D, in which the design drawings were adapted to have a fibers' amount of about 60% within the CSA, so that the results obtained when analyzing these new specimens were comparable to those previously tested.

The first pattern, Jute Fiber (JF), has been designed taking a cue from the microstructure of the jute fiber (fig. 94), specifically the arrangement of the cells within the lignin matrix. In this way, an extremely variable pattern was obtained: the fibers are arranged randomly within the CSA of the specimen and have variable dimensions. This pattern recalls the TM pattern, whose fibers, nevertheless, were not characterized by variable sizes, that is an additional factor in this pattern. It was thought that adding another random factor might further enhance the pattern's mechanical behavior. The matrix contains 13 fibers, each different from the other (Fig. 95).

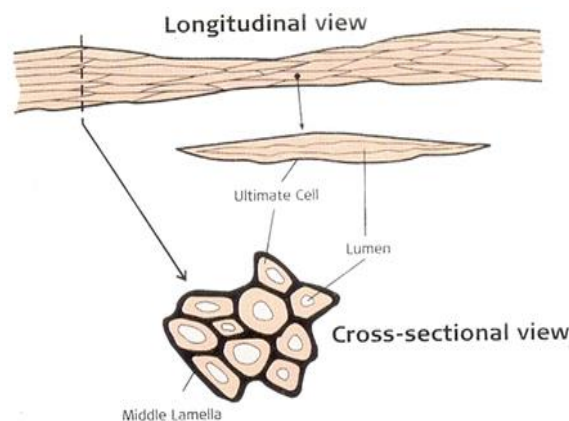


**Figure 94.** Microstructure of the CSA of jute fiber [147].

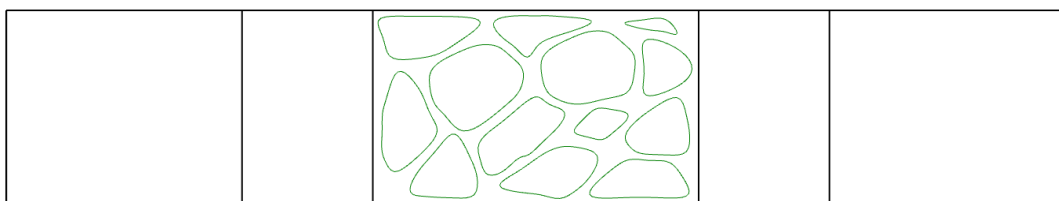


**Figure 95.** Designed JF pattern in Rhino 3D.

The second pattern, Y-shaped (YS), is taken from the particular structure of the nylon fibers, which has, precisely, a CSA shaped like the letter Y (Fig. 96). These fibers appear stretch and elastic, with a

modulus of elasticity higher than the steel. Each fiber in the designed pattern has the shape of two letter Y merged together forming a single structure, to obtain a stronger specimen. In the CSA there are overall five identical fibers, placed alternately with each other: three straight and two rotated by 180 degrees (Fig. 97).

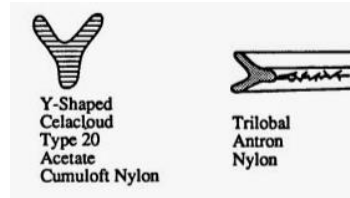


Figure 96. Y-shaped nylon fibers [148].

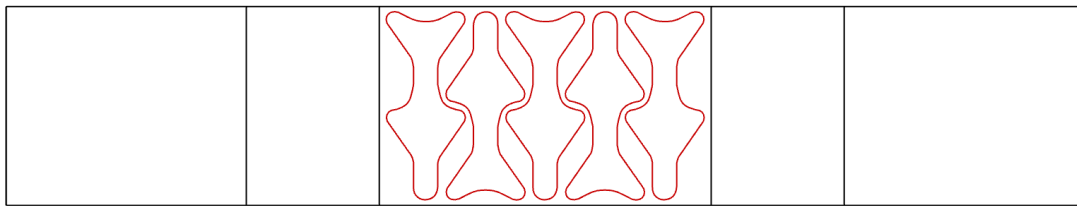


Figure 97. Designed YS pattern in Rhino 3D.

## 6.2 Finite element (FEM) mechanical simulation

### 6.2.1 Model setup

The patterns so designed were exported from Rhino 3D and imported in ANSYS to carry out a finite elements simulation (FEM) and evaluate their mechanical performances. To avoid the overload of the computer and reduce computation time, whenever possible, the symmetry of the specimens was exploited, to have as few elements as possible in the mesh. The YS pattern was split in two halves, symmetrically to the longitudinal axis. Then, one of this part was split in two again, this time about a transverse plane, placed in the middle of the specimen (Fig. 98), obtaining other two halves. Regarding the other pattern (JF), since its CSA was not symmetric as that of the previous one, it was split only once with a transverse plane in the middle (Fig. 99).

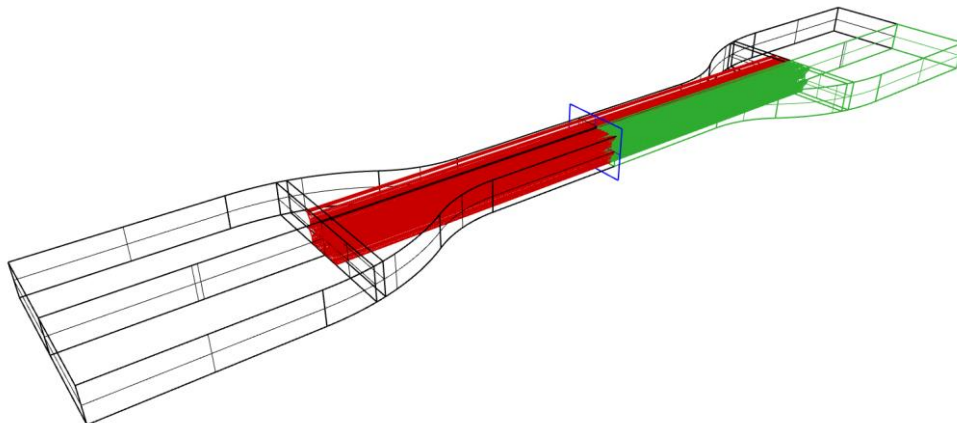
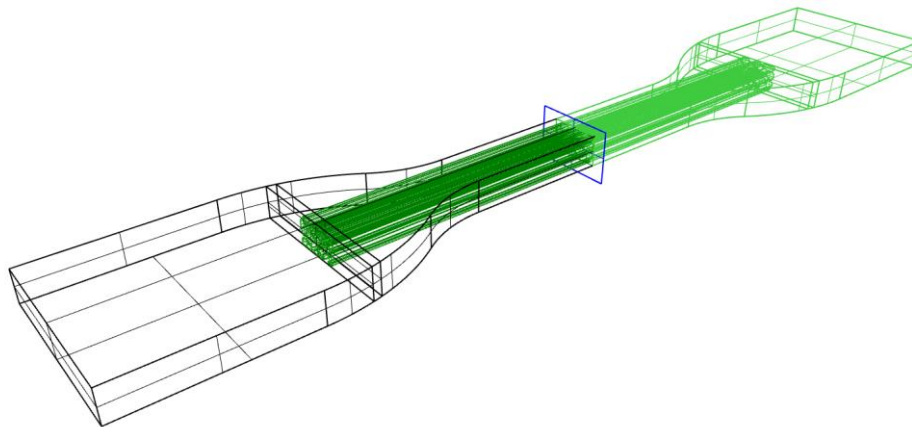


Figure 98. Splitting in four parts of the specimen with YS pattern: in red the pattern, in green the exported part, and in blue the transverse plane.



**Figure 99.** Splitting in two parts of the specimen with JF pattern: in dark green the pattern, in light green the exported part, and in blue the transverse plane.

The features of the digital materials (Tab. 15 and 16) were imported in the Engineering Data of ANSYS and assigned to the respective parts of the specimen. The specimen is made of three components, which are all composed of Agilus30, but the matrix has a Shore A60 and the fibers a Shore A70. To the distal part was assigned the Agilus30 with Shore A60, like the matrix. However, this part is no longer to be taken into consideration during the analysis results since it is considered non deformable. In fact, the pattern is present only in the central part of the specimen, as shown in fig. 98 and 99. Mechanical properties of Agilus30 Shore A60.

**Table 15.** Mechanical properties of Agilus30 Shore A60.

Agilus30 A60		
Property	Value	Unit
Density	1.15	g/cm <sup>3</sup>
Young's modulus	1.44	MPa
Poisson's ratio	0.30	-
Bulk modulus	1.20	MPa
Shear modulus	0.55	MPa
Tensile Yield Strength	1.60	MPa

**Table 16.** Mechanical properties of Agilus30 with Shore A70.

Agilus30 A70		
Property	Value	Unit
Density	1.15	g/cm <sup>3</sup>
Young's modulus	2.20	MPa
Poisson's ratio	0.33	-
Bulk modulus	2.16	MPa
Shear modulus	0.83	MPa
Tensile Yield Strength	2.28	MPa

Later, the setting of the two meshes. In the following figures 100 and 101, taken from Rhino 3D, the main dimensions, and especially the most critical, of the YS and JF patterns' components were highlighted and labeled, in order to consciously choose the size of the mesh to be set for the mechanical analysis. For both the specimens, it was decided to set a mesh of cells with tetrahedral geometry. The quality of the mesh plays a significant role in the accuracy and stability of the numerical computation. There are several factors involved in the mesh quality, but we considered only the skewness (Fig. 103), the element quality (Fig. 104) and the aspect ratio (Fig. 105). The skewness is defined as the difference between the shape of an element and the shape of an equilateral element with the same volume. The maximum skewness for a tetrahedral mesh should

be kept below 0.95, with an average value of less than 0.33. The element quality indicates the regularity of the mesh elements' shape. It is a dimensionless quantity between 0 and 1, where 1 represents a perfectly regular element. The aspect ratio measures the stretching of a cell and is the ratio of its two main dimensions (max/min). Generally, it is best to avoid aspect ratios above 5 [149], [150].

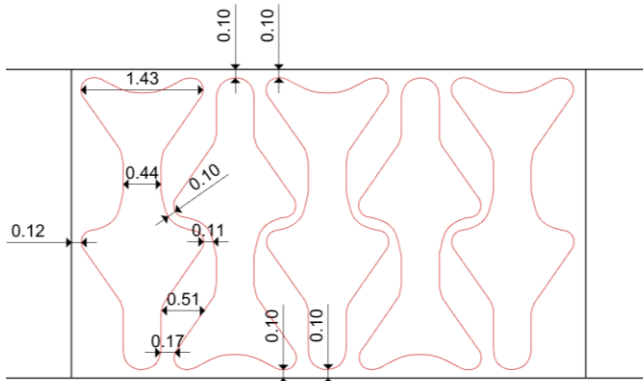


**Figure 100.** Most relevant dimensions (in mm) of the YS pattern.

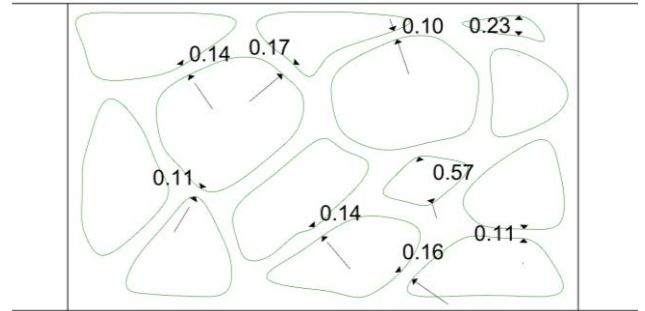


**Figure 101.** Most relevant dimensions (in mm) of the JF pattern.

### 5.5.1.1 YS pattern's mesh

Since the minimum distance between the fibers of the YS pattern is 0.10 mm, it was decided to mesh the matrix with elements 0.08 mm thick. Despite the big volume occupied by the matrix, it was not possible to choose a less dense mesh and then reduce the computation time, because of the closeness of the elements within the CSA of the specimen, in which distorted elements would be inevitably generated. The dimension of the fibers' mesh elements was set at 0.10 mm, because these are structures full of curvatures. Finally, the distal part of the specimen, which is simply a big parallelepiped of Agilus30, was meshed with elements of 1.30 mm (Fig. 102).

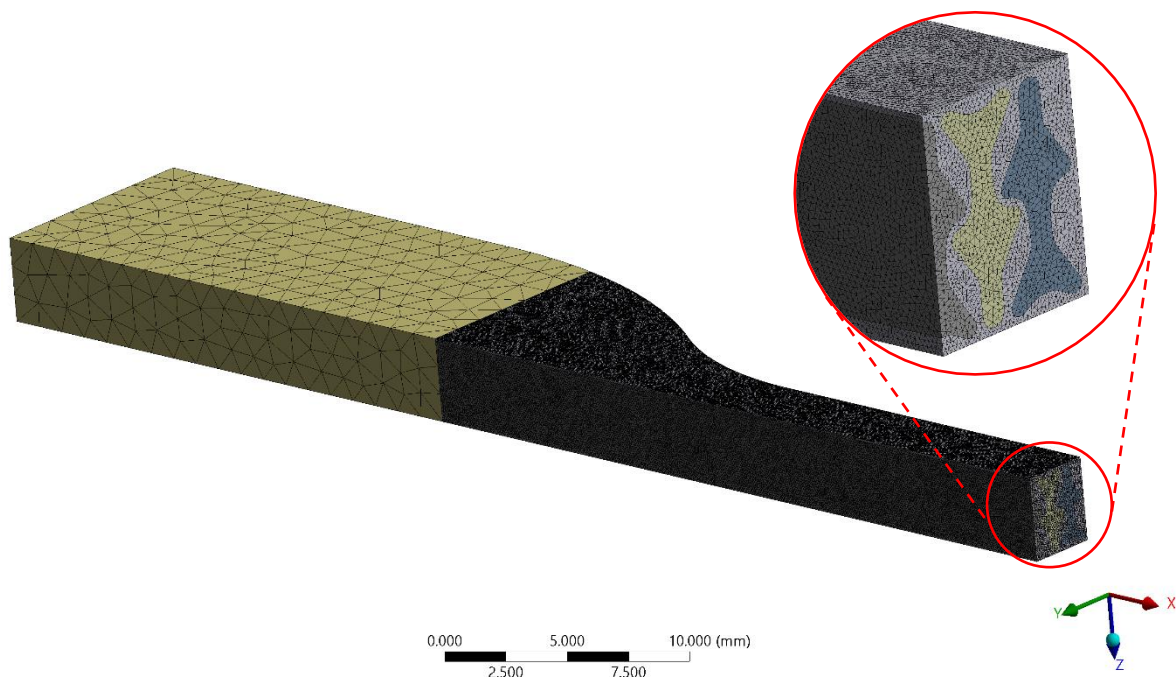


**Figure 102.** Mesh of the YS pattern with a zoom of the CSA. Please notice the different sizes of the elements in the extremity and those in the other components.

As shown in fig. 103, the YS pattern’s mesh has a skewness of about 0.21, on a weighted average, with a concentration of elements at 0.13 and 0.25. Regarding the element quality (Fig. 104), the mean value is about 0.85 with a peak at 0.88, thus the elements are almost perfectly regular. Looking the chart of the aspect ratio (Fig. 105), a high peak at about 1.80 appears and the other columns are very small. Globally, this can be considered a really good mesh.

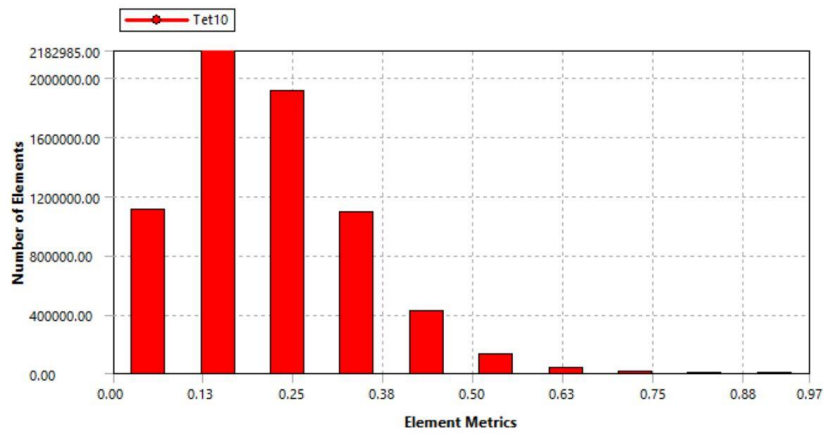


Figure 103. Skewness of the YS pattern’s mesh.

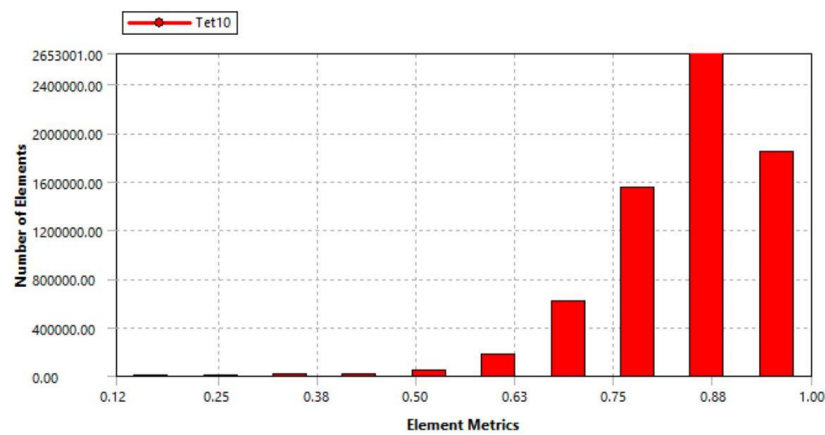


Figure 104. Element quality of the YS pattern’s mesh.

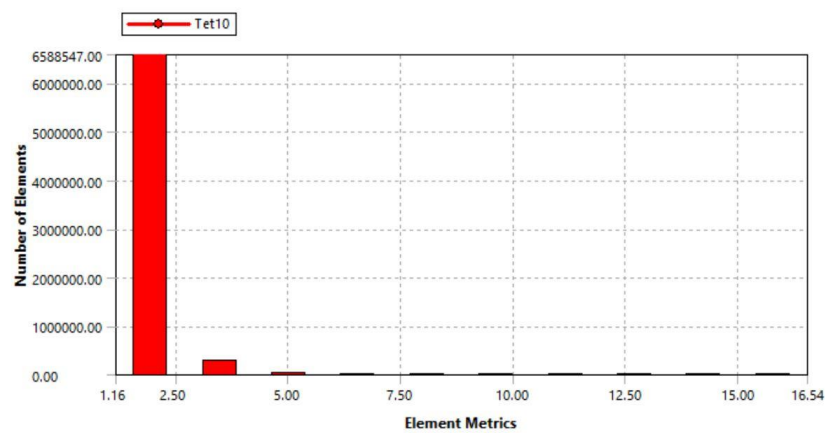
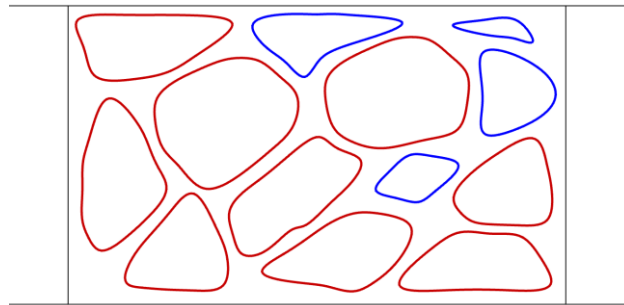


Figure 105. Aspect ratio of the YS pattern’s mesh.

### 5.5.1.2 JF pattern’s mesh

The fibers of this pattern are differently spaced; however, the minimum distance appears to be 0.10 mm, as for the YS pattern. Therefore, the matrix of the specimen was meshed with cells of 0.10 mm.

The fibers of the JF pattern have a high variability in dimensions, thus it was necessary to choose different mesh elements' sizes. The fibers were divided into two groups, the smallest ones (blue) and the others (red), as shown in fig. 106. The blue fibers were meshed with elements of 0.10 mm, like the matrix, and the red ones with elements of 0.20 mm. Also in this case, the distal part of the specimen did not need a mesh too finely, thus it was meshed with elements of 1.00 mm, as shown in fig. 107.



**Figure 106.** Groups of fibers for different meshing.

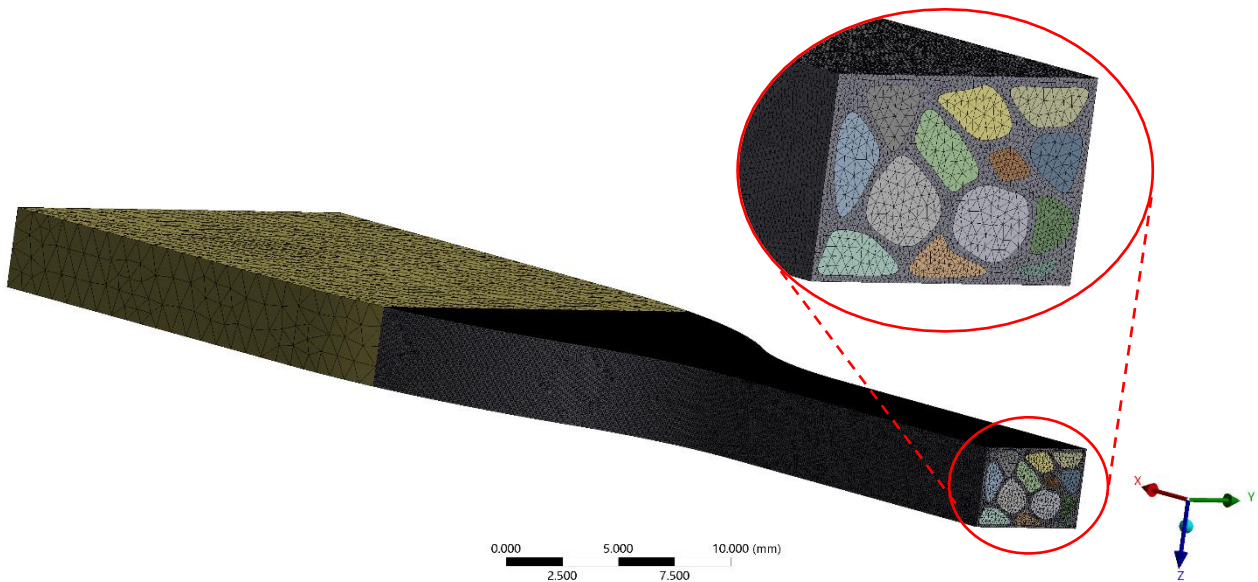


**Figure 107.** Mesh of the JF pattern with a zoom of the CSA. Please notice the different sizes of the elements in the extremity and those in the other components.

In the evaluation of the mesh quality, it appears very similar to that of the previous pattern. The average value of the skewness is about 0.19, with a concentration of elements at 0.13 and 0.25. The element quality is shifted to right and has a mean value of 0.87 with a peak at 0.88. Finally, the aspect ratio shows only one peak, at about 3, and the other columns are negligible; this indicates that all the cells are stretched in the same way. Comparing the two aspect ratio charts, the YS pattern has a peak more shifted to the left than the JF pattern; this indicates that the first pattern has cells more tetrahedral than the other one. No big difference was detected instead between the element quality and the skewness of the two meshes.

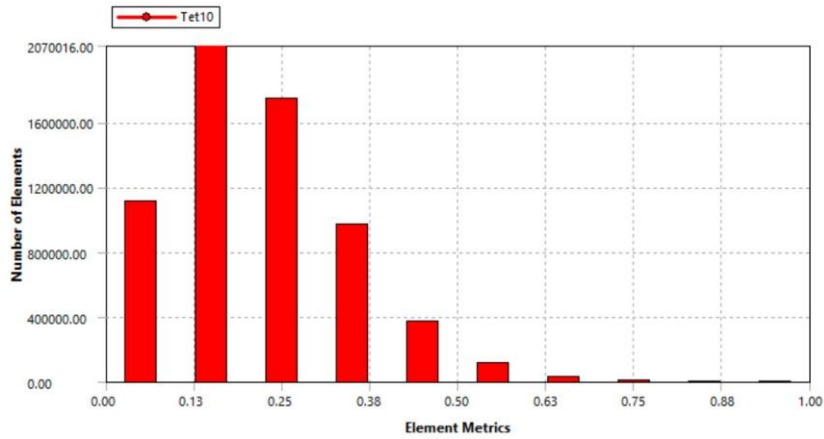


Figure 108. Skewness of the JF pattern's mesh.

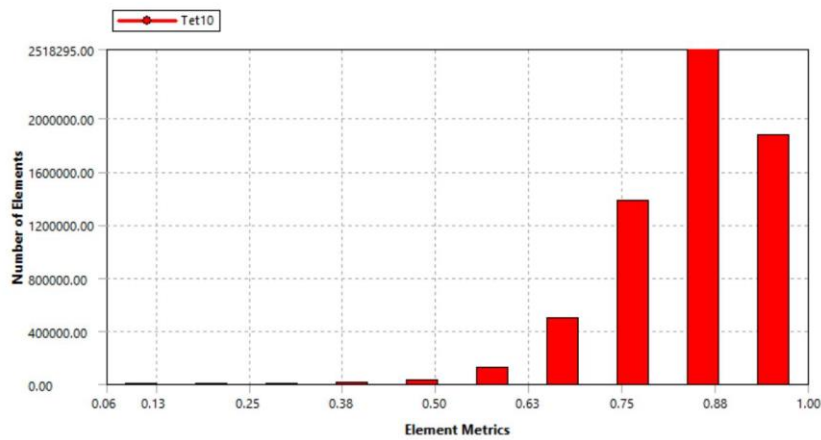


Figure 109. Element quality of the JF pattern's mesh.

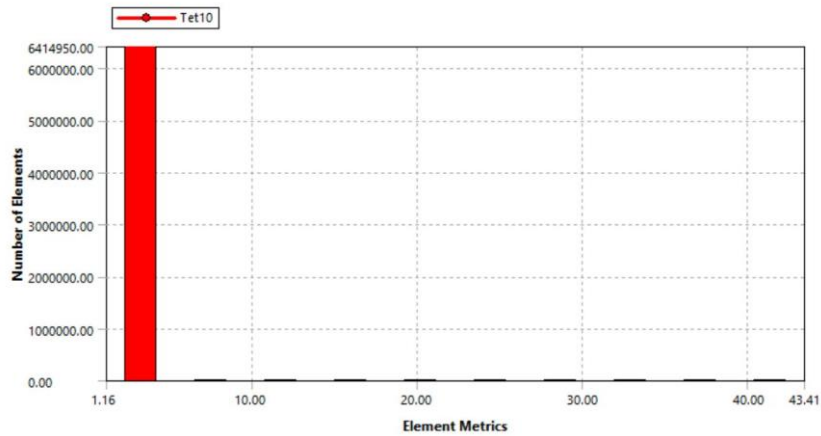


Figure 110. Aspect ratio of the JF pattern's mesh.

## 6.2.2 Analysis settings

To simulate the movement of the testing machine, one end of the specimen needs to keep still along X-axis, the direction of displacement, and the other end must be pulled at a constant rate only along that direction. Therefore, a null movement along X-axis was set at the right end, but the specimens were free to move in the YZ-plan, meaning they can contract. For the YS pattern, to have a tensile strength, the displacement was set unidirectional along X-axis with a negative value, since the positive values of the X-axis were in the opposite direction. For the JF pattern, it was set positive

instead, because the specimen lengthens along the positive values of the X-axis. The specimen must undergo a total displacement of about 50 mm, but, since we have half of its original length, a displacement of about 25 mm was set. This value was chosen because the specimens are made of Agilus A60 and Agilus A70; these base materials (U1 and V1) underwent, respectively, a maximum elongation of 56.91 and 46.46 mm. Thus, 50 mm is the approximate average value of displacement. This movement should not be instantaneous, to avoid the failure of the specimen, but in the form of a ramp of 25/30 steps, setting the first step at 0.83 mm and the last one at 29 mm for YS pattern and 27 mm for JF pattern. In fact, 0.83 mm/s, that is 25 mm/min, was the speed of the testing machine used to test the previous specimens.

### 6.2.3 Results

For every pattern three different parameters were analyzed, the equivalent stress, the directional deformation along X-axis, and the directional deformation along Y-axis.

#### 5.5.2.1 YS pattern simulation results

The stress field of the YS pattern shows how the fibers withstand a higher load than the matrix (Fig. 111). Moreover, there is no stress concentration at the junction between fibers and matrix. This means that the specimen responds very well, and this geometry has a reinforcing function throughout the structure, by not burdening the loads on the matrix, which is less resistant being made of a softer material. By hiding the fibers and adjusting the scale, the maximum value of stress reached by the matrix is about 1.01 MPa (Fig. 112). The region most subjected to load is the middle of the specimen, as we desired, because its breaking point should always be in the constant section. The blue halo existing at the connecting region between the distal part and the rest of the specimen reinforces the choice to place the pattern only in the CSA of the specimen, since some distortions could have happened in this area. Furthermore, a discontinuity can be found at the junction between the matrix and the distal part, maybe due to the fibers which reinforce the matrix. The fibers reached a value of stress of 1.50 MPa, very higher than the matrix (Fig. 113).

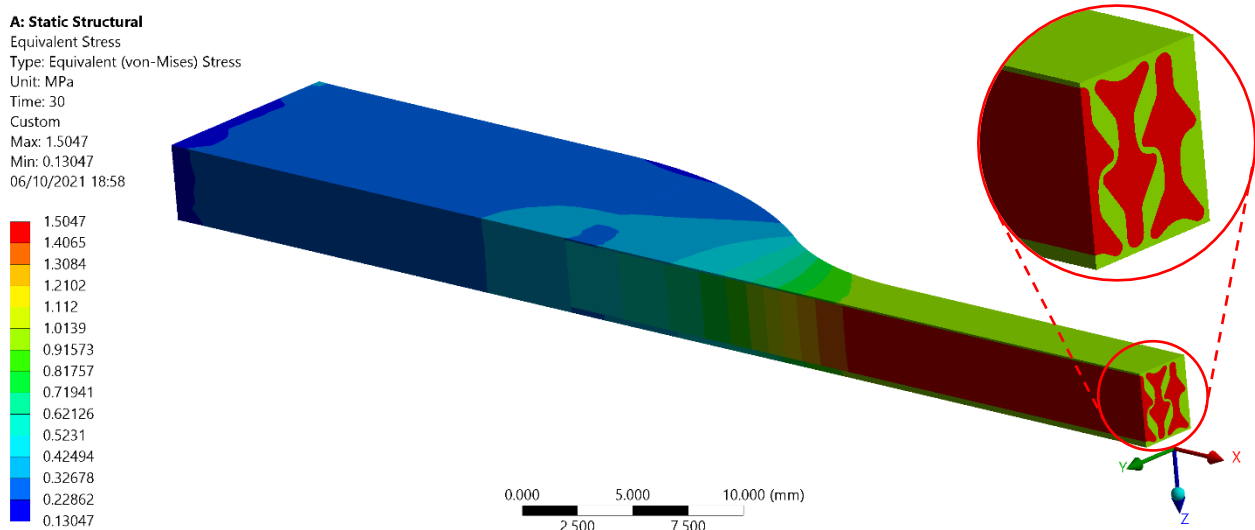


**Figure 111.** Equivalent stress of the specimen YS: the fibers withstand a higher load (red) than the matrix (green).

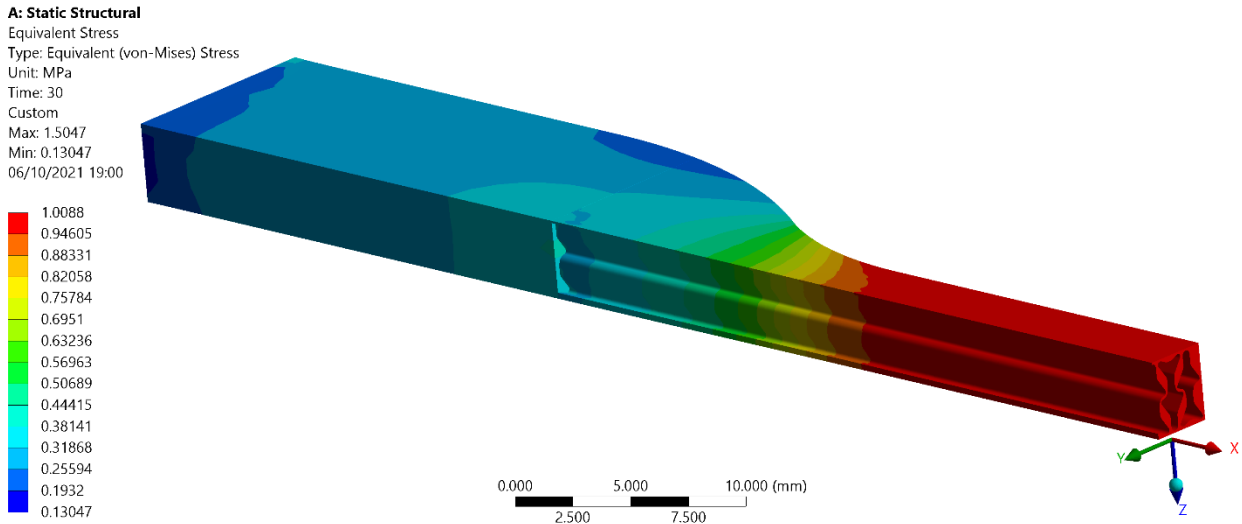


**Figure 112.** Equivalent stress of the specimen YS with a focus on the matrix, hiding the fibers. Please note that the maximum load withstood by the matrix is about 1 MPa.

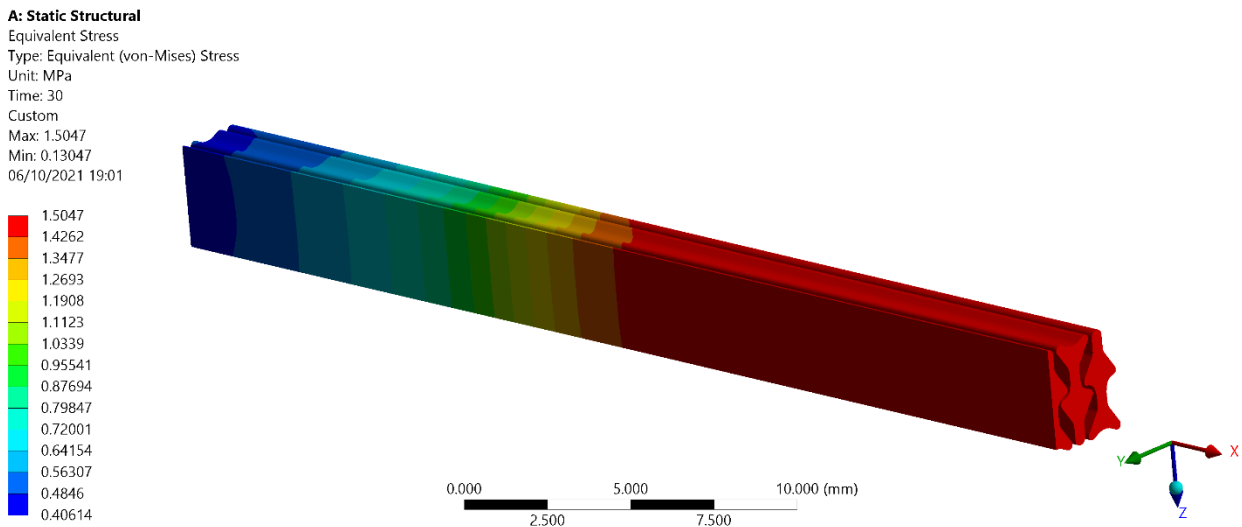


**Figure 113.** Equivalent stress of the specimen YS with a focus on the fibers, hiding the matrix and the distal part. Please note that the maximum load withstood by the fibers is about 1.5 MPa, higher than the matrix.

As regard the displacement, at the end of the simulation, the specimen appears longer and narrower, as shown in the colorimetric maps in fig. 114 and 115. The deformation along the Y-axis indicates how was the reduction of the CSA of the specimen. On the plane of symmetry XZ there is almost zero displacement, while at the outer side the specimen underwent a high displacement. The maximum movement was detected at the curvature of the specimen, which suffered high deformations (0.65 mm). The elongation of the specimen is represented by the deformation along the X-axis, which has a minimum value (-29.16 mm) – the maximum one since the displacement has negative values – in correspondence of the pulling end of the specimen, that is the distal part; indeed, the other end could not move during the test. There seem to be no discontinuities in this colorimetric map.

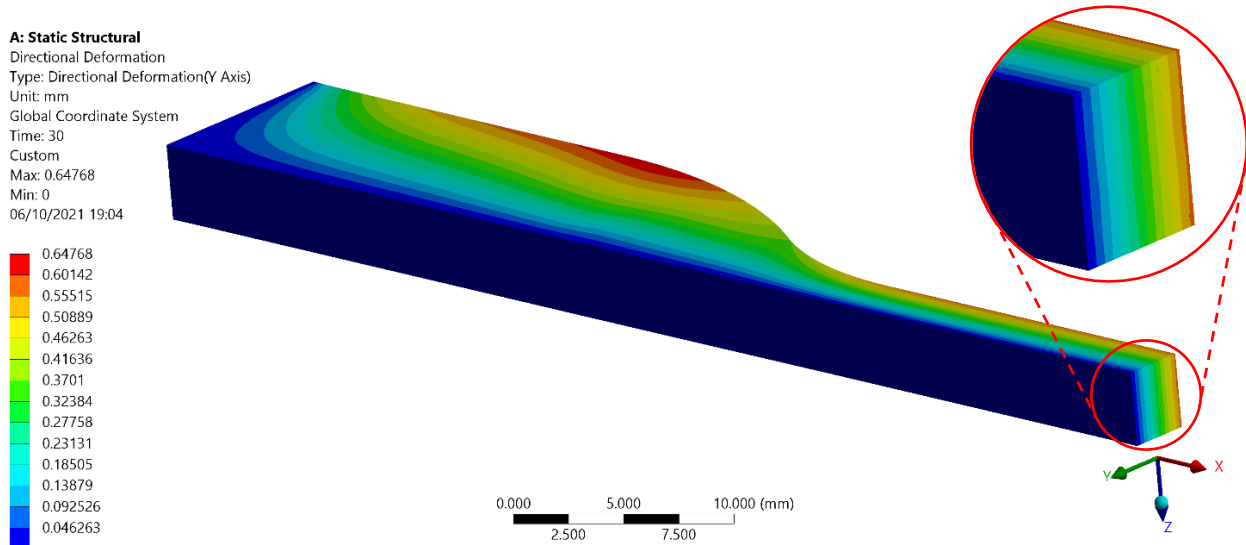


**Figure 114.** Deformation of the specimen YS along the Y-axis. Please note the almost zero displacement in the middle of the specimen (symmetry plan) and a higher value of deformation at outer side.

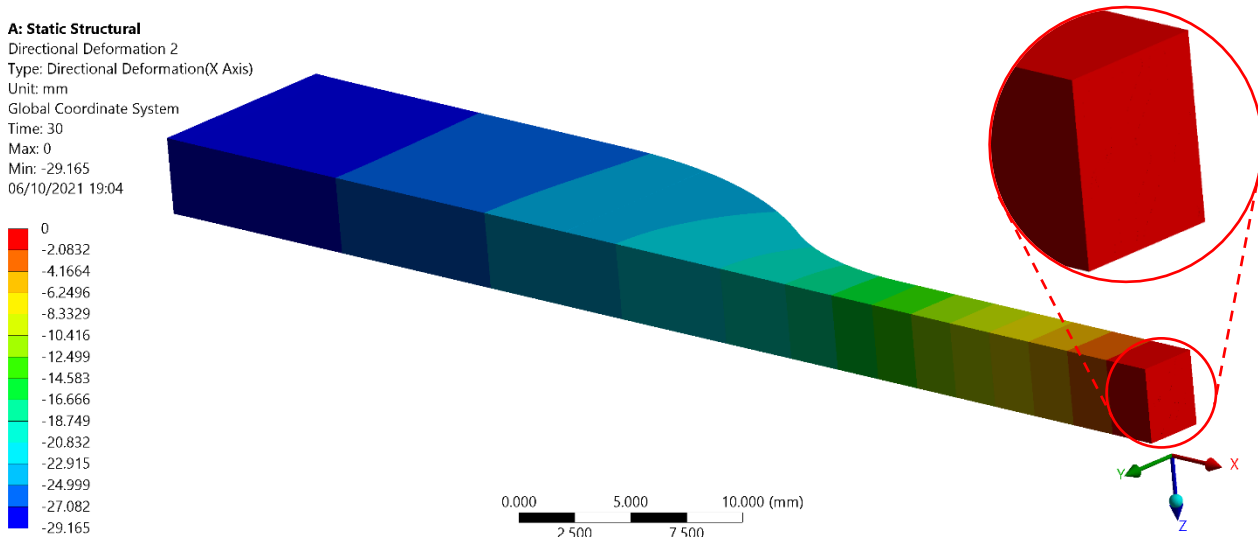


**Figure 115.** Deformation of the specimen YS along the X-axis. Please note the almost zero displacement in the middle of the specimen (symmetry plan), which is bound, and a high negative value at the distal part, subjected to the maximum displacement, since it was pulled.

### 5.5.2.2 JF pattern simulation results

As before, even for the JF pattern, the fibers withstand a higher load than the matrix (Fig. 116). Indeed, the maximum value of stress reached by the matrix is about 0.88 MPa (Fig. 117), while that reached by the fibers is 1.30 MPa (Fig. 118). Unlike the other specimen, this presents uneven surfaces. In particular, in the region where the geometry gets a lot narrower, peaks of stress were detected, as shown in fig. 118, where the maximum stress is labeled in correspondence of the thinnest extremity of the smallest fiber. Moreover, by hiding the fibers, an orange halo can be seen at the curvature of the specimen (Fig. 117), at the beginning of the constant region. This stress concentration probably would cause the rupture of the specimen exactly in that point, what we do not want to happen. Indeed, the specimen should break in its middle or at least in the constant region. As before, a discontinuity can be found at the junction between the matrix and the distal part (Fig. 116), even if less visible than for the previous specimen since this is not split in two.

**B: Static Structural**

Equivalent Stress  
Type: Equivalent (von-Mises) Stress  
Unit: MPa  
Time: 28  
Custom  
Max: 1.8293  
Min: 0.126  
11/10/2021 18:24

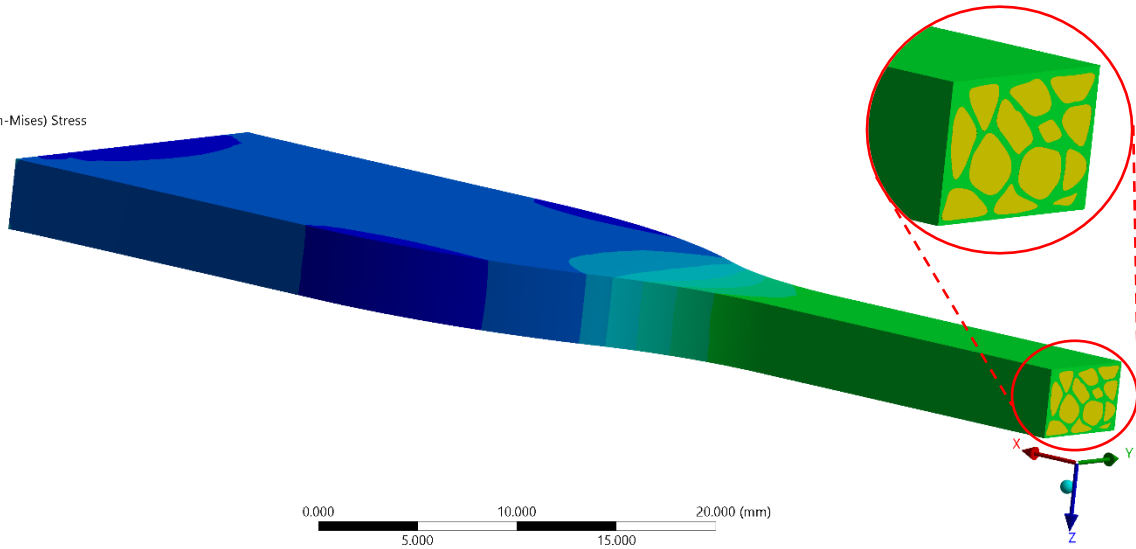
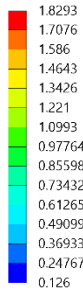


**Figure 116.** Equivalent stress of the specimen JF: the fibers withstand a slightly higher load (yellow) than the matrix (green).

**B: Static Structural**

Equivalent Stress  
Type: Equivalent (von-Mises) Stress  
Unit: MPa  
Time: 28  
Custom  
Max: 1.8293  
Min: 0.126  
11/10/2021 18:27

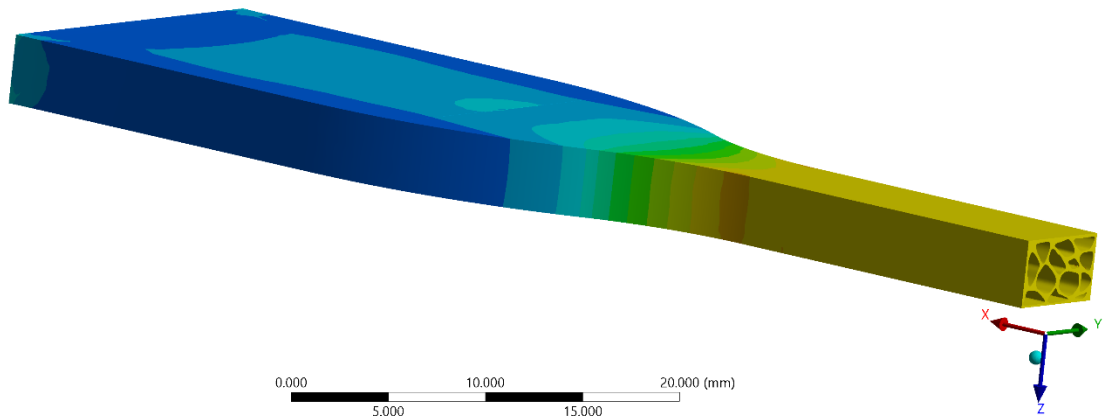
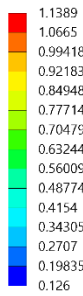


**Figure 117.** Equivalent stress of the specimen JF with a focus on the matrix, hiding the fibers. Please note the peak at the curvature and that the maximum load withstood by the matrix is about 0.88 MPa.

**B: Static Structural**

Equivalent Stress  
Type: Equivalent (von-Mises) Stress  
Unit: MPa  
Time: 28  
Custom  
Max: 1.8293  
Min: 0.126  
11/10/2021 18:25

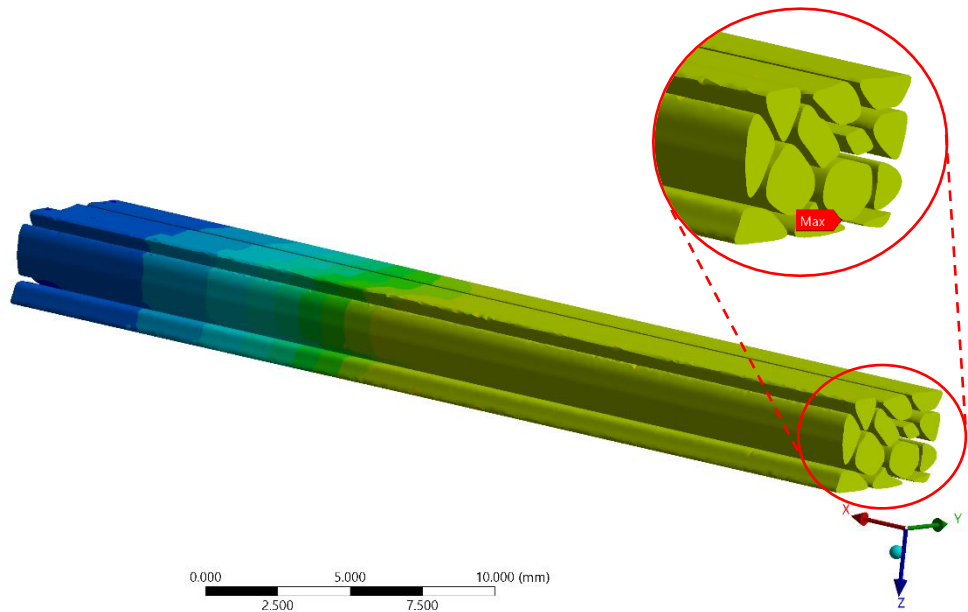
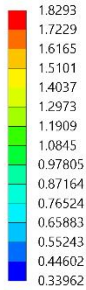


**Figure 118.** Equivalent stress of the specimen JF with a focus on the fibers, hiding the matrix and the distal part. Please note that the maximum load withstood by the fibers is about 1.30 MPa, higher than the matrix. The maximum stress value (1.83 MPa) is labeled in the zoom of the figure.

Regarding the deformation, as expected, the specimen narrowed in the YZ plan (Fig. 119) and got longer along the X-axis (Fig. 120). The specimen shows a narrowing of the CSA. Also in this case, the maximum displacement was detected at the curvature of the specimen, which suffered high deformations (0.63 mm). There seem to be no discontinuities in this colorimetric map of the CSA, thus the fibers deform in synch with the matrix. The elongation of the specimen is represented by the deformation along the X-axis, which has a maximum value (27.08 mm) in correspondence of the pulling end of the specimen, that is the distal part, which is the only one end being able to move during the test.

**B: Static Structural**

Directional Deformation 2  
Type: Directional Deformation(Y Axis)  
Unit: mm  
Global Coordinate System  
Time: 28  
Max: 0.63263  
Min: -0.62811  
11/10/2021 18:22

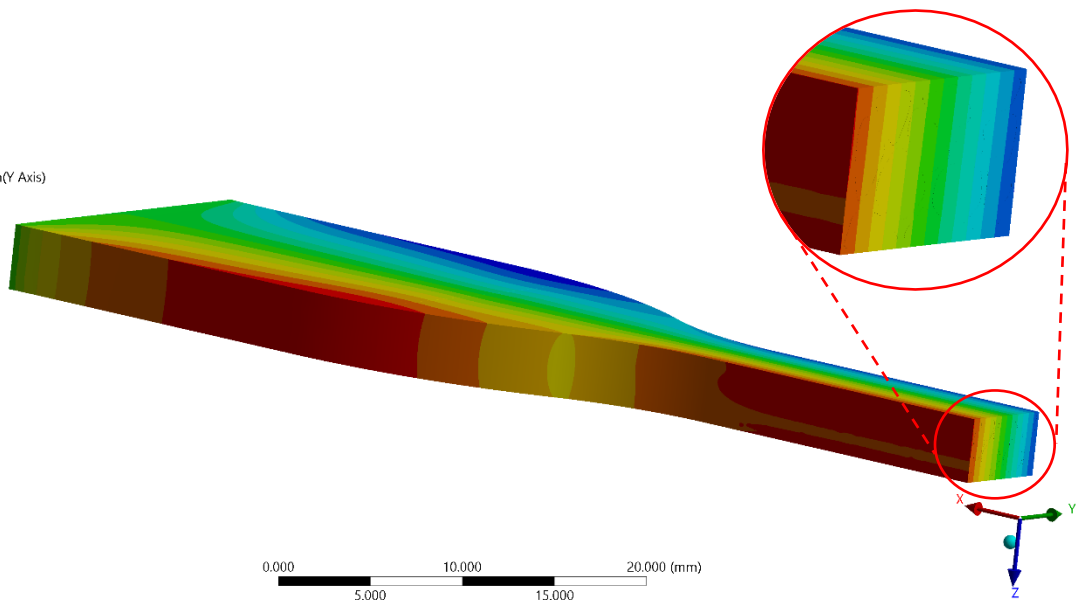
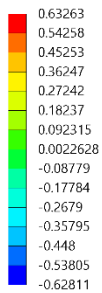


**Figure 119.** Deformation of the specimen JF along the Y-axis. The contraction is nearly symmetrical, looking the maximum and minimum values, and zero in the middle.

**B: Static Structural**  
 Directional Deformation  
 Type: Directional Deformation(X Axis)  
 Unit: mm  
 Global Coordinate System  
 Time: 28  
 Max: 27.082  
 Min: 0  
 11/10/2021 18:22

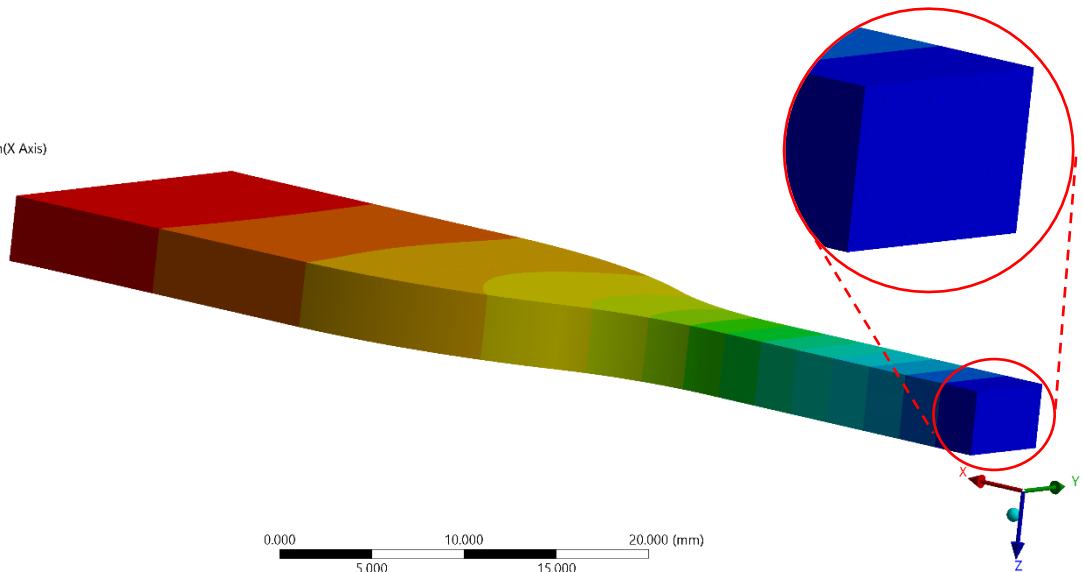
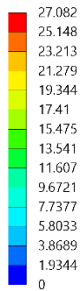


**Figure 120.** Deformation of the specimen JF along the X-axis. Please note the almost zero displacement in the middle of the specimen (symmetry plan), which is bound, and a high value at the distal part, subjected to the maximum displacement, since it was pulled.

## 6.3 YS and JF patterns vs specimen V

### 6.3.1 Testing machine stress vs equivalent stress

Comparing these designed patterns to the other specimens, we could not compute their modulus of elasticity, since we did not have a stress-strain curve as in the previous tests. However, the comparison was made between the maximum deformation and the highest value of stress undergone by the specimens. The base materials involved, which have Shore A60 and A70, reached, respectively, an elongation of 56.91 and 46.46 mm and a tensile strength at break of 1.59 and 2.28 MPa. For the YS pattern a maximum value of elongation of 29.16 mm was set; therefore, the whole specimen would elongate of 58.32 mm. The JF pattern, instead, reached an elongation of 27.08 mm, that corresponds to 54.16 mm for the entire specimen. The corresponding stress values were computed by dividing the maximum load reached by the specimen by its surface area (CSA), which is 21.60 mm, as stated by the ASTM D638-14 [77]. The specimen with JF pattern, at an elongation value of 54.16 mm, was subjected to 1.83 MPa of stress. Hence, at a slightly lower extension, this specimen withstands higher loads than Agilus A60. The specimen with YS pattern was instead subjected to a stress of 1.50 MPa at 58.32 mm of lengthening. The deformation value is a little higher than Agilus A60 and the stress withstood is a little lower.

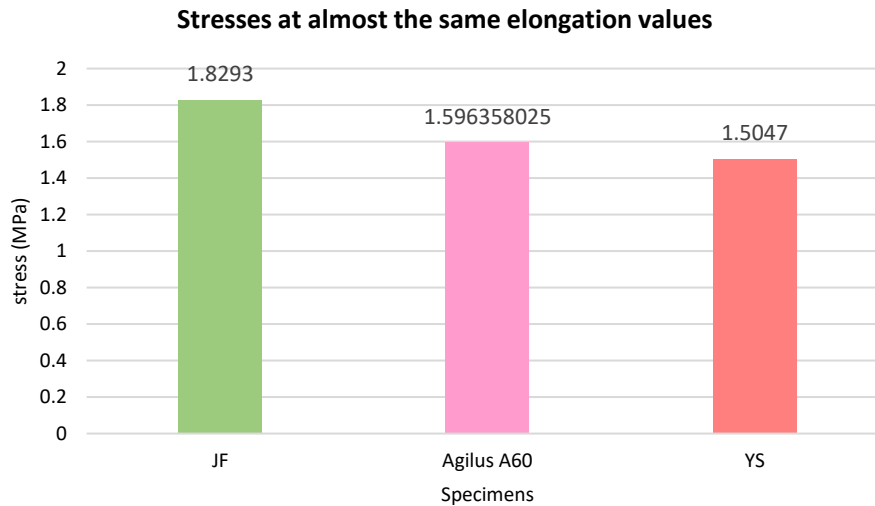


**Figure 121.** JF and YS pattern vs base material Agilus A60: stress values.

As shown in fig. 111 and 116, it is clear that the fibers withstand higher loads than the matrix in both the specimens, meaning the two designed patterns strengthen the entire structure. However, this occurred in the specimen V too, having a pattern which improved the mechanical performances at a macroscopic level. The aim of this simulations, indeed, was to compare the new designed specimens to the specimen V, the one chosen from the previous physical tests. The first factor to be considered is the stress withstood by the specimens at the same elongation value. The specimen V broke at an average elongation value of 57.51 mm, reaching a tensile strength of 2.07 MPa. Hence, we compared the maximum stress values of the YS and JF pattern with the stress value reached by the specimen V at, respectively, 58 and 54 mm of elongation. As said before, the average elongation value of the specimen V is 57.51 mm, lower than 58.32 mm, which is the elongation value reached by the YS pattern. However, one sample of the specimen V lengthened 59.30 mm; thus, the stress value corresponding to 58 mm of elongation was computed by considering only this one. This problem did not arise for the JF pattern; therefore, the computed stress value is a mean between the three samples of the specimen V.

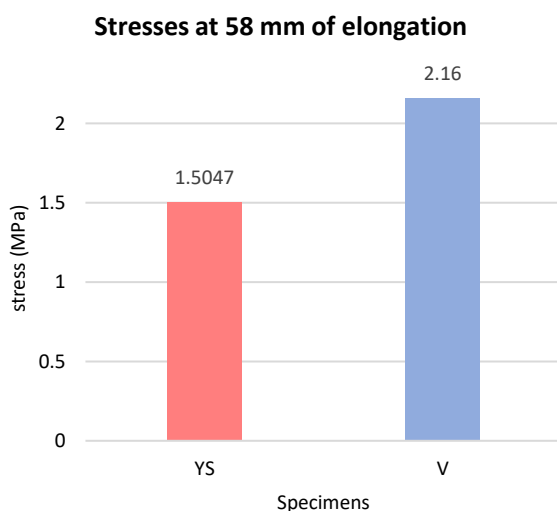


**Figure 122.** YS pattern vs specimen V: stress values.

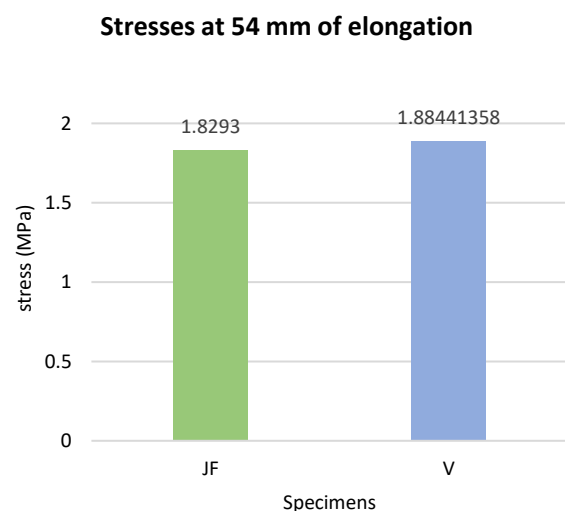


**Figure 123.** JF pattern vs specimen V: stress values.

As shown in fig. 122, at the same value of elongation, the pattern YS is subjected to a definitely lower stress without breaking. The JF pattern, instead, does not seem to improve enough the mechanical performances of the specimen V. Indeed, the stress values reached are almost the same (Fig. 123), only a slight decrease was detected.

### 6.3.2 Deformation along Y-axis vs extensometer E2

Another factor considered in this analysis was the narrowing of the CSA. In fact, a specimen which suffers from a too much decreased surface area, at comparable values of deformation, is less robust and breaks up earlier. Looking the chart in fig. 124, the base material of Agilus A60 decreases its thickness more than the other two specimens, which result more resistant. This happens although the three specimens reached similar values of elongation, which are, respectively, 54.16, 56.91, and 58.32 mm.

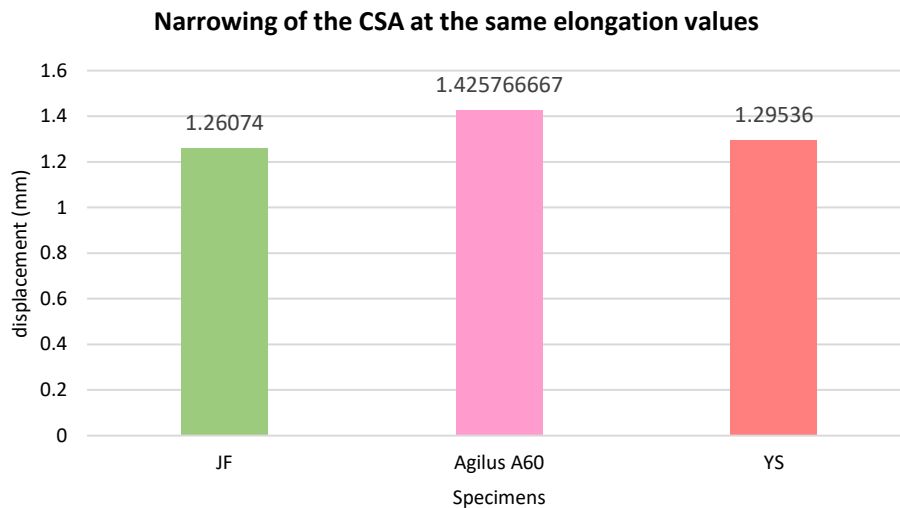


**Figure 124.** Comparison between the narrowing of the two patterns and the base material Agilus A60.

Comparing the new patterns to the specimen V and considering the maximum values of elongation, the narrowing of the three specimens is very similar, as shown in fig. 125, even if the values of elongation are slightly different. In fact, we considered 54.16 mm of elongation for the JF pattern and 58.32 mm for the YS pattern. Regarding the specimen V, since this value has been acquired by using DIC, towards the breaking the extensometer is no longer able to perform measurements; therefore, it was considered only the narrowing value corresponding to the sample which reached the highest elongation value, that was 52.07 mm. Having a lower deformation elongation, the specimen V appears a little more thinned than the others, which have higher values of elongation.

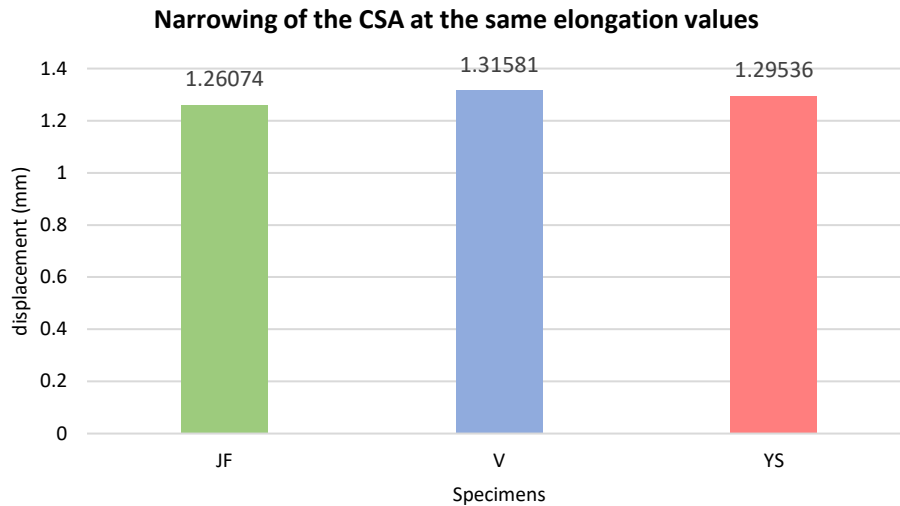


*Figure 125. Comparison between the narrowing of the three different specimens.*

## 6.4 Final considerations about the two new patterns

This chapter focused on the designing of new patterns which could enhance the mechanical properties of the TM pattern, the one picked from the previous mechanical tests. The TM pattern is based on the hierarchical structure of tendon bundles within a proteoglycan-rich matrix, since this was the material that we aimed to replicate. The JF pattern is based on the jute fiber's structure and is similar to the TM pattern, but adds another variability factor, that is the size of the fibers. Lastly, the YS pattern is designed to mimic the shape of the nylon fibers by coupling and enlarging them to fill the CSA. All these patterns have the same percentages of fibers and matrix, which are 60% and 40%; therefore, they could be compared. Considering the base materials of which they are composed, the JF and YS patterns improve the mechanical properties of the whole structures. Particularly, the specimen with JF pattern can withstand higher loads than the base materials, reaching high values of deformation. Therefore, the pattern JF seems to affect the mechanical behavior of the specimen, proving to be elastic but also stiff. Compared to the specimen V, at the same elongation value, the stress withstood is a little lower. This means that adding the randomness in size could bring only a small improvement, making the material slightly more elastic. However, the issue of the stress concentration at the curvature remains, as shown in fig. 117; this would probably provoke the rupture of the specimen there. Moreover, high stress values were detected also at the connecting points between the fibers and the matrix, which could cause the flaking of the specimen and, consequently, a premature failure.

The specimen with YS pattern is able to reach high values of deformation at low stress fields, compared to the specimen V, but also to the base materials. This means it is an extremely elastic material. Moreover, the fibers support the matrix, which is subjected to a stress of 1 MPa only (Fig. 112). Finally, the specimen would probably break in the middle as we desire, because there are no discontinuities at the interface between the two components. It's weird having all this elasticity in a specimen composed of Agilus A60 and Agilus A70, which are quite hard materials. It could be due to the shape of the fibers, which occupy much of the CSA vertically, allowing the specimen to

uniformly deform and reach an elongation value above the average of the specimens made of the same base materials. This specimen is perfect to mimic very flexible materials; however, since the tendon and ligament are also a bit stiff, this pattern could give too much elasticity to the specimen and make it not enough strong.

As regards the narrowing of the CSA, it can be stated that the fibers reinforce the entire structure in general, as shown in the fig. 124 and 125. Indeed, the three specimens with a pattern, even if different, showed almost the same narrowing values at similar values of elongation. Instead, the base material with Agilus A60, although it reached almost the same elongation value, was subjected to a definitely higher narrowing of the CSA.

In conclusion, as expected, both the patterns affect the macroscopic properties of the specimen and showed some improvements compared to the base materials and to the TM pattern too. However, the JF pattern appeared almost comparable to the specimen V; therefore, there are no significant differences to state that there is a real enhancement. Regarding the YS pattern, it reached a high deformation at a lower stress value than the specimen V, meaning this pattern makes the entire structure more deformable, although it is made of the same base materials (Agilus A60 and A70). Overall, these are mathematical models, and they are always an approximation of reality. Therefore, the YS pattern deserves to be 3D printed and evaluated with DIC and tensile testing to carry out a more realistic comparison.

## 7. Conclusions and future developments

The aim of this project was to find the best combination of materials to simulate the mechanical behavior of tendons and ligaments. Four different bioinspired patterns were mechanically tested, in different configurations, to identify the most performant geometry and materials. Basing on the obtained results, to enhance the mechanical properties of the specimens at a macroscopic level, the pattern should be characterized by hard fibers (A70) in a slightly softer matrix (A60), with a greater amount of fibers than matrix. Particularly, the best pattern, which was the Tendon Mimic (TM), had random fibers, which occupied 60% of CSA, within the matrix. Keeping the same materials and the same fiber/matrix ratio, two other patterns were designed and submitted to mechanical simulations, to evaluate the enhancement of the mechanical properties, compared to the best pattern. The YS pattern responded very well, showing a homogeneous stress distribution and no discontinuities at the interface between fibers and matrix. The results from the specimen JF showed, instead, that adding another variability factor, i.e. the size of the fibers, does not improve considerably the mechanical properties of the specimen. Moreover, this increases the possibility of having peaks of stress. However, these mechanical simulations confirmed that the fibers reinforce the entire structure in general, making the specimen more resistant to failure. Therefore, two different specimens were picked to simulate, respectively, the tendon and the ligament. Since the ligament shows a gentle stress-strain curve, it could be better represented by the specimen V, which is the specimen with the lowest Pearson's coefficient among the best four. The tendon, instead, has a far steeper curve, thus the most suitable specimen was that with the highest Pearson's coefficient among the specimens chosen for every pattern, which is A1. To simulate the pathological conditions of the tendon, a specimen with worsened mechanical properties, compared to the specimen A1 and belonging to the same pattern category, was chosen, i.e. the specimen C1. Since creating specimens with a pattern seems to be the right way, the picked specimens could be 3D printed in the correct shape and inserted in a multi-material model to simulate the tendon and the ligament. Alternatively, the search of a better pattern could be carried out, by 3D printing the YS pattern, to physically characterize it using DIC and tensile testing machine. In fact, the real materials available for the 3D printer are not linear as in the mechanical simulation. Therefore, this pattern could give different results compared to that obtained using ANSYS. Moreover, in measuring the deformation of the specimens, the values obtained by DIC and by tensile testing machine, following the ASTM D638, appeared very different. Actually, the Standard overestimates the real value of strain since it considers the deformation of the distal part negligible. As shown by DIC, this part underwent a high deformation too; therefore, the DIC should be the first-choice method to evaluate the deformation of the specimens, giving more accurate results and allowing the measurement in different regions of the surface.

## Figures summary

<b>Figure 1.</b> Hierarchical structure of collagen fibers in tendon [4].....	2
<b>Figure 2.</b> Three main components of wool fiber [10].....	3
<b>Figure 3.</b> Hierarchical structure of a wool fiber [10]. ....	3
<b>Figure 4.</b> The five levels of the hierarchical structure of spider silk [11]. ....	4
<b>Figure 5.</b> Hierarchical arrangement of a bamboo fiber with its polylamellate structure [16].....	5
<b>Figure 6.</b> Jute fiber hierarchical structure [19]. ....	6
<b>Figure 7.</b> Hierarchical structure of flax fiber, showing the different arrangement of the microfibrils in the sub-layers ( $\theta=10^\circ$ ), with a zoom on the composition of a bundle of microfibrils (mesofibril). 6	6
<b>Figure 8.</b> Hemp fiber hierarchical structure [25]. ....	7
<b>Figure 9.</b> Condensation polymerization to form Nylon fibers [29].....	8
<b>Figure 10.</b> Binder jetting system [42].....	10
<b>Figure 11.</b> Example of directed energy deposition [43]. ....	10
<b>Figure 12.</b> FDM: an example of materials extrusion technology [31]. ....	10
<b>Figure 13.</b> Polyjet modeling process [44]. ....	10
<b>Figure 14.</b> SLS: an example of powder bed fusion technology [31]. ....	10
<b>Figure 15.</b> Schematic of LOM: a sheet lamination method [31].....	10
<b>Figure 16.</b> SLA vs DLP: two examples of vat polymerization technology [44].....	11
<b>Figure 17.</b> Stress-strain curves of Agilus30 and other elastomeric materials at room temperature [67]. ....	13
<b>Figure 18.</b> Identification of the testing machine components. ....	18
<b>Figure 19.</b> Dimensions and technical specifications of MTS Insight 2. ....	19
<b>Figure 20.</b> Load-elongation curve of a tendon/ligament [87]. ....	21
<b>Figure 21.</b> Stress-strain curve of a tendon/ligament [89]. ....	21
<b>Figure 22.</b> ACL and Achilles' tendon stress-strain behavior. Note how tendon's curve appears steeper than ACL's one. ....	22
<b>Figure 23.</b> stress-strain curves of physiological (Control) and pathological (Tendinopathy) Achilles tendons [92]. ....	22
<b>Figure 24.</b> Different steps of DIC technique [101]. ....	24
<b>Figure 25.</b> Typical speckle patterns [99]. ....	26
<b>Figure 26.</b> (a) 2D and (b) 3D DIC calibration [101]; (c) calibration plate or grid [103]. ....	27
<b>Figure 27.</b> Computation of the residuals to determine the calibration quality [111].....	28
<b>Figure 28.</b> Perspective projection model or pinhole model [99].....	28
<b>Figure 29.</b> The transformation from the world coordinates to the sensor coordinates [99]. ....	29
<b>Figure 30.</b> The basic principle of the 3D-DIC technique [115].....	30
<b>Figure 31.</b> Matching and triangulation of a set of images acquired before and after deformation [115]. ....	30
<b>Figure 32.</b> Block diagram of B-spline interpolation [117].....	31
<b>Figure 33.</b> The surface of the specimen with the illustration of the correlation algorithm parameters [102]. ....	32

<b>Figure 34.</b> Diagram of the Iterative Least Square method (ILS) [116].	33
<b>Figure 35.</b> Representation of the first problem of subset-based method: points near the boundary [116].	34
<b>Figure 36.</b> (a) VIC-EDU system top and front view; (b) VIC-EDU system datasheet [119].	34
<b>Figure 37.</b> Fixing of the baseplate to the tripod head [105].	36
<b>Figure 38.</b> Commands to rotate images and set exposure time [105].	36
<b>Figure 39.</b> Example of overexposed image (noticeable red spots) [105].	37
<b>Figure 40.</b> Aoi tools [105].	38
<b>Figure 41.</b> Plotting tools to set axis and contour limits [105].	41
<b>Figure 42.</b> Extraction tools command windows to visualize different lines and modify the line's variable [105].	41
<b>Figure 43.</b> Stress-strain curves of connective tissues and Hydrotane [124].	43
<b>Figure 44.</b> The engineering stress-strain curves of NBR elastomers with different slope, that is the elastic modulus [126].	44
<b>Figure 45.</b> Stress-strain curves of vinyl methyl silicone rubber (VMQ) enriched with different percentages of MWCNTs [127].	44
<b>Figure 46.</b> Hierarchical structure of the tendon with the substructures involved in the TL pattern underlined in red [128].	45
<b>Figure 47.</b> Different views of the tendon-like (TL) pattern: top view and CSA.	45
<b>Figure 48.</b> A) Deep equine tendon CSA and B) segmented fiber bundles.	46
<b>Figure 49.</b> Different views of the three variations of tendon-mimic (TM) pattern: top view and CSA.	47
<b>Figure 50.</b> Detailed structure of the three variations of the TM pattern.	47
<b>Figure 51.</b> Different views of the three variations of bamboo-like (BL) pattern: top view and CSA.	48
<b>Figure 52.</b> Different views of the three variations of helix bamboo-like (HB) pattern: top view and CSA.	49
<b>Figure 53.</b> Different arrangements of the microfibrils inside the concentric layers: double helices in red (outer layer) and blue (middle layer) and linear fibril in green (inner layer).	49
<b>Figure 54.</b> ASTM 638-14 Type IV specimen, dimensions in millimeters.	53
<b>Figure 55.</b> Length of the constant region of the specimen and build orientation.	53
<b>Figure 56.</b> Experimental setup: UTS testing machine and DIC system.	54
<b>Figure 57.</b> Creation of the black speckle pattern on the specimens using a toothbrush.	56
<b>Figure 58.</b> Specimens U1 covered with black pattern: a) without the background and b) with the background.	56
<b>Figure 59.</b> Physical setup of the VIC EDU system.	57
<b>Figure 60.</b> Regulation of the brightness of a specimen using VIC-Snap.	57
<b>Figure 61.</b> a) carrying out the calibration process; b) calibration plate or grid.	58
<b>Figure 62.</b> Modulus of elasticity of the 44 specimens, according to the four patterns (TL, TM, BL, HB).	60
<b>Figure 63.</b> Tensile strength at break of the 44 specimens, according to the four patterns (TL, TM, BL, HB).	60
<b>Figure 64.</b> Strain at break of the 44 specimens, according to the four patterns (TL, TM, BL, HB).	61

<b>Figure 65.</b> Comparison between the mechanical parameters (elastic modulus, tensile strength at break and elongation at break) of the specimens U1, A1 and J1. ....	63
<b>Figure 66.</b> Comparison between the mechanical properties of the best specimens and the base materials. ....	63
<b>Figure 67.</b> Flow chart of the mechanical data processing. ....	64
<b>Figure 68.</b> Stress-strain curves of the picked specimens.....	65
<b>Figure 69.</b> Area of interest printed on the specimen's surface and start point placed at the bottom of it. ....	67
<b>Figure 70.</b> Deformation parameters (exx, eyy, Von Mises strain) of the specimen C. Please notice the position and orientation of E0, E1, and E2 (superimposed to the strain field in the images). ....	68
<b>Figure 71.</b> Deformation parameters (exx, eyy, Von Mises strain) of the specimen V.....	69
<b>Figure 72.</b> Deformation parameters (exx, eyy, Von Mises strain) of the specimen A1. ....	70
<b>Figure 73.</b> Deformation parameters (exx, eyy, Von Mises strain) of the specimen J1.....	71
<b>Figure 74.</b> First image (before starting the tensile test) of the three samples of specimen U, as acquired by the DIC system. ....	72
<b>Figure 75.</b> First image (before starting the tensile test) of the three samples of specimen W, as acquired by the DIC system. ....	72
<b>Figure 76.</b> Comparison between stains measured with different methods. ....	73
<b>Figure 77.</b> A) Strains of the different parts of the specimen, measured with DIC system; B) Strains of the constant region of the specimen measured with the testing machine and the DIC system. ....	74
<b>Figure 78.</b> Day 1 vs day 31: decrease of the tensile strength at break of the specimens.....	93
<b>Figure 79.</b> Day 1 vs day 31: decrease of the strain at break of the specimens. ....	93
<b>Figure 80.</b> Day 1 vs day 31: increase of the elastic modulus of the specimens. ....	93
<b>Figure 81.</b> Day 1 vs day 31: tensile strength at break of the specimens. ....	106
<b>Figure 82.</b> Day 1 vs day 31: strain at break of the specimens. ....	107
<b>Figure 83.</b> Day 1 vs day 31: elastic modulus of the specimens. ....	107
<b>Figure 84.</b> Comparison between the percentage area of the two patterns' substructures. ....	108
<b>Figure 85.</b> Comparison between the mechanical properties of the TL and BL pattern specimens: tensile strength at break.....	109
<b>Figure 86.</b> Comparison between the mechanical properties of the TL and BL pattern specimens: strain at break. ....	109
<b>Figure 87.</b> Comparison between the mechanical properties of the TL and BL pattern specimens: elastic modulus. ....	110
<b>Figure 88.</b> Measured elastic modulus vs empirical elastic modulus of the base materials: trend of the values. ....	111
<b>Figure 89.</b> Tendon vs ligament stress strain curves.....	112
<b>Figure 90.</b> Stress-strain curves with the highest (specimen D1: 0.997) and the lowest Pearson's coefficient (specimen P: 0.956). ....	112
<b>Figure 91.</b> Stress-strain curve of the specimens V (Pearson's coefficient: 0.963) and A1 (Pearson's coefficient: 0.979), which could resemble the ligament and tendon mechanical behavior.....	113
<b>Figure 92.</b> stress-strain curves of physiological (Control) and pathological (Tendinopathy) Achilles tendons [92]. ....	113

<b>Figure 93.</b> A) stress-strain curves of the specimens C1 and B) comparison between the stress-strain curves of the specimens A1 and C1. ....	114
<b>Figure 94.</b> Microstructure of the CSA of jute fiber [147]. ....	115
<b>Figure 95.</b> Designed JF pattern in Rhino 3D. ....	115
<b>Figure 96.</b> Y-shaped nylon fibers [148]. ....	116
<b>Figure 97.</b> Designed YS pattern in Rhino 3D. ....	116
<b>Figure 98.</b> Splitting in four parts of the specimen with YS pattern: in red the pattern, in green the exported part, and in blue the transverse plane. ....	116
<b>Figure 99.</b> Splitting in two parts of the specimen with JF pattern: in dark green the pattern, in light green the exported part, and in blue the transverse plane. ....	117
<b>Figure 100.</b> Most relevant dimensions (in mm) of the YS pattern. ....	118
<b>Figure 101.</b> Most relevant dimensions (in mm) of the JF pattern. ....	118
<b>Figure 102.</b> Mesh of the YS pattern with a zoom of the CSA. Please notice the different sizes of the elements in the extremity and those in the other components. ....	118
<b>Figure 103.</b> Skewness of the YS pattern's mesh. ....	119
<b>Figure 104.</b> Element quality of the YS pattern's mesh. ....	119
<b>Figure 105.</b> Aspect ratio of the YS pattern's mesh. ....	119
<b>Figure 106.</b> Groups of fibers for different meshing. ....	120
<b>Figure 107.</b> Mesh of the JF pattern with a zoom of the CSA. Please notice the different sizes of the elements in the extremity and those in the other components. ....	120
<b>Figure 108.</b> Skewness of the JF pattern's mesh. ....	121
<b>Figure 109.</b> Element quality of the JF pattern's mesh. ....	121
<b>Figure 110.</b> Aspect ratio of the JF pattern's mesh. ....	121
<b>Figure 111.</b> Equivalent stress of the specimen YS: the fibers withstand a higher load (red) than the matrix (green). ....	122
<b>Figure 112.</b> Equivalent stress of the specimen YS with a focus on the matrix, hiding the fibers. Please note that the maximum load withstood by the matrix is about 1 MPa. ....	123
<b>Figure 113.</b> Equivalent stress of the specimen YS with a focus on the fibers, hiding the matrix and the distal part. Please note that the maximum load withstood by the fibers is about 1.5 MPa, higher than the matrix. ....	123
<b>Figure 114.</b> Deformation of the specimen YS along the Y-axis. Please note the almost zero displacement in the middle of the specimen (symmetry plan) and a higher value of deformation at outer side. ....	124
<b>Figure 115.</b> Deformation of the specimen YS along the X-axis. Please note the almost zero displacement in the middle of the specimen (symmetry plan), which is bound, and a high negative value at the distal part, subjected to the maximum displacement, since it was pulled. ....	124
<b>Figure 116.</b> Equivalent stress of the specimen JF: the fibers withstand a slightly higher load (yellow) than the matrix (green). ....	125
<b>Figure 117.</b> Equivalent stress of the specimen JF with a focus on the matrix, hiding the fibers. Please note the peak at the curvature and that the maximum load withstood by the matrix is about 0.88 MPa. ....	125

<b>Figure 118.</b> Equivalent stress of the specimen JF with a focus on the fibers, hiding the matrix and the distal part. Please note that the maximum load withstood by the fibers is about 1.30 MPa, higher than the matrix. The maximum stress value (1.83 MPa) is labeled in the zoom of the figure. ....	126
<b>Figure 119.</b> Deformation of the specimen JF along the Y-axis. The contraction is nearly symmetrical, looking the maximum and minimum values, and zero in the middle. ....	126
<b>Figure 120.</b> Deformation of the specimen JF along the X-axis. Please note the almost zero displacement in the middle of the specimen (symmetry plan), which is bound, and a high value at the distal part, subjected to the maximum displacement, since it was pulled. ....	127
<b>Figure 121.</b> JF and YS pattern vs base material Agilus A60: stress values.....	128
<b>Figure 122.</b> YS pattern vs specimen V: stress values. ....	128
<b>Figure 123.</b> JF pattern vs specimen V: stress values.....	128
<b>Figure 124.</b> Comparison between the narrowing of the two patterns and the base material Agilus A60. ....	129
<b>Figure 125.</b> Comparison between the narrowing of the three different specimens. ....	130

## Tables summary

<b>Table 1.</b> TL pattern’s design specifications: radius value and transversal area percentages in the CSA. ....	45
<b>Table 2.</b> Areas of segment fiber bundles and their mean value. Picked fiber bundles marked in yellow. ....	46
<b>Table 3.</b> BL pattern’s design specifications: radius value and transversal area percentages in the CSA. ....	48
<b>Table 4.</b> HB pattern’s design specifications: radius value and transversal area percentages in the CSA. ....	49
<b>Table 5.</b> Shore A hardness values of the specimens with TL pattern.....	50
<b>Table 6.</b> Shore A hardness values of the specimens with TM pattern. ....	50
<b>Table 7.</b> Shore A hardness values of the specimens with BL pattern.....	51
<b>Table 8.</b> Shore A hardness values of the specimens with HB pattern.....	52
<b>Table 9.</b> Shore A hardness values of base materials. ....	52
<b>Table 10.</b> Pearson’s coefficient and coefficient of variation (CV) for all the specimens. The yellow highlighted rows represent the best specimen of every pattern, while the green one represents the chosen specimen.....	66
<b>Table 11.</b> Poisson’s ratio for all the specimens. At the bottom, in yellow the best specimen of every pattern and in green the chosen specimen. ....	72
<b>Table 12.</b> Variation (%) of the mechanical parameters of the BL specimens.....	92
<b>Table 13.</b> Variation (%) of the mechanical parameters of the BL specimens.....	107
<b>Table 14.</b> Measured elastic modulus vs empirical elastic modulus of the base materials: values. ....	110
<b>Table 15.</b> Mechanical properties of Agilus30 Shore A60.....	117
<b>Table 16.</b> Mechanical properties of Agilus30 with Shore A70. ....	117

## References

- [1] *Structural Biological Materials - Design and Structure-Property Relationships*, vol. 4. Elsevier, 2000. doi: 10.1016/S1470-1804(00)X8001-7.
- [2] P. Fratzl and R. Weinkamer, 'Nature's hierarchical materials', *Progress in Materials Science*, vol. 52, no. 8, pp. 1263–1334, Nov. 2007, doi: 10.1016/j.pmatsci.2007.06.001.
- [3] E. Baer, A. Hiltner, and D. Jarus, 'Relationship of hierarchical structure to mechanical properties', *Macromol. Symp.*, vol. 147, no. 1, pp. 37–61, Dec. 1999, doi: 10.1002/masy.19991470106.
- [4] S. Y. Tang, 'Natural composites: The structure-function relationships of bone, cartilage, tendon/ligament, and the intervertebral disc', in *Biomedical Composites*, Elsevier, 2017, pp. 1–16. doi: 10.1016/B978-0-08-100752-5.00001-9.
- [5] C. B. Frank, 'Ligament structure, physiology and function', p. 3.
- [6] R. B. Martin, D. B. Burr, and N. A. Sharkey, 'Mechanical Properties of Ligament and Tendon', in *Skeletal Tissue Mechanics*, R. B. Martin, D. B. Burr, and N. A. Sharkey, Eds. New York, NY: Springer New York, 1998, pp. 309–348. doi: 10.1007/978-1-4757-2968-9\_8.
- [7] J. A. Weiss and J. C. Gardiner, 'Computational Modeling of Ligament Mechanics', p. 71.
- [8] J. Fan, 'Hierarchy of Wool Fibers and Fractal Dimensions', p. 4.
- [9] H. Zahn, J. Föhles, M. Nlenhaus, A. Schwan, and M. Spel, 'Wool as a Biological Composite Structure', *Ind. Eng. Chem. Prod. Res. Dev.*, vol. 19, no. 4, pp. 496–501, Dec. 1980, doi: 10.1021/i360076a005.
- [10] U. H. Erdogan, Y. Seki, and F. Selli, 'Wool fibres', in *Handbook of Natural Fibres*, Elsevier, 2020, pp. 257–278. doi: 10.1016/B978-0-12-818398-4.00011-6.
- [11] A. Tarakanova, D. Ebrahimi, Z. Qin, and M. J. Buehler, 'Silk-Based Hierarchical Materials for High Mechanical Performance at the Interface of Modeling, Synthesis, and Characterization', in *Handbook of Materials Modeling*, W. Andreoni and S. Yip, Eds. Cham: Springer International Publishing, 2018, pp. 1–28. doi: 10.1007/978-3-319-50257-1\_82-1.
- [12] W. Qiu, A. Patil, F. Hu, and X. Y. Liu, 'Hierarchical Structure of Silk Materials Versus Mechanical Performance and Mesoscopic Engineering Principles', *Small*, vol. 15, no. 51, p. 1903948, Dec. 2019, doi: 10.1002/smll.201903948.
- [13] L. Fan, J.-L. Li, Z. Cai, and X. Wang, 'Bioactive hierarchical silk fibers created by bioinspired self-assembly', *Nat Commun*, vol. 12, no. 1, p. 2375, Dec. 2021, doi: 10.1038/s41467-021-22673-4.
- [14] 'Natural fibers and their composites', in *Tribology of Natural Fiber Polymer Composites*, Elsevier, 2008, pp. 1–58. doi: 10.1533/9781845695057.1.
- [15] D. Liu, J. Song, D. P. Anderson, P. R. Chang, and Y. Hua, 'Bamboo fiber and its reinforced composites: structure and properties', p. 32, 2012.
- [16] N. Parameswaran and W. Liese, 'On the fine structure of bamboo fibres', p. 16.
- [17] N. Chand and M. Fahim, 'Jute-reinforced polymer composites', in *Tribology of Natural Fiber Polymer Composites*, Elsevier, 2021, pp. 111–130. doi: 10.1016/B978-0-12-818983-2.00004-9.
- [18] R. Mia, Md. A. Islam, B. Ahmed, and J. I. A. Mojumdar, 'Woolenization of Jute Fibre', *ESJ*, vol. 13, no. 30, p. 314, Oct. 2017, doi: 10.19044/esj.2017.v13n30p314.
- [19] 'Jute Fibre Properties and End Uses | Part 02', *Textile Study Center*, Mar. 10, 2018. <https://textilestudycenter.com/jute-fibre-properties-and-end-uses/> (accessed Sep. 09, 2021).

- [20] C. Baley, A. Le Duigou, A. Bourmaud, and P. Davies, 'Influence of drying on the mechanical behaviour of flax fibres and their unidirectional composites', *Composites Part A: Applied Science and Manufacturing*, vol. 43, no. 8, pp. 1226–1233, Aug. 2012, doi: 10.1016/j.compositesa.2012.03.005.
- [21] L. Yan, N. Chouw, and K. Jayaraman, 'Flax fibre and its composites – A review', *Composites Part B: Engineering*, vol. 56, pp. 296–317, Jan. 2014, doi: 10.1016/j.compositesb.2013.08.014.
- [22] J. P. Manaia, A. T. Manaia, and L. Rodrigues, 'Industrial Hemp Fibers: An Overview', *Fibers*, vol. 7, no. 12, p. 106, Dec. 2019, doi: 10.3390/fib7120106.
- [23] B. Wang, M. Sain, and K. Oksman, 'Study of Structural Morphology of Hemp Fiber from the Micro to the Nanoscale', *Appl Compos Mater*, vol. 14, no. 2, pp. 89–103, Aug. 2007, doi: 10.1007/s10443-006-9032-9.
- [24] D. Dai and M. Fan, 'Characteristic and Performance of Elementary Hemp Fibre', *MSA*, vol. 01, no. 06, pp. 336–342, 2010, doi: 10.4236/msa.2010.16049.
- [25] J. W. Kaczmar, J. Pach, and C. Burgstaller, 'The chemically treated hemp fibres to reinforce polymers', *Polimery*, vol. 56, no. 11/12, pp. 817–822, Nov. 2011, doi: 10.14314/polimery.2011.817.
- [26] A. R. Bunsell, 'High-performance Fibers', in *Encyclopedia of Materials: Science and Technology*, II., Elsevier, 2005, pp. 1–10.
- [27] V. Jaiganesh, S. Manivannan, and S. Manivannan, 'Optimization of Process Parameters on Friction Stir Welding of Nylon 6 Polymer Plate', p. 7, 2014.
- [28] B. S. Gupta, 'Manufacture, types and properties of biotextiles for medical applications', in *Biotextiles as Medical Implants*, Elsevier, 2013, pp. 3–47. doi: 10.1533/9780857095602.1.3.
- [29] R. A. Ortega, E. S. Carter, and A. E. Ortega, 'Nylon 6,6 Nonwoven Fabric Separates Oil Contaminates from Oil-in-Water Emulsions', *PLoS ONE*, vol. 11, no. 7, p. e0158493, Jul. 2016, doi: 10.1371/journal.pone.0158493.
- [30] S. Ezeiruaku, 'Review of Additive Manufacturing and Characterization of Additive Manufacturing Machine', 2016, doi: 10.13140/RG.2.1.3630.6009.
- [31] J. R. C. Dizon, A. H. Espera, Q. Chen, and R. C. Advincula, 'Mechanical characterization of 3D-printed polymers', *Additive Manufacturing*, vol. 20, pp. 44–67, Mar. 2018, doi: 10.1016/j.addma.2017.12.002.
- [32] ASTM International, 'ASTM F2792-12a', *Standard terminology for additive manufacturing technologies*, 2012, doi: 10.1520/F2792-12A.
- [33] N. Shahrubudin, T. C. Lee, and R. Ramlan, 'An Overview on 3D Printing Technology: Technological, Materials, and Applications', *Procedia Manufacturing*, vol. 35, pp. 1286–1296, 2019, doi: 10.1016/j.promfg.2019.06.089.
- [34] J. Zhang, N. Amini, D. A. V. Morton, and K. P. Hapgood, 'Binder jetting of well-controlled powder agglomerates for breakage studies', *Advanced Powder Technology*, vol. 32, no. 1, pp. 19–29, Jan. 2021, doi: 10.1016/j.apt.2020.11.012.
- [35] X. Wang, M. Jiang, Z. Zhou, J. Gou, and D. Hui, '3D printing of polymer matrix composites: A review and prospective', *Composites Part B: Engineering*, vol. 110, pp. 442–458, Feb. 2017, doi: 10.1016/j.compositesb.2016.11.034.
- [36] M. Kutz, *Applied Plastics Engineering Handbook*, II. Chadds Ford, PA, USA: Elsevier, 2017.
- [37] D.-H. Ko, K.-W. Gyak, and D.-P. Kim, 'Emerging microreaction systems based on 3D printing techniques and separation technologies', *Journal of Flow Chemistry*, vol. 7, no. 3–4, pp. 72–81, Sep. 2017, doi: 10.1556/1846.2017.00013.
- [38] S. Waheed *et al.*, '3D printed microfluidic devices: enablers and barriers', *Lab Chip*, vol. 16, no. 11, pp. 1993–2013, 2016, doi: 10.1039/C6LC00284F.

- [39] S. Naidu, 'Polyjet Technology', *MKS Technology Pvt. Ltd.* <http://www.mkstechgroup.com/polyjet-technology/> (accessed May 12, 2021).
- [40] M. Layani, X. Wang, and S. Magdassi, 'Novel Materials for 3D Printing by Photopolymerization', *Adv. Mater.*, vol. 30, no. 41, p. 1706344, Oct. 2018, doi: 10.1002/adma.201706344.
- [41] J. Garcia, Z. Yang, R. Mongrain, R. L. Leask, and K. Lachapelle, '3D printing materials and their use in medical education: a review of current technology and trends for the future', *BMJ STEL*, vol. 4, no. 1, pp. 27–40, Jan. 2018, doi: 10.1136/bmjstel-2017-000234.
- [42] G. Garechana, R. Río-Belver, I. Bidosola, and E. Cilleruelo-Carrasco, 'A method for the detection and characterization of technology fronts: Analysis of the dynamics of technological change in 3D printing technology', *PLoS ONE*, vol. 14, no. 1, p. e0210441, Jan. 2019, doi: 10.1371/journal.pone.0210441.
- [43] S. L. Sing, C. F. Tey, J. H. K. Tan, S. Huang, and W. Y. Yeong, '3D printing of metals in rapid prototyping of biomaterials: Techniques in additive manufacturing', in *Rapid Prototyping of Biomaterials*, Elsevier, 2020, pp. 17–40. doi: 10.1016/B978-0-08-102663-2.00002-2.
- [44] C. Groth, N. D. Kravitz, P. E. Jones, J. W. Graham, and W. R. Redmond, 'Three-Dimensional Printing Technology', no. 8, p. 12, 2014.
- [45] C. W. Hull, 'The Birth of 3D Printing', *D Printing*, p. 7.
- [46] J. Kwon, J. Ock, and N. Kim, 'Mimicking the Mechanical Properties of Aortic Tissue with Pattern-Embedded 3D Printing for a Realistic Phantom', *Materials*, vol. 13, no. 21, p. 5042, Nov. 2020, doi: 10.3390/ma13215042.
- [47] F. Rengier *et al.*, '3D printing based on imaging data: review of medical applications', *Int J CARS*, vol. 5, no. 4, pp. 335–341, Jul. 2010, doi: 10.1007/s11548-010-0476-x.
- [48] A. Sensini and L. Cristofolini, 'Biofabrication of electrospun scaffolds for the regeneration of tendons and ligaments', *Materials*, vol. 11, no. 10, pp. 1–43, 2018, doi: 10.3390/ma11101963.
- [49] Q. Yan *et al.*, 'A Review of 3D Printing Technology for Medical Applications', *Engineering*, vol. 4, no. 5, pp. 729–742, Oct. 2018, doi: 10.1016/j.eng.2018.07.021.
- [50] M. N. Nadagouda, V. Rastogi, and M. Ginn, 'A review on 3D printing techniques for medical applications', *Current Opinion in Chemical Engineering*, vol. 28, pp. 152–157, Jun. 2020, doi: 10.1016/j.coche.2020.05.007.
- [51] Z. Al-Dulimi, M. Wallis, D. K. Tan, M. Maniruzzaman, and A. Nokhodchi, '3D printing technology as innovative solutions for biomedical applications', *Drug Discovery Today*, vol. 26, no. 2, pp. 360–383, Feb. 2021, doi: 10.1016/j.drudis.2020.11.013.
- [52] V. M. Vaz and L. Kumar, '3D Printing as a Promising Tool in Personalized Medicine', *AAPS PharmSciTech*, vol. 22, no. 1, p. 49, Jan. 2021, doi: 10.1208/s12249-020-01905-8.
- [53] M. Heller *et al.*, 'Applications of patient-specific 3D printing in medicine', *International Journal of Computerized Dentistry*, vol. 19, no. 4, pp. 323–339, 2016.
- [54] D. M. Kalaskar, *3D Printing in Medicine*. 2017.
- [55] A. Sensini and L. Cristofolini, 'Biofabrication of electrospun scaffolds for the regeneration of tendons and ligaments', *Materials*, vol. 11, no. 10, pp. 1–43, 2018, doi: 10.3390/ma11101963.
- [56] Z. Al-Dulimi, M. Wallis, D. K. Tan, M. Maniruzzaman, and A. Nokhodchi, '3D printing technology as innovative solutions for biomedical applications', *Drug Discovery Today*, vol. 26, no. 2, pp. 360–383, 2021, doi: 10.1016/j.drudis.2020.11.013.
- [57] Stratasys, 'Medical Customers Across the Globe adopt Stratasys J750 Digital Anatomy 3D Printer', 2020.
- [58] Stratasys, *Empower Medical Innovation*.
- [59] J. V. Chen, A. B. C. Dang, and A. Dang, 'Comparing cost and print time estimates for six commercially-available 3D printers obtained through slicing software for clinically relevant

- anatomical models', *3D Print Med*, vol. 7, no. 1, p. 1, Dec. 2021, doi: 10.1186/s41205-020-00091-4.
- [60] Stratasys, 'Stratasys J735 and J750'. [Online]. Available: <https://www.stratasys.com/>
- [61] Stratasys, 'Brochure J750 Digital Anatomy Printer'. Stratasys, 2020.
- [62] Stratasys Ltd., 'J750™ Digital Anatomy™ 3D Printer', 2021. <https://www.stratasys.com/3d-printers/j750-digital-anatomy>
- [63] Stratasys Ltd., 'Stampante 3D J750™ Digital Anatomy™', 2021. <https://www.stratasys.com/it/3d-printers/j750-digital-anatomy>
- [64] Stratasys, 'Agilus30', *Stratasys*. <https://www.stratasys.com/materials/search/agilus30> (accessed Jul. 10, 2021).
- [65] Stratasys, 'Agilus30 - Best Practice Polyjet'. 2021.
- [66] Stratasys, 'PolyJet 3D Printers (Systems and Materials)'. 2018.
- [67] S. Akbari *et al.*, 'Enhanced multimaterial 4D printing with active hinges', *Smart Mater. Struct.*, vol. 27, no. 6, p. 065027, Jun. 2018, doi: 10.1088/1361-665X/aabe63.
- [68] Stratasys, 'Vero', *Stratasys*. <https://www.stratasys.com/materials/search/vero> (accessed Jul. 10, 2021).
- [69] Spring SRL, 'Scheda generale Polyjet'. Spring SRL. [Online]. Available: [www.springitalia.com](http://www.springitalia.com)
- [70] Stratasys, 'VeroClear', *Stratasys*. <https://www.stratasys.com/materials/search/veroclear> (accessed Jul. 12, 2021).
- [71] Stratasys, 'Tango', *Stratasys*. <https://www.stratasys.com/materials/search/tango> (accessed Jul. 12, 2021).
- [72] F. F. Abayazid and M. Ghajari, 'Material characterisation of additively manufactured elastomers at different strain rates and build orientations', *Additive Manufacturing*, vol. 33, p. 101160, May 2020, doi: 10.1016/j.addma.2020.101160.
- [73] L. Severseike, V. Lee, T. Brandon, C. Bakken, and V. Bhatia, 'Polyjet 3D printing of tissue-mimicking materials: how well can 3D printed synthetic myocardium replicate mechanical properties of organic myocardium?', *Bioengineering*, preprint, Oct. 2019. doi: 10.1101/825794.
- [74] P. Maroti *et al.*, 'Printing orientation defines anisotropic mechanical properties in additive manufacturing of upper limb prosthetics', *Mater. Res. Express*, vol. 6, no. 3, p. 035403, Dec. 2018, doi: 10.1088/2053-1591/aaf5a9.
- [75] V. Slesarenko and S. Rudykh, 'Towards mechanical characterization of soft digital materials for multimaterial 3D-printing', *International Journal of Engineering Science*, vol. 123, pp. 62–72, Feb. 2018, doi: 10.1016/j.ijengsci.2017.11.011.
- [76] K. Hofer, 'Materials testing', *Encyclopedia Britannica*, Jun. 2018, Accessed: Aug. 27, 2021. [Online]. Available: <https://www.britannica.com/technology/materials-testing>
- [77] ASTM International, 'ASTM D638-14', *Standard Test Method for Tensile Properties of Plastics*, 2014, doi: 10.1520/D0638-14.
- [78] ASTM International, 'ASTM D412-16', *Standard Test Methods for Vulcanized Rubber and Thermoplastic Elastomers - Tension*, 2016, doi: 10.1520/D0638-14.
- [79] TestResources, 'ASTM D412 Tension Testing for Rubber and Elastomers', *Test Machines, Grips and Fixtures*, 2021. <https://www.testresources.net/applications/standards/astm/astm-d412-tension-testing-for-rubber-and-elastomers/> (accessed Aug. 28, 2021).
- [80] TestResources, 'Impact test', *Test Machines, Grips and Fixtures*, 2021. <https://www.testresources.net/applications/test-types/impact-test/> (accessed Aug. 28, 2021).

- [81] TestResources, 'Fracture Test', *Test Machines, Grips and Fixtures*, 2021. <https://www.testresources.net/applications/test-types/fracture-test/> (accessed Aug. 28, 2021).
- [82] Illinois Tool Works Inc., 'Tensile Testing and Tensile Testing Machines', *Instron*. <https://www.instron.com/it-it/our-company/library/test-types/tensile-test?region=Italy> (accessed Aug. 28, 2021).
- [83] UKEssays, 'Theory Of Tensile Test Engineering Essay', Nov. 2018. <https://www.ukessays.com/essays/engineering/> (accessed Aug. 29, 2018).
- [84] R. Hunt, 'Tensile Testing for 3D Printing Materials', *Protolabs*, Mar. 24, 2020. <https://www.protolabs.com/resources/blog/tensile-testing-for-3d-printing-materials/> (accessed Aug. 29, 2021).
- [85] Michigan Technological University, 'Tensile Test Experiment', *Michigan Tech*, 2021. <https://www.mtu.edu/materials/k12/experiments/tensile/> (accessed Aug. 27, 2021).
- [86] MTS Systems Corporation, 'MTS Insight Electomechanical Testing System'. 2009.
- [87] D. Özer Kaya, 'Architecture of tendon and ligament and their adaptation to pathological conditions', in *Comparative Kinesiology of the Human Body*, Elsevier, 2020, pp. 115–147. doi: 10.1016/B978-0-12-812162-7.00009-6.
- [88] A. A. Biewener, 'Tendons and Ligaments: Structure, Mechanical Behavior and Biological Function', in *Collagen*, P. Fratzl, Ed. Boston, MA: Springer US, 2008, pp. 269–284. doi: 10.1007/978-0-387-73906-9\_10.
- [89] J. H.-C. Wang, 'Mechanobiology of tendon', *Journal of Biomechanics*, vol. 39, no. 9, pp. 1563–1582, Jan. 2006, doi: 10.1016/j.jbiomech.2005.05.011.
- [90] C. Maganaris, P. Chatzistergos, N. Reeves, and M. Narici, 'Quantification of Internal Stress-Strain Fields in Human Tendon: Unraveling the Mechanisms that Underlie Regional Tendon Adaptations and Mal-Adaptations to Mechanical Loading and the Effectiveness of Therapeutic Eccentric Exercise.', *Frontiers in Physiology*, vol. 8, no. 91, Feb. 2017, doi: 10.3389/fphys.2017.00091.
- [91] P. Corrigan, D. Cortes, and R. Pohlig, 'Tendon Morphology and Mechanical Properties Are Associated With the Recovery of Symptoms and Function in Patients With Achilles Tendinopathy', *The Orthopaedic Journal of Sports Medicine*, vol. 8, no. 4, 2020, doi: 10.1177/2325967120917271.
- [92] 'Tendinopathy alters mechanical and material properties of the Achilles tendon', *J Appl Physiol (1985)*, vol. 108, no. 3, pp. 670–5, Mar. 2010, doi: 10.1152/jappphysiol.00259.2009.
- [93] C. Helland *et al.*, 'Mechanical properties of the patellar tendon in elite volleyball players with and without patellar tendinopathy', *Br J Sports Med*, vol. 47, no. 13, pp. 862–868, Sep. 2013, doi: 10.1136/bjsports-2013-092275.
- [94] G. M. Hassan, 'Deformation measurement in the presence of discontinuities with digital image correlation: A review', *Optics and Lasers in Engineering*, vol. 137, p. 106394, Feb. 2021, doi: 10.1016/j.optlaseng.2020.106394.
- [95] K. F. Mallett and E. M. Arruda, 'Digital image correlation-aided mechanical characterization of the anteromedial and posterolateral bundles of the anterior cruciate ligament', *Acta Biomaterialia*, vol. 56, pp. 44–57, Jul. 2017, doi: 10.1016/j.actbio.2017.03.045.
- [96] D. Solav, K. M. Moerman, A. M. Jaeger, K. Genovese, and H. M. Herr, 'MultiDIC: An Open-Source Toolbox for Multi-View 3D Digital Image Correlation', *IEEE Access*, vol. 6, pp. 30520–30535, 2018, doi: 10.1109/ACCESS.2018.2843725.
- [97] Correlated Solutions Inc., 'Vic-3D software manual version 8.4'.

- [98] P. L. Reu *et al.*, 'DIC Challenge: Developing Images and Guidelines for Evaluating Accuracy and Resolution of 2D Analyses', *Exp Mech*, vol. 58, no. 7, pp. 1067–1099, Sep. 2018, doi: 10.1007/s11340-017-0349-0.
- [99] M. Sutton, J. J. Orteu, and H. Schreier, *Image Correlation for Shape, Motion and Deformation Measurements*. Boston: Springer, 2009.
- [100] W. Broughton, 'Testing the mechanical, thermal and chemical properties of adhesives for marine environments', in *Adhesives in Marine Engineering*, Elsevier, 2012, pp. 99–154. doi: 10.1533/9780857096159.2.99.
- [101] 'A practical guide to DIC'. [Online]. Available: <https://digitalimagecorrelation.org/>
- [102] M. Palanca, G. Tozzi, and L. Cristofolini, 'The use of digital image correlation in the biomechanical area: a review', *International Biomechanics*, vol. 3, no. 1, pp. 1–21, Jan. 2016, doi: 10.1080/23335432.2015.1117395.
- [103] S. J. Song and N. He, 'Digital Image Processing and Coordinate Transformation for Vic-3D System', *AMM*, vol. 333–335, pp. 1002–1006, Jul. 2013, doi: 10.4028/www.scientific.net/AMM.333-335.1002.
- [104] Y. L. Dong and B. Pan, 'A Review of Speckle Pattern Fabrication and Assessment for Digital Image Correlation', *Exp Mech*, vol. 57, no. 8, pp. 1161–1181, Oct. 2017, doi: 10.1007/s11340-017-0283-1.
- [105] Correlated Solutions Inc., 'Testing guide'.
- [106] G. Lionello and L. Cristofolini, 'A practical approach to optimizing the preparation of speckle patterns for digital-image correlation', *Meas. Sci. Technol.*, vol. 25, no. 10, p. 107001, Oct. 2014, doi: 10.1088/0957-0233/25/10/107001.
- [107] G. Stoilov, V. Kavardzhikov, and D. Pashkouleva, 'A Comparative Study of Random Patterns for Digital Image Correlation', *Journal of Theoretical and Applied Mechanics*, vol. 42, no. 2, pp. 55–66, Jun. 2012, doi: 10.2478/v10254-012-0008-x.
- [108] M. Lawson and J. Sirohi, 'Measurement of Deformation of Rotating Blades Using Digital Image Correlation', presented at the 52nd AIAA/ASME/ASCE/AHS/ASC Structures, Structural Dynamics and Materials Conference, Denver, Colorado, Apr. 2011. doi: 10.2514/6.2011-1876.
- [109] C. J. Woods, M. O. Heller, and M. Browne, 'Assessing the Effect of Unicondylar Knee Arthroplasty on Proximal Tibia Bone Strains Using Digital Image Correlation', *IJBES*, vol. 4, no. 3, pp. 01–06, Jul. 2017, doi: 10.5121/ijbes.2017.4301.
- [110] M. Lesser, 'Charge coupled device (CCD) image sensors', in *High Performance Silicon Imaging*, Elsevier, 2014, pp. 78–97. doi: 10.1533/9780857097521.1.78.
- [111] P. Reu, 'Calibration: Stereo Calibration', *Experimental Techniques*, vol. 38, no. 1, pp. 1–2, Jan. 2014, doi: 10.1111/ext.12048.
- [112] M. A. Sutton, J. H. Yan, V. Tiwari, H. W. Schreier, and J. J. Orteu, 'The effect of out-of-plane motion on 2D and 3D digital image correlation measurements', *Optics and Lasers in Engineering*, vol. 46, no. 10, pp. 746–757, Oct. 2008, doi: 10.1016/j.optlaseng.2008.05.005.
- [113] J. Heikkila and O. Silven, 'A four-step camera calibration procedure with implicit image correction', in *Proceedings of IEEE Computer Society Conference on Computer Vision and Pattern Recognition*, San Juan, Puerto Rico, 1997, pp. 1106–1112. doi: 10.1109/CVPR.1997.609468.
- [114] Y. Wang, P. Lava, S. Coppieters, P. V. Houtte, and D. Debruyne, 'Application of a Multi-Camera Stereo DIC Set-up to Assess Strain Fields in an Erichsen Test: Methodology and Validation', *Strain*, vol. 49, no. 2, pp. 190–198, Apr. 2013, doi: 10.1111/str.12027.
- [115] F. Chen, X. Chen, X. Xie, X. Feng, and L. Yang, 'Full-field 3D measurement using multi-camera digital image correlation system', *Optics and Lasers in Engineering*, vol. 51, no. 9, pp. 1044–1052, Sep. 2013, doi: 10.1016/j.optlaseng.2013.03.001.

- [116] B. Pan, 'Recent Progress in Digital Image Correlation', *Exp Mech*, vol. 51, no. 7, pp. 1223–1235, Sep. 2011, doi: 10.1007/s11340-010-9418-3.
- [117] L. Luu, Z. Wang, and M. Vo, 'Accuracy enhancement of digital image correlation with B-spline interpolation', *Optics Letters*, vol. 36, no. 16, pp. 3070–3072, Aug. 2011.
- [118] H. Lu and P. D. Cary, 'Deformation measurements by digital image correlation: Implementation of a second-order displacement gradient', *Experimental Mechanics*, vol. 40, no. 4, pp. 393–400, Dec. 2000, doi: 10.1007/BF02326485.
- [119] Correlated Solutions Inc., 'brochure'. [Online]. Available: <https://correlatedsolutions.com/>
- [120] Correlated Solutions Inc., 'VIC-3D 9 with iris'. [Online]. Available: <https://www.correlatedsolutions.com/>
- [121] Correlated Solutions Inc., 'The VIC-3D 9 System'. [Online]. Available: <https://www.correlatedsolutions.com/>
- [122] A. D. Vardimon, D. Robbins, and T. Brosh, 'In-vivo von Mises strains during Invisalign treatment', *American Journal of Orthodontics and Dentofacial Orthopedics*, vol. 138, no. 4, pp. 399–409, Oct. 2010, doi: 10.1016/j.ajodo.2008.11.027.
- [123] TNO DIANA, 'Equivalent Von Mises Strain', *dianafea.com*, 2012. <https://dianafea.com/manuals/> (accessed Jul. 19, 2021).
- [124] R. De Santis, F. Sarracino, F. Mollica, P. A. Netti, L. Ambrosio, and L. Nicolais, 'Continuous fibre reinforced polymers as connective tissue replacement', *Composites Science and Technology*, vol. 64, no. 6, pp. 861–871, May 2004, doi: 10.1016/j.compscitech.2003.09.008.
- [125] Mitsubishi Chemical America Inc., 'HydroThane', *AdvanSource Biomaterials*, 2021. <http://www.advbiomaterials.com/products/hydrophilic/hydrothane.html> (accessed Sep. 12, 2021).
- [126] H. Wang, W. Liu, J. Huang, D. Yang, and X. Qiu, 'Bioinspired Engineering towards Tailoring Advanced Lignin/Rubber Elastomers', *Polymers*, vol. 10, no. 9, p. 1033, Sep. 2018, doi: 10.3390/polym10091033.
- [127] A. Bannykh, S. Katz, Z. Barkay, and N. Lachman, 'Preserving Softness and Elastic Recovery in Silicone-Based Stretchable Electrodes Using Carbon Nanotubes', *Polymers*, vol. 12, no. 6, p. 1345, Jun. 2020, doi: 10.3390/polym12061345.
- [128] A. Filley, 'Tendonitis vs tendinosis: the inflammation vs degeneration debate', *Sports Injury Bulletin*. <https://www.sportsinjurybulletin.com/tendonitis-vs-tendinosis-the-inflammation-vs-degeneration-debate/> (accessed Sep. 22, 2021).
- [129] Stratasys, 'Anatomical 3D printer materials', *Stratasys*. <https://www.stratasys.com/materials/search/digital-anatomy> (accessed Sep. 25, 2021).
- [130] A. Cazón, P. Morer, and L. Matey, 'PolyJet technology for product prototyping: Tensile strength and surface roughness properties', *Proceedings of the Institution of Mechanical Engineers, Part B: Journal of Engineering Manufacture*, vol. 228, no. 12, pp. 1664–1675, Dec. 2014, doi: 10.1177/0954405413518515.
- [131] J. Mueller, K. Shea, and C. Daraio, 'Mechanical properties of parts fabricated with inkjet 3D printing through efficient experimental design', *Materials & Design*, vol. 86, pp. 902–912, Dec. 2015, doi: 10.1016/j.matdes.2015.07.129.
- [132] D. Blanco, P. Fernandez, and A. Noriega, 'Nonisotropic experimental characterization of the relaxation modulus for PolyJet manufactured parts', *J. Mater. Res.*, vol. 29, no. 17, pp. 1876–1882, Sep. 2014, doi: 10.1557/jmr.2014.200.
- [133] A. Kęsy and J. Kotliński, 'Mechanical properties of parts produced by using polymer jetting technology', *Archives of Civil and Mechanical Engineering*, vol. 10, no. 3, pp. 37–50, Jan. 2010, doi: 10.1016/S1644-9665(12)60135-6.

- [134] F. Noyes and E. Grood, 'The strength of the anterior cruciate ligament in humans and Rhesus monkeys', *The Journal of Bone & Joint Surgery*, vol. 58, no. 8, pp. 1074–1082, Dec. 1976, doi: 10.2106/00004623-197658080-00006.
- [135] M. Heller, 'Applications of patient-specific 3D printing in medicine Patientenspezifische Anwendungen von 3-D-Druck in der Medizin', *International Journal of Computerized Dentistry*, p. 18.
- [136] K. Larson, 'Can You Estimate Modulus From Durometer Hardness for Silicones?', p. 5.
- [137] B. Reuss, 'Convert Durometer to Young's Modulus', *Computer Aided Technology*, Jul. 14, 2011. <https://www.cati.com/> (accessed Sep. 20, 2021).
- [138] R. Hedayati, A. Güven, and S. van der Zwaag, '3D gradient auxetic soft mechanical metamaterials fabricated by additive manufacturing', *Appl. Phys. Lett.*, vol. 118, no. 14, p. 141904, Apr. 2021, doi: 10.1063/5.0043286.
- [139] S. J. P. Callens, C. H. Arns, A. Kuliesh, and A. A. Zadpoor, 'Decoupling Minimal Surface Metamaterial Properties Through Multi-Material Hyperbolic Tilings', *Adv. Funct. Mater.*, vol. 31, no. 30, p. 2101373, Jul. 2021, doi: 10.1002/adfm.202101373.
- [140] D. M. J. Dykstra, J. Busink, B. Ennis, and C. Coulais, 'Viscoelastic Snapping Metamaterials', *Journal of Applied Mechanics*, vol. 86, no. 11, p. 111012, Nov. 2019, doi: 10.1115/1.4044036.
- [141] D. M. J. Dykstra, J. Busink, B. Ennis, and C. Coulais, 'Viscoelastic Metamaterials', p. 11.
- [142] A. Bossart, D. M. J. Dykstra, J. van der Laan, and C. Coulais, 'Oligomodal metamaterials with multifunctional mechanics', *Proc Natl Acad Sci USA*, vol. 118, no. 21, p. e2018610118, May 2021, doi: 10.1073/pnas.2018610118.
- [143] G. Dämmer, S. Gablenz, A. Hildebrandt, and Z. Major, 'Design of an Additively Manufacturable Multi-Material Light-Weight Gripper with integrated Bellows Actuators', *Adv. sci. technol. eng. syst. j.*, vol. 4, no. 2, pp. 23–33, 2019, doi: 10.25046/aj040204.
- [144] M. J. Mirzaali, A. Caracciolo, H. Pahlavani, S. Janbaz, L. Vergani, and A. A. Zadpoor, 'Multi-material 3D printed mechanical metamaterials: Rational design of elastic properties through spatial distribution of hard and soft phases', *Appl. Phys. Lett.*, vol. 113, no. 24, p. 241903, Dec. 2018, doi: 10.1063/1.5064864.
- [145] 'Polymer Properties', *crow*, 2015. <http://polymerdatabase.com/> (accessed Sep. 20, 2021).
- [146] Wikipedia, 'Poisson's ratio', *wikipedia*, 2021. <https://en.wikipedia.org/> (accessed Sep. 20, 2021).
- [147] T. Sanyal, 'Jute, Jute Fiber, and Jute Yarn', in *Jute Geotextiles and their Applications in Civil Engineering*, Singapore: Springer Singapore, 2017, pp. 7–17. doi: 10.1007/978-981-10-1932-6\_2.
- [148] 'How heat affects Textile Fiber's properties', *MultieducationBd*, Jan. 20, 2012. <http://multieducationbd.blogspot.com/> (accessed Oct. 03, 2021).
- [149] Comsol, 'Mesh Element Quality and Size'. <https://doc.comsol.com/> (accessed Oct. 07, 2021).
- [150] ANSYS, Inc., 'Mesh quality', *afs.enea*, Jan. 29, 2009. <https://www.afs.enea.it/> (accessed Oct. 07, 2021).